Boundary-Layer Linear Stability Theory

Leslie M. Mack
Jet Propulsion Laboratory
California Institute of Technology
Pasadena, California 91109
U.S.A.

AGARD Report No. 709, Part 3

1984

Contents

List of Figures

List of Tables

Preface

This document is a reproduction of the original. Effort was made to faithfully reproduce the original document while incorporating more modern features through LaTeX typesetting such as fully hyperlinked table of contents, list of figures, list of tables, reference citations, and figures references as well as a functional PDF table of contents. Additional effort was made to double check references and correct them where necessary. Conversion was performed by Alex Craig (`sacraig@email.arizona.edu`) and Jerrod Hofferth, June 2013. Any errors may be reported. The original may be found under the following DTIC handle: `http://www.dtic.mil/docs/citations/ADP004046`.

Last update: February 12, 2018

Chapter 1

Introduction

1.1 Historical background

Most fluid flows are turbulent rather than laminar and the reason why this is so has been the object of study by several generations of investigators. One of the earliest explanations was that the laminar flow is unstable, and the linear instability theory was first developed to explore this possibility. Such an approach tells nothing about turbulence, or about the details of its initial appearance, but it does explain why the original laminar flow can no longer exist. A series of early papers by Rayleigh (1880, 1887, 1892, 1895, 1913) produced many notable results concerning the instability of inviscid flows, such as the discovery of inflectional instability, but little progress was made toward the original goal. Viscosity was commonly thought to act only to stabilize the flow, and flows with convex velocity profiles thus appeared to be stable. In a review of 30 years of effort, Noether (1921) wrote: "The method of small disturbances, which can be considered essentially closed, has led to no useful results concerning the origin of turbulence."

Although Taylor (1915) had already indicated that viscosity can destabilize a flow that is otherwise stable, it remained for Prandtl (1921), in the same year as Noether's review paper, to independently make the same discovery as Taylor and set in motion the investigations that led to a viscous theory of boundary-layer instability a few years later (Tollmien, 1929). A series of papers by Schlichting (1933a,b, 1935, 1940), and a second paper by Tollmien (1935) that resulted in a well-developed theory with a small body of numerical results. Any expectation that instability and transition to turbulence are synonymous in boundary layers was dashed by the low value of the critical Reynolds number $\mathrm{Re}_{\mathrm{cr}}$, i.e. the x Reynolds number at which instability first appears. Tollmien's value of $\mathrm{Re}_{\mathrm{cr}}$ for the Blasius boundary layer was 60,000, and even in the high turbulence wind tunnels of that time, transition was observed to occur between $\mathrm{Re}_{\mathrm{t}} = 3.5 \times 10^5$ and 1×10^6. In what can be considered the earliest application of linear stability theory to transition prediction, Schlichting (1933a) calculated the amplitude ratio of the most amplified frequency as a function of Reynolds number for a Blasius boundary layer, and found that this quantity had values between five and nine at the observed Re_{t}.

Outside of Germany, the stability theory received little acceptance because of the failure to observe the predicted waves, mathematical obscurities in the theory, and also a general feeling that a linear theory could not have anything useful to say about the origin of turbulence, which is inherently nonlinear. A good idea of the low repute of the theory can be gained by reading the paper of Taylor (1938) and the discussion on this subject in the Proceedings of the 5th Congress of Applied Mechanics held in 1938. It was in this atmosphere of disbelief that one of the most celebrated experiments in the history of fluid mechanics was carried out. The experiment of Schubauer and Skramstad (1947), which was performed in the early 1940's but not published until some years later because of wartime censorship, completely reversed the prevailing opinion and fully vindicated the Göttingen proponents of the theory. This experiment unequivocally demonstrated the existence of instability waves in a boundary layer, their connection with transition, and the quantitative description of their behavior by the theory of Tollmien and Schlichting. it made and enormous impact at the time of its publication, and by its very completeness seemed to answer most of the questions concerning the linear theory. To a large extent, subsequent experimental work on transition went in other directions, and the possibility that linear theory can be quantitatively related to transition has not received a decisive

experimental test. On the other hand, it is generally accepted that flow parameters such as pressure gradient, suction and heat transfer qualitatively affect transition in the same manner predicted by the linear theory, and in particular that a flow predicted to be stable by the theory should remain laminar. This expectation has often been deceived. Even so, the linear theory, in the form of the e^9, or N-factor, method first proposed by Smith and Gamberoni (1956) and Van Ingen (1956), is today in routine use in engineering studies of laminar flow control [see, e.g., Hefner and Bushnell (1979)]. A good introduction to the complexities of transition and the difficulties involved in trying to arrive at a rational approach to its prediction can be found in three reports by Morkovin (1968, 1978, 1983), and a review article by Reshotko (1976).

The German investigators were undeterred by the lack of acceptance of the stability theory elsewhere, and made numerous applications of it to boundary layers with pressure gradients and suction. This work is summarized by Schlichting (1979). We may make particular mention of the work by Pretsch (1942), as he provided the only large body of numerical results for exact boundary-layer solutions before the advent of the computer age by calculating the stability characteristics of the Falkner-Skan family of velocity profiles. The unconvincing mathematics of the asymptotic theory was put on a more solid foundation by Lin (1945) and Wasow (1948), and this work has been successfully continued by Reid and his collaborators (Lakin et al., 1978).

When in about 1960 the digital computer reached a stage of development permitting the direct solution of the primary differential equations, numerical results were obtained from the linear theory during the next ten years for many different boundary-layer flows: three-dimensional boundary layers [Brown (1959), following the important theoretical contribution of of Stuart in Gregory et al. (1955)]; free-convectoin boundary layers (Kurtz and Crandall, 1962; Nachtsheim, 1963); compressible boundary layers (Brown, 1962; Mack, 1965b, 1969); boundary layers on complient walls (Landahl and Kaplan, 1965); a recomputations of Falkner-Skan flows (Wazzan et al., 1968a); unsteady boundary layers (Obremski et al., 1969); and heated-wall water boundary layers (Wazzan et al., 1968b). More recent work has focused on three-dimensional boundary layers in response to the renewed interest in laminar-flow control for swept wings (Srokowski and Orszag, 1977; Mack, 1977, 1979a,b, 1981; Nayfeh, 1980a,b; Cebeci and Stewartson, 1980a,b; Lekoudis, 1979, 1980). A notable contribution to linear stability theory that stands somewhat apart from the principal line of development has been provided by Gaster (1968, 1975, 1978, 1981a,b, 1982a,b) in a series of papers on the wave packets produced by a pulsed point source in a boundary layer. Gaster's work on this problem also includes a major stability experiment (Gaster and Grant, 1975).

There are a number of general references that are helpful to anyone interested in the linear theory. Review articles are by Schlichting (1959); Shen (1964); Stuart (1963) and Reid (1965). Books are by Lin (1955); Betchov and Criminale (1967), and Drazin and Reid (1981). Schlichting's book on boundary-layer theory (1979) contains two chapters on stability theory and transition, and Monin and Yaglom's book on tubulence (1971a; 1971b) contains a lengthy chapter on the same subject, as does the book by White (1974) on viscous flow theory. Reviews of transition have been given by Dryden (1959); Tani (1969, 1981); Morkovin (1968, 1978, 1983) and Reshotko (1976). An extensive discussion of both stability theory and transition, not all at high speeds in spite of the title, may be found in the recorded lectures of Mack and Morkovin (1971).

1.2 Elements of stability theory

Before we get into the main body of the subject, a brief introduction is in order to orient those who are new to this field. The stability theory is mainly concerned with individual sine waves propagating in the boundary layer parallel to the wall. These waves are waves of vorticity and are commonly referred to as Tollmien-Schlichting waves, or TS waves, or simply as instability waves. The amplitude of the waves, which vary through the boundary layer and die off exponentially in the freestream, are small enough so that a linear theory may be used. The frequency of a wave is ω and the wavenumber is $k = 2\pi/\lambda$, where λ is the wavelength. The wave may be two-dimensional, with the lines of constant phase normal to the freestream direction (and parallel tot he wall), or it may be oblique, in which case the wavenumber is a vector $\vec{k}$ at angle ψ to the freestream direction with streamwise (x) component α and spanwise (z) component β. The phase velocity c is always less than the freestream velocity U_1, so that at some point in the boundary layer the mean velocity is equal to c. This point is called the critical point, or critical layer, and it plays a central role in the mathematical theory. The wave amplitude usually has a maximum near the critical layer.

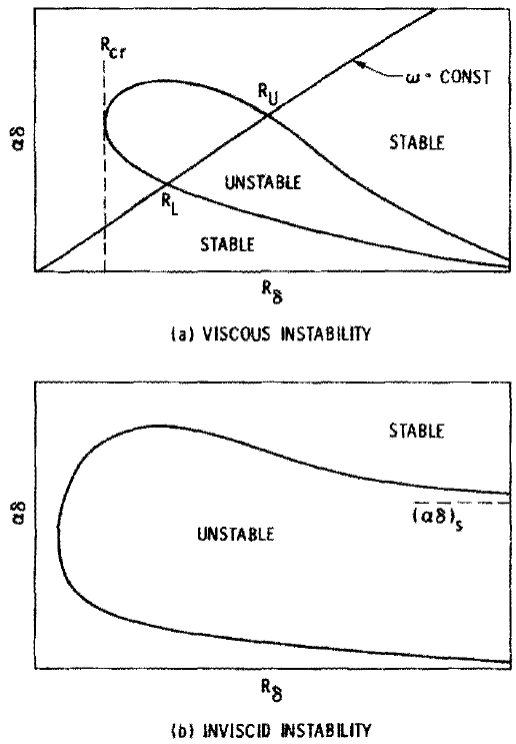

Figure 1.1: Typical neutral-stability curves.

At any given distance from the origin of the boundary layer, or better, at any given Reynolds number $Re = U_1 x/\nu$, where ν is the kinematic viscosity, an instability wave of frequency ω will be in one of three states: damped, neutral, or amplified. The numerical results calculated from the stability theory are often presented in the form of diagrams of neutral stability which show graphically the boundaries between regions of stability and instability in (ω, Re) space or (k, Re) space. There are two general kinds of neutral-stability diagrams to be found, as shown in Fig. 1.1 for a two-dimensional wave in a two-dimensional boundary layer. In this figure, the dimensionless wavenumber $\alpha\delta$ is plotted against R_δ, the Reynolds number based on the boundary-layer thickness δ. Waves are neutral at those values of $\alpha\delta$ and R_δ which lie on the contour marked neutral; they are amplified inside of the contour, and are damped everywhere else. With a neutral-stability curve of type (a), all wavenumbers are damped at sufficiently high Reynolds numbers. In this case, the mean flow is said to have viscous instability. Since decreasing Reynolds number, or increasing viscosity, can lead to instability, it is apparent that viscosity does not act solely to damp out waves, but can actually have a destabilizing influence. The incompressible flat-plate (Blasius) boundary layer, and all incompressible boundary layers with a favorable pressure gradient, are examples of flows which are unstable only through the action of viscosity. With a neutral-stability curve of type (b), a non-zero neutral wavenumber $(\alpha\delta)_s$ exists at $Re \to \infty$, and wavenumbers smaller than $(\alpha\delta)_s$ are unstable no matter how large the Reynolds number becomes. A mean flow with a type (b) neutral-stability curve is said to have inviscid instability. The boundary layer in an adverse pressure gradient is an example of a flow of this kind.

In both cases (a) and (b), all waves with $\alpha\delta$ less than the peak value on the neutral-stability curve are unstable for some range of Reynolds numbers. The Reynolds number $Re_{\rm cr}$ below which no amplification is possible is called the minimum critical Reynolds number. It is often an objective of stability theory to determine $Re_{\rm cr}$, although it must be cautioned that this quantity only tells where instability starts, and cannot be relied upon to indicate the relative instability of various mean flows further downstream. It is definitely not proper to identify $Re_{\rm cr}$ with the transition point.

A wave which is introduced into a steady boundary layer with a particular frequency will preserve that

frequency as it propagates downstream, while the wavenumber will change. As shown in Fig. 1.1, a wave of frequency ω which passes through the unstable region will be damped up to $(Re)_{\mathrm{L}}$, the first point of neutral stability. Between $(Re)_{\mathrm{L}}$ and $(Re)_{\mathrm{U}}$, the second neutral point, it will be amplified; downstream of $(Re)_{\mathrm{U}}$ it will be damped again. If the amplitude of a wave becomes large enough before $(Re)_{\mathrm{U}}$ is reached, then the nonlinear processes which eventually lead to transition will take over, and the wave will continue to grow even though the linear theory says it should damp.

The theory can be used to calculate amplification and damping rates as well as the frequency, wavenumber and Reynolds number of neutral waves. For example, it is possible to computer the amplification rate as a function of frequency at a given Re. The neutral-stability curve only identifies the band of unstable frequencies, but the amplification rate tells how fast each frequency is growing, and which frequency is growing the fastest. Even more useful than the amplification rate is the amplitude history of a wave of constant frequency as it travels through the unstable region. In the simplest form of the theory, this result can be calculated in the form of a ratio of the amplitude to some initial amplitude once the amplification rates are known. Consequently, it is possible to identify, given some initial disturbance spectrum, the frequency whose amplitude has increased the most at each Reynolds number. It is presumably one of these frequencies which, after it reaches some critical amplitude, triggers the whole transition process.

We have divided the following material into three major parts: the incompressible stability theory is in Part I, the compressible stability theory is in Part II, and three-dimensional stability theory, both incompressible and compressible, is in Part III. The field of laminar instability is a vast one, and many topics that could well have been included have been left out for lack of space. We have restricted ourselves strictly to boundary layers, but even here have omitted all flows where gravitational effects are important, low-speed boundary layers with wall heating or cooling, and the important subject of Görtler instability. Within the topics that have been included, we give a fairly complete account of what we consider to be the essential ideas, and of what is needed to understand the published literature and make intelligent use of a computer program for the solution of boundary-layer stability problems. Attention is concentrated principally on basic ideas, but also on the formulations which are incorporated into computer codes based on the shooting-method of solving the stability equations. Only selected numerical results are included, and these have been chosen for their illustrative value, and not with any pretension to comprehensive coverage. Numerous references are given, but the list is by no means complete. in particular, a number of USSR references have not been included because of my unfamiliarity with the Russian language. Much use has been made of a previous work (Mack, 1969), which is still the most complete source for compressible boundary-layer stability theory.

Part I

Incompressible Stability Theory

Chapter 2

Formulation of Incompressible Stability Theory

2.1 Derivation of parallel-flow stability equations

The three-dimensional (3D) Navier-Stokes equations of a viscous, incompressible fluid in Cartesian coordinates are

$$\frac{\partial \bar{u}_i^*}{\partial t^*} + \bar{u}_j^* \frac{\partial \bar{u}_i^*}{\partial x_j^*} = -\frac{1}{\rho^*}\frac{\partial \bar{p}^*}{\partial x_i^*} + \nu^* \nabla^2 \bar{U}_i^*, \tag{2.1a}$$

$$\frac{\partial \bar{u}_i^*}{\partial x_i^*} = 0, \tag{2.1b}$$

where $\bar{u}_i^* = (\bar{u}^*, \bar{v}^*, \bar{w}^*)$, $x_i^* = (x^*, y^*, z^*)$, and $i, j = (1, 2, 3)$ according to the summation convention. The asterisks denote dimensional quantities, and overbars denote time-dependent quantities. The velocities $\bar{u}^*$, $\bar{v}^*$, $\bar{w}^*$ are in the x^*, y^*, z^* directions, respectively, where x^* is the streamwise and z^* the spanwise coordinate; $\bar{p}^*$ is the pressure; ρ^* is the density; ν^* is the kinematic viscosity μ^*/ρ^*, with μ^* the viscosity coefficient. Equations 2.1a are teh momentum equations, and Eq. 2.1b is the continuity equation. We first put the equations in dimensionless form with the velocity scale U_r^{*2}, the length scale L^*, and the pressure scale $\rho^* U_r^{*2}$ Both L^* and U_r^* are unspecified for the present. The Reynolds number is defined as

$$R = \frac{U_r^* L^*}{\nu^*}. \tag{2.2}$$

The dimensionless equations are identical to Eqs. 2.1 except that ν^* is replaced by $1/R$, and ρ^* is absorbed into the pressure scale.

We next divide each flow variable into a steady mean-flow term (denoted by an upper-case letter) and an unsteady small disturbance term (denoted by a lower-case letter):

$$\begin{aligned} \overline{U}_i(x, y, z, t) &= U_i(x, y, z) + u_i(x, y, z, t), \\ \bar{p}(x, y, z, t) &= P(x, y, z) + p(x, y, z, t). \end{aligned} \tag{2.3}$$

When these expressions are substituted into Eqs. 2.1, the mean-flow terms subtracted out, and the terms which are quadratic in the disturbances dropped, we arrive at the following dimensionless linearized questions for the disturbance quantities:

$$\frac{\partial u_i}{\partial t} + u_j \frac{\partial U_i}{\partial x_j} + U_j \frac{\partial u_i}{\partial x_j} = -\frac{\partial p}{\partial x_i} + \nu \nabla^2 u_i, \tag{2.4a}$$

$$\frac{\partial u_i}{\partial x_i} = 0. \tag{2.4b}$$

For a truly parallel mean flow, of which a simple two-dimensional example is a fully-developed channel flow, the normal velocity V is zero and U and W are functions only of y. The parallel-flow equations, when written out, are

$$\frac{\partial u}{\partial t} + U\frac{\partial u}{\partial x} + W\frac{\partial u}{\partial z} + v\frac{dU}{dy} = -\frac{\partial p}{\partial x} + \nu\nabla^2 u, \tag{2.5a}$$

$$\frac{\partial v}{\partial t} + U\frac{\partial v}{\partial x} + W\frac{\partial v}{\partial z} = -\frac{\partial p}{\partial y} + \nu\nabla^2 v, \tag{2.5b}$$

$$\frac{\partial w}{\partial t} + U\frac{\partial w}{\partial x} + W\frac{\partial w}{\partial z} + v\frac{dW}{dy} = -\frac{\partial p}{\partial z} + \nu\nabla^2 w, \tag{2.5c}$$

$$\frac{\partial u}{\partial x} + \frac{\partial v}{\partial y} + \frac{\partial w}{\partial z} = 0. \tag{2.5d}$$

These equations are in separable form, i.e., they permit the normal mode solutions

$$[u, v, w, p]^T = [\hat{u}(y), \hat{v}(y), \hat{w}(y), \hat{p}(y)]^T \exp\left[i(\alpha x + \beta z - \omega t)\right] \tag{2.6}$$

where α and β are the x and z components of the wavenumber vector $\vec{k}$, ω is the frequency, and $\hat{u}(y)$, $\hat{v}(y)$, $\hat{w}(y)$ and $\hat{p}(y)$ are the complex functions, or eigenfunctions, which gives the mode structure through the boundary layer, and are to be determined by the ordinary differential equations given below. It is a matter of convenience to work with the complex normal modes; the physical solutions are the real parts of Eqs. 2.6. The normal modes are traveling waves in the x, z plane, and in the most general case, α, β, and ω are all complex. If they are real, the wave is of neutral stability and propagates in the x, z plane with constant amplitude[1] and phase velocity $c = \omega/k$, where $k = (\alpha^2 + \beta^2)^{1/2}$ is the magnitude of $\vec{k}$. The angle of $\vec{k}$ with respect to the x axis is $\psi = \tan^{-1}(\beta/\alpha)$. if any of α, β or ω are complex, the amplitude will change as the wave propagates.

When Eqs. 2.6 are substituted into Eqs. 2.5, we obtain the following ordinary differential equations for the modal functions:

$$i(\alpha U + \beta W - \omega)\hat{u} + DU\hat{v} = -i\alpha\hat{p} + \frac{1}{R}\left[D^2 - \left(\alpha^2 + \beta^2\right)\right]\hat{u}, \tag{2.7a}$$

$$i(\alpha U + \beta W - \omega)\hat{v} + = -D\hat{p} + \frac{1}{R}\left[D^2 - \left(\alpha^2 + \beta^2\right)\right]\hat{v}, \tag{2.7b}$$

$$i(\alpha U + \beta W - \omega)\hat{w} + DW\hat{v} = -i\beta\hat{p} + \frac{1}{R}\left[D^2 - \left(\alpha^2 + \beta^2\right)\right]\hat{w}, \tag{2.7c}$$

$$\alpha\hat{u} + \beta\hat{w} + D\hat{v} = 0, \tag{2.7d}$$

where $D = d/dy$. For a boundary layer, the boundary conditions are that at the wall the no-slip condition applies,

$$\hat{u}(0) = 0, \quad \hat{v}(0) = 0, \quad \hat{w}(0) = 0, \tag{2.8a}$$

and that far from the wall all disturbances go to zero,

$$\hat{u}(y) \to 0, \quad \hat{v}(y) \to 0, \quad \hat{w}(y) \to 0 \text{ as } y \to \infty. \tag{2.8b}$$

Since the boundary conditions are homogeneous, we have an eigenvalue problem and solutions of Eqs. 2.7 that satisfy the boundary conditions will exist only for particular combinations of α, β, and ω. The relation for the eigenvalues, usually called the dispersion relation, can be written as

$$\omega = \Omega(\alpha, \beta). \tag{2.9}$$

There are six real quantities in Eq. 2.9; any two of them can be solved for as eigenvalues of Eqs. 2.7 and 2.8, and the other four have to be specified. The evaluation of the dispersion relation for a given Reynolds number and boundary-layer profile (U, W) is the principal task of stability theory. The eigenvalues, along with the corresponding eigenfunctions $\hat{u}$, $\hat{v}$, $\hat{w}$, and $\hat{p}$, give a complete specification of the normal modes. The normal modes, which are the natural modes of oscillation of the boundary layer, are customarily called Tollmien-Schlichting (TS) waves, or instability waves.

[1]The term amplitude will always refer to the peak or rms amplitude, never to the instantaneous amplitude

2.2 Non-parallel stability theory

Except for the asymptotic suction boundary layer, most boundary layers grow in the downstream direction, and even for a wave of constant frequency α, β, $\hat{u}$, $\hat{v}$, $\hat{w}$, and $\hat{p}$ are all functions of x (and z in a general 3D boundary layer). What we have to deal with is a problem of wave propagation in a nonuniform medium. Since the complete linearized equations 2.4 are not separable, they do not have the normal modes of Eq. 2.6 as solutions. The most straightforward approach is to simply set the non-parallel terms to zero on the grounds that the boundary-layer growth is small over a wavelength, and it is the local boundary-layer profile that will determine the local wave motion. This approach, called the quasi- or locally-parallel theory, has been almost universally adopted. It retains the parallel-flow normal modes as local solutions, but is, of course, an extra approximation beyond linearization and leaves open the question of how important the admittedly slow growth of the boundary layer really is. It also makes for difficulties in comparisons between theory and experiment.

The first complete non-parallel theories were developed independently by (in order of journal publication date) Bouthier (1972, 1973); Gaster (1974) and Saric and Nayfeh (1975). Gaster use the method of successive approximations; the others used the method of multiple scales. There has been considerable controversy on this subject, mainly because of the way in which (Saric and Nayfeh, 1975, 1977) chose to present their numerical results, but it is now generally agreed that the three theories are equivalent. Gaster's calculations of neutral-stability curves for the Blasius boundary layer have since been verified to be correct by Van Stijn and Van De Vooren (1983), and have the additional virtue of being based on quantities that can be measured experimentally. The calculations show the non-parallel terms to have little effect on local instability except at very low Reynolds numbers. However, this does not mean that non-parallel effects can be neglected when dealing with waves over distances of many wavelengths.

In the multiple-scale theory, in addition to the usual "fast" x scale over which the phase changes, there is a "slow" x scale, $x_1 = \varepsilon x$, where ε is a small quantity identified with $1/R$. The slow scale governs the boundary-layer growth, the change of the eigenfunctions, and a small additional amplitude modulation. The disturbances are expressed in the form

$$u = u^{(0)} + \varepsilon u^{(1)} + \ldots, \tag{2.10}$$

with similar expressions for v, w, and p. The mean flow is given by

$$\begin{aligned} U(x,y) &= U^{(0)}(x_1) + \ldots, \\ W(x,y) &= W^{(0)}(x_1) + \ldots, \\ V(x,y) &= \varepsilon V^{(0)}(x_1) + \ldots. \end{aligned} \tag{2.11}$$

Here the mean boundary layer is independent of z, and this is the only kind of boundary layer that we will consider in this work. Examples are 2D planar boundary layers and boundary layers on a rotating disk, on a cone at zero incidence and on the infinite-span swept wing.

When Eqs. 2.11 are substituted into Eqs. 2.4 and equal powers of ε collected, the zeroth-order equations for $u^{(0)}$, $v^{(0)}$, $w^{(0)}$ and $p^{(0)}$ are identical to the parallel flow equations 2.5. The normal modes, however, have the more general form

$$u^{(0)}(x,y,z,t) = A(x_1)\hat{u}^{(0)}(x_1,y)\exp\left[i\theta^{(0)}(x,z,t)\right], \tag{2.12}$$

where the phase function is

$$\theta^{(0)}(x,z,t) = \int^x \alpha^{(0)}(x_1)\,dx + \beta^{(0)}(x_1)z - \omega^{(0)}(x_1)t, \tag{2.13}$$

and $A(x_1)$ is a complex amplitude modulation function. The dispersion relation also becomes a function of x_1:

$$\omega^{(0)} = \Omega^{(0)}(\alpha^{(0)}, \beta^{(0)}; x_1). \tag{2.14}$$

The non-parallel theories as developed by Bouthier, Gaster, and Saric and Nayfeh calculate the dispersion relation only to the zeroth order, just as in the quasi-parallel theory. The next order (ε^1) enters only as a solvability condition of the first-order equations. This condition determines the function $A(x_1)$.

We shall use only the quasi-parallel theory in the remainder of this work. Consequently, all of the zeroth-order quantities are calculated as functions of x in accordance with Eqs. 2.12, 2.13 and 2.14. However, the quasi-parallel theory cannot determine the quantity $A(x_1)$ and this is simply set equal to the initial amplitude A_0. In the non-parallel theory, the product $A\hat{u}$ is a unique quantity, independent of the normalization of the eigenfunction $\hat{u}$, that give a precise meaning to the amplitude of the flow variable $\hat{u}$ as a function of y and permits direct comparisons of theory and experiment. In the quasi-parallel theory, only the contribution of the amplitude that comes from the imaginary parts of α, β and ω can be accounted for. The corrections due to the function $A(x_1)$ and the x dependence of eigenfunctions are outside of the scope of the theory. This lack of physical reality in the the quasi-parallel theory introduces an uncertainty in the calculation of wave amplitude and complicates comparisons with experiment. more on the use of the quasi-parallel theory can be found in Section 2.6.

2.3 Temporal and spatial theories

If α and β are real, and ω is complex, the amplitude with change with time; if α and β are complex, and ω is real, the amplitude will change with x. The former case is referred to as the temporal amplification theory; the latter as the spatial amplification theory. If all three quantities are complex, the disturbance will grow in space and time. The original, and for many years the only, form of the theory was the temporal theory. However, in a steady mean flow the amplitude of a normal mode is independent of time and changes only with distance. The spatial theory, which was introduced by Gaster (1962, 1963, 1965a,b), gives this amplification change in a more direct manner than does the temporal theory.

2.3.1 Temporal amplification theory

With $\omega = \omega_r + i\omega_i$ and α and β real, the disturbance can be written

$$u(x, y, z, t) = \hat{u}(y) \exp(\omega_i t) \exp\left[i \left(\int^x \alpha \, dx + \beta z - \omega_r t \right) \right]. \tag{2.15}$$

The magnitude of the wavenumber vector $\vec{k}$ is

$$k = \sqrt{\alpha^2 + \beta^2}, \tag{2.16}$$

and the angle between the direction of the $\vec{k}$ and the x axis is

$$\psi = \tan^{-1}\left(\frac{\beta}{\alpha} \right). \tag{2.17}$$

The phase velocity c, which is the velocity with which the constant-phase lines move normal to themselves, has the magnitude

$$c = \frac{\omega_r}{k}, \tag{2.18}$$

and is in the direction of $\vec{k}$. If A represents the magnitude of $\hat{u}$ at some particular y, say the y for which $\hat{u}$ is a maximum, then it follows from Eq. 2.15 that

$$\frac{1}{A}\frac{dA}{dt} = \omega_i. \tag{2.19}$$

We can identify ω_i as the temporal amplification rate. Obviously A could have been chosen at any y, or for another flow variable besides u, and Eq. 2.19 would be the same. It is this property that enables us to talk about the "amplitude" of an instability wave in the same manner as the amplitude of a water wave, even though the true wave amplitude is a function of y and the particular flow variable selected. We may distinguish three possible cases:

$$\begin{aligned} &\omega_i < 0 \qquad \text{damped wave,} \\ &\omega_i = 0 \qquad \text{neutral wave,} \\ &\omega_i > 0 \qquad \text{amplified wave.} \end{aligned} \tag{2.20}$$

The complex frequency may be written

$$\omega = k\tilde{c} = k(\tilde{c}_r + i\tilde{c}_i). \tag{2.21}$$

The real part of $\tilde{c}$ is equal to the phase velocity c, and $k\tilde{c}_i$ is the temporal amplification rate. The quantity $\tilde{c}$ appears frequently (as c) in the literature of stability theory. However, it cannot be used in the spatial theory, and since general wave theory employs only $\vec{k}$ and ω, with the phase velocity being introduced as necessary, we shall adopt the same procedure.

2.3.2 Spatial amplification theory

In spatial theory, ω is real and the wavenumber components α and β are complex. With

$$\alpha = \alpha_r + i\alpha_i, \qquad \beta = \beta_r + i\beta_i, \tag{2.22}$$

we can write the normal modes in the form

$$u(x,y,z,t) = \hat{u}(y) \exp\left[-\left(\int^x \alpha_i \, dx + \beta_i z\right)\right] \exp\left[i\left(\int^x \alpha_r \, dx + \beta_r z - \omega t\right)\right]. \tag{2.23}$$

By analogy with the temporal theory, we may define a real wavenumber vector $\vec{k}$ with magnitude

$$k = \sqrt{\alpha_r^2 + \beta_r^2}. \tag{2.24}$$

The angle between the direction of $\vec{k}$ and the x axis is

$$\psi = \tan^{-1}\left(\frac{\beta_r}{\alpha_r}\right), \tag{2.25}$$

and the phase velocity is

$$c = \frac{\omega}{k}. \tag{2.26}$$

It follows from Eq. 2.23 that

$$\frac{1}{A}\frac{dA}{dx} = -\alpha_i, \tag{2.27}$$

and we can identify $-\alpha_i$ as the amplification rate int eh x direction. In like manner, $-\beta_i$ is the amplification rate int eh z direction. Indeed, the spatial amplification rate is a vector like the wavenumber vector with magnitude

$$|\sigma| = \sqrt{\alpha_i^2 + \beta_i^2}, \tag{2.28}$$

and angle

$$\bar{\psi} = \tan^{-1}\left(\frac{-\beta_i}{-\alpha_i}\right) \tag{2.29}$$

with respect to the x axis. The amplification rate $-\beta_i$ is at this point a free parameter, and its selection is left for future consideration.

For the special boundary layer to be considered in this work (see page 17), we define a spatial wave to be amplified or damped according to whether its amplitude increases or decreases in the x direction. Therefore, the three possible cases which correspond to Eq. 2.20 are:

$$\begin{aligned} -\alpha_i &< 0 \qquad \text{damped wave,} \\ -\alpha_i &= 0 \qquad \text{neutral wave,} \\ -\alpha_i &> 0 \qquad \text{amplified wave.} \end{aligned} \tag{2.30}$$

2.3.3 Relation between temporal and spatial theories

A laminar boundary layer is a dispersive medium for the propagation of instability waves. That is, different frequencies propagate with different phase velocities, so that the individual harmonic components of a group of waves at one time will be dispersed (displaced) from each other at some later time. In a conservative system, where energy is not exchanged between the waves and the medium, an overall quantity such as the energy density or amplitude propagates with the group velocity. Furthermore, the group velocity can be considered a property of the individual waves, and to follow a particular normal mode we use the group velocity of that mode. Because of damping and amplification, instability waves in a boundary layer do not constitute a conservative system, and the group velocity is in general complex. However, some of the ideas of conservative systems are still useful. If we consider an observer moving at the group velocity of a normal mode, the wave in the moving frame of reference will appear to undergo temporal amplification, while in the frame at rest, it undergoes spatial amplification. Thus we can write

$$\frac{d}{dt} = c_r \frac{d}{dx_g}, \tag{2.31}$$

where in this argument c_r is the magnitude of $\vec{c_r}$, the real part of the group velocity vector $\vec{c}$, and x_g is the coordinate in the direction of $\vec{c}_r$. Therefore, if ω_i is the temporal amplification rate, the spatial amplification rate in the direction parallel to $\vec{c}_r$ is immediately given to be

$$-(\alpha_i)_g = \frac{\omega_i}{c_r}. \tag{2.32}$$

The problem of converting a temporal to a spatial amplification rate was first encountered by Schlichting (1933a), who used the two-dimensional version of Eq. 2.32 without comment. The same relation was also used later by Lees (1952), and justified on intuitive grounds, but the first mathematical derivation was given by Gaster (1962) for the 2D case, and the relation bears his name. Gaster's derivation is straightforward and can be generalized to three dimensions with the result given above in Eq. 2.32. It is essential to note that the Gaster relation is only an approximation that is valid for small amplification rates. Within the approximation, the frequency and wavenumber of the spatial wave are the same as for the temporal wave. If we use the complex group velocity in teh above derivation, we arrive at the separate transformations for constant frequency and constant wavenumber obtained by Nayfeh and Padhye (1979) from another point of view. In this approach, Eq. 2.32 corresponds to a transformation of constant wavenumber.

We can also make use of Eq. 2.32 to arrive at a useful result for spatial waves. The same argument that led to Eq. 2.32 also applies to a component of the group velocity. Therefore,

$$-(\alpha_i)_{\bar{\psi}} = \frac{\omega_i}{c_r}\cos(\bar{\psi} - \phi_r), \tag{2.33}$$

where $-(\alpha_i)_{\bar{\psi}}$ is the spatial amplification rate in the arbitrary direction $\bar{\psi}$. The quantity ϕ_r is the real part of the complex group velocity angle ϕ defined by

$$c_x = c\cos\phi, \qquad c_z = c\sin\phi, \tag{2.34}$$

where c_x and c_z are the complex x and z components of $\vec{c}$, and c is the complex magnitude of $\vec{c}$. Eliminating ω_i/c_r by Eq. 2.32, we arrive at

$$(\alpha_i)_{\bar{\psi}} = \frac{(\alpha_i)_g}{\cos(\bar{\psi} - \phi_r)}. \tag{2.35}$$

This relation, which may appear rather obvious, is not a general relation valid for two arbitrary angles. It is only valid when one of the two angles is ϕ_r. When both angles are arbitrary, a more complicated relation exists and has been derived by Nayfeh and Padhye (1979). There is also a small change in $\vec{k}$ unless the group-velocity angle is real. We might close this subject by noting that while the various Nayfeh-Padhye transformation formulae use the complex group velocity, they too are not exact because the group velocity is considered to be constant in the transformation. We recommend to the interested reader to examine the instructive numerical examples given by Nayfeh and Padhye.

2.4 Reduction to fourth-order system

Equations 2.7 constitute a sixth-order system for the variables $\hat{u}$, $\hat{v}$, $\hat{w}$, $\hat{p}$, $D\hat{u}$, and $D\hat{w}$, as can be shown by rewriting them as six first-order equations. This system may be reduced to fourth order for the determination of eigenvalues. One approach is to multiply Eq. 2.7a by α and Eq. 2.7c by β and add, and then multiply Eq. 2.7c by α and Eq. 2.7a by β and subtract, to arrive at the following system of equations for the variables $\alpha\hat{u} + \beta\hat{w}$, $\hat{v}$, $\alpha\hat{w} - \beta\hat{u}$, and β:

$$i(\alpha U + \beta W - \omega)(\alpha\hat{u} + \beta\hat{w}) + (\alpha DU + \beta DW)\hat{v} = -i(\alpha^2 + \beta^2)\hat{p} + \frac{1}{R}[D^2 - (\alpha^2 + \beta^2)](\alpha\hat{u} + \beta\hat{w}), \quad (2.36a)$$

$$i(\alpha U + \beta W - \omega)\hat{v} = -D\hat{p} + \frac{1}{R}[D^2 - (\alpha^2 + \beta^2)]\hat{v}, \quad (2.36b)$$

$$i(\alpha U + \beta W - \omega)(\alpha\hat{w} - \beta\hat{u}) + (\alpha DW + \beta DU)\hat{v} = \frac{1}{R}[D^2 - (\alpha^2 + \beta^2)](\alpha\hat{w} - \beta\hat{u}), \quad (2.36c)$$

$$i(\alpha\hat{u} + \beta\hat{w}) + D\hat{v} = 0, \quad (2.36d)$$

where Eqs. 2.7b and 2.7d have been duplicated for convenience as Eqs. 2.36b and 2.36d. The point to note is that Eqs. 2.36a, 2.36b, and 2.36d are a fourth-order system for the dependent variables $\alpha\hat{u} + \beta\hat{w}$, $\hat{v}$, and $\hat{p}$. The fourth variable of this system is $\alpha D\hat{U} + \beta D\hat{w}$. The dependent variable $\alpha\hat{w} - \beta\hat{u}$ appears only in Eq. 2.36c. Therefore, we may determine the eigenvalues from the fourth-order system, and if subsequently the eigenfunctions $\hat{u}$ and $\hat{w}$ are needed, they are obtained by solving the second order equation 2.36c.

2.4.1 Transformation to 2D equations - temporal theory

The above equations are the ones that we will use, but they also offer a basis to discuss some transformations that have been used in the past. If α and β are real, the interpretation of the equations is evident. Equation 2.36a is the momentum equation in the direction parallel to $\vec{k}$, and Eq. 2.36c is the momentum equation in the direction normal to $\vec{k}$ in the x, z plane. Indeed, if we use the transformations

$$\tilde{\alpha}\tilde{U} = \alpha U + \beta W, \qquad \tilde{\alpha}\tilde{W} = \alpha W - \beta U, \quad (2.37a)$$

$$\tilde{\alpha}\tilde{u} = \alpha\hat{u} + \beta\hat{w}, \qquad \tilde{\alpha}\tilde{w} = \alpha\hat{w} - \beta\hat{u}, \quad (2.37b)$$

$$\tilde{\alpha}^2 = \alpha^2 + \beta^2 \quad (2.37c)$$

and leave ω, R, $\hat{v}$, and $\hat{w}$ unchanged, Eqs. 2.36 become

$$i(\tilde{\alpha}\tilde{U} - \omega)\tilde{u} + D\tilde{U}\hat{v} = i\tilde{\alpha}\hat{p} + \frac{1}{R}(D^2 - \tilde{\alpha}^2)\tilde{u}, \quad (2.38a)$$

$$i(\tilde{\alpha}\tilde{U} - \omega)\hat{v} = -D\hat{p} + \frac{1}{R}(D^2 - \tilde{\alpha}^2)\hat{v}, \quad (2.38b)$$

$$i(\tilde{\alpha}\tilde{U} - \omega)\tilde{w} + D\tilde{W}\hat{v} = \frac{1}{R}(D^2 - \tilde{\alpha}^2)\tilde{w}, \quad (2.38c)$$

$$i\tilde{\alpha}\tilde{u} + D\hat{v} = 0. \quad (2.38d)$$

$$(2.38e)$$

These transformed equations are of the form of Eqs. 2.7 for a two-dimensional wave ($\beta = 0$) in a two-dimensional boundary layer ($W = 0$) except for the presence of Eq. 2.38c. We may observe from Eq. 2.7c that even with $\beta = 0$, a $\hat{w}$ velocity component will exist whenever there is a W because of the vorticity production term $DW\hat{v}$.

This in a 3D boundary layer with velocity profiles (U, W) at Reynolds number R, the eigenvalues of an oblique temporal wave can be obtained from the eigenvalues of a 2D wave of the frequency in a 2D boundary layer at the same Reynolds number with the velocity profile of the 3D boundary layer in the direction of the wavenumber vector. The key result that it is the latter velocity profile that governs the instability was obtained by Stuart (Gregory et al., 1955) in his classic study of the stability of three-dimensional boundary layers, and by Dunn and Lin (1955) (see also Lin (1955)) in their study of the stability of compressible boundary layers. We shall refer to this velocity profile as the directional profile.

A slightly different transformation was employed by Squire (1933) and bears his name. Squire's original transformation was for a 2D boundary layer and the Orr-Sommerfeld equation (see Section 2.5.1),

$$\tilde{U} = U + W\tan\psi, \qquad \tilde{W} = W - U\tan\psi, \tag{2.39a}$$

$$\tilde{u} = \hat{u} + \hat{w}\tan\psi, \qquad \tilde{w} = \hat{w} - \hat{u}\tan\psi, \tag{2.39b}$$

$$\tilde{\alpha} = \alpha^2 + \beta^2, \qquad \frac{\tilde{\omega}}{\tilde{\alpha}} = \frac{\omega}{\alpha}, \qquad \tilde{\alpha}\tilde{R} = \alpha R \tag{2.39c}$$

$$\frac{\tilde{p}}{\tilde{\alpha}^2} = \frac{p}{\alpha^2}, \qquad \frac{\tilde{v}}{\tilde{\alpha}} = \frac{v}{\alpha}. \tag{2.39d}$$

When Eqs. 2.39 are substituted into Eqs. 2.36, the resultant equations are the same as Eqs. 2.38 except that ω, R, $\hat{v}$, and $\hat{p}$ are replaced by the corresponding tilde quantities. Thus the transformed equations, except for the $\tilde{w}$ equation which does not enter the eigenvalue problem, are again in 2D form, but now the Reynolds number ahs also been transformed to the new coordinate system. This transformation relates the eigenvalues of an oblique temporal wave of frequency ω in a 3D boundary layer with velocity profiles (U, W) at Reynolds number R to a 2D wave of frequency $\omega/\cos\phi$ in a 2D boundary layer at Reynolds number $R\cos\psi$ with velocity profile $U + W\tan\psi$. It can be interpreted as the same rotation of coordinates as the transformation of Eq. 2.37 plus the redefinition of the reference velocity from U_r^* to $U_r^*\cos\psi$.

For a 3D boundary layer, the generalized Squire transformation is merely a different way of doing what has already been accomplished by Eqs. 2.36. However, for a two-dimensional boundary layer ($W = 0$), which was the case considered by Squire, $\tilde{U} = U$ and the dimensionless velocity profile is unchanged by the transformation. This means that numerical stability results for oblique temporal waves can be immediately obtained from known results for 2D waves in the same velocity profile. Furthermore, since $\tilde{R} = R\cos\psi$, the smallest Reynolds number at which a wave of any frequency becomes unstable (minimum critical Reynolds number) must always occur for a 2D wave. This is the celebrated Squire theorem. It applies only to the minimum critical Reynolds number and not to the critical Reynolds number of a particular frequency, for which instability may well occur first for an oblique wave. It should also be noted that the theorem applies only to a self-similar boundary layer where the velocity profile is independent of R.

2.4.2 Transformation to 2D equations - spatial theory

When α and β are complex, the interpretation of the transformation equations 2.37 as a rotation of coordinates is lost, because the transformed velocity profiles are complex. There is one exception, however. In general, the quantity $\alpha/\tilde{\alpha}$, which for a temporal wave is $\cos\psi$, is complex. However, if $\alpha_i/\beta_i = \alpha_r/\beta_r$, that is if the spatial amplification rate vector is parallel to the wavenumber vector, $\alpha/\tilde{\alpha}$ is still real and equal to $\cos\psi$. Thus it would appear that the eigenvalues of a spatial wave could still be calculated from the 2D equations in the tilde coordinates. Unfortunately, this expectation is not correct. When α and β are real,

$$\alpha = \tilde{\alpha}\cos\psi, \tag{2.40}$$

but there is no justification for applying Eq. 2.40 separately to the real and imaginary parts of a complex α when $\alpha/\tilde{\alpha}$ is complex. We are able, however, to derive the correct transformation rule from Eq. 2.35. With $\tilde{\psi} = \psi$ and $\tilde{\alpha}_i = (\alpha_i)_\psi$,

$$(-\alpha_i)_g = -\tilde{\alpha}_i\cos(\psi - \phi_r), \tag{2.41a}$$

and with $\psi = 0$,

$$-\alpha_i = \frac{(-\alpha_i)_g}{\cos\phi_r}. \tag{2.41b}$$

Eliminating $(-\alpha_i)_g$, we obtain

$$-\alpha_i = -\tilde{\alpha}_i\frac{\cos(\psi - \phi_r)}{\cos\phi_r}. \tag{2.41c}$$

Consequently, Eq. 2.40 can be used for α_i only when the real part of the group-velocity angle is zero. There is also a small shift in the wavenumber vector whenever $\phi_i \neq 0$.

An alternative procedure for spatial waves is to use the equations that result from the transformations of Eq. 2.39, but to not invoke Eq. 2.40 when $\alpha/\tilde{\alpha}$ is complex. The quantities $\tilde{R}$ and $\tilde{\omega}$ are complex, as are $\tilde{U}$ and

$\tilde{W}$ for a 3D boundary layer, but this causes no difficulty in a numerical solution. Such a procedure, which amounts to a generalized complex Squire transformation, was incorporated into the JPL viscous stability code VSTAB/VSP. The approach with Eqs. 2.36, which has the advantage that no transformations are needed in determining the eigenvalues, is used in the newer JPL stability codes VSTAB/3D, VSTAB/AF, and SFREQ/EV. It should be noted that even in the spatial theory, the governing real velocity profile is the profile in the direction of $\vec{k}$.

2.5 Special forms of the stability equations

2.5.1 Orr-Sommerfeld equation

A single fourth-order equation can be derived from Eqs. 2.36 by eliminating $\alpha\hat{u}+\beta\hat{w}$ from Eq. 2.36a by 2.36d, and, after differentiation, eliminating $D\hat{p}$ by 2.36b. The result is

$$[D^2-(\alpha^2+\beta^2)]^2\hat{v} = iR\{(\alpha U+\beta W-\omega)[D^2-(\alpha^2+\beta^2)]-(\alpha D^2U+\beta D^2W)\}\hat{v}, \tag{2.42}$$

with boundary conditions

$$\begin{aligned} \hat{v}(0) &= 0, \qquad & D\hat{v}(0) &= 0, \\ \hat{v}(y) &\to 0, \qquad & D\hat{v}(y) &\to 0 \text{ as } y\to 0. \end{aligned} \tag{2.43}$$

When $W=0$, Eq. 2.42 reduces to the equation for a 2D boundary layer obtained by Squire (1933). When in addition $\beta=0$,

$$(D^2-\alpha^2)^2\hat{v} = iR[(\alpha U-\omega)(D^2-\alpha^2)-\alpha D^2U]\hat{v} \tag{2.44}$$

This is the Orr-Sommerfeld equation and is the basis for most of the work that has been done in incompressible stability theory. it is often derived from the vorticity equation, in which case $\hat{v}$ is the eigenfunction of the stream function. The Orr-Sommerfeld equation is valid for a two-dimensional wave in a two-dimensional boundary layer. However, the generalized Squire transformation, Eq. 2.39, reduces the 3D equation 2.42 to Eq. 2.44 in the tilde coordinates. Consequently, for 3D boundary layers all oblique temporal waves can be obtained by solving a 2D problem for the renormalized velocity profile in the direction of the wave number vector, and when the boundary layer is two-dimensional, for the same velocity profile. The 2D Orr-Sommerfeld equation and the same transformation can also be used for spatial oblique waves, but in this case R is complex, and for a 3D boundary layer so is $\overline{U}$. The inviscid form of the complex Squire transformation was used by Gaster (1968) for an unbounded 2D shear flow, and the complete viscous form by Gaster (1975) for a Blasius boundary layer. When one is not trying to make use of previously computer two-dimensional eigenvalues, it is perhaps simpler to use Eq. 2.42 to calculate 3D eigenvalues as needed, thus avoiding transformations in R and ω.

2.5.2 System of first-order equations

There are a number of stability problems that cannot be reduced to a fourth-order system, and therefore are not governed by the Orr-Sommerfeld equation. A more flexible approach is to work from the outset with a system of first-order equations. With the definitions

$$\begin{aligned} Z_1 &= \alpha\hat{u}+\beta\hat{w}, \quad & Z_2 &= \alpha D\hat{u}+\beta D\hat{w}, \quad & Z_3 &= \hat{v}, \quad & Z_4 &= \hat{p} \\ Z_5 &= \alpha\hat{w}-\beta\hat{u}, \quad & Z_6 &= \alpha D\hat{w}-\beta D\hat{u}, \end{aligned} \tag{2.45}$$

Eqs. 2.36 can be written as six first-order equations:

$$DZ_1 = Z_2, \tag{2.46a}$$
$$DZ_2 = \left[\alpha^2 + \beta^2 + iR(\alpha U + \beta W - \omega)\right] Z_1 + R(\alpha DU + \beta DW) Z_3 + iR\left(\alpha^2 + \beta^2\right) Z_4, \tag{2.46b}$$
$$DZ_3 = -iZ_1, \tag{2.46c}$$
$$DZ_4 = -\frac{i}{R} Z_2 - \left[i(\alpha U + \beta W - \omega) + \frac{\alpha^2 + \beta^2}{R}\right] Z_3, \tag{2.46d}$$
$$DZ_5 = Z_6, \tag{2.46e}$$
$$DZ_6 = (\alpha DW - \beta DU) R Z_3 + \left[\alpha^2 + \beta^2 + iR(\alpha U + \beta W - \omega)\right] Z_5. \tag{2.46f}$$

The boundary conditions are

$$\begin{aligned} &Z_1(0) = 0, \qquad Z_3(0) = 0, \qquad Z_5(0) = 0, \\ &Z_1(y) \to 0, \qquad Z_3(y) \to 0, \qquad Z_5(y) \to 0 \text{ as } y \to \infty. \end{aligned} \tag{2.47}$$

The fact that the first four Eqs. 2.46 do not contain Z_5 or Z_6 confirms that eigenvalues can be obtained from a fourth-order system even though the stability equations constitute a sixth-order system. It is only the determination of all the eigenfunctions that requires the solution of the full sixth-order system. The above formulation is applicable when α and β are complex as well as real, and to 3D as well as 2D boundary layers. Only the transformations of Eq. 2.37b enter in this formulation, and then only in the definitions of the dependent variables Z_1, Z_2, Z_5 and Z_6. No transformations are involved in determination of the eigenvalues. Another point to note is that only the first derivatives of U and W appear in Eqs. 2.46 instead of the second derivatives which are present in the Orr-Sommerfeld equation.

2.5.3 Uniform mean flow

In the freestream, the mean flow is uniform and Eqs. 2.46 have constant coefficients. Therefore, the solutions are of the form

$$Z^{(i)}(y) = A^{(i)} \exp(\lambda_i y), \qquad (i = 1, 6), \tag{2.48}$$

where the $Z^{(i)}$ are the six-component solution vectors, the λ_i are the characteristic values (the term eigenvalue is reserved for the α, β, ω which satisfy the dispersion relation), and the $A^{(i)}$ are the six-component characteristic vectors 9not to be confused with the wave amplitude A in Eq. 2.12). The characteristic values occur in pairs, and are easily found to be

$$\lambda_{1,2} = \mp\left(\alpha^2 + \beta^2\right)^{1/2}, \tag{2.49a}$$
$$\lambda_{3,4} = \mp\left[\alpha^2 + \beta^2 + iR(\alpha U_1 + \beta W_1 - \omega)\right]^{1/2}, \tag{2.49b}$$
$$\lambda_{5,6} = \lambda_{3,4}, \tag{2.49c}$$

where U_1 and W_1 are the freestream values of $U(y)$ and $W(y)$. Only the upper signs satisfy the boundary conditions at $y \to \infty$. The components of the characteristic vector $A^{(1)}$ are

$$A_1^{(1)} = -i\left(\alpha^2 + \beta^2\right)^{1/2}, \tag{2.50a}$$
$$A_2^{(1)} = i\left(\alpha^2 + \beta^2\right), \tag{2.50b}$$
$$A_3^{(1)} = 1, \tag{2.50c}$$
$$A_4^{(1)} = i\frac{\alpha U_1 + \beta W_1 - \omega}{\left(\alpha^2 + \beta^2\right)^{1/2}}, \tag{2.50d}$$
$$A_5^{(1)} = 0, \tag{2.50e}$$
$$A_6^{(1)} = 0. \tag{2.50f}$$

For real α, β and ω this solution is the linearized potential flow over a wavy wall moving in the direction of the wavenumber vector with the phase velocity ω/k. It can be called the inviscid solution, although this designation is valid only in the freestream.

The components of the characteristic vector $A^{(3)}$ are

$$A_1^{(3)} = 1, \tag{2.51a}$$

$$A_2^{(3)} = \left[\alpha^2 + \beta^2 + iR(\alpha U_1 + \beta W_1 - \omega)\right]^{1/2}, \tag{2.51b}$$

$$A_3^{(3)} = \left[\alpha^2 + \beta^2 - iR(\alpha U_1 + \beta W_1 - \omega)\right]^{-1/2}, \tag{2.51c}$$

$$A_4^{(3)} = 0, \tag{2.51d}$$

$$A_5^{(3)} = 0, \tag{2.51e}$$

$$A_6^{(3)} = 0. \tag{2.51f}$$

This solution represents a viscous wave and can be called the first viscous solution.

The characteristic vector $A^{(5)}$ is a second viscous solution and its components are

$$A_1^{(5)} = 0, \tag{2.52a}$$

$$A_2^{(5)} = 0, \tag{2.52b}$$

$$A_3^{(5)} = 0, \tag{2.52c}$$

$$A_4^{(5)} = 0, \tag{2.52d}$$

$$A_5^{(5)} = 1, \tag{2.52e}$$

$$A_6^{(5)} = -\left[\alpha^2 + \beta^2 + iR(\alpha U_1 + \beta W_1 - \omega)\right]^{1/2}. \tag{2.52f}$$

The three linearly independent solutions $A^{(1)}$, $A^{(3)}$ and $A^{(5)}$ are the key to the numerical method that we will use to obtain the eigenvalues, as they provide the initial conditions for the numerical investigation.

We can observe that the second viscous solution can also be valid in the boundary layer as a pure mode if Z_1, Z_3 and Z_4 are all zero. This follows from Eqs. 2.46. In the notation of Eq. 2.37b, the only non-zero flow variable, Z_5, is $\tilde{\alpha}\tilde{w}$, where in the temporal theory $\tilde{w}$ is the eigenfunction of the fluctuation velocity normal to $\vec{k}$. But since $\eta = \partial w/\partial x - \partial u/\partial z$ is the fluctuation vorticity component normal to the wall, Z_5 is also $-i\hat{\eta}$, where $\hat{\eta}$ is the eigenfunction of η. This interpretation is valid for both the temporal and spatial theories. The eigensolutions of the second-order equation 2.46f with $Z_3 = 0$ satisfy the boundary condition $\hat{\eta}(0) = 0$ and give the vorticity modes in the boundary layer. These modes were first considered by Squire (1933), and were proven by him to be always stable. Recently it was shown by Herbert (1983a,b) that the Squire modes provide an important mechanism of subharmonic secondary instability at low, but finite, amplitudes of a primary 2D instability wave.

2.6 Wave propagation in a growing boundary layer

We have already discussed some aspects of this problem in Section 2.2, and we have chosen to use the quasi-parallel rather than non-parallel theory. In the quasi-parallel theory, the normal-mode solutions are of the form

$$u(x, y, z, t) = A_0 \hat{u}(y; x) \exp[i\theta(x, y, z, t)], \tag{2.53}$$

with similar expressions for the other flow variables. The slowly varying amplitude $A(x)$ of the nonparallel solution Eq. 2.12 has been set equal to the constant A_0, and

$$\theta(x, z, t) = \int^x \alpha(x)\, dx + \beta(x_1)z - \omega(x_1)t. \tag{2.54}$$

Equation 2.54 is the same as Eq. 2.13. We have left β and ω as functions of the slow scale x_1 in order to make it clear that $\partial\theta/\partial x = \alpha$, just as for strictly parallel flow. The eigenvalues α, β and ω satisfy

the local dispersion relation Eq. 2.14 and the eigenfunction $\hat{u}(y;x)$ is also a slowly varying function of x. Consequently, at each x a different eigenvalue problem has to be solved because of the change in the boundary layer thickness, or velocity profiles, or, as is usually the case, both. The problem we must resolve is how to "connect" the possible eigenvalues at each x so that they represent a continuous wave train propagating through the growing boundary layer.

In a steady boundary layer, which is the only kind that we shall consider, the dimensional frequency of a normal mode is constant. For a 2D wave in a 2D boundary layer, $\beta = 0$, and the complex wavenumber α in the spatial theory, or the real wavenumber α and the imaginary part of the frequency ω_i in the temporal theory, are obtained as eigenvalues for the local boundary-layer profiles. The only problem here is the relatively minor one of calculating the wave amplitude as a function of x from the amplification rate, adn we shall discuss this in Section 2.6.2.

2.6.1 Spanwise wavenumber

When the wave is oblique, $\beta \neq 0$, and it is not obvious how to proceed. According to the dispersion relation, α is a function of β as well as of x. How do we chose β at each x? The answer is provided by the same procedure as used in conservative wave theory. When we differentiate Eq. 2.54 with respect to x (not x_1) and z, we obtain

$$\frac{\partial \theta}{\partial x} = \alpha, \qquad \frac{\partial \theta}{\partial z} = \beta, \tag{2.55a}$$

or

$$\nabla \theta = \vec{k}_c, \tag{2.55b}$$

where $\vec{k}_c$ is the complex vector wavenumber. This it follows directly that

$$\vec{\nabla} \times \vec{k}_c = 0, \tag{2.55c}$$

and $\vec{k}_c$ is irrotational. This condition is a generalization to a nonconservative system of the well-known result for the real wavenumber vector in conservative kinematic wave theory.

In the boundary layers we will consider here, the mean flow is independent of z. Consequently, if we restrict ourselves to spatial waves of constant β at the initial x, they can be represented by a single normal mode because the eigenvalue α will also be independent of z. Therefore, according to Eq. 2.55c the sought-after downstream condition on β is

$$\beta = \text{const.} \tag{2.56}$$

One caution is that if the reference length L^* is itself a function of x, as it will be if $L^* = \delta^*$ for example, the argument has to be slightly modified and Eq. 2.56 refers to β^* rather than β.

It still remains to specify the initial value of β. naturally occurring instability waves in a boundary layer will be a superposition of normal modes, with a spectrum over both ω and β that will depend on the particular origin of the waves. It is probably only in a controlled experiment with a suitable wavemaker that a single normal mode can be excited. For example, the vibrating ribbon first used by Schubauer and Skramstad (1947) in their celebrated experiment excites a spatial 2D normal mode with the frequency of the ribbon. It is also possible to conceive of wavemakers that excite single oblique normal modes in boundary layers which are independent of z. Such normal modes will have an initial β_r which matches that of the wavemaker, and, because the wave can grow only in x, the initial β_i must be zero. These normal modes are well-suited for use in stability calculations for the estimation of the location of transition. In the calculations, β_r is assigned as a parameter, β_i is zero, and Eq. 2.56 controls the downstream values of β_r. Not only do these normal modes represent physical waves that can be produced by a suitable wavemaker, but they are also convenient to use in all calculations of normal modes, such as transition prediction, where we are interested in the largest possible growth of any normal mode, or the point-source calculations of Chapter 7. In earlier work on two-dimensional planar boundary layers, some results from which will appear in later sections, the angle ψ was chosen as the parameter to hold constant, rather than β_r, as the wave propagates downstream. Although α_r^* is nearly constant in such boundary layers, it changes enough so that the assumption of constant ψ is not equivalent to Eq. 2.56. In the work on three-dimensional boundary layers presented in Chapters 13 and 14, Eq. 2.56 is applied to the spanwise wavenumbers, but the direction of the spatial amplification rate is either parallel to the local potential flow, or, occasionally, in the direction of the real part of the group-velocity angle.

2.6.2 Some useful formulae

It is worthwhile at this point to list some formulae that will be of use for stability calculations in growing boundary layers. Only 2D boundary layers are considered here; 3D boundary layers are taken up separately in Part III. First, we choose as the length scale,

$$L^* = \sqrt{\frac{\nu^* x^*}{U_1^*(x^*)}}, \tag{2.57}$$

which is the usual length scale of the Falkner-Skan family of boundary layers, and of many nonsimilar boundary-layer solutions. Other length scales that have been used are the boundary layer thickness, the displacement thickness, and the inverse unit Reynolds number. The velocity scale is $U_1^*(x^*)$, the local velocity at the edge of the boundary layer. With these choices, the Reynolds number in the stability equation is

$$R = \frac{U_1^*(x^*)L^*}{\nu^*} = \sqrt{\frac{U_1^* x^*}{\nu^*}} = \sqrt{Re}. \tag{2.58}$$

The dimensionless coordinate normal to the wall,

$$y = \left(\frac{y^*}{x^*}\right) R, \tag{2.59}$$

is the usual independent variable of boundary layer theory.

The dimensionless quantities α, β, ω, R and y referenced to L^* may be converted to other length scales, such as displacement or momentum thickness, by multiplying by the dimensionless (with respect to L^*) displacement or momentum thickness. The latter quantities are almost always obtained as part of a boundary-layer calculation. To convert α, β and ω to dimensionless quantities based on the inverse unit Reynolds number ν^*/U_1^*, it is only necessary to divide α, β and ω by R.

The dimensional circular frequency ω^* of a normal mode is constant as the wave travels downstream, but the dimensionless frequency

$$\omega = \frac{\omega^* L^*}{U_1^*}, \tag{2.60}$$

is a function of x. it has become almost standard to use

$$F = \frac{\omega^* \nu^*}{U_1^{*2}} = \frac{\omega}{R} \tag{2.61}$$

in place of ω as the dimensionless frequency. However, F is also a function of x for anything but a flat-plate boundary layer. For the Falkner-Skan family of velocity profiles, the dimensionless velocity gradient,

$$m = \frac{x^*}{U_1^*}\frac{dU_1^*}{dx^*}, \tag{2.62}$$

is constant and related to the usual Hartree parameter β_h (the subscript h is used to avoid confusion with the waveanumber component β), by

$$\beta_h = \frac{2m}{m+1}. \tag{2.63}$$

The variable dimensionless frequency of constant ω^* is

$$F(R) = F(R_0)\left(\frac{R_0}{R}\right)^{\frac{4m}{m+1}}, \tag{2.64}$$

where R_0 is the Reynolds number at the initial x station. When a stability code can handle several frequencies at once, it is more convenient to use some fixed velocity as the reference velocity so that F will remain constant for each frequency. For the nonsimilar boundary layers on airfoils, the JPL stability codes use the velocity in the undisturbed freestream.

With L^* a function of x^*, the irrotationality condition Eq. 2.56 applies to the dimensional spanwise wavenumber. For the Falkner-Skan family, the dimensionless β for constant β^* is given by

$$\frac{\beta(R)}{\beta(R_0)} = \left(\frac{R}{R_0}\right)^{\frac{1-m}{1+m}} . \tag{2.65}$$

We note that for a Blasius boundary layer ($m = 0$), β increases linearly with R. The dimensional wavenumber α_r^* is almost, but not quite, constant, because there is a small increase in the phase velocity with increasing R. As a result, the wave angle ψ increases as the wave travels downstream. This increase is at most a few degrees for a planar a boundary layer. However, on an axisymmetric body, it is the circumferential wavenumber per radian that is constant. Thus, neglecting the small decrease in α_r^*, $\tan\psi$ is inversely proportional to the radius. For instance, on a cone, where the radius is increasing, an oblique wave is rapidly converted to a nearly 2D wave as it travels downstream; on a body with decreasing radius, the effect is reversed.

2.6.3 Wave amplitude

In the quasi-parallel theory, the amplitude ratio of a spatial normal mode of frequency ω^* with $\beta_i = 0$ is obtained from the imaginary part of the phase function Eq. 2.54:

$$\ln\left(\frac{A}{A_0}\right) = -\int_{x_0^*}^{x^*} \alpha_i^* \, dx^* \tag{2.66}$$

in accord with Eq. 2.27. Here A_0 is the amplitude at the intitial station x_0^*, and the integral is evaluated with constant ω^* and β^*. if x_0^* is the start of the instability region for the frequency ω^*, $\ln(A/A_0)$ is the N factor that is the basis of the e^N method of transition prediction. As discussed in Section 2.2, A may represent any flow variable at any y location. It may be helpful to think of A as, say, the maximum value of $|\hat{u}|$ in the boundary alyer, as this is a quantity that can be determined experimentally. Along with the amplitude, the time-independent phase relative to the initial phase at x_0^*, z_0^* is

$$\chi(x) - \chi(x_0) = \int_{x_0^*}^{x^*} \alpha_r^* \, dx^* + \beta_r^* \left(z^* - z_0^*\right). \tag{2.67}$$

The phase is a vital quantity in superposition calculations (Chapter 7), but otherwise it is usually not computed.

For the Falkner-Skan family, the amplitude ratio in terms of R is

$$\ln\left(\frac{A}{A_0}\right) = -\frac{2}{m+1}\int_{R_0}^{R} \alpha_i \, dR, \tag{2.68}$$

where the integrand α_i is calculated as an eigenvalue with the F of Eq. 2.64 and the β of Eq. 2.65. For a nonsimilar boundary layer, $U_1^*(x^*)$ is not an analytical function, and the integration has to be with respect to x^*. A formula that is used in the JPL stability codes is

$$\ln\left(\frac{A}{A_0}\right) = -R_c \int_{(x_c)_0}^{x_c} \frac{\alpha_i}{R}\frac{U_1^*}{U_\infty^*} \, dx_c, \tag{2.69}$$

where α_i is based on the local L^*; U_∞^* is the velocity of the undisturbed freestream; x_c is x^*/c_h^*, where c_h^* is the chord; $R_c = U_\infty^* c_h^*/\nu^*$ is the full chord Reynolds number; and the integral is again evaluated for constant ω^* and β^*.

Chapter 3

Incompressible Inviscid Theory

The system of first-order equations 2.46, or the Orr-Sommerfeld equation in either 2D or 3D form, Eq. 2.42 or 2.44, governs the motion of linear waves at finite Reynolds numbers. With the highest derivative of $\hat{v}$ in the Orr-Sommerfeld equation multiplied by $1/R$, which is usually a small quantity, it is apparent that mathematical and numerical methods of some complexity are required to obtain the eigenvalues and eigenfunctions. On the other hand, if viscosity is considered to act only in the establishment of the mean flow, but to have a negligible effect on the instability waves, the equations take on a much simpler form. For example, the 2D Orr-Sommerfeld equation reduces to

$$\left[(\alpha U - \omega)\left(D^2 - \alpha^2\right) - \alpha D^2 U\right]\hat{v} = 0. \tag{3.1}$$

This is the fundamental equation of the inviscid stability theory, and is usually referred to as the Rayleigh equation. It is of second order and so only the two boundary conditions

$$\hat{v}(0) = 0, \quad \hat{v}(y) \to 0 \text{ as } y \to \infty, \tag{3.2}$$

can be satisfied. The normal velocity at the wall is zero, but the no slip condition is not satisfied.

The inviscid theory has dealt largely with 2D temporal waves. Since all of the essential ideas are included within this framework, we shall adopt the same procedure in this Section. The Rayleigh equation 3.1 has a singularity at $y = y_c$ where $\alpha U = \omega$. This singularity is of great importance in the theory, and is called the critical layer, or critical point. It does not occur in the Orr-Sommerfeld equation, but even so the Rayleigh equation is simpler to work with than the Orr-Sommerfeld equation, and an extensive inviscid stability theory has been developed over the past 100 years. The early work was mainly by Rayleigh (1880, 1887, 1892, 1895, 1913), but a great number of authors have made contributions in more recent times. An excellent review of the subject may be found in the article by Drazin and Howard (1966). Only those aspects of the theory which are necessary for a general understanding, and have relevance to boundary-layer flows, will be taken up in this Section. We also restrict ourselves to boundary layers with monotonic velocity profiles. These profiles have only a single critical layer. We defer until Section 12 the discussion of the important directional velocity profiles of 3D boundary layers which have two critical layers.

The inviscid theory has been used for two purposes. One is to provide two of the four independent solutions that are needed in the asymptotic viscous theory. The other is an inviscid stability theory per se. We shall not discuss the asymptotic theory, so it is only the second use that is of interest here. Not many numerical results have been worked out from the inviscid theory for incompressible boundary layers. However, one of the two chief instability mechanisms is inviscid in nature, so that some knowledge of the theory is essential for an understanding of boundary-layer instability. The presentation here will also serve as a necessary prelude to compressible stability theory, where the inviscid theory has a larger role to play.

3.1 Inflectional instability

3.1.1 Some mathematical results

There are a number of general mathematical results that can be established in the inviscid theory, in contrast to the viscous theory where few such results are known. We shall give two which demonstrate that no unstable or neutral temporal waves can exist unless the velocity profile has a point of inflection. The first result concerns unstable waves. If we multiply Eq. 3.1 by $\hat{v}^*$, the complex conjugate of $\hat{v}$, and then subtract the complex conjugate of the resultant equation, we obtain

$$D\left(\hat{v}^* D\hat{v} - \hat{v} D\hat{v}^*\right) - \frac{2i\omega_i D^2 U |\hat{v}|^2}{|\alpha U - \omega|^2} = 0. \tag{3.3}$$

The first term of Eq. 3.3 can be made more meaningful by relating it to the Reynolds stress, which, in dimensionless form, is

$$\tau = -\frac{\alpha}{2\pi} \int_0^{2\pi/\alpha} uv \, dx. \tag{3.4}$$

If we recall the necessity of first taking the real parts of u and v before multiplying, and make use of the continuity equation, we obtain

$$D\tau = \frac{\omega_i D^2 U \langle v^2 \rangle}{|\alpha U - \omega|^2}, \tag{3.5}$$

where $(1/2)|\hat{v}|^2 e^{2\omega_i t}$ has been replaced by $\langle v^2 \rangle$, the average over a wavelength of the square of the velocity fluctuation v.

Eq. 3.5 is a special case of a formula derived by Foote and Lin (1950) (see also Lin, 1954, 1955). When Eq. 3.5 is integrated from $y = 0$ to infinity, the Reynolds stress at the wall and in the freestream is zero by the boundary conditions. Therefore, since $D^2U = 0$ in the freestream,

$$\omega_i \int_0^{y_\delta} \frac{\langle v^2 \rangle D^2 U}{|\alpha U - \omega|^2} \, dy = 0, \tag{3.6}$$

where y_δ is the dimensionless boundary-layer thickness. It follows from Eq. 3.6 that if $\omega_i \neq 0$, D^2U must change sign somewhere in the interval $0 < y < y_\delta$. Consequently, it has been proven that the velocity profile must have a point of inflection for there to be an unstable wave. This result was first obtained by Rayleigh. Later, Fjortoft (1950) strengthened Rayleigh's necessary condition to $D^2U(U - U_s) < 0$ somewhere in the flow, where U_s is the mean velocity at the inflection point. This condition is equivalent to requiring that the modulus of DU have a maximum for there to be an instability. It is always satisfied in a boundary layer with an inflection point, because $DU \to 0$ as $y \to \infty$ and $|DU|$ cannot have only a minimum. It was subsequently proven by Tollmien (1935) that for most of the profiles which occur in boundary layers, including 3D boundary layers, the condition $D^2U = 0$ is also sufficient. Another result of Rayleigh, for which the proof will not be given, established that the phase velocity of an unstable wave always lies between the maximum and minimum values of U. This result was later generalized by Howard (1961) into an elegant semicircle theorem which relates both ω_r/α and ω_i/α to the maximum and minimum values of U.

The second result concerns neutral waves. It follows from Eq. 3.5 that with $\omega_i = 0$, the Reynolds stress must be constant everywhere except for a possible discontinuity at the critical layer y_c. When Eq. 3.5 is integrated across the boundary layer, the only contribution to the integral comes from the immediate neighborhood of y_c. Hence,

$$\tau\left(y_c + 0\right) - \tau\left(y_c - 0\right) = -\left(\frac{D^2U}{DU}\right)_c \langle v^2 \rangle \lim_{\omega_i \to 0} \int_{U(y_c - 0)}^{U(y_c + 0)} \frac{\omega_i}{\left(\alpha U - \omega_r\right)^2 + \omega_i^2} \, dU. \tag{3.7}$$

The integration variable has been changed from y to U. In the limit of $\omega_i \to 0$, the integrand of Eq. 3.7 acts as a delta function, and the integral has a value of π/α. Consequently,

$$\tau\left(y_c+0\right)-\tau\left(y_c-0\right)=\frac{\pi}{\alpha}\left(\frac{D^2U}{DU}\right)_c\langle v_c^2\rangle. \tag{3.8}$$

Since $\tau\left(y_c+0\right)$ and $\tau\left(y_c-0\right)$ are both zero by the boundary condition, D^2U_c must also be zero, and it has been proven that a wave of neutral stability can exist only when the velocity profile has a point of inflection. Furthermore, $\omega_r/\alpha = U_c$ and the phase velocity of a neutral wave is equal to the mean velocity at the inflection point.

The chief analytical feature of the Rayleigh equation 3.1 is the singularity at $\alpha U = \omega$. Since ω is in general complex, so is y_c. Of course the mean velocity U is real in the physical problem, but it may be analytically continued onto the complex plane by a power-series expansion of U or by some other method. Two approaches to obtaining analytical solutions of the inviscid equation are the power spectra series in α^2 used by Heisenberg (1924) and Lin (1945), and the method of Frobenius used by Tollmien (1929). The two solutions obtained by Tollmien are

$$\hat{v}_1(y)=\left(y-y_c\right)P_1\left(y-y_c\right), \tag{3.9a}$$

$$\hat{v}_2(y)=P_2\left(y-y_c\right)+\left(\frac{D^2U}{DU}\right)_c\left(y-y_c\right)P_1\left(y-y_c\right)\log\left(y-y_c\right), \tag{3.9b}$$

where

$$\begin{aligned}P_1\left(y-y_c\right)&=1+\left(\frac{D^2U}{2DU}\right)_c\left(y-y_c\right)+\frac{1}{6}\left[\left(\frac{D^3U}{DU}\right)_c+\alpha^2\right]\left(y-y_c\right)^2+\ldots,\\ P_2\left(y-y_c\right)&=1+\left[\left(\frac{D^3U}{2DU}\right)_c-\left(\frac{D^2U}{DU^2}\right)_c+\frac{1}{2}\alpha^2\right]\left(y-y_c\right)^2+\ldots.\end{aligned} \tag{3.10}$$

The first solution is regular, but $\hat{v}_2$ is not in general regular near y_c because of the logarithmic term. However, for a neutral wave D^2U_c is zero, and in this one case $\hat{v}_2$ is also regular.

To summarize what we have learned in this section, for a velocity profile without an inflection point, (e.g., the Blasius boundary layer), there can be neither unstable nor neutral waves (save for the trivial solution $\alpha = 0$, $\omega = 0$). When there is an inflection point, a neutral wave with a phase velocity equal to the mean velocity at the inflection point can exist, and in boundary layers unstable waves with phase velocities between 0 and 1 can and will exist.

3.1.2 Physical interpretations

The mathematical theory is complete in itself, and with the use of the Reynolds stress also makes the physical consequences of an inflection point clear. However, there have been attempts to formulate physical arguments that in some manner bring in the concept of negative stiffness, which is the way one usually thinks about unstable wave motions. The first of these was by Taylor (1915), and appeared as an addendum to a major paper in which he developed his vorticity transfer theory. He applied this theory to deriving an expression for the vertical transfer of disturbance momentum, which immediately showed that if D^2U is of the same sign everywhere, the disturbance momentum can only increase or decrease everywhere, a situation incompatible with the inviscid boundary conditions. However, if D^2U changes sign, then momentum can be transferred from one place to another without affecting the boundaries, thus permitting instability. Later arguments made use of vorticity concepts. The most detailed is by Lin (1945, 1955), and is supported by a considerable mathematical development. Lighthill (1963, p. 92) gives a very helpful presentation with three diagrams, and finally Gill (1965a) has constructed an argument that makes use of Kelvin's (1880) cat's-eye diagram of the streamlines in the vicinity of an inflection point to demonstrate that only a maximum in DU can cause instability. All of these presentations are worth careful study.

3.2 Numerical integration

The analytical methods are not adequate for producing numerical solutions of the Rayleigh equation except in certain special cases. Only direct numerical integration of Eq. 3.1 can produce solutions accurately and

quickly for the great variety of velocity profiles encountered in practice. There are at least two methods available. In the first, which was developed by Conte and Miles (1959), the integration is restricted to the real axis and is carried past the critical point by the Tollmien solutions. In the second method, which was developed by Zaat (1958), the solution is produced entirely by numerical integration, and the critical point is avoided by use of an indented contour in the complex plane. It is as easy to perform the numerical integration along such a contour as along the real axis, provided the analytic continuation of U away from the real axis is available. This approach, except for a difference in the method of analytic continuation, which was used by Mack (1965a) to integrate the compressible inviscid equations. It was later extended to incompressible flow, and is incorporated into the JPL inviscid stability code ISTAB.

For numerical integration, Eq. 3.1 is replaced by the two first-order equations for $\hat{v}$ and $\hat{p}$ which follow from Eqs. 2.36 when $R \to \infty$:

$$D\hat{v} = \frac{\alpha}{\alpha U - \omega} \left(DU\hat{v} + i\alpha\hat{p} \right), \tag{3.11a}$$

$$D\hat{p} = -i \left(\alpha U - \omega \right) \hat{v}. \tag{3.11b}$$

The solutions in the freestream, where $U = 1$ and $DU = 0$, are

$$\hat{v} = e^{-\alpha y}, \tag{3.12a}$$

$$\hat{p} = -i \left(1 - \frac{\omega}{\alpha} \right) e^{-\alpha y}, \tag{3.12b}$$

where we have chosen the normalization to agree with Eqs. 2.50. These expressions provide the initial values for the numerical integration to start at some $y = y_1 > y_\delta$. For chosen values of α and $\omega_r + i\omega_i$, the integration proceeds from y_1 to the wall along the real y axis and an indented rectangular contour around the critical point when necessary. The velocity U is continued on to the indented contour by a power-series expansion in $y - y_c$. The necessary derivatives of U are obtained from the boundary-layer equations. A Newton-Raphson search procedure, in which any two of α, ω_r, ω_i are perturbed, is used to find the eigenvalues, i.e., an α and $\omega_r + i\omega_i$ for which the boundary condition $\hat{v}(0) = 0$ is satisfied. If α is held constant, then the Cauchy-Riemann equations can be used to eliminate one perturbation because the function $\Omega(\alpha)$ in the dispersion relation is analytic.

3.3 Amplified and damped inviscid waves

3.3.1 Amplified and damped solutions as complex conjugates

In the use of the inviscid theory in the asymptotic viscous theory, the choice of the branch of the logarithm in Eq. 3.9b constitutes a major problem. The same difficulty also shows up in the inviscid theory itself, but in a much less obvious manner. Since $DU > 0$ for the type of boundary layer we are considering in this Section, it follows that for an amplified wave ($\omega_i > 0$) the critical layer lies above the real y axis [$(y_c)_i > 0$]; for a damped wave ($\omega_i < 0$) it is below the real axis [$(y_c)_i < 0$]. For a neutral wave ($\omega_i = 0$), the critical layer is on the real axis, but since $D^2U_c = 0$ the logarithmic term drops out of Eq. 3.9b and the solution is regular. With the critical layer located off the real axis for amplified and damped waves, it would seem that there is nothing to hinder integration along the real axis. Indeed, it can be seen by manipulating the inviscid equation (3.1) that if $\hat{v}_r + i\hat{v}_i$ is a solution for $\omega_r + i\omega_i$, then $\hat{v}_r - i\hat{v}_i$ is a solution for $\omega_r - i\omega_i$. Thus amplified and damped solutions are complex conjugates, and the existence of one implies the existence of the other. From this point of view, the criterion for instability is that ω is complex, and the only stability is neutral stability with ω real. Since Eq. 3.6 applies for $\omega_i < 0$ as well as for $\omega_i > 0$, neither amplified nor damped waves can exist unless there is an inflection point. The Blasius boundary layer has no inflection point (except at $y = 0$), and according to this argument no inviscid waves are possible, amplified, damped or neutral (except for $\alpha = 0$, $\omega = 0$). But viscous solutions certainly exist; what happens to these solutions in the limit as $R \to \infty$?

3.3.2 Amplified and damped solutions as $R \to \infty$ limit of viscous solutions

The clarification of this point is due to Lin (1945), who showed that if the inviscid solutions are regarded as the infinite Reynolds limit of viscous solutions, a consistent inviscid theory can be constructed in which damped solutions exist that are not the complex conjugates of amplified solutions. To achieve this result, integration along the real axis is abandoned for damped waves. Instead, the path of integration is taken under the singularity just as it is for the inviscid solutions that are used in the asymptotic viscous theory, and $\ln(y - y_c) = \ln|y - y_c| - i\pi$ for $y < y_c$. For damped waves, the effect of viscosity is present even in the limit $R \to \infty$, and a completely inviscid solution cannot be valid along the entire real axis. Lin's arguments were physical and heuristic, but a rigorous justification was given by Wasow (1948).

It is also possible to arrive at Lin's result from a strictly numerical approach. In Section 3.2, no mention was made of how to indent the contour of integration. The two possibilities are shown in Fig. 3.1. For an inviscid neutral solution ($\omega_i = 0$), $\hat{v}$ is purely imaginary and $\hat{p}$ is real. It makes no difference if the contour is indented below the real axis, as in Fig. 3.1a, or above, as in Fig. 3.1b. The same eigenvalue α is obtained in either case. If $\omega_i \neq 0$, the integration can be restricted to the real axis. However, unless $D^2U = 0$ somewhere in the boundary layer, there are no amplified solutions, or their complex conjugates the damped solutions. But if we use contour (a) for damped waves, and contour (b) for amplified waves, both solutions exist even with $D^2U \neq 0$. Some eigenvalues computed for the Blasius velocity profile are given in Table 3.1, where the eigenvalues have been made dimensionless by reference to L^* [Eq. 2.57], which enters the inviscid problem through the boundary-layer similarity variable $y = y^*/L^*$. As can be verified from Eqs. 3.11, the solutions with $\omega_r - i\omega_i$ and contour (a) are related to the solutions with $\omega_r + i\omega_i$ and contour (b) by

$$\begin{aligned} \hat{v}^{(a)} + i\hat{v}^{(a)} &= \hat{v}^{(b)} - i\hat{v}^{(b)}, \\ \hat{p}^{(a)} + i\hat{p}^{(a)} &= -\hat{p}^{(b)} + i\hat{p}^{(b)}. \end{aligned} \tag{3.13}$$

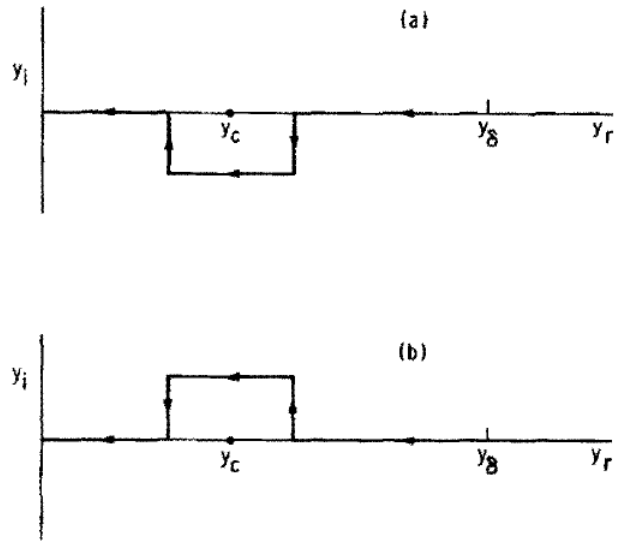

Figure 3.1: Alternative indented contours for numerical integration of inviscid equations.

Which option do we pick, (a) or (b)? Since the neutral-stability curve for the Blasius profile is of the type shown in Fig. 1.1a, waves of all wavenumbers are damped in the limit $R \to \infty$. Consequently, if the inviscid solutions are required to be the $R \to \infty$ limit of viscous solutions, it is evident that contour (a) must be used, just as in the asymptotic theory and in agreement with Lin. Without an inflection point, there are no inviscid amplified solutions. For a velocity profile with $D^2U = 0$ at y_s, where the subscript s refers to the inflection point, both amplified and damped waves exist for each contour, unlike the Blasius case. The

Table 3.1: Inviscid eigenvalues of Blasius velocity profile computed with indented contours

Contour	α	ω_r	$\omega_i \times 10^3$
(a)	0.128	0.0333	-2.33
(b)	0.128	0.0333	2.33
(a)	0.180	0.0580	-6.80
(b)	0.180	0.0580	6.80

neutral wavenumber is α_s, and can be obtained with either contour. With contour (a), the wavenumbers of the amplified waves are located below α_s, and the wavenumbers of the damped waves are located above α_s; contour (b) gives the opposite results. Comparison with the viscous neutral-stability curve, which is of the type shown in Fig. 1.1b, shows that contour (b) must be rejected in this case also.

The damped solutions with contour (a) do not exist everywhere on the real axis. According to Lin (1955, p. 136), there is an interval of the real axis in the vicinity of the critical layer where viscosity will always have an effect even in the limit of $R \to \infty$, and where the inviscid solution is not a valid asymptotic approximation to the viscous solution. In the final paragraph of his book, Lin remarked that in this interval the viscous solution has an oscillatory behavior. This remark was confirmed analytically by Tatsumi and Gotch (1971), and verified numerically by Davey (1981) at an extremely high Reynolds number using the compound matrix method.

As a numerical example of damped inviscid eigenvalues, Fig. 3.2 gives $-\omega_i$, the temporal damping rate, as a function of α for the Blasius velocity profile. The calculation was performed along an indented contour of type (a). The inviscid damping rates are, for the most part, much larger than the viscous amplification rates. That damped inviscid eigenvalues calculated with a type (a) contour are the $R \to \infty$ limit of viscous eigenvalues was confirmed numerically by Davey in the paper mentioned in the preceding paragraph. For $\alpha = 0.179$, the inviscid eigenvalue is $\omega/\alpha = 0.32126 - 0.03671i$; the viscous eigenvalue computed by Davey at $R = 1 \times 10^6$ is $\omega/\alpha = 0.32166 - 0.03629i$.

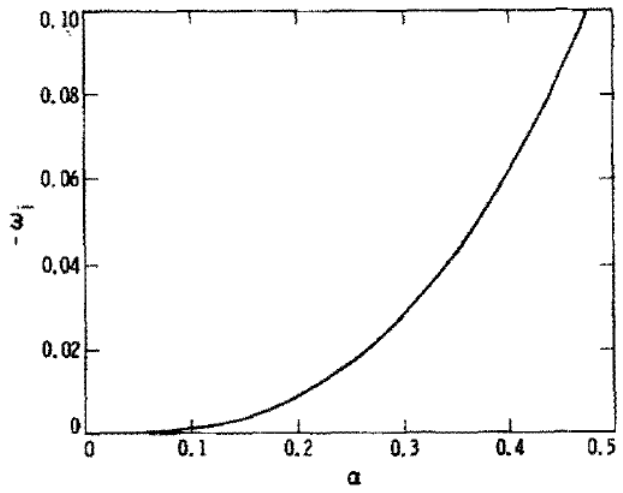

Figure 3.2: Inviscid temporal damping rate vs. wavenumber for Blasius boundary layer.

Chapter 4

Numerical Techniques

4.1 Types of methods

Since the early 1960's, the asymptotic theories developed by Tollmien (1929) and Lin (1945) have been largely superseded as a means of producing numerical results in favor of direct solutions of the governing differential equations on a digital computer. The numerical methods that have been employed fall roughly into three categories: (1) finite-difference methods, used first by Thomas (1953) in his pioneering numerical work on plane Poiseuille flow, and later by Kurtz (1961), Osborne (1967), and Jordinson (1970), among others; (2) spectral methods, used first by Gallagher and Mercier (1962) for Couette flow with Chandrasekhar and Reid functions, and later improved by Orszag (1971) with the use of Chebyshev polynomials; and (3) shooting methods, used first by Brown and Sayre (1954). All of these methods have advantages and disadvantages which show up in specialized situations, but they are all equally able to do the routine eigenvalue computations required in transition-prediction calculations. However, a shooting method has been used for almost all of the numerical results given in the present lectures, and it is this method that will be described here.

4.2 Shooting methods

After the early work of Brown and Sayre (1954) and Brown (1959, 1960, 1961, 1962), computer codes for boundary-layer problems that were also based on shooting methods were developed by Nachtsheim (1963), Mack (1965a), Landahl and Kaplan (1965), Radbill and Van Driest (1966), Wazzan et al. (1968b), Davey (1973), and Cebeci and Stewartson (1980a), among others. Most of these codes solve the Orr-Sommerfeld equation; exceptions are the compressible stability code of Brown (1961), and the codes of Mack (1965a), which were also originally developed for compressible flow and only later extended to incompressible flow. Almost all of the codes have the feature that the numerical integration proceeds from the freestream to the wall. The exceptions are the codes of Brown and of Nachtsheim (1963), where the integration proceeds in the opposite direction [in a later report on plane Poiseuille flow, Nachtsheim (1964) used a method that integrates in both directions].

Various integrators have been used to implement the shooting method. Perhaps the most common is some form of the Runge-Kutta method, but the Adams-Moulton and Keller box method have also been used. One choice that has to be made is whether to use a fixed or variable step-size integrator. The latter is better in principle, but it adds to the computational overhead, and thus to the expense, and it may be as difficult to construct a proper error test and then choose the error limits as it is to select the proper fixed step size. It must also be remembered that the variable step-size methods do not really address the right problem. What we are interested in is a certain accuracy of the eigenvalues and eigenfunctions, not in the per-step truncation error of the independent solutions, which is what the variable step-size methods control. These methods seem to require more integration steps than fixed step-size methods, which adds to the expense, and the only compensation is to relieve the user of the need to select the step size. The JPL viscous stability codes have used a fixed step-size fourth-order Runge-Kutta integrator for many years without ever encountering

a problem that required a variable step-size integrator. A severe test of any integrator is to calculate the discrete eigenvalue spectrum, because the higher viscous modes have rapidly oscillating eigenfunctions. The fixed step-size integrator had little difficulty in calculating a number of additional temporal modes for plane Poiseuille flow, and its ultimate failure in a portion of the complex ω/α plane for Blasius flow was caused by a round-off error problem that apparently cannot be cured by any of the usual methods (Mack, 1976, p. 501).

The early applications of shooting methods suffered from the problem of parasitic error growth. This growth arises because of the presence of a rapidly growing solution in the direction of integration that is associated with the large characteristic value λ_3 in the freestream, which the numerical round-off error will follow. The parasitic error eventually completely contaminates the less rapidly growing solution, associated with the characteristic value λ_1 in the freestream. The essential advance in coping with this problem, which had previously limited numerical solutions to moderate Reynolds numbers, was made by Kaplan and Moore (1964). The Kaplan method "purifies" the contaminated solution by filtering out the parasitic error whenever it becomes large enough to destroy the linear independence of the solutions. An illuminating presentation and application of the Kaplan method may be found in Betchov and Criminale (1967). Three recent methods that cope exceptionally well with the contamination problem are the Riccati method (Davey, 1977, 1979), the method of compound matrices of Ng and Reid (1979, 1980), and the method of order reduction (Van Stijn and Van De Vooren, 1982).

4.3 Gram-Schmidt orthonormalization

A widely used method, that was originally developed for systems of linear differential equations by Godunov (1961) and Bellman and Kalaba (1965) and applied to the boundary-layer stability problem by Radbill and Van Driest (1966) and Wazzan et al. (1968b), is that of Gram-Schmidt orthonormalization. This method has the advantage that it is easier to generalize to higher-order systems than is the Kaplan filtering technique. However, the geometrical argument often adduced in its support, that this procedure preserves linear independence by keeping the solution vectors orthogonal, cannot be correct because the solution vector space does not have a metric. In such vector spaces, vectors are either parallel or non-parallel; the concept of orthogonality does not exist. Instead, the orthonormalization method works on exactly the same basis as Kaplan filtering: the "small" solution is replaced by a linear combination of the "small" and "large" solutions which is itself constrained to be "small".

For the simplest case of a two-dimensional wave in a two-dimensional boundary layer, there are two solutions, $Z^{(1)}$ and $Z^{(3)}$, each consisting of four components. In the freestream, $Z^{(1)}$ is the inviscid and $Z^{(3)}$ is the viscous solution. Although this identification is lost in the boundary layer, $Z^{(3)}$ continues to grow more rapidly with decreasing y than does $Z^{(1)}$. The parasitic error will follow $Z^{(3)}$, and when the difference in the "magnitudes" of $Z^{(3)}$ and $Z^{(1)}$ as defined by an arbitrarily assigned metric becomes sufficiently large, $Z^{(1)}$ will no longer be independent of $Z^{(3)}$. Well before this occurs, the Gram-Schmidt orthonormalization algorithm is applied. The "large" solution $Z^{(3)}$ is normalized component by component to give the new solution

$$S^{(3)} = \frac{Z^{(3)}}{\sqrt{\left\{ Z^{(3)*} Z^{(3)} \right\}}}, \tag{4.1}$$

where an asterisk refers to a complex conjugate and $\{\}$ to a scalar product. The metric adopted for the vector space is the usual Euclidian norm. The scalar product of $Z^{(1)}$ and $S^{(3)}$ is used to form the vector

$$S^{(1)} = \frac{\left[Z^{(1)*} - \left(S^{(3)*} Z^{(1)} \right) S^{(3)} \right]}{\sqrt{\left(\overline{S}^{(1)*} \overline{S}^{(1)} \right)}}, \tag{4.2}$$

which replaces $Z^{(1)}$, and where $\overline{S}$ refers to the quantity in the numerator.

The numerical integration continues with $S^{(1)}$ and $S^{(3)}$ in place of $Z^{(1)}$ and $Z^{(3)}$, and when in turn $|S^{(3)}|$ exceeds the set criterion of, say, 10^5 with single precision arithmetic and a 36 bit computer word, the orthonormalization is repeated. With homogeneous boundary conditions at the wall, it makes no difference

in the determination of the eigenvalues whether the $Z^{(i)}$ or $S^{(i)}$ are used. A linear combination of the two solutions satisfies the $\beta(0) = 0$ boundary condition, but the $\hat{v}(0) = 0$ boundary condition will in general not be satisfied unless α, β, and ω satisfy the dispersion relation.

Although the orthonormalization procedure has no effect on the method of determining eigenvalues, it does complicate the calculation of the eigenfunctions. The solution vectors of the numerical integration are linear combinations of the original solution vectors $Z^{(1)}$ and $Z^{(3)}$, and it is necessary to "unravel" these combinations. Two well-known applications of orthonormalization have been given by Conte (1966) and by Scott and Watts (1977). The latter authors incorporated their method in the general purpose code SUPORT that has been used in several stability investigations. A different procedure from either of these was worked out for the JPL stability codes (1971), and is readily applicable to any order of differential equations.

4.4 Newton-Raphson search procedure

The Newton-Raphson method has been found to be satisfactory for obtaining the eigenvalues. The boundary condition on $Z^{(1)}$ (or $S^{(1)}$) is satisfied at the conclusion of each integration by a linear combination of the two solutions at $y = 0$. In the spatial theory with ω and β fixed, the guess value of α_r is perturbed by a small amount and the integration repeated. Because $\hat{v}(0)$ is an analytic function of the complex variable α, the Cauchy-Riemann equations

$$\frac{\partial \hat{v}_i(0)}{\partial \alpha_i} = \frac{\partial \hat{v}_r(0)}{\partial \alpha_r}, \tag{4.3a}$$

$$\frac{\partial \hat{v}_r(0)}{\partial \alpha_i} = -\frac{\partial \hat{v}_i(0)}{\partial \alpha_r}, \tag{4.3b}$$

can be applied to eliminate the need for a second integration with α_i perturbed. We may note that $\hat{v}(0)$ is an analytic function of α even after orthonormalization with the usual definition of the scalar product, remarks to the contrary in the literature notwithstanding.

The corrections $\delta\alpha_r$ and $\delta\alpha_i$ to the initial guesses α_r and α_i are obtained from the residual $\hat{v}(0)$ and the numerical (linear) approximations to the partial derivatives by

$$\frac{\partial \hat{v}_r(0)}{\partial \alpha_r}\delta\alpha_r - \frac{\partial \hat{v}_r(0)}{\partial \alpha_i}\delta\alpha_i = -\hat{v}_r(0), \tag{4.4a}$$

$$\frac{\partial \hat{v}_i(0)}{\partial \alpha_r}\delta\alpha_r - \frac{\partial \hat{v}_i(0)}{\partial \alpha_i}\delta\alpha_i = -\hat{v}_i(0), \tag{4.4b}$$

The corrected α_r and α_i are used to start a new iteration, and the process continues until $\delta\alpha_r$ and $\delta\alpha_i$ have been reduced below a preset criterion.

Chapter 5

Viscous Instability

5.1 Kinetic-energy equation

The approach to instability theory based on the energy equation was originated by Reynolds (1895), and has proven to be especially helpful in the nonlinear theory. An extended account of recent work has been given by Joseph (1976). In the linear theory, the eigenmodes of the Orr-Sommerfeld equation already supply us with complete information on the instability characteristics of any flow, so the energy method is mainly useful as an aid to our physical understanding. We start by defining

$$e = \frac{1}{2}\left(u^2 + v^2\right) \tag{5.1}$$

to be the kinetic energy of a small 2D disturbance. When we multiply the dimensionless x and y parallel-flow momentum equations by u and v, respectively, and add, we obtain

$$\left(\frac{\partial}{\partial t} + U\frac{\partial}{\partial x}\right)e + uv\frac{dU}{dy} = -u\frac{\partial p}{\partial x} - v\frac{\partial p}{\partial y} + \frac{1}{R}\left(u\nabla^2 u + v\nabla^2 v\right). \tag{5.2}$$

If we integrate Eq. 5.2 from $y = 0$ to infinity and average over a wavelength, we find, for a temporal disturbance,

$$\frac{\partial E}{\partial t} = \int_0^\infty \tau\frac{dU}{dy}\,dy - \frac{1}{R}\int_0^\infty \left\langle\zeta^2\right\rangle\,dy, \tag{5.3}$$

where E is the total disturbance kinetic energy per wavelength, $\tau = -\langle uv\rangle$ is the Reynolds stress, and

$$\zeta = \frac{\partial u}{\partial y} - \frac{\partial v}{\partial x} \tag{5.4}$$

is the z-component of the fluctuation vorticity. A derivation of Eq. 5.3 may be found in the review article of Prandtl (1934, p. 180). The last term can be rewritten as

$$\int_0^\infty \left\langle\zeta^2\right\rangle\,dy = 2\int_0^\infty \left\langle\left(\frac{\partial u}{\partial y}\right)^2 + \left(\frac{\partial v}{\partial x}\right)^2\right\rangle\,dy + \int_0^\infty \left\langle\left(\frac{\partial u}{\partial y} + \frac{\partial v}{\partial x}\right)^2\right\rangle\,dy, \tag{5.5}$$

which is more readily identified as the viscous dissipation. It is customary to write Eq. 5.3 as

$$\frac{\partial E}{\partial t} = \bar{P} - \bar{D}, \tag{5.6}$$

where

$$\bar{P} = \int_0^\infty \tau\frac{dU}{dy}\,dy \tag{5.7a}$$

is the total energy production term over a wavelength, and

$$\bar{D} = \int_0^\infty \langle \zeta^2 \rangle \, dy \tag{5.7b}$$

is the viscous dissipation. A disturbance will amplify, be neutral, or damp depending on whether P is greater than, equal to, or less than D. Consequently, there can only be instability if τ is sufficiently positive over enough of the boundary layer so that the production term can outweigh the dissipation term.

5.2 Reynolds stress in the viscous wall region

The inviscid theory gives the result that a flow with a convex velocity profile, of which the Blasius boundary layer is an example, can support only damped instability waves. Originally the prevailing view was that a flow that is stable in the absence of viscosity can only be more stable when viscosity is present. We see from Eq. 3.8 that in a Blasius boundary layer, where $D^2U < 0$, a wave of any phase velocity less than the freestream velocity creates a positive Reynolds stress for $y < y_c$. Therefore, the only way an instability wave can exist is if the viscosity causes a positive Reynolds stress to build up near the wall. It was this possibility that Taylor (1915) recognized, but his observation went unnoticed. A few years later, Prandtl (1921) was led to the same idea, and calculated the Reynolds stress near the wall from a simple mathematical model.

It is of interest to note that Prandtl was moved to investigate the possibility of viscous instability by an experiment in which he saw, or thought he saw, amplifying instability waves in a flow that was supposed to be stable. In view of the importance of this discovery, we shall quote a few lines from his paper:

> Previous mathematical investigations on the origin of turbulence ahve led to the opinion that small disturbances of a viscous, laminar flow between two walls are always damped... In order to learn how turbulence actually originates, I had built at Göttingen an open channel...and observed the flow by the Ahlborn method (sprinkled lycopodium powder)... Wave forms with slowly increasing amplitude were occasionally observed... These waves of increasing amplitude contradicted the dogma of the stability of laminar motion with respect to small disturbances, so that at first I tended to believe that I had not seen this infrequent phenomenon completely right.
>
> We now applied ourselves to the theoretical treatment, and, to anticipate a little, we found, contrary to the dogma, an instability of the small disturbances.

Prandtl's argument was later refined by Lin (1954, 1955), but we shall follow essentially the original derivation here. An inviscid wave is assumed to exist in the boundary layer, and viscosity to act only in a narrow region near the wall. To simplify the analysis, $U(y)$ is taken to be zero in this region. With this assumption, the 2D dimensionless, parallel flow x momentum equation simplifies to

$$\frac{\partial u}{\partial t} = -\frac{\partial p}{\partial x} + \frac{1}{R}\frac{\partial^2 u}{\partial y^2}, \tag{5.8}$$

where the terms vDU and $\partial^2 u/\partial x^2$ have been dropped. Outside of the wall viscous region, Eq. 5.8 reduces

$$\frac{\partial u}{\partial t} = -\frac{\partial p}{\partial x}. \tag{5.9}$$

The disturbance velocity u consists of two parts: an inviscid part u_i that satisfies Eq. 5.9, and a viscous part u_v that satisfies the difference between Eqs. 5.8 and 5.9. It is the total velocity $u = u_i + u_v$ that satisfies the no-slip boundary condition. Hence,

$$\frac{\partial u_v}{\partial t} = \frac{1}{R}\frac{\partial^2 u_v}{\partial y^2}. \tag{5.10}$$

The solution of Eq. 5.10 for ω real is

$$u_v(y) = -u_i(0) \exp\left[-(1-i)y\sqrt{\frac{\omega R}{2}}\right] \exp[i(\alpha x - \omega t)], \tag{5.11}$$

where the boundary conditions

$$u(0) = u_i(0) + u_v(0) \text{ and } u(y) \to u_i(y) \text{ as } y \to \infty \tag{5.12}$$

have been applied.

The additional longitudinal disturbance velocity u_v, which is needed to satisfy the no-slip condition, induces, through the continuity equation, an additional normal disturbance velocity.

$$v_v(y) = -\int_0^y \frac{\partial u_v}{\partial y} dy, \tag{5.13}$$

which yields, upon substitution of Eq. 5.11,

$$v_v(y) = (1-i)\alpha u_i(0)\sqrt{\frac{1}{2\omega R}}\left\{\exp\left[-(1-i)y\sqrt{\frac{\omega R}{2}}\right] - 1\right\}\exp[i(\alpha x - \omega t)]. \tag{5.14}$$

Outside of the viscous region ($y \to \infty$) v_v is independent of y and u_v is zero. From Eq. 5.14,

$$v_v(\infty) = -(1-i)\left(\frac{\alpha u_i(0)}{\sqrt{2\omega R}}\right)\exp[i(\alpha x - \omega t)]. \tag{5.15}$$

The consequences of Eq. 5.15 for the Reynolds stress are as follows. For an inviscid neutral disturbance, u and v are 90° out of phase (see Eqs. 2.50a and 2.50c) and τ is zero. However, for any other disturbance u and v are correlated, and there is a Reynolds stress. Since u_v is zero outside of the wall viscous layer, it can contribute nothing to the τ there. However, v_v persists for some distance outside of the wall layer, and since it is shifted 135° with respect to u, it will produce a Reynolds stress. This Reynolds stress must equal the Reynolds stress set up by the disturbance in the vicinity of the critical layer, and which, in the absence of viscosity, would extend to the wall. We have already derived a formula for this stress in Section 3.1 (Eq. 3.8).

The formula for the Reynold stress at the edge of the wall viscous region can be derived from Eq. 5.15. We find

$$\tau_e = -\langle u_i v_v \rangle = \frac{1}{2}\sqrt{\frac{\alpha}{2\omega R}}[u_i(0)]^2. \tag{5.16}$$

If the ratio $\tau_e/\langle v_v^2 \rangle$ is formed, we have

$$\frac{\tau_e}{\langle v_v^2 \rangle} = \frac{1}{2\alpha}\sqrt{\frac{2}{\omega R}}. \tag{5.17}$$

A general expression for τ in the wall viscous region can be obtained from Eqs. 5.11 and 5.14, and this expression would give the increase of τ from zero at the wall to the value given by Eq. 5.17 at the edge of the viscous region. However, Eq. 5.17 establishes the essential result that τ is positive, and thus viscosity acts as Taylor thought it would, and builds up a Reynolds tress to match the inviscid Reynolds stress, or, in Taylor's precise view, permits the momentum of the disturbance to be absorbed at the wall. According to Eq. 5.7a, with a positive stress energy will be transferred from the mean flow to the disturbance. consequently, the wall viscous region, which is formed to satisfy the no-slip boundary condition for the disturbance, has the effect of creating a Reynolds stress which acts to destabilize the flow. This mechanism must be present to some extent for all disturbance, but whether a particular disturbance is actually amplified or damped will depend on the magnitude and distribution of the Reynolds stress through the entire boundary layer, and on the magnitude of the dissipation term.

As a note of caution, it must be recalled that the preceding analysis rests on the neglect of U in the wall viscous region. Therefore, we can expect the results to be valid only at high values of R, when the wall viscous region is thin compared to the boundary-layer thickness, and when the critical layer is outside of the wall viscous region.

Chapter 6

Numerical Results - 2D Boundary Layers

In this chapter, we shall present a number of numerical results which have been chosen to illustrate important aspects of the theory, as well as the give an idea of the numerical magnitudes of the quantities we have been discussing in the previous chapters.

6.1 Blasius boundary layer

The Blasius boundary layer, because of its simplicity, has received the most attention. The uniform external flow means that not only is the boundary layer self-similar, but there is only a single parameter, the Reynolds number. As there is no inflection point in the velocity profile, the only instability is viscous instability. Thus we are able to study this form of instability without the competing influence of any other mechanism of instability.

The first result of importance is the parallel-flow neutral stability curve for 2D waves, which is shown in Fig. 6.1 as three separate curves for: (a) the dimensionless frequency F (Eq. 2.60); (b) the dimensionless wavenumber α based on L^* (Eq. 2.57); and (c) the dimensionless phase velocity c based on U_1^*. Normal modes for which F, α and c lie on the curves are neutral; those for which F, α and c lie in the interior of the curves are unstable; everywhere else the normal modes are damped. The neutral-stability curves are a convenient means of identifying at each Reynolds number the F, α and c bands for which a wave is unstable. Figure 6.1a also contains two additional curves which give the frequencies of the maximum spatial amplification rate and of the maximum amplitude ratio A/A_0, where A_0 is the amplitude at the lower-branch neutral point of the frequency in question. Both maxima are with respect to frequency at constant Reynolds number. We have used σ in Fig. 6.1a to denote $-\alpha_i$, the spatial amplification rate in teh streamwise direction, and will continue to do so in the remainder of this document. The corresponding wavenumbers for the additional curves are given in Fig. 6.1b. The ratio of wavelength to boundary-layer thickness is $2\pi/\alpha_r y_\delta$, and y_δ, the y (Eq. 2.59) for which $U = 0.999$, is equal to 6.01. Consequently, the unstable waves at $R = 1000$ have wavelengths between 5.55δ ($19.4\delta^*$) and 14.1δ ($49.2\delta^*$)[1]. According to Fig. 6.1c, the unstable phase velocities at this Reynolds number are between $0.282U_1^*$ and $0.335U_1^*$.

We must keep in mind that the neutral stability curves of Fig. 6.1 have been calculated from the quasi-parallel theory, which does not distinguish between flow variables or location in the boundary layer. All of the non-parallel neutral curves calculated by Gaster (1974) define a slightly greater unstable zone, with the greatest differences coming at the lowest Reynolds numbers as might be expected. The difficulties involved in making accurate measurements of wave growth at low Reynolds numbers have so far precluded the experimental determination of what can be regarded as an unequivocally "correct" neutral-stability curve for any flow variable.

[1] δ is the dimensional boundary-layer thickness, y_δ is the dimensionless boundary-layer thickness δ/L^*, and, in accord with the standard notation, δ^* is the dimensional displacement thickness.

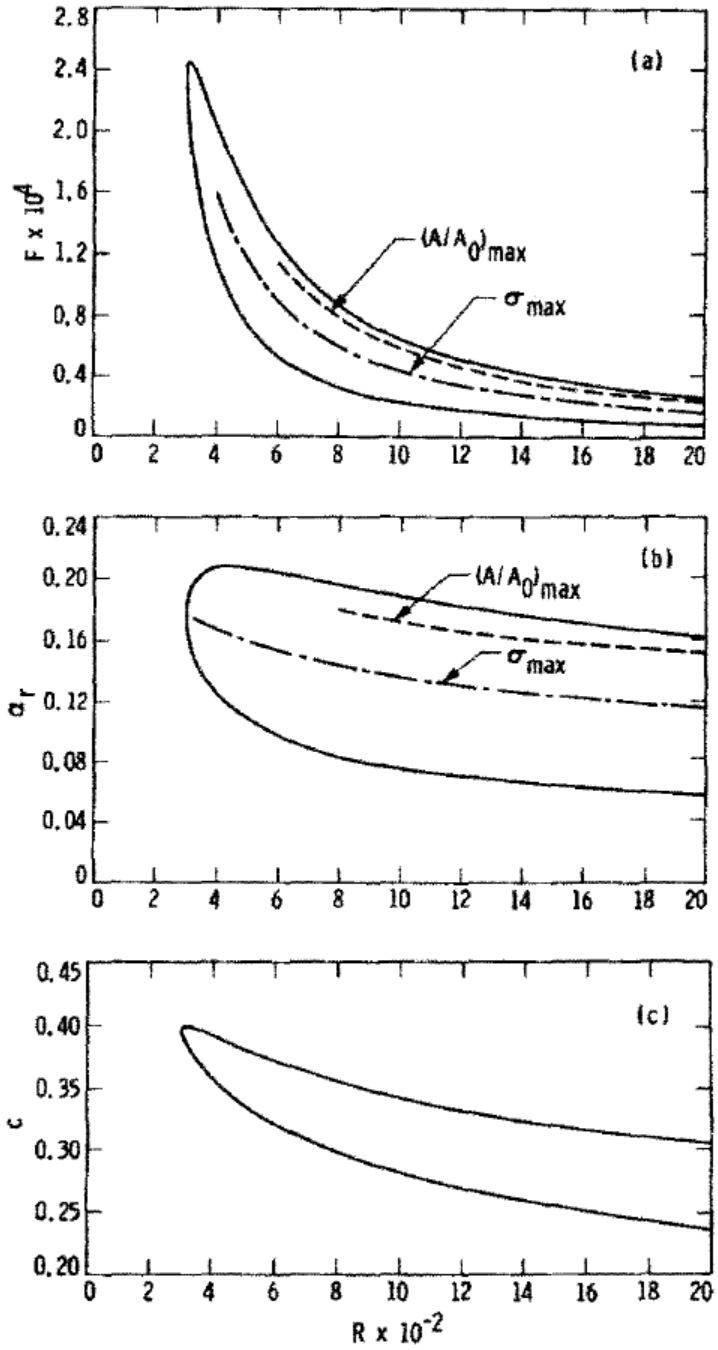

Figure 6.1: Neutral-stability curves for Blasius boundary layer: (a) F vs. R; (b) α_r vs. R; (c) c vs. R; $-\cdot-$, $\sigma_{\max}$; $---$, $(A/A_0)_{\max}$; both maxima are with respect to frequency at constant R.

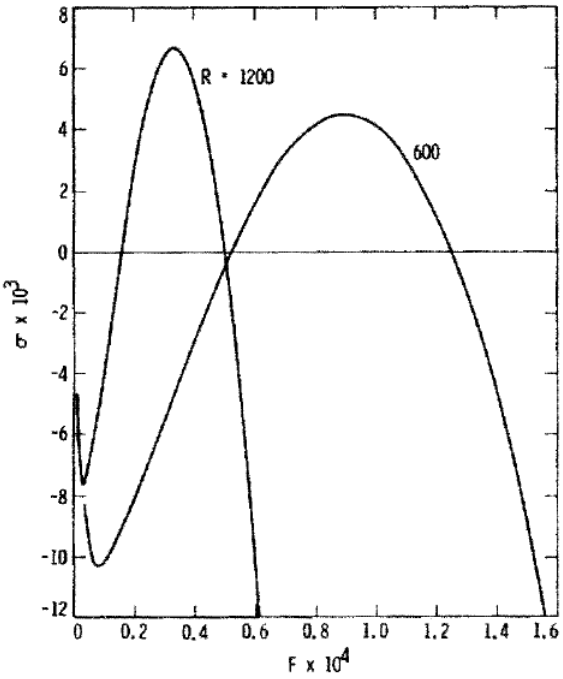

Figure 6.2: Distribution of 2D spatial amplification rate with frequency in Blasius boundary layer at $R = 600$ and 1200.

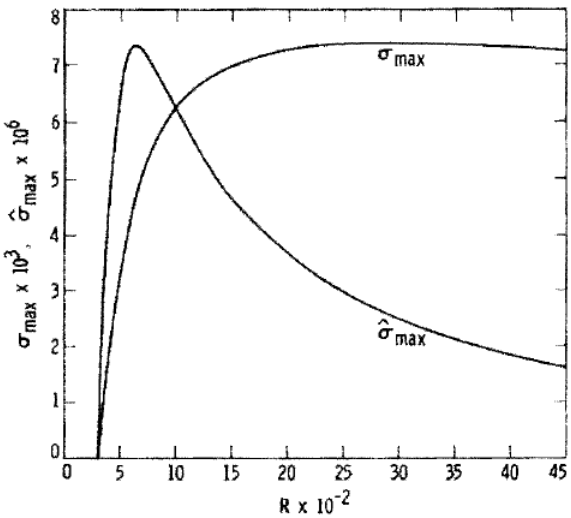

Figure 6.3: Maximum 2D spatial amplification rates $\sigma_{\max}$ and $\hat{\sigma}_{\max}$ as functions of Reynolds number for Blasius boundary layer.

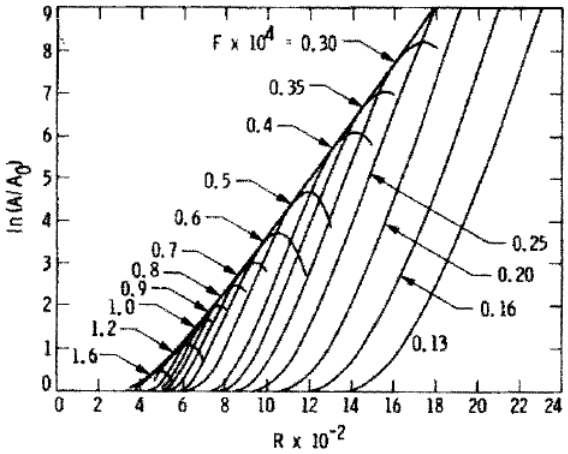

Figure 6.4: 2D $\ln(A/A_0)$ as function of R for several frequencies plus envelope curve; Blasius boundary layer.

The next quantity to examine is the dimensionless spatial amplification rate σ based on L^*. This amplification rate is shown in Fig. 6.2 for 2D waves as a function fo the dimensionless frequency F at the two Reynolds numbers $R = 600$ and 1200. From the definition of the amplification rate in Eq. 2.27, the fractional change in amplitude over a distance equal to one boundary-layer thickness is σy_δ. Thus the most unstable wave of frequency $F = 0.33 \times 10^{-4}$ at $R = 1200$ grows by 4.0% over a boundary-layer thickness. The amplification rate based on ν^*/U_1^*, $\hat{\sigma} = \sigma/R$, gives the fractional wave growth over a unit increment in Re. Thus this same wave grows by 5.6% over an increment in Re of 10,000.

The maximum amplification rates $\sigma_{\max}$ and $\hat{\sigma}_{\max}$, where the maxima are with respect to frequency (or wavenumber) at constant Reynolds number, are shown in Fig. 6.3 as functions of Reynolds number. The amplification rate $\hat{\sigma}$, which gives the wave growth per unit of Reynolds number, peaks at the low Reynolds number of $R = 630$. The amplification ate $\hat{\sigma}$, which is proportional to the wave growth per boundary-layer thickness, does not peak until until $R = 2740$ [calculated by Kümmerer (1973)]. The dimensional amplification rate is proportional to $\hat{\sigma}$ for a fixed unit Reynolds number. Figure 6.3 shows that the decline in the dimensional amplification rate with increasing x-Reynolds number is almost counteracted by the increase in Reynolds number. However, if the measure of viscous instability is taken to be the wave growth over a fixed x^* increment as expressed by $\hat{\sigma}$, then by this criterion the maximum viscous instability occurs at low Reynolds number.

The logarithm of the amplitude ratio, A/A_0, is shown in Fig. 6.4 for 2D waves as a function of R for a number of frequencies F. The envelope curve, which gives the maximum amplitude ratio possible at any Reynolds number, is also shown in teh figure along with the corresponding frequencies. It is this type of diagram that is used in engineering studies of boundary-layer transition. When $\ln(A/A_0)$, which is often called the N factor, reaches some predetermined value, say nine as suggested by Smith and Gamberoni (1956), or ten as suggested by Jaffe et al. (1970), transition is considered to take place, or at least to start.

The distribution of the logarithm of the amplitude ratio with frequency is shown in Fig. 6.5 for several Reynolds numbers. This figure illustrates the filtering action of the boundary layer. The simultaneous narrowing of the bandwidth of unstable frequencies and the large increase in amplitude ratio as the Reynolds number increases means that an initial uniform power spectrum of instability waves tends to a spectrum at high Reynolds number that has a sharp peak at the most amplified frequency. The inset in Fig. 6.5 gives the bandwidth, defined as the frequency range over which the amplitude ratio is within $1/e$ of the peak value, as a function of Reynolds number.

The Squire theorem (section 2.4.1) has told us that it is a 2D wave that first becomes unstable. Furthermore, at any Reynolds number it is a 2D wave that has the maximum amplification rate and also the maximum amplitude ratio. Thus the envelope curve of amplitude ratio when all oblique waves are considered as well as 2D waves is still as shown in Fig. 6.4. However, for a given frequency the 2D wave is not necessarily the most unstable, as is shown in Fig. 6.6. In this figure, teh spatial amplification rate σ, calculated with

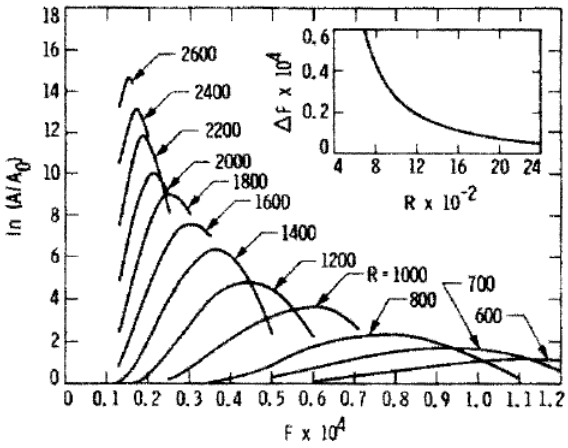

Figure 6.5: Distribution of 2D $\ln(A/A_0)$ with frequency at several Reynolds numbers, and bandwidth of frequency response as a function of Reynolds number; Blasius boundary layer.

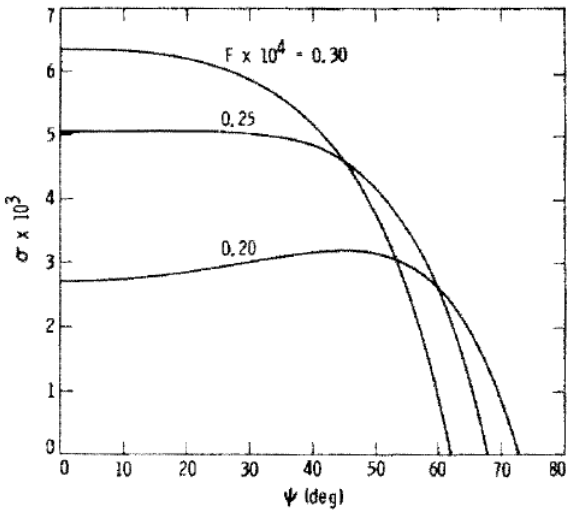

Figure 6.6: Effect of wave angle on spatial amplification rate at $R = 1200$ for $F \times 10^4 = 0.20$, 0.25 and 0.30; Blasius boundary layer.

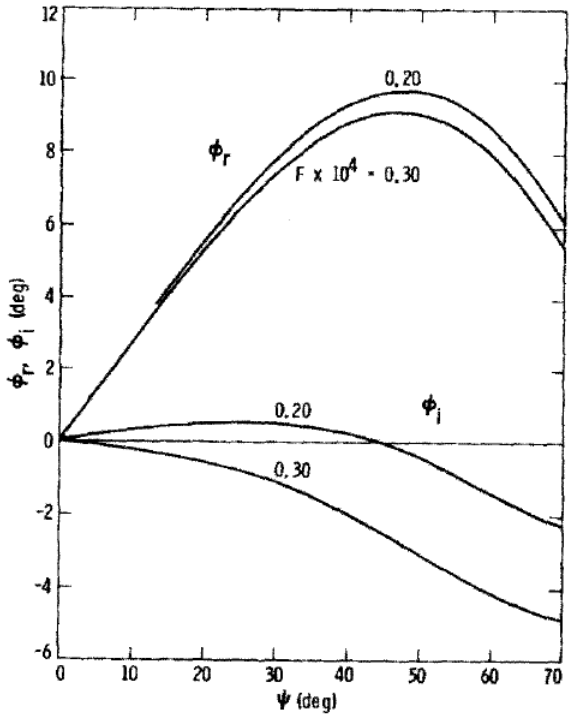

Figure 6.7: Complex group-velocity angle vs. wave angle at $R = 1200$ for $F \times 10^4 = 0.20$ and 0.30; Blasius boundary layer.

$\overline{\psi} = 0$, is plotted against the wave angle ψ for three frequencies at $R = 1200$. At this Reynolds number, the maximum amplification rate occurs for $F = 0.33 \times 10^{-4}$. Above this frequency, 2D waves are certainly the most unstable. However, below about 0.26×10^{-4} and oblique wave is the most unstable, and the wave angle of the maximum amplification rate increases with decreasing frequency.

In the calculations for Fig. 6.6, the complex wavenumber was obtained as a function of the spanwise wavenumber β_r with $\beta_i = 0$ and the frequency real and constant. Thus the complex group-velocity angle ϕ can be readily obtained from $\partial\alpha/\partial\beta_r$ $(= \tan\phi)$, and the results are given in Fig. 6.7 for $F \times 10^4 = 0.20$ and 0.30. The real part of ϕ is limited to less than $10°$, and ϕ_i can be either plus or minus. It is evident that at the maximum of σ, where $\partial\alpha/\partial\beta_r$ is real, ϕ_i must be zero. With the group-velocity angle known, the accuracy of the simple relation Eq. 2.35 for σ as a function of $\overline{\psi}$ can be checked. We choose $F = 0.20 \times 10^{-4}$ and $\psi = 45°$ in order to have ϕ real. Table 6.1 gives k, the wavenumber; $\bar{\sigma}$, the amplification rate parallel to $\overline{\psi}$ (both of these are calculated as an eigenvalue); $\sigma(\overline{\psi})$, the component of $\bar{\sigma}$ in the x direction for the specified $\overline{\psi}$; and $\sigma(0)$, the amplification rate in the x direction for $\overline{\psi} = 0$ as calculated from Eq. 2.41c, the spatial-theory replacement for the Squire transformation derived from Eq. 2.35, but with ψ replaced by $\overline{\psi}$. In the latter calculation we have used $\phi_r = 9.65°$, the value obtained with $\overline{\psi} = 0$. The transformation woks very well; the small discrepancies from the correct $\overline{\psi} = 0$ value are due to ϕ_r being a weak function of $\overline{\psi}$ instead of constant as assumed in the derivation.

We observe in Table 6.1 that the real Squire transformation, which is the $\sigma(\overline{\psi})$ entry for $\overline{\psi} = \psi$, is in error by 14.4%, whereas the correct transformation is in error by only 0.1%. When the same calculation is repeated for the other frequency of Fig. 6.7, $F = 0.30 \times 10^{-4}$, for which $\phi_i = -2.48°$ at $\psi = 45°$ instead of $0°$ as for the frequency of the Table, equally good results are obtained for $\sigma(0)$ from the transformation. However, k is no longer constant, but increases with $\overline{\psi}$; for $\overline{\psi} = 75°$ it is 0.4% larger than at $\overline{\psi} = 0°$. Nayfeh and Padhye (1979) provide a formula for this change.

In Fig. 6.8, $\ln(A/A_0)$ is given at several Reynolds numbers for $F = 0.20 \times 10^{-4}$ as calculated with the irrotationality condition, Eq. 2.64, applied to the wavenumber vector. The abscissa is the initial wave angle

htbp]

Table 6.1: Effect of $\overline{\psi}$ on amplification rate and test of transformation rule. $F = 0.20 \times 10^{-4}$, $R = 1200$, $\psi = 45°$.

$\overline{\psi}$	k	$\bar{\sigma} \times 10^3$	$\sigma(\overline{\psi}) \times 10^3$ eigenvalue	$\sigma(0) \times 10^3$ transformation
0.0	0.1083	3.201	3.201	3.201
9.7	0.1083	3.156	3.111	3.201
15.0	0.1083	3.170	3.062	3.201
30.0	0.1083	3.368	2.916	3.203
45.0	0.1083	3.873	2.739	3.204
60.0	0.1083	4.955	2.478	3.207
75.0	0.1083	7.601	1.967	3.216

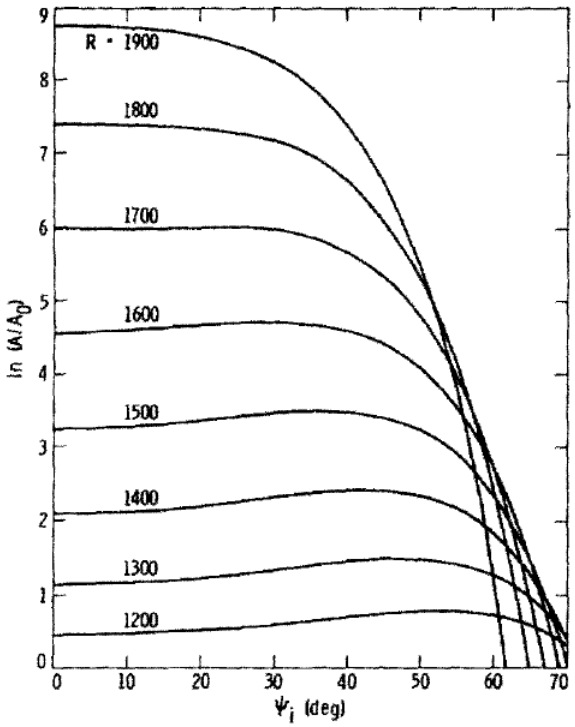

Figure 6.8: Effect of wave angle on $\ln(A/A_0)$ at several Reynolds numbers for $F = 0.20 \times 10^{-4}$; Blasius boundary layer.

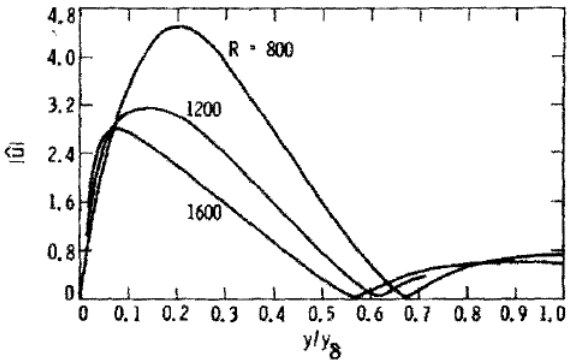

Figure 6.9: Eigenfunctions of $\hat{u}$ amplitude at $R = 800$, 1200 and 1600 for $F = 0.30 \times 10^{-4}$; Blasius boundary layer.

at $R = 900$. The change in the wave angle from $R = 900$ to 1900 is 1.7° for the wave that has an initial wave angle of 45°. This figure shows that the greater amplification rate of oblique waves in the instability region near the lower branch of the neutral curve translates into an amplitude ratio that is greater than the 2D value. However, $\ln(A/A_0)$ for an oblique wave is never more than 0.35 greater than the 2D value. Figure 6.8 also shows that just as the frequency bandwidth narrows with increasing R, so does the bandwidth in spanwise wavenumber. Although at the lower Reynolds numbers the response extends to the large wave angles, at $R = 1900$ the amplitude ratio is down to $1/e$ of its 2D value at $\psi = 37°$, and on the envelope curve this angle will be still smaller. For example, the $1/e$ amplitude for $F = 0.60 \times 10^{-4}$ at the envelope-curve Reynolds number ($R = 900$) occurs at $\psi = 29°$; for $F = 0.30 \times 10^{-4}$, at $\psi = 26°$. Even so, it is necessary when thinking about wave amplitudes in the boundary layer to keep in mind that both a frequency band and spanwise-wavenumber band must be considered, not just a 2D wave.

So far we have only been considering the eigenvalues and not the eigenfunctions. The eigenfunctions give the possibility of penetrating further into the physics of instability, and we shall take them up briefly at this point. Eigenfunctions are readily obtained with any of the current numerical methods, but were difficult to compute with the old asymptotic theory. The first eigenfunctions were obtained by Schlichting (1935), and the good agreement of the measurements of Schubauer and Skramstad (1947) with these calculations was a key factor in establishing the validity of the linear stability theory. The problem now is more one of finding a reasonable way to present the great mass of numerical data that can be computed, and to extract useful information from this data. Some progress has been made in the latter direction by Hama et al. (1980). For different amplitudes of 2D waves, these authors calculated streamline patterns, contours of constant total velocity, Reynolds stress and all terms of the local spatial energy balance.

Figure 6.9 gives the amplitude of the eigenfunction $\hat{u}$ of the streamwise velocity fluctuation u at $R = 800$, 1200 and 1600 for the 2D wave of frequency $F = 0.30 \times 10^{-4}$. The corresponding phases are given in Fig. 6.10. As may be seen from Fig. 6.1a, these Reynolds numbers are, respectively, just below the lower branch of the neutral stability curve, near the maximum of σ, and on the envelope curve of the amplitude ratio. The eigenfunction normalization of Figs. 6.9 and 6.10 is $\hat{p}(0) = (2^{-1/2}, 0)$. The eigenfunctions have not been renormalized to, say, a constant peak amplitude as is often done, in order to emphasize that in the quasi-parallel theory the normalization is completely arbitrary. Nothing can be learned as to the effect of the variability of the eigenfunction with Reynolds number on the wave amplitude within the framework of this theory. Attempts have been made to do this, and plausible looking results obtained, but this approach is without theoretical justification. It has already been pointed out in Section 2.2 that the meaningful quantity for the amplitude modulation is the product of $A(x_1)$ adn the eigenfunction, and this product, which has a fixed value regardless of the normalization of the eigenfunction, can only be calculated from the nonparallel theory.

For the wave of Fig. 6.9, the critical layer is at about $y = 0.15$ and varies only slightly with Reynolds number. Thus the location of the amplitude peak, which is a strong function of R, is only coincidentally

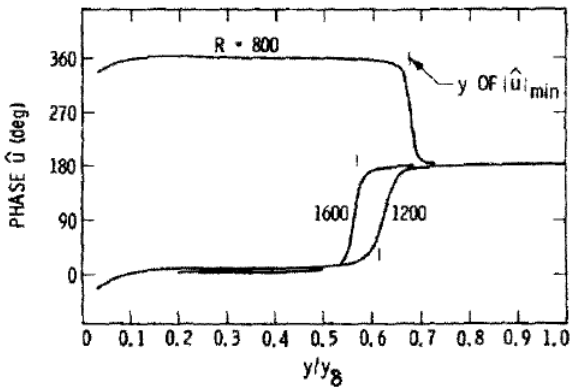

Figure 6.10: Eigenfunctions of $\hat{u}$ phase at $R = 800$, 1200 and 1600 for $F = 0.30 \times 10^{-4}$; Blasius boundary layer.

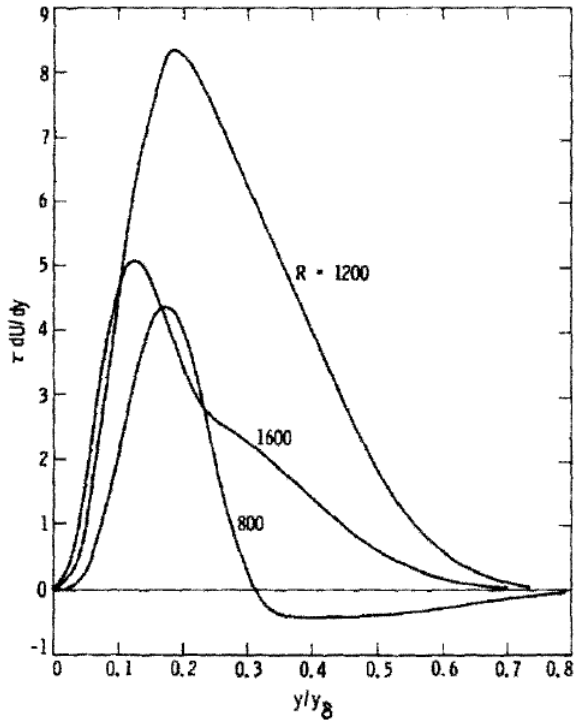

Figure 6.11: Energy production term at $R = 800$, 1200 and 1600 for $F = 0.30 \times 10^{-4}$; Blasius boundary layer.

at the critical point. As R increases, the viscous layer near the wall becomes thinner as expected. The characteristic phase change of approximately 180° in the outer part of the boundary layer has nothing to do with the 180° phase change at the critical layer in the inviscid solution (Eq. 3.9b), but is a kinematical consequence of a wave with zero amplitude at both the wall and at $y \to \infty$. At some y_m greater than the y of maximum amplitude, where viscosity has little influence, the slope of the streamlines relative to the phase velocity has a maximum. Thus the velocity-streamtube area relation changes sign, and at all $y > y_m$ the u fluctuation from this effect is opposite in sign to the fluctuation that arises from the wavy motion in a monotonically increasing velocity profile. At some $y_b > y_m$, these two effects can exactly balance for a neutral inviscid wave, and almost balance for nonneutral, viscous waves. For the latter, as shown in Fig. 6.10, there is a nearly 180° shift in the phase of $\hat{u}$. The fact that the phase can either advance or retreat in this region was first noted by Hama et al. (1980), and its significance, if any, is unknown.

It was shown in Section 5.1 that the kinetic energy of a 2D instability wave is produced by the term $\tau dU/dy$, where τ is the Reynolds stress built up by the action of viscosity. Reynolds stress distributions have been given by Jordinson (1970) and Kümmerer (1973), among others. The energy production term is shown in Fig. 6.11 for the frequency and three Reynolds numbers of Figs. 6.9 and 6.10. The peak production does not occur at the critical layer at any of the three Reynolds numbers. We see that energy production is by no means limited to the region between the wall and the critical layer, as might be expected from the simple theory of Chapter 5. At $R = 1200$, where the amplification rate is near its maximum, there is significant energy production over about half of the boundary-layer thickness. In these examples, the Reynolds stress is positive except for the slightly damped wave at $R = 800$, where there is a small negative contribution over the outer 70% of the boundary layer. The damping at $R = 800$ is due to viscous dissipation, not to a negative production term. Hama et al. (1980) give an example at low Reynolds number where the production term is negative over the entire boundary layer.

6.2 Falkner-Skan boundary layers

The influence of pressure gradient on boundary-layer stability can be studied conveniently by means of the Falkner-Skan family of self-similar boundary layers, where the Hartree parameter β_h (Eq. 2.62) serves as a pressure-gradient parameter. The range of β_h is from -0.19883774 (separation profile) through 0 (Blasius profile) to 1.0 (2D stagnation point profile). Extensive numerical calculations for Falkner-Skan profiles have been carried out by Wazzan et al. (1968a, see also Obremski et al. (1969)), and by Kümmerer (1973). Figure 6.12, taken from Mack (1977), gives the influence of β_h on the N-factor envelope curve. It is clear that a favorable pressure gradient ($\beta_h > 0$) stabilizes the boundary layer, and an adverse pressure gradient ($\beta_h < 0$) destabilizes it. The strong instability for adverse pressure gradients is caused by an inflection point in the velocity profile that moves away from the wall as β_h becomes more negative. The adverse pressure gradient Falkner-Skan boundary layers are particularly instructive because they provide us with examples of boundary layers with both viscous and inflectional instability.

The amplification rate $\hat{\sigma}$ is unsuitable for studying inflectional instability, which is basically an inviscid phenomenon, as it is zero at $R \to \infty$ regardless of whether the boundary layer is stable or unstable in the inviscid limit. The calculations of Kümmerer (1973) include both σ and $\hat{\sigma}$ and show that the mximum amplification rate $\sigma_{\max}$ moves from $R = 2740$ for the Blasius boundary layer to $R \to \infty$ as β_h decreases from zero. When $\sigma_{\max}$ is at $R \to \infty$, which occurs before β_h reaches the separation value, we can say that the boundary layer is dominated by inflectional instability. In these cases, viscosity acts primarily to damp out the disturbances just as envisioned by the early investigators. When we take up compressible boundary layers in Part II, we shall encounter another example where the dominant instability changes from viscous to inflectional as a parameter (the freestream Mach number) varies.

The frequencies along the envelope curves of Fig. 6.12 are given in Fig. 6.13. We may observe that in boundary layers with favorable pressure gradients, where viscous instability is the only source of instability, it is the low frequency waves which are the most amplified. On the contrary, for boundary layers with adverse pressure gradients, where inflectional instability is dominant, it is high-frequency waves which are the most amplified.

In a natural disturbance environment, a wide spectrum of normal modes may be expected to exist in the boundary layer. It is helpful to know the sharpness of the response in estimating when the disturbance

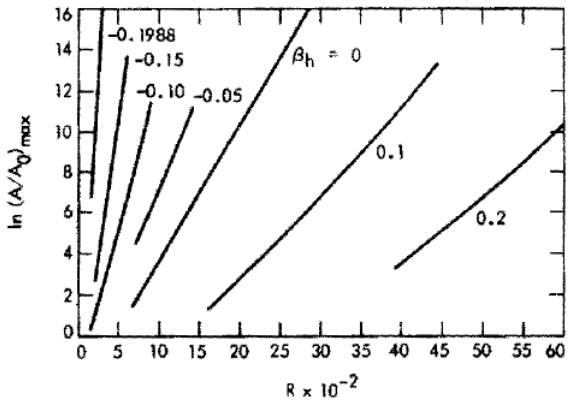

Figure 6.12: 2D envelope curves of $\ln(A/A_0)$ for Falkner-Skan family of boundary layers..

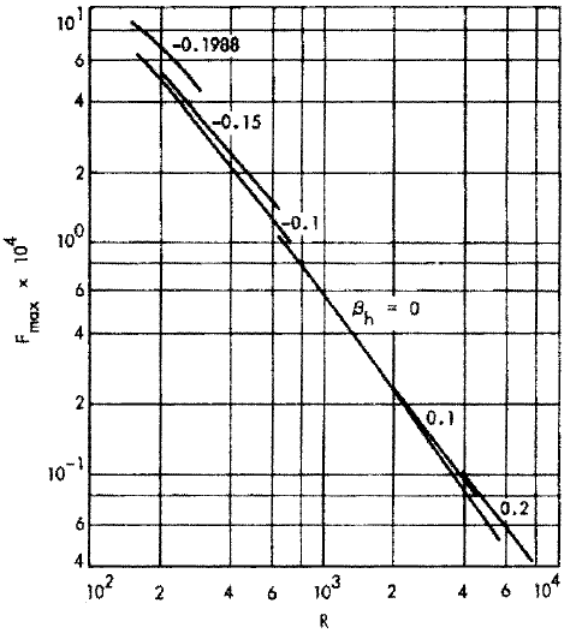

Figure 6.13: 2D envelope-curve frequencies of Falkner-Skan boundary layers.

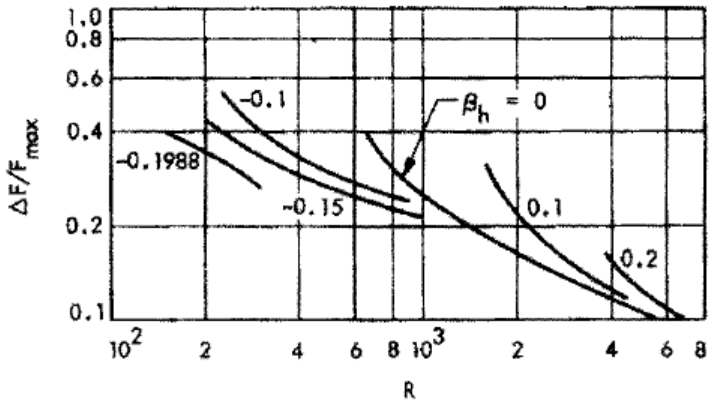

Figure 6.14: Frequency bandwidth along 2D envelope curves for Falkner-Skan boundary layers.

amplitude is large enough to initiate transition. A measure of this quantity is given in Fig. 6.14, where a frequency bandwidth of the 3D waves along the envelope curve, expressed as a fraction of the most amplified frequency, is shown for the Falkner-Skan family. This bandwidth is not identical to the one in the inset of Fig. 6.5, as it gives only the frequency range less than the most amplified frequency for which the amplitude ratio is within $1/e$ of the peak value. The filtering action of the boundary layer is again evident in the narrowing of the bandwidth with increasing Reynolds number for a given boundary layer, and we see that the more unstable adverse pressure-gradient boundary layers have the strongest filtering action.

6.3 Non-similar boundary layers

The self-similar boundary layers are useful for illustrating basic instability mechanisms, but in practice, boundary layers are non-similar. A computer code to perform stability calculations for non-similar boundary layers is more complicated than for self-similar boundary layers, but only because of the necessity of calling up a different velocity profile at each Reynolds number, or of interpolating between different profiles. The stability calculations themselves are the same as in any Reynolds number dependent boundary layer. The eigenvalues are calculated as a function of Reynolds number, and then can be subsequently used to calculate N factors, or for any other purpose, exactly as if the boundary layer were self-similar. Such calculations have been done on a routine basis at least as far back as the paper of Jaffe et al. (1970).

6.4 Boundary layers with mass transfer

Suction stabilizes a boundary layer, and blowing destabilizes it. This result was established by the early investigators, and extensive stability calculations were carried out with the asymptotic theory. Suction can stabilize a boundary layer with or without an inflection point. The stability mechanism is similar to the action of a pressure gradient. Suction gives a "fuller" velocity profile, just as does a favorable pressure gradient; blowing gives a velocity profile with an inflection point, just as does an adverse pressure gradient. Suction is the primary method proposed for laminar flow control on aircraft, where it has been investigated mainly in connection with three-dimensional boundary layers. A summary account of early work on this subject may be found in the book of Schlichting (1979). More recent work on this subject carried out by him and his coworkers may be found in the Lecture Notes of an AGARD/VKI Special Course (Pfenninger, 1977).

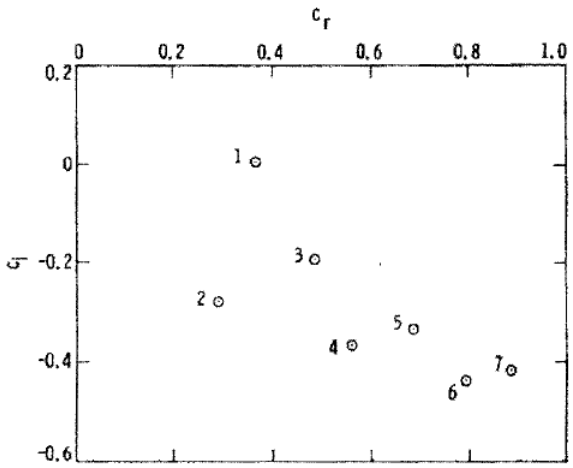

Figure 6.15: Temporal eigenvalue spectrum of Blasius boundary layer for $\alpha = 0.179$, $R = 580$.

6.5 Boundary layers with heating and cooling

Heating an air boundary layer destabilizes it, and cooling stabilizes it. The proper calculation of this effect requires the compressible stability theory which is given in Part II. An example for a low-speed boundary layer may be found in Section 10.3.

For a water boundary layer, the effect is the opposite, and heating the wall has been extensively studied as a means of stabilization. This mechanism of stabilization is solely through the effect on the viscosity, and can be studied with the incompressible stability theory provided only that the viscosity is taken to be a function of temperature. The initial work on this subject was by Wazzan et al. (1968b).

6.6 Eigenvalue spectrum

An arbitrary disturbance cannot be represented by a single normal mode, or by a superposition of normal modes. These modes represent only a single number of an entire eigenvalue spectrum, and it is this spectrum that is required for an arbitrary disturbance. It can be proved that for a bounded shear flow, such as plane Poiseuille flow, the eigenvalue spectrum is discrete and infinite (Lin, 1961). That is, for a given wavenumber and Reynolds number, there is an infinite discrete sequence of complex frequencies whose eigenfunctions satisfy the boundary conditions. Each element of the sequence constitutes a mode. This is the more precise meaning of the term mode; what we have called the normal modes all belong to the first, or least stable, of these more general modes. To distinguish between the two usages of the term mode, we shall refer to the discrete sequence as the viscous modes. Only the first viscous mode can be unstable; all of the others are heavily damped, which is the reason why they are unimportant in almost all practical stability problems. Calculations of the discrete temporal eigenvalue spectrum of plane Poiseuille flow have been carried out by Grosch and Salwen (1968), Orszag (1971) and Mack (1976).

It was long believed that the eigenvalue spectrum of boundary-layer flows is also discrete. however, a calculation by Jordinson (1971) for a single value of α and R uncovered only a finite discrete spectrum for the Blasius boundary layer. These calculations were in some error numerically, but a later investigation by Mack (1976), which worked out the correct temporal spectrum, confirmed the conclusion of Jordinson. As shown in Fig. 6.15, at $\alpha = 0.179$, $R = 580$, the case considered by Jordinson, there are only seven viscous modes. Mode 1 is amplified; Modes 2-7 are strongly damped. In Fig. 6.15, the eigenvalues are shown in complex c space, rather than ω space, because $c_r = 1.0$ has a special significance in this problem.

Although the number of discrete modes is a function of both wavenumber and Reynolds number, the number remains finite and comparatively small. It was shown by Mack (1976) on teh basis of numerical

examples with finite-width channels in which the upper boundary moved to $y \to \infty$, and with polynomial velocity profiles of various orders, that both the semi-infinite flow interval and the continuity of the velocity profile at the edge of the boundary layer, are responsible for the non-existence of the infinite part of the discrete spectrum of bounded flows. As a finite discrete spectrum is still unable to represent an arbitrary disturbance, where are the missing eigenvalues?

It is a not uncommon occurrence in eigenvalue problems to have only a finite discrete spectrum. The remaining part of the spectrum is then a continuous spectrum. An example is the inviscid stability equation, which has a continuous spectrum associated with the singularity at the critical layer. It was already suggested by Jordinson (1971) that the discrete viscous spectrum is supplemented by a continuous spectrum along the $c_r = 1$ axis. The proof by Lin (1961) that a viscous continuous spectrum cannot exist for a bounded flow does not apply to an unbounded flow. Mack (1976) supported Jordinson's expectation by means of a few numerical calculations of continuous-spectrum eigenvalues, and also showed that the continuous spectrum is always damped because of the restriction $c_i < -\alpha/R$. A more complete and definitive study of the continuous spectrum was subsequently carried out by Grosch and Salwen (1978), who are responsible for clarifying many aspects of this problem. Also a paper by Murdock and Stewartson (1977) must be mentioned. Results for the discrete spatial spectrum of the Blasius boundary layer have been given by Corner et al. (1976).

Chapter 7

Harmonic Point Sources of Instability Waves

7.1 General remarks

In the previous Chapters, we have been considering the behavior of the individual normal-mode solutions of the linearized, quasi-parallel stability questions. This primary attention to the normal modes has been the usual course in the most theoretical and experimental work on boundary-layer stability. The fundamental stability experiments of Schubauer and Skramstad (1947) in low-speed flow, and of Kendall (1967) in high-speed flow were both designed to produce a particular normal mode. Even the much used e^N method of transition prediction is based on the amplitude ratio of the most amplified normal mode. In most actual flow situations, however, a spectrum of instability waves is present. If the boundary layer were truly parallel, the most unstable mode would eventually be the dominant one, and all the other modes would be of negligible importance. As boundary layers found in practice are not parallel, the changing Reynolds number means that the identity of the most unstable mode also changes as the wave system moves downstream, and no single mode can grow indefinitely. Disturbance energy will always be distributed over a finite bandwidth. If the modes all come from a single source, or are otherwise phase related, then interference effects will cause the evolution of the wideband amplitude to further depart from the amplitude evolution of a single normal mode. This difference was vividly demonstrated in the experiment of Gaster (1975), where the amplitude at the center of a wave packet produced by a pulsed point source changed little with increasing distance from the source, even though the amplitude of the most amplified normal mode was increasing several times.

The wave-packet problem was treated first by Criminale and Kovasnay (1962) and by Gaster (1968). Neither the straight wave fronts of the former, nor the caustic of the latter, were observed experimentally, because in each case approximations that were needed to produce numerical results turned out not to be valid. Later, Gaster (1975) obtained results in good agreement with experiment by replacing the method of steepest descent used earlier by direct numerical integration. He was also able to demonstrate the validity of the method of steepest descent for a 2D wave packet in a strictly parallel flow by exact calculation of the necessary eigenvalues (Gaster, 1981b, 1982a). Finally, he showed how to extend this method to a growing boundary layer (Gaster, 1981a, 1982b), where the mean flow downstream of the source is a function of Reynolds number.

In this Chapter we shall examine a simpler problem than the wave packet, namely the stationary wave pattern produced by a harmonic point source. This wave motion has the same number of space dimensions as a 3D wave packet, but is really a 2D wave propagation problem that is closely related to Gaster's 2D wave packets. The propagation space here is x, z, the plane of the flow, rather than x, t as in the latter problem. The fact that the wave motion is two dimensional makes it possible to obtain detailed numerical results both numerical integration and by Gaster's (1981a; 1982b) extension of the method of steepest descent for a growing boundary layer (Mack and Kendall, 1983). In the point-source problems, no attempt is made to find a complete mathematical solution. Instead it is merely assumed, following Gaster (1975), that the source produces a continuous spectrum of the least stable normal modes. For a pulsed 2D (line) source, the

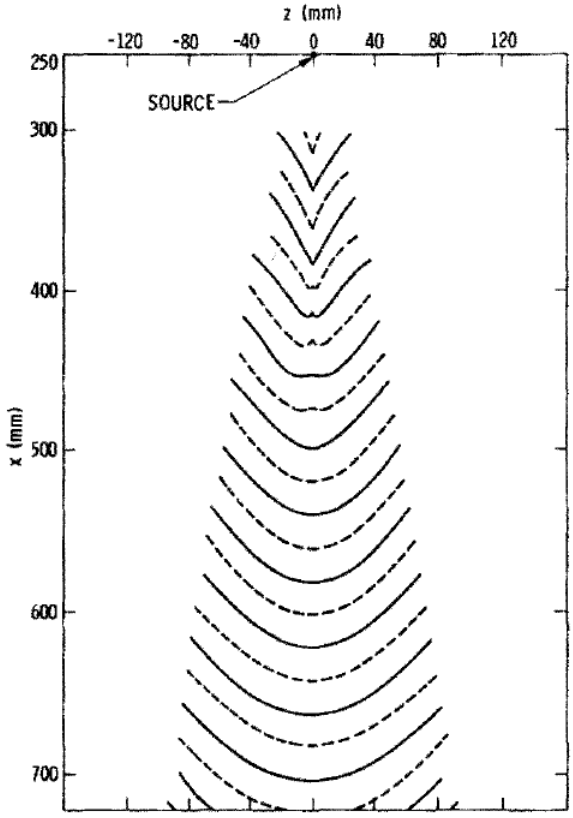

Figure 7.1: Constant-phase lines of wave pattern from harmonic point source in Blasius boundary layer; $F = 0.92 \times 10^{-4}$, $R_s = 390$. [After Gilev et al. (1981)]

spectrum is over frequency; for a pulsed 3D (point) source, the spectrum is over frequency and spanwise wavenumber; for a harmonic point source, the spectrum is over spanwise wavenumber. It is usually, but not always, assumed that the spectral densities are uniform ("white noise" spectra).

The solution for a harmonic point source is obtained by evaluating the integral for the complex amplitude over all possible spanwise wavenumbers. The most straightforward method is to use direct numerical integration; a second method is to evaluate the integral asymptotically by the method of steepest descent as was done for parallel flows by Cebeci and Stewartson (1980a,b), and, in more detail, by Nayfeh (1980a,b). Some numerical results for Blasius flow were cited by Cebeci and Stewartson (1980b), but within the framework of the e^N method of transition prediction. Only the exponential term of the amplitude was evaluated, and the saddle-point condition was the one for parallel flow.

Experiments on the harmonic point source have been carried out by Gilev et al. (1981), and by Mack and Kendall (1983). In these experiments, extensive hot-wire measurements of amplitude and phase were made in the downstream and spanwise directions in a Blasius boundary layer. In Gilev et al. (1981), a Fourier analysis of the data yielded the oblique normal modes, but no comparisons with theory were made. One significant result was the mapping out of the lines of constant phase in the x, z plane as shown in Fig. 7.1. At least three distinct regions can be identified in this figure. Close to the source, the curvature is convex, and far away it is concave. In an intermediate region, a "dimple" appears at the center line. A region of concave curvature gradually extends outward to encompass the entire outer portion of the wave pattern, while the dimple spreads, flattens and finally disappears. All of these features are duplicated in the wave pattern calculated by numerical integration (Mack and Kendall, 1983).

Figure 7.1 shows that there is a maximum inclination of each constant-phase line that is much less than the maximum wave angle of unstable normal modes. This feature follows directly from the method of steepest

descent, where the saddle-point condition limits the Reynolds-number dependent maximum wave angle to 40°–45°. This restriction was noted in unpublished calculations by Mack and by Padhye and Nayfeh (private communication), as well as by Cebeci and Stewartson (1980b).

In the quasi-parallel theory, amplitude is defined as the integral of the spatial amplification rate, and is not identified with any particular flow variable or distance y from the wall. In the Gaster-Grant (1975) experiment, amplitude was measured at the outer peak of the amplitude distribution; in Gilev et al. (1981) at a fixed y^*/δ in the boundary layer, and also at a fixed y^* just outside of the boundary layer; and in Mack and Kendall (1983), at the inner peak of the amplitude distribution. A comparison of the calculated amplitudes with the measurements thus demonstrates whether the amplitude of the quasi-parallel theory has any relevance to the point-source problems. Exact correspondence can hardly be expected, if for no other reason than the fact that the disturbance energy is distributed over an ever increasing boundary-layer thickness as the waves move downstream.

The integral over all spanwise wavenumbers for the dimensional velocity fluctuation u_t (the subscript t denotes time dependence) from a source of frequency ω^* located at x_s^*, z_s^* is

$$u_t^*(x^*, z^*, t^*) = \exp(-i\omega^* t^*) \int_{-\infty}^{\infty} g^*(\beta^*) \exp\left[i\chi\left(\beta^*; x^*, z^*\right)\right] d\beta^*, \tag{7.1}$$

where $g^*(\beta^*)$ is the (complex) amplitude distribution function of dimensions velocity $\times$ length, the frequency is real,

$$\chi(x^*, z^*) = \int_{x_s^*}^{x^*} \alpha^*(x^*; \beta^*, \omega^*) dx^* + \beta^*(z^* - z_s^*) \tag{7.2}$$

is the time-dependent part of the phase, and the wavenumber components α^* and β^* are complex. The eigenfunctions are ignored so that u_t is independent of y^*, and u_t could equally well be considered as any other flow variable. This integral will be evaluated below by direct numerical integration, and by and adaptation of citeauthorGaster1981a's (1981a; 1982b) asymptotic method.

7.2 Numerical integration

We place the source at $z_s^* = 0$, drop the time factor, and define the dimensionless variables

$$\begin{aligned} \hat{\alpha} &= \frac{\alpha^* \nu^*}{U_1^*}, \qquad & \hat{\beta} &= \frac{\beta^* \nu^*}{U_1^*}, \\ \hat{x} &= \frac{U_1^* x^*}{\nu^*}, \qquad & \hat{z} &= \frac{U_1^* z^*}{\nu^*}, \\ u &= \frac{u^*}{U_1^*}, \qquad & g &= \frac{2\pi g^*}{\nu^*}, \end{aligned} \tag{7.3}$$

where u^* is the time-independent part of u_t^*, and the reference velocity is the freestream velocity U_1^* We have chosen the inverse unit Reynolds number ν^*/U_1^* as the reference length so that $\hat{\beta}$, as well as β^* will satisfy the irrotationality condition in the simplest form, Eq. 2.56. With these choices, the dimensionless $\hat{x}$ and $\hat{z}$ are the usual x and z Reynolds numbers. The reason for the normalization constant 2π in the definition of g will appear in Section 7.4. With the definitions of Eqs. 7.2, Eq. 7.1 becomes

$$u(\hat{x}, \hat{z}; F) = \frac{1}{2\pi} \int_{-\infty}^{\infty} g(\hat{\beta}) \exp\left[i\chi\left(\hat{\beta}; \hat{x}, \hat{z}\right)\right] d\hat{\beta}. \tag{7.4}$$

With $z_s^* = 0$, the phase is

$$\chi\left(\hat{\beta}; \hat{x}, \hat{z}\right) = \int_{\hat{x}_s}^{\hat{x}} \hat{\alpha}\, d\hat{x} + \hat{\beta}\hat{z}. \tag{7.5}$$

We take $\hat{\beta}$ to be real for convenience, which means that we are going to sum over spatial normal modes of the type we have been using all along. If we write

$$\chi = \chi_{xr} + i\chi_i + \hat{\beta}\hat{z}, \tag{7.6a}$$

where

$$\chi_{xr} = \int_{\hat{x}_s}^{\hat{x}} \hat{\alpha}_r \, d\hat{x}, \qquad \chi_i = \int_{\hat{x}_s}^{\hat{x}} \hat{\alpha}_i \, d\hat{x}, \tag{7.6b}$$

the real and imaginary parts of u are

$$u_r\left(\hat{x},\hat{z}\right) = \frac{1}{\pi}\int_0^{\pi} g\left(\hat{\beta}\right)\exp\left(-\chi_i\right)\cos\left(\chi_{xr}\right)\cos\left(\hat{\beta}\hat{z}\right)\, d\hat{\beta}, \tag{7.7a}$$

and

$$u_i\left(\hat{x},\hat{z}\right) = \frac{1}{\pi}\int_0^{\pi} g\left(\hat{\beta}\right)\exp\left(-\chi_i\right)\sin\left(\chi_{xr}\right)\cos\left(\hat{\beta}\hat{z}\right)\, d\hat{\beta}. \tag{7.7b}$$

We have taken advantage of the symmetry in $\hat{\beta}$ of $g(\hat{\beta})$, χ_{xr} and χ_i to restrict the interval of integration to the positive $\hat{\beta}$ axis. Equations 7.7 are the specific integrals to be evaluated by numerical integration. It is convenient to present the numerical results in terms of the peak, or envelope, amplitude

$$A\left(\hat{x},\hat{z}\right) = \sqrt{u_r^2 + u_i^2}, \tag{7.8a}$$

and the local phase

$$\theta\left(\hat{x},\hat{z}\right) = \tan^{-1}\left(\frac{u_i}{u_r}\right). \tag{7.8b}$$

Both of these quantities can be measured experimentally.

The numerical integration of Eqs. 7.7 proceeds as follows: With the dimensionless frequency F equal to the frequency of the source, the phase integrals χ_{xr} and χ_i of Eq. 7.6b are evaluated as functions of $\hat{x}$ with constant $\hat{\beta}$ for a band of spanwise wavenumbers from the eigenvalues $\hat{\alpha}(\hat{x};\hat{\beta},F)$. The Fourier cosine integrals are evaluated at enough $\hat{z}$ stations at each $\hat{x}$ to resolve the wave pattern. Highly oblique waves are damped, with the damping rate increasing with increasing obliquity. Consequently, the integrals of Eq. 7.7 will always converge for $\hat{x} > \hat{x}_s$ if large enough values of $\hat{\beta}$ are used. At $\hat{x} = \hat{x}_s$, $\chi = \hat{\beta}\hat{z}$ and $g(\hat{\beta})$ is the Fourier cosine transform of $u_r(\hat{z})$. In particular, if $g(\hat{\beta}) = 1$, then u_r is a δ-function in $\hat{z}$; if $g(\hat{\beta})$ is a Gaussian, then so is u_r.

7.3 Method of steepest descent

The method of numerical integration is straightforward, but requires the evaluation of a few hundred eigenvalues for good resolution of the wave patter. A different approach is to evaluate the integral of Eq. 7.4 asymptotically by the method of steepest descent, or saddle-point method. This method allows certain results to be obtained with fewer calculations, and also has the advantage that the dominant wave at each $\hat{x},\hat{z}$ seems to correspond directly to what is observed.

Equation 7.4, with $g(\hat{\beta}) = 1$, is written

$$u\left(\hat{x},\hat{z}\right) = \lim_{\hat{x}\to\infty}\frac{1}{2\pi}\int_C \exp\left[\left(\hat{x}-\hat{x}_s\right)\Phi\left(\hat{\beta}\right)\right]\, d\hat{\beta}, \tag{7.9}$$

where C is the contour of steepest descent int eh complex $\hat{\beta}$ plane, and

$$\left(\hat{x}-\hat{x}_s\right)\Phi = i\int_{\hat{x}_s}^{\hat{x}} \hat{\alpha}\left(\hat{x};\hat{\beta}\right)\, d\hat{x} + i\hat{\beta}\left(\hat{x}-\hat{x}_s\right). \tag{7.10}$$

The limit $\hat{x} \to \infty$ is taken with $\hat{z}/(\hat{x} - \hat{x}_s)$ held constant. The condition for the saddle point $\hat{\beta}_c$ is

$$\frac{\partial \Phi}{\partial \hat{\beta}} = 0, \tag{7.11}$$

which is equivalent to the two real conditions

$$\int_{\hat{x}_s}^{\hat{x}} \left(\frac{\partial \hat{\alpha}}{\partial \hat{\beta}} \right)_r d\hat{x} = -\hat{z}, \tag{7.12a}$$

$$\int_{\hat{x}_s}^{\hat{x}} \left(\frac{\partial \hat{\alpha}}{\partial \hat{\beta}} \right)_i d\hat{x} = 0. \tag{7.12b}$$

These integrals are evaluated with the complex $\hat{\beta}$ held constant, so that we are dealing with spatial waves that satisfy the generalized irrotationality condition of kinematic wave theory.

The saddle-point conditions of Eq. 7.12 are of the same type as introduced by Gaster (1981a, 1982b) for a 2D wave packet in a growing boundary layer. Usually the saddle-point method is applied to problems where the wave-propagation medium (here the boundary layer) is independent of $\hat{x}$, but Gaster demonstrated the correctness of the present procedure when the medium is a function of $\hat{x}$. In a strictly parallel flow, the boundary layer meets the more restricted requirement of $\hat{x}$ independence, and the saddle-point conditions simplify to

$$\left(\frac{\partial \hat{\alpha}}{\partial \hat{\beta}} \right)_r = -\frac{\hat{z}}{(\hat{x} - \hat{x}_s)}, \tag{7.13a}$$

$$\left(\frac{\partial \hat{\alpha}}{\partial \hat{\beta}} \right)_i = 0. \tag{7.13b}$$

For a constant-frequency wave,

$$\frac{\partial \hat{\alpha}}{\partial \hat{\beta}} = -\frac{\dfrac{\partial \omega}{\partial \hat{\beta}}}{\dfrac{\partial \omega}{\partial \hat{\alpha}}} = -\tan \phi \tag{7.14}$$

where ϕ is the complex angle of the group-velocity vector, and we see that the parallel-flow saddle-point condition is equivalent to requiring the group-velocity angle to be real. Consequently, the observed wave pattern in a parallel flow consists of waves of constant complex spanwise wavenumber $\hat{\beta}_c$ moving along group-velocity trajectories in the real $\hat{x}, \hat{z}$ plane. This saddle-point condition has been applied to a browing boundary layer by Cebeci and Stewartson (1980a,b) and by Nayfeh (1980a,b). This procedure can yield satisfactory results in a restricted region of the $\hat{x}, \hat{z}$ plane, but cannot be valid everywhere as the correct asymptotic representation of Eq. 7.9 is in terms of Eq. 7.12 saddle points rather than Eq. 7.13 saddle points. The "rays" defined by Eq. 7.12 are not physical rays in the usual sense. For a complex $\hat{\beta}_c$ that satisfies Eq. 7.12, $\hat{z}$ is complex at all $\hat{x} > \hat{x}_s$ except at the final, or observation point. The trajectory that is traced out in the $\hat{x}, \hat{z}$ plane by satisfying Eq. 7.12 at successive $\hat{x} > \hat{x}_s$ for the same $(\hat{\beta}_c)_r$ has a different $(\hat{\beta}_c)_i$ at each point. In a parallel flow, a single normal mode defines an entire ray; here a single normal mode defines only a single point.

With Φ expanded in a power series in $\hat{\beta} - \hat{\beta}_c$, and with only hte first nonzero term retained (assuming it is the second derivative), Eq. 7.9 becomes

$$u = \frac{1}{2\pi} \exp \left[(\hat{x} - \hat{x}_s) \, \Phi \left(\hat{\beta}_c \right) \right] \int_C \exp \left[\frac{\hat{\beta}_c}{2} \frac{\partial^2 \Phi}{\partial \hat{\beta}^2} (\hat{x} - \hat{x}_s) \left(\hat{\beta} - \hat{\beta}_c \right) \right] d\hat{\beta}. \tag{7.15}$$

We write

$$\hat{\beta}_c \frac{\partial^2 \Phi}{\partial \hat{\beta}^2} = \hat{D} \exp (i\theta_d), \tag{7.16a}$$

$$\hat{\beta} - \hat{\beta}_c = \pm is \exp (i\theta_s), \tag{7.16b}$$

where s is the path length measured from teh saddle point, and θ_s is its inclination. With the contour C selected to pass through $\hat{\beta}_c$ from left to right at the constant angle $\theta_s = -\theta_d/2$, the final result is

$$u(\hat{x},\hat{z}) = \left[\frac{1}{2\pi}\left(\hat{x}-\hat{x}_s\right)\hat{D}\right]^{1/2} \exp\left[\left(\hat{x}-\hat{x}_s\right)\Phi\left(\hat{\beta}_c\right)\right] \exp\left[i\left(\frac{\pi}{4}-\frac{\theta_d}{2}\right)\right]. \tag{7.17}$$

Replacing $\hat{D}$, $\hat{x}$, $\hat{\alpha}$ and $\hat{\beta}$ by D, R, α and β, where the reference length is L^* of Eq. 2.57, we obtain

$$u(R,\hat{z}) = \sqrt{\frac{2}{\pi D}} \exp\left(-\chi_i + i\chi_r\right), \tag{7.18}$$

where

$$D = 2\left|\int_{R_s}^{R} R^2 \frac{\partial^2\alpha}{\partial\beta^2} dR\right|, \tag{7.19}$$

$$\chi_r = 2\int_{R_s}^{R} \alpha_r(R;\beta_c)\, dR + \frac{(\beta_c)_r\hat{z}}{R} + \frac{\pi}{4} - \frac{\theta_d}{2}, \tag{7.20a}$$

$$\chi_i = 2\int_{R_s}^{R} \alpha_i(R;\beta_c)\, dR + \frac{(\beta_c)_i\hat{z}}{R}, \tag{7.20b}$$

and θ_d is the argument of the complex integral in Eq. 7.19. We continue to use $\hat{z}$ for the z-Reynolds number.

In these variables, the saddle-point conditions are

$$2\int_{R_s}^{R} \left(\frac{\partial\alpha}{\partial\beta}\right)_r R\, dR = -\hat{z}, \tag{7.21a}$$

$$\int_{R_s}^{R} \left(\frac{\partial\alpha}{\partial\beta}\right)_i R\, dR = 0. \tag{7.21b}$$

With the parallel-flow saddle-point conditions of Eqs. 7.13, Eq. 7.18 is still valid, but D and θ_d have different meanings. With $\partial^2\hat{\alpha}/\partial\hat{\beta}^2$ constant,

$$D = \sqrt{R\left(R^2 - R_s^s\right)\frac{\partial^2\alpha}{\partial\beta^2}}, \tag{7.22}$$

and θ_d is the argument of $\partial^2\hat{\alpha}/\partial\hat{\beta}^2$ rather than of its integral.

For a given R and $\hat{z}$, a double iteration procedure is needed to find the complex $\hat{\beta}_c$ that satisfies Eq. 7.12. As each iteration involves the recalculation of eigenvalues and $\partial^2\hat{\alpha}/\partial\hat{\beta}^2$ from R_s to R, the computational requirements are large. If only R is given, then an iteration of $\hat{\beta}_i$ for a sequence of $\hat{\beta}_r$ will produce the wave pattern at that R with much less computation, but the specific $\hat{z}$ at which the amplitude and phase are calculated will not be known in advance. Or, both $\hat{\beta}_r$ and $\hat{\beta}_i$ can be specified, and R advanced until the integral in Eq. 7.12b changes sign. This will not always happen, but when it does, a saddle point and its location in the $R,\hat{z}$ plane are obtained without iteration.

Because of the iteration requirement, the saddle-point method is less suited than numerical integration to the detailed calculation of the entire wave pattern, but it can more readily produce results at just a few locations. Its greatest advantage, however, is that along the centerline ($z = 0$) the amplitude and phase can be obtained at a specified R without iteration, and a single integration pass from R_s to R produces results at all intermediate R at which eigenvalues are calculated. This is possible because the saddle point is at $\hat{\beta} = 0$ all along the centerline, and only Eq. 7.19 has to be used, and not Eqs. 7.12. We can also note that there is no real saving by using the approximate Eq. 7.22 in place of Eq. 7.19, because $\partial^2\alpha/\partial\beta^2$ has to be calculated in any case, and only the numerical integration of this derivative is eliminated.

7.4 Superposition of point sources

We can imagine sources of instability waves to occur not just as single point sources, but as multiple point sources and as distributed sources. For several discrete sources, the formulas of the preceding Section apply, and we just have to add the contributions from various sources. We can use this same approach for distributed sources: The distributed source is represented by discrete, closely spaced, infinitesimal point sources. In this Section, we apply this idea to line sources.

We replace the function $g^*(\beta^*)$ in Eq. 7.1 with a more general function

$$g^*\left(\beta^*, x_s^*, z_s^*\right) = \frac{1}{2\pi} u_s^*\left(x_s^*, z_s^*\right) \Delta\xi_s^* g\left(\hat{\beta}\right), \tag{7.23}$$

where u_s^*, the source strength, has the same dimensions as u_t^*, and ξ_s^* is the arc length along the source. We substitute Eq. 7.23 into Eq. 7.1 without the time factor, use the definitions of Eq. 7.3, adn arrive at

$$\Delta u(\hat{x}, \hat{z}) = \frac{1}{2\pi} u_s \Delta\xi_s \int_{-\infty}^{\infty} g\left(\hat{\beta}\right) \exp(i\chi) d\hat{\beta} \tag{7.24a}$$

for the contribution to u at $\hat{x}, \hat{z}$ of an infinitesimal line source at $\hat{x}_s, \hat{z}_s$. In Eq. 7.24a, $u_s = u_s^*/U_1^*$, $\xi_s = \xi_s^* U_1^*/\nu^*$, and

$$\chi\left(\beta; \hat{x}, \hat{z}\right) = \int_{\hat{x}_s}^{\hat{x}} \hat{\alpha}\, d\hat{x} + \hat{\beta}\left(\hat{z} - \hat{z}_s\right). \tag{7.24b}$$

A finite-length source which extends from $s_1 = (\hat{x}_s, \hat{z}_s)_1$ to $s_2 = (\hat{x}_s, \hat{z}_s)_2$ will produce at $\hat{x}, \hat{z}$ the velocity

$$u(\hat{x}, \hat{z}) = \frac{1}{2\pi} \int_{s_1}^{s_2} u_s\, d\xi_s \int_{-\infty}^{\infty} g\left(\hat{\beta}\right) \exp(i\chi)\, d\hat{\beta}, \tag{7.25}$$

where the ξ_s integration proceeds along the line source.

As the simplest possible example, we apply Eq. 7.25 to a 2D infinite-length line source, i.e., a source which extends from $\hat{z} \to -\infty$ to $\hat{z} \to \infty$ at a constant $\hat{x}_s$. With $g(\hat{\beta}) = 1$, so that all oblique normal modes have the same initial amplitude and phase, we obtain

$$u(\hat{x}, \hat{z}) = \frac{1}{2\pi} \int_{-\infty}^{\infty} u_s\, d\hat{z} \int_{-\infty}^{\infty} \exp(i\chi)\, d\hat{\beta}. \tag{7.26}$$

The integral over $\hat{z}_s$ must converge because the $\hat{\beta}$ integral is just the point-source solution Eq. 7.3. A physical interpretation of Eq. 7.26 is that Eq. 7.3 can be regarded as either the distribution of u with respect to $\hat{z}$ at the observation station $\hat{x}$ due to a single source at $\hat{x}_s, 0$, or as the variation of u at the single observation point $\hat{x}, 0$ as the point source at $\hat{x}_s$ moves from $\hat{z}_s \to -\infty$ to $\hat{z}_s \to \infty$. Consequently, if the point-source solution is weighted by u_s and integrated with respect to $\hat{z}_s$, the resultant amplitude and phase must be that produced by an infinite-length spanwise line source.

At $\hat{x} = \hat{x}_s$, the phase function χ reduces to $\hat{\beta}(\hat{z} - \hat{z}_s$ and Eq. 7.26 becomes

$$u\left(\hat{x}_s, \hat{z}\right) = \frac{1}{2\pi} \int_{-\infty}^{\infty} u_s\, d\hat{z}_s \int_{-\infty}^{\infty} \cos\left[\hat{\beta}\left(\hat{z} - \hat{z}_s\right)\right] d\hat{\beta}. \tag{7.27}$$

We recognize the $\hat{\beta}$ integral as the Dirac δ-function:

$$\cos\left[\hat{\beta}\left(\hat{z} - \hat{z}_s\right)\right] d\hat{\beta} = 2\pi\delta\left(\hat{z} - \hat{z}_s\right), \tag{7.28}$$

Therefore, $u(\hat{x}, \hat{z}) = u_s$ as it should, and we see the reason for the factor 2π in the definition of the function g in Eqs. 7.3 and 7.23. Thus when applied to an infinite-length line source of constant amplitude A_s and

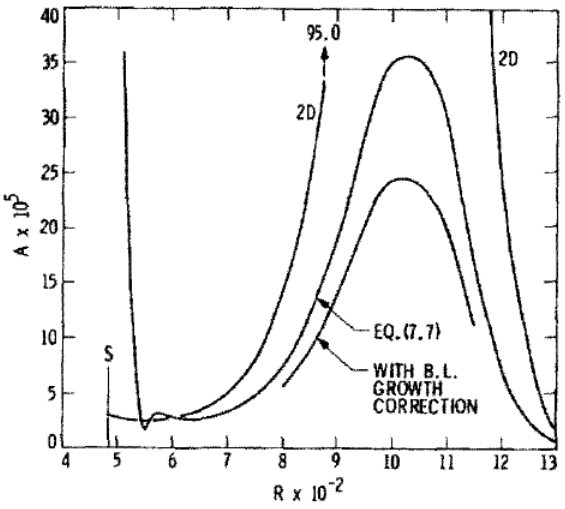

Figure 7.2: Centerline amplitude distribution behind harmonic point source as calculated by numerical integration, and comparison with 2D normal mode; $F = 0.60 \times 10^{-4}$, $R_s = 485$, Blasius boundary layer.

of constant phase, Eq. 7.25 must yield the amplitude ratio A/A_s of a 2D normal mode. This property of the point-source solution offers a convenient check on numerical results. Furthermore, if $u_s = A_s \sin(\hat{\beta}_s \hat{z}_s)$ (standing wave) or $A_s \exp(i\hat{\beta}_s \hat{z}_s)$ (traveling wave), Eq. 7.25 will give the amplitude ratio of an oblique normal mode of spanwise wavenumber $\hat{\beta}_s$. Applications of Eq. 7.25 to finite-length 2D and oblique line sources have been given by Mack (1984a).

7.5 Numerical and experimental results

The wave pattern behind a harmonic point source of frequency $F = 0.60 \times 10^{-4}$ located at $R_s = 485$ has been worked out in detail by Mack and Kendall (1983). We shall quote a few results here. Figure 7.2 gives the centerline amplitude distribution downstream of the source as calculated by numerical integration from Eq. 7.7 with $\hat{g}(\hat{\beta}) = 1$. The amplitude distribution of the 2D normal mode is shown for comparison, where A_0 has been chosen to equal the amplitude at $R = 630$. The initial steep drop in the amplitude is reversed near the lower branch of the 2D neutral-stability curve, but this first minimum is followed by a broad second minimum before the sustained amplitude growth gets under way. The peak amplitude occurs at the upper-branch location of $R = 1050$. However, the magnitude of the peak amplitude is less than half of the normal-mode amplitude. The reduction in amplitude is due to the sideways spreading of the wave energy in the point-source problem.

The wave energy also spreads in the y direction because of the growth of the boundary layer. This effect is not included in the calculation because of the use of parallel-flow eigenvalues, even though the correct Reynolds-number dependent eigenvalues have been used. In the point-source wave-packet problem, Gaster (1975) found that the boundary-layer growth could not be ignored, and he introduced a correction based on a simple energy argument. With the assumption that the wave energy is proportional to the square of the amplitude, A^2 would be constant in the absence of damping or amplification or sideways spreading. This argument suggests that the amplitude from Eq. 7.7 be multiplied by $R^{-1/2}$ to correct for boundary-layer growth, adn the result is shown in Fig. 7.2. This correction is sizable, and if correct cannot be neglected.

A characteristic feature of experimental phase measurements on the centerline is that if the phase is extrapolated backwards to zero the apparent location of the source is downstream of the actual source location. Figure 7.3 demonstrates why this is so. The phase initially rises at a slower rate, and it is only after an adjustment in the region where amplification starts that the phase then increases at the faster rate of the measurements.

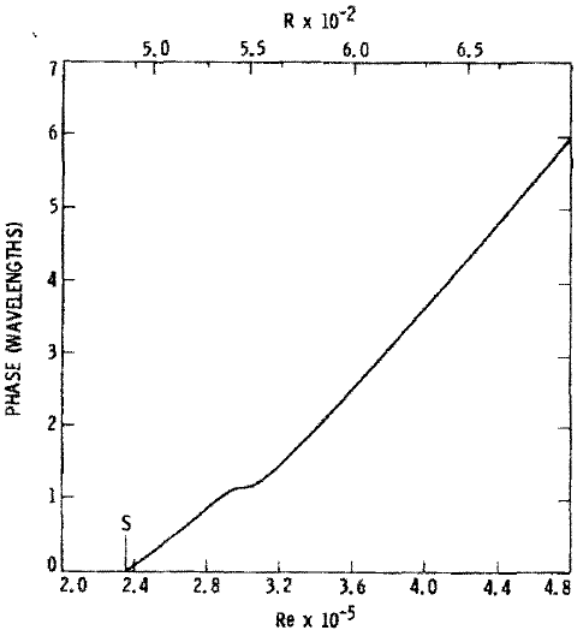

Figure 7.3: Centerline phase distribution behind harmonic point source as calculated by numerical integration; $F = 0.60 \times 10^{-4}$, $R_s = 485$, Blasius boundary layer.

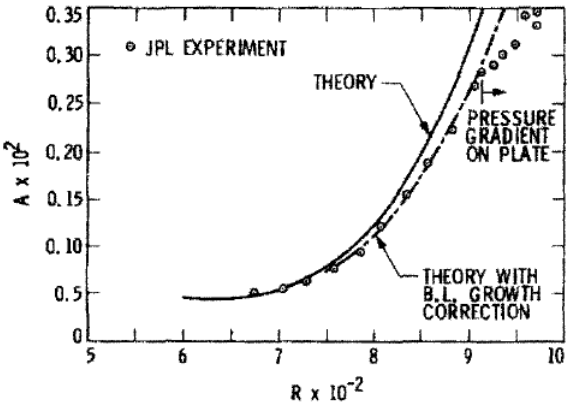

Figure 7.4: Comparison of measured and calculated cecnterline amplitude distributions behind harmonic point source; $F = 0.60 \times 10^{-4}$, $R_s = 485$, Blasius boundary layer.

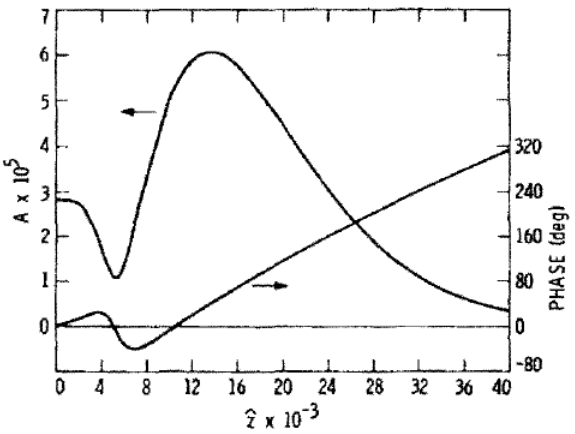

Figure 7.5: Spandwise amplitude and phase distribution at $R = 700$ behind harmonic point source; $F = 0.60 \times 10^{-4}$, $R_s = 485$, Blasius boundary layer.

The centerline amplitude distribution has also been calculated from Eq. 7.18 of the extended saddle-point method. Starting at about $R = 650$, the saddle-point results are virtually identical with those obtained from numerical integration in both amplitude and phase. Even the parallel-flow saddle-point method gives a good result to about the region of maximum amplitude, after which there is a slight departure. Consequently, Eq. 7.18 gives us a way to obtain the centerline amplitude accurately everywhere except quite close to the source with only a little more calculation than is needed to obtain the normal-mode A/A_0.

The important question now is whether or not the amplitude distribution of Fig. 7.2 has anything to do with an experimentally determined amplitude. The answer is given in Fig. 7.4 (Mack and Kendall, 1983). For the same conditions as the calculations, a hot-wire anemometer was moved downstream in a Blasius boundary layer. At each Reynolds number station, the maximum fluctuation amplitude in the boundary layer was determined by a vertical traverse of the hot wires. The source strength was well within the range for which the response at the hot wire varied linearly with the source amplitude. The amplitude in Fig. 7.4 is the actual measured amplitude expressed as a fraction of the freestream velocity. The level of the calculated amplitude has been adjusted accordingly. The calculated amplitude increases more rapidly than in the experiment, but the Gaster correction for boundary-layer growth makes the two amplitude distributions identical up to about $R = 890$, where the measurements depart abruptly from the theory. This disagreement was traced to a favorable pressure gradient on the flat plate that started precisely at the point of departure. The good agreement in this one example of the calculation with the Gaster growth correction and the measurement in the zero pressure-gradient region, while hardly conclusive, does suggest that when dealing with wave motion over many wavelengths, the growth at the boundary layer cannot be neglected.

The off-centerline wave pattern is of considerable complexity, as shown by Gilev et al. (1981). The peak amplitude occurs initially off centerline, and it is only well downstream of the source that it is found on the centerline. A typical calculated spanwise amplitude and phase distribution is shown in Fig. 7.5. The complex evolution of the phase that appears in Fig. 7.1 is reproduced quite closely by Eq. 7.7, but the calculated off-centerline amplitude is less exact. Indeed, the saddle-point method, even in its extended form, fails to give off-centerline amplitude peaks of sufficient magnitude, and only agrees well with the numerical-integration results after these peaks have disappeared. The parallel-flow saddle-point method fails badly in calculating the off-centerline wave pattern. The difficulty of correctly computing the amplitude with the present methods is probably related to the complicated nature of the eigenfunctions. In order for amplitude calculations to agree as well with experiment as do the phase calculations, it will be necessary to include the eigenfunctions in the calculations. However, even with this limitation, the numerical-integration method does remarkably well in reproducing the measured wave pattern, and provides another example of the utility of linear stability theory in dealing with point source problems.

Part II

Compressible Stability Theory

Chapter 8

Formulation of Compressible Stability Theory

8.1 Introductory remarks

The theory of a compressible laminar boundary layer differs sufficiently from the incompressible theory to warrant being treated as a separate subject. The basic approach and many of the ideas are the same, and for this reason, the incompressible theory can be regarded as an indispensable prelude to the study of the compressible theory. For example, all of the material in Sections 2.2, 2.3 and 2.6 applies also to the compressible theory. The motivation for the study of the stability of compressible boundary layers is the problem of transition to turbulence, just as it is for the incompressible theory. However, the relation of stability to transition is even more of an open question than at low speeds. Experiments have been performed that firmly establish the existence of instability waves in supersonic and hypersonic boundary layers (Laufer and Vrebalovich, 1960; Kendall, 1967, 1975), but there are none that really demonstrate when, and under which circumstances, transition is actually caused by linear instability. A series of stabiity experiments with "naturally" occurring transition in wind tunnels has been carried out by Demetriades (1977) and Stetson et al. (1983, 1984), but many of their observations have yet to be reconciled with theory. mention must also be made of the remarkable flight experiment by Dougherty (1980) that is probably the best evidence to date that transition in a low-disturbance environment at supersonic speeds is caused by laminar instability. For further information on the intricacies of transition at supersonic and hypersonic speeds, we recommend a study of the report by Morkovin (1968).

The first attempt to develop a compressible stability theory was made by Küchemann (1938). Viscosity, the mean temperature gradient and the curvature of the velocity profile were all neglected. The latter two assumptions later proved to have been too restrictive. The most important theoretical investigation to date of the stability of the compressible boundary layer was carried out by Lees and Lin (1946). The developed an asymptotic theory in close analogy to the incompressible asymptotic theory of Lin (1945), and, in addition, gave detailed consideration to a purely inviscid theory. The Rayleigh theories were extended to compressible flow, and the energy method was used as the basis for a discussion of waves moving supersonically with respect to the freestream. The quantity $D(\rho DU)$, where $D = d/dy$, was found to play the same role in the inviscid compressible theory as does D^2U in the incompressible theory. As a consequence, the flat-plate compressible boundary layer is unstable to purely inviscid waves, quite unlike the incompressible Blasius boundary layer where the instability is viscous in origin.

The close adherence of Lees and Lin to the incompressible theory, and the inadequacy of the asymptotic theory except at very low Mach numbers, meant that some major differences between the incompressible and compressible theories were not uncovered until extensive calculations had been carried out on the basis of a direct numerical solution of the differential equations. In the incompressible theory, it is possible to make substantial progress by ignoring three-dimensional waves, because a 2D wave will always have the largest amplitude ratio at any Reynolds number. This is no longer true above about a Mach number of 1.0. A second notable difference is that in the incompressible theory there is a unique relation between the wavenumber

and phase velocity, whereas in the compressible theory there is an infinite sequence of wavenumbers for each phase velocity whenever the mean flow relative to the phase velocity is supersonic (Mack, 1963, 1964, 1965b, 1969; Gill, 1965b). These additional solutions are called the higher modes. They are of practical importance for boundary layers because it is the first of the additional solutions, the second mode, that is the most unstable according to the inviscid theory. Above about $M_1 = 4$, it is also the most unstable at almost all finite Reynolds numbers.

Subsequent to the work of Lees and Lin, a report of Lees (1947) presented neutral-stability curves for insulated-wall flat plate boundary layers up to $M_1 = 1.3$, and for cooled-wall boundary layers at $M_1 = 0.7$. This report also included the famous prediction that cooling the wall acts to stabilize the boundary layer. However, this prediction must be considerably modified because of the existence of the higher modes. These modes require for their existence only a region of supersonic relative flow, and thus cannot be eliminated by cooling the wall. Indeed, the are actually destabilized by cooling (Mack, 1965b, 1969).

8.2 Linearized parallel-flow stability equations

A comprehensive account of the compressible stability theory must start with the derivation of the governing equations from the Navier-Stokes equations for a viscous, heat conducting, perfect gas, which in dimensional form are

$$\frac{\partial \bar{u}_i}{\partial t^*} + \bar{u}_j^* \frac{\partial \bar{u}_i}{\partial x_j^*} = \frac{1}{\bar{\rho}^*} \frac{\partial \bar{\tau}_{ij}^*}{\partial x_j^*}, \tag{8.1a}$$

$$\frac{\partial \bar{\rho}^*}{\partial t^*} + \frac{\partial}{\partial x_j^*} \left(\bar{\rho}^* \bar{u}_j^* \right) = 0, \tag{8.1b}$$

$$\bar{\rho}^* c_v^* \left(\frac{\partial \bar{T}^*}{\partial t^*} + \bar{u}_j^* \frac{\partial \bar{T}^*}{\partial x_j^*} \right) = \frac{\partial}{\partial x_j^*} \left(\bar{\kappa}^* \frac{\partial \bar{T}^*}{\partial x_j^*} \right) + \bar{\tau}_{ij}^* \bar{e}_{ij}^*, \tag{8.1c}$$

$$\bar{p}^* = \bar{\rho}^* R^* \bar{T}^*, \tag{8.1d}$$

where

$$\bar{e}_{ij}^* = \frac{1}{2} \left(\frac{\partial \bar{u}_i^*}{\partial x_j^*} + \frac{\partial \bar{u}_j^*}{\partial x_i^*} \right), \tag{8.2a}$$

$$\bar{\tau}_{ij}^* = 2\bar{\mu}^* \bar{e}_{ij}^* + \left[\frac{2}{3} \left(\bar{\lambda}^* - \bar{\mu}^* \right) \bar{e}_{kk}^* - \bar{p}^* \right] \delta_{ij}. \tag{8.2b}$$

Again asterisks denote dimensional quantities, overbars time-dependent quantities, and the summation convention has been adopted as in Chapter 2. The equations are, respectively, of momentum, continuity, energy and state. The quantities which did not appear in the incompressible equations are $\bar{T}^*$, the temperature; $\bar{\kappa}^*$, the coefficient of thermal conductivity; R^*, the gas constant; c_v^*, the specific heat at constant volume, which will be assumed constant; and $\bar{\lambda}^*$, the coefficient of second viscosity ($= 1.5\times$ bulk viscosity coefficient).

The stability equations are obtained from the Navier-Stokes equations by the same procedure that we used for incompressible flow in Section 2.1. First, all quantities are divided into mean flow and fluctuation terms. With primes used to denote fluctuations of the transport coefficients,

$$\begin{aligned} \bar{u}^* &= U^* + u^*, & \bar{p}^* &= P^* + p^*, \\ \bar{T}^* &= T^* + \theta^*, & \bar{\rho}^* &= \rho^* + \varrho^*, \\ \bar{\mu}^* &= \mu^* + \mu'^*, & \bar{\kappa}^* &= \kappa^* + \kappa'^*, \qquad \bar{\lambda}^* = \lambda^* + \lambda'^*, \end{aligned} \tag{8.3}$$

where the first variable on each RHS is a steady mean-flow quantity, and the second is an unsteady fluctuation.

Next, the equations are linearized, the mean-flow terms are subtracted out, and, finally, the parallel-flow assumption is made. The resulting equations are then made dimensionless with respect to the local freestream velocity U_1^*, a reference length L^*, and the freestream values of all state variables (including pressure). Both viscosity coefficients are referred to μ_1^* and κ^* is referred to $c_p^* \mu_1^*$, where c_p^* is the specific heat at constant

pressure. The transport coefficients are functions only of temperature, so that their fluctuations can be written

$$\mu' = \frac{d\mu}{dT}\theta, \qquad \kappa' = \frac{d\kappa}{dT}\theta, \qquad \lambda' = \frac{d\lambda}{dT}\theta. \tag{8.4}$$

Therefore, μ, κ, and λ in the following equations, along with ρ, are mean-flow quantities, not fluctuations. The dimensionless, linearized x-momentum equation is

$$\begin{aligned}\rho\left(\frac{\partial u}{\partial t}+\ U\frac{\partial u}{\partial x}+v\frac{dU}{dy}+W\frac{\partial u}{\partial z}\right) = \\ -\frac{1}{\gamma M_1^2}\frac{\partial p}{\partial x}+\frac{1}{R}\left[2\mu\frac{\partial^2 u}{\partial x^2}+\mu\left(\frac{\partial^2 u}{\partial y^2}+\frac{\partial^2 u}{\partial z^2}+\frac{\partial^2 v}{\partial x\partial y}+\frac{\partial^2 w}{\partial x\partial z}\right)\right. \\ +\frac{2}{3}(\lambda-\mu)\left(\frac{\partial^2 u}{\partial x^2}+\frac{\partial^2 v}{\partial x\partial y}+\frac{\partial^2 w}{\partial x\partial z}\right)+\frac{d\mu}{dT}\frac{dT}{dy}\left(\frac{\partial u}{\partial y}+\frac{\partial v}{\partial x}\right) \\ \left.+\ \frac{d\mu}{dT}\left(\frac{d^2U}{dy^2}\theta+\frac{dU}{dy}\frac{\partial\theta}{\partial y}\right)+\frac{d^2\mu}{dT^2}\frac{dT}{dy}\frac{dU}{dy}\theta\right].\end{aligned} \tag{8.5a}$$

The y-momentum equation is

$$\begin{aligned}\rho\left(\frac{\partial v}{\partial t}+\ U\frac{\partial v}{\partial x}+W\frac{\partial v}{\partial z}\right) = \\ -\frac{1}{\gamma M_1^2}\frac{\partial p}{\partial y}+\frac{1}{R}\left[2\mu\frac{\partial^2 v}{\partial y^2}+\mu\left(\frac{\partial^2 v}{\partial x^2}+\frac{\partial^2 v}{\partial z^2}+\frac{\partial^2 u}{\partial x\partial y}+\frac{\partial^2 w}{\partial y\partial z}\right)\right. \\ +\frac{2}{3}(\lambda-\mu)\left(\frac{\partial^2 u}{\partial x\partial y}+\frac{\partial^2 v}{\partial y^2}+\frac{\partial^2 w}{\partial y\partial z}\right)+\frac{d\mu}{dT}\left(2\frac{dT}{dy}\frac{\partial v}{\partial y}+\frac{dU}{dy}\frac{\partial\theta}{\partial x}+\frac{dW}{dy}\frac{\partial\theta}{\partial z}\right) \\ \left.+\ \frac{2}{3}\left(\frac{d\lambda}{dT}-\frac{d\mu}{dT}\right)\frac{dT}{dy}\left(\frac{\partial u}{\partial x}+\frac{\partial v}{\partial y}+\frac{\partial w}{\partial z}\right)\right].\end{aligned} \tag{8.5b}$$

The z-momentum equation is

$$\begin{aligned}\rho\left(\frac{\partial w}{\partial t}+\ U\frac{\partial w}{\partial x}+v\frac{dW}{dy}+W\frac{\partial w}{\partial z}\right) = \\ -\frac{1}{\gamma M_1^2}\frac{\partial p}{\partial z}+\frac{1}{R}\left[2\mu\frac{\partial^2 w}{\partial z^2}+\mu\left(\frac{\partial^2 w}{\partial y^2}+\frac{\partial^2 w}{\partial x^2}+\frac{\partial^2 v}{\partial y\partial z}+\frac{\partial^2 u}{\partial x\partial z}\right)\right. \\ +\frac{2}{3}(\lambda-\mu)\left(\frac{\partial^2 w}{\partial x^2}+\frac{\partial^2 v}{\partial y\partial z}+\frac{\partial^2 u}{\partial x\partial z}\right)+\frac{d\mu}{dT}\frac{dT}{dy}\left(\frac{\partial w}{\partial y}+\frac{\partial v}{\partial z}\right) \\ \left.+\ \frac{d\mu}{dT}\left(\frac{d^2W}{dy^2}\theta+\frac{dW}{dy}\frac{\partial\theta}{\partial y}\right)+\frac{d^2\mu}{dT^2}\frac{dT}{dy}\frac{dW}{dy}\theta\right].\end{aligned} \tag{8.5c}$$

The continuity equation is

$$\frac{\partial\varrho}{\partial t}+\rho\left(\frac{\partial u}{\partial x}+\frac{\partial v}{\partial y}+\frac{\partial w}{\partial z}\right)+v\frac{d\rho}{dy}+U\frac{\partial\varrho}{\partial x}+W\frac{\partial\varrho}{\partial z}=0. \tag{8.5d}$$

The energy equation is

$$\rho\left(\frac{\partial\theta}{\partial t}+ U\frac{\partial\theta}{\partial x}+v\frac{dT}{dy}+W\frac{\partial\theta}{\partial z}\right)= \\ -(\gamma-1)\left(\frac{\partial u}{\partial x}+\frac{\partial v}{\partial y}+\frac{\partial w}{\partial z}\right)+\frac{\gamma\mu}{PrR}\left[\frac{\partial^2\theta}{\partial x^2}+\frac{\partial^2\theta}{\partial y^2}+\frac{\partial^2\theta}{\partial z^2}+\frac{1}{\kappa}\frac{d\kappa}{dT}\frac{d^2T}{dy^2}\theta\right. \\ \left.+\frac{2}{\kappa}\frac{d\kappa}{dT}\frac{dT}{dy}\frac{\partial\theta}{\partial y}+\frac{1}{\kappa}\frac{d^2\kappa}{dT^2}\left(\frac{dT}{dy}\right)^2\theta\right]+\gamma(\gamma-1)M_1^2\frac{1}{R}\left[2\mu\frac{dU}{dy}\left(\frac{\partial u}{\partial y}+\frac{\partial v}{\partial x}\right)\right. \\ \left.+2\mu\frac{dW}{dy}\left(\frac{\partial v}{\partial y}+\frac{\partial w}{\partial y}\right)+\frac{d\mu}{dT}\left(\frac{dU}{dy}\right)^2\theta+\frac{d\mu}{dT}\left(\frac{dW}{dy}\right)^2\theta\right].. \tag{8.5e}$$

The equation of state is

$$p=\frac{\varrho}{\rho}+\frac{\theta}{T}. \tag{8.5f}$$

Previously undefined quantities which appear in these equations are M_1, the local Mach number at the edge of the boundary layer; γ, the ratio of specific heats; and $Pr = c_p^*\mu^*/\kappa^*$, the Prandtl number, which is a function of temperature. Equations 8.5 are the compressible counterparts of the incompressible stability equations 2.5, and are valid for a 3D disturbance in a 3D mean flow. It should be noted that unlike most compressible stability analyses, Eq. 8.5e, the energy equation, is valid for a variable Prandtl number. The constant Prandtl number form is recovered by replacing κ with μ in the three terms in which it occurs.

The boundary conditions at $y = 0$ are

$$u(0)=0, \qquad v(0)=0, \qquad w(0)=0, \qquad \theta(0)=0. \tag{8.6a}$$

The boundary conditions on the velocity fluctuations are the usual no-slip conditions, and the boundary condition on the temperature fluctuation is suitable for a gas flowing over a solid wall. For almost any frequency, it is not possible for the wall to do anything other than to remain at its mean temperature. The only exception is for a stationary, or near stationary, crossflow disturbance, when $\theta(0) = 0$ is replaced by $D\theta(0) = 0$. The boundary conditions at $y \to \infty$ are

$$u(y), v(y), w(y), p(y), \theta(y) \text{ are bounded as } y \to \infty. \tag{8.6b}$$

This boundary condition is less restrictive than requiring all disturbances to be zero at infinity, but in supersonic flow waves may propagate to infinity and we wish to include those that do so with constant amplitude.

8.3 Normal-mode equations

We now specialize the disturbances to normal modes as in Section 2.3:

$$[u, v, w, p, \varrho, \theta]^{\mathrm{T}} = [\hat{u}(y), \hat{v}(y), \hat{w}(y), \hat{p}(y), \hat{\varrho}(y), \hat{\theta}(y)]^{\mathrm{T}} \exp\left[i\left(\int \alpha\, dx + \beta\, dz + \omega t\right)\right], \tag{8.7}$$

where we have adopted the quasi-parallel form of the complex phase function. The normal modes may grow either temporally or spatially or both, depending on whether ω or $\vec{k}$, or both, are complex. The discussion in Section 2.3 applies to the compressible theory just as well as to the incompressible theory.

When Eqs. 8.7 are substituted into Eqs. 8.5, and the same linear combinations of x and z momentum equations are formed as in Section 2.4 for the variables

$$\tilde{\alpha}\tilde{u} = \alpha\hat{u} + \beta\hat{w}, \qquad \tilde{\alpha}\tilde{w} = \alpha\hat{w} - \beta\hat{u}, \tag{8.8}$$

we obtain a system of equations which are the compressible counterparts of Eqs. 2.36. The momentum equation in the direction parallel to the wavenumber vector $\vec{k}$ is

$$\begin{aligned}\rho[i(\alpha U+\beta W-\omega)\tilde{\alpha}\tilde{u}+(\alpha DU+\beta DW)\hat{v}] = \\ -i\left(\alpha^2+\beta^2\right)\left(\frac{\hat{p}}{\gamma M_1^2}\right)+\frac{\mu}{R}\left[\tilde{\alpha}D^2\tilde{u}+\left(\alpha^2+\beta^2\right)(iD\hat{v}-2\tilde{\alpha}\tilde{u})\right] \\ +\frac{2}{3}\frac{\lambda-\mu}{R}\left(\alpha^2+\beta^2\right)(iD\hat{v}-\tilde{\alpha}\tilde{u})+\frac{1}{R}\left\{\frac{d\mu}{dT}\left(\alpha D^2U+\beta D^2W\right)\hat{\theta}\right. \\ \left.+\left(\frac{d\mu}{dT}D\hat{\theta}+\frac{d^2\mu}{dT^2}DT\hat{\theta}\right)(\alpha DU+\beta DW)+\frac{d\mu}{dT}DT\left[\tilde{\alpha}D\tilde{u}+i\left(\alpha^2+\beta^2\right)\hat{v}\right]\right\}. \end{aligned} \tag{8.9a}$$

The y momentum equation is

$$\begin{aligned}i\rho(\alpha U+\beta W-\omega)\hat{v} = \\ -\frac{D\hat{p}}{\gamma M_1^2}+\frac{\mu}{R}\left[2D^2\hat{v}+i\tilde{\alpha}D\tilde{u}-\left(\alpha^2+\beta^2\right)\hat{v}\right]+\frac{2}{3}\frac{\lambda-\mu}{R}\left(D^2\hat{v}+i\tilde{\alpha}\tilde{u}\right) \\ +\frac{1}{R}\left[i\frac{d\mu}{dT}(\alpha DU+\beta DW)\hat{\theta}+2\frac{d\mu}{dT}DTD\hat{v}+\frac{2}{3}\frac{d\mu}{dT}(\lambda-\mu)DT(D\hat{v}+i\tilde{\alpha}\tilde{u})\right]. \end{aligned} \tag{8.9b}$$

The momentum equation in the direction normal to $\vec{k}$ is

$$\begin{aligned}\rho[i(\alpha U+\beta W-\omega)\tilde{\alpha}\tilde{w}+(\alpha DW+\beta DU)\hat{v}] = \\ +\frac{\mu}{R}\left[\tilde{\alpha}D^2\tilde{w}+\left(\alpha^2+\beta^2\right)\tilde{\alpha}\tilde{w}\right]+\frac{1}{R}\left[\frac{d\mu}{dT}DT\tilde{\alpha}D\tilde{w}\right. \\ \left.+\frac{d\mu}{dT}\left(\alpha D^2W-\beta D^2U\right)\hat{\theta}+\left(\frac{d\mu}{dT}D\hat{\theta}+\frac{d^2\mu}{dT^2}DT\hat{\theta}\right)(\alpha DW-\beta DU)\right]. \end{aligned} \tag{8.9c}$$

The continuity equation is

$$i(\alpha U+\beta W-\omega)\hat{\varrho}+\rho(D\hat{v}+i\tilde{\alpha}\tilde{u})+Dp\hat{v}=0. \tag{8.9d}$$

The energy equation is

$$\begin{aligned}\rho[i(\alpha U+\beta W-\omega)\hat{\theta}+DT\hat{v}] = \\ -(\gamma-1)(D\hat{v}+i\tilde{\alpha}\tilde{u})+\frac{\gamma\mu}{PrR}\left\{D^2\hat{\theta}-\left(\alpha^2+\beta^2\right)\hat{\theta}+\frac{1}{\kappa}\left[\frac{d\kappa}{dT}D^2T+\frac{d^2\kappa}{dT^2}(DT)^2\right]\hat{\theta}\right. \\ \left.+\frac{1}{\kappa}\frac{d\kappa}{dT}DTD\hat{\theta}\right\}+\gamma(\gamma-1)M_1^2\frac{1}{R}\left\{2i\mu\left(\alpha DU+\beta DW\right)\hat{v}+\frac{d\mu}{dT}\left(DU^2+DW^2\right)\hat{\theta}\right. \\ \left.+\frac{2\mu}{\alpha^2+\beta^2}\left[\left(\alpha DU+\beta DW\right)\tilde{\alpha}D\tilde{u}+\left(\alpha DW-\beta DU\right)\tilde{\alpha}D\tilde{w}\right]\right\}. \end{aligned} \tag{8.9e}$$

The equation of state is

$$\hat{p}=\frac{\hat{\varrho}}{\rho}+\frac{\hat{\theta}}{T}. \tag{8.9f}$$

To reiterate, in these equations the eigenfunctions of the fluctuations are functions only of y and are denoted by a carent or a tilde; the mean-flow velocities U and W are also functions of y, as are the other mean-flow quantities: density ρ $(=1/T)$, temperature T, viscosity coefficients μ and λ, thermal conductivity coefficient κ, and Prandtl number. The specific heats are constant. The reference velocity for U and W is the same as for R and M_1, and the reference length for y is the same as in R.

8.4 First-order equations

8.4.1 Eighth-order system

Equations 8.9 are the basic equations of the compressible stability theory, but are not yet in a form suitable for numerical computation. For this purpose we need a system of first-order equations as in Section 2.5.2. With the dependent variables defined by

$$\begin{aligned} Z_1 &= \alpha\hat{u} + \beta\hat{w}, & Z_2 &= DZ_1, & Z_3 &= \hat{v}, \\ Z_4 &= \frac{\hat{p}}{\gamma M_1^2}, & Z_5 &= \hat{\theta}, & Z_6 &= D\hat{\theta}, \\ Z_7 &= \alpha\hat{w} - \beta\hat{u}, & Z_8 &= DZ_7, \end{aligned} \tag{8.10}$$

Equations 8.9 can be written as eight first-order differential equations

$$DZ_i(y) = \sum_{j=1}^{8} a_{ij}(y) Z_i(y), \qquad (i = 1, 8), \tag{8.11}$$

and the fact that this reduction is possible proves that Eqs. 8.9 constitute an eight-order system. The lengthy equations for the matrix elements are listed in Appendix A.

The boundary conditions are

$$\begin{aligned} &Z_1(0) = 0, && Z_3(0) = 0, && Z_5(0) = 0, && Z_7(0) = 0, \\ &Z_1(y), && Z_3(y), && Z_5(y), && Z_7(y) \text{ are bounded as } y \to \infty. \end{aligned} \tag{8.12}$$

8.4.2 Sixth-order system

Equations 8.11 can be solved by the same numerical techniques as used for the fourth-order system of incompressible theory. However, the fact that there are 16 real equations and four independent solutions means that the computer time required to calculate an eigenvalue is increased by several times. It is therefore important to know if it is possible to make use of a system of lesser order, as in the determination of eigenvalues. We note that for a 2D wave in a 2D boundary layer, the system already is of sixth order, as there can be no velocity component, either mean for fluctuating, in the z direction. Is there an exact reduction available from eighth to sixth order? The answer, unfortunately, as mentioned by Dunn and Lin (1955) and explicitly by Reshotko (1962), is no.

The theory of Dunn and Lin (1955) achieved the reduction to sixth order by an order of magnitude argument valid for large Reynolds numbers. The motivation was to put the equations in a form where an improved 2D asymptotic theory could be applied to oblique waves in a 2D boundary layer. However, neither this theory nor the direct numerical solutions of the Dunn-Lin sixth-order system of equations, turned out to give adequate numerical results above a low supersonic Mach number.

We may observe from the coefficient matrix of Eq. 8.11 listed in Appendix A that the only term that couples the first six equations to the last two is a_{68}. This coefficient comes from the last term of the energy equation (8.9e), and is one of four dissipation terms. It is the product of the gradient of the mean velocity normal to $\vec{k}$ and the gradient of the fluctuation velocity in the same direction. It was proposed by Mack (1969) to simply set this term equal to zero, and use the resultant sixth-order system for the calculation of eigenvalues. The numerical evidence, as discussed further in Section 10.4, is that except near the critical Reynolds number this approximation gives amplification rates within a few percent of those obtained from the full eighth-order system, and is most accurate at higher Mach numbers.

8.5 Uniform mean flow

In the freestream $U = U_1$, $W = W_1$, $T = 1$, $\mu = 1$, $\kappa = 1/Pr_1$, all y derivatives of mean-flow quantities are zero, and Eqs. 8.11 reduce to a system of equations with constant coefficients. In spite of the greater

complexity of these equations compared to those for incompressible flow, we are still able to arrive at analytical solutions. The lengthy derivation is given in Appendix B (Mack, 1965a). The exact freestream solutions are the ones to use to calculate the initial values for a numerical integration of Eqs. 8.11, but they do not lend themselves to a ready physical interpretation. For this purpose, we examine the limit of large Reynolds number. The characteristic values simplify to

$$\lambda_{1,2} = \mp \left[\alpha^2 + \beta^2 - M_1^2 \left(\alpha U_1 + \beta W_1 - \omega\right)^2\right]^{1/2}, \tag{8.13a}$$

$$\lambda_{3,4} = \mp \left[iR \left(\alpha U_1 + \beta W_1 - \omega\right)\right]^{1/2}, \tag{8.13b}$$

$$\lambda_{5,6} = \mp \left[iPrR \left(\alpha U_1 + \beta W_1 - \omega\right)\right]^{1/2}, \tag{8.13c}$$

$$\lambda_{7,8} = \lambda_{3,4}. \tag{8.13d}$$

We can identify our solutions as, in order, the inviscid solution, the first viscous velocity solution, a viscous temperature solution, which is new and does not appear in the incompressible theory, and the second viscous velocity solution. We shall only use the upper signs in what follows, as these are the solutions which enter the eigenvalue problem.

The components of the characteristic vector of the inviscid solution are

$$A_1^{(1)} = -i \left(\alpha^2 + \beta^2\right)^{1/2}, \tag{8.14a}$$

$$A_3^{(1)} = \frac{\left(\alpha^2 + \beta^2 - M_1^2 \left(\alpha U_1 + \beta W_1 - \omega\right)^2\right)^{1/2}}{\left(\alpha^2 + \beta^2\right)^{1/2}}, \tag{8.14b}$$

$$A_4^{(1)} = \frac{i \left(\alpha U_1 + \beta W_1 - \omega\right)}{\left(\alpha^2 + \beta^2\right)^{1/2}}, \tag{8.14c}$$

$$A_5^{(1)} = \frac{i(\gamma - 1) M_1^2 \left(\alpha U_1 + \beta W_1 - \omega\right)}{\left(\alpha^2 + \beta^2\right)^{1/2}}. \tag{8.14d}$$

The normalization has been changed to correspond to the incompressible solutions of Eq. 2.50. It can be noted that these expressions are correct when we set $M_1 = 0$.

The components of the characteristic vector corresponding to the first viscous velocity solution are

$$A_1^{(3)} = 1, \tag{8.15a}$$

$$A_3^{(3)} = \frac{i}{\left[iR \left(\alpha U_1 + \beta W_1 - \omega\right)\right]^{1/2}}, \tag{8.15b}$$

$$A_4^{(3)} = 0, \qquad A_5^{(3)} = 0. \tag{8.15c}$$

This solution is identical to the λ_3 incompressible solution only in the limit of large Reynolds numbers.

The components of the characteristic vector corresponding to the viscous temperature solution are

$$A_1^{(5)} = 0, \tag{8.16a}$$

$$A_3^{(5)} = -\frac{i \left(\alpha U_1 + \beta W_1 - \omega\right)^{1/2}}{(iPrR)^{1/2}}, \tag{8.16b}$$

$$A_4^{(5)} = 0, \tag{8.16c}$$

$$A_5^{(5)} = 1. \tag{8.16d}$$

The components of the characteristic vector corresponding to the second viscous velocity solution are

$$A_1^{(7)} = 0, \qquad A_3^{(7)} = 0, \qquad A_4^{(7)} = 0, \qquad A_5^{(7)} = 0, \tag{8.17a}$$

$$A_7^{(7)} = 1, \tag{8.17b}$$

$$A_8^{(7)} = -\left[\alpha^2 + \beta^2 + iR \left(\alpha U_1 + \beta W_1 - \omega\right)\right]^{1/2}. \tag{8.17c}$$

This solution is exact and is the same spanwise viscous wave solution as in incompressible flow.

We may observe that the viscous velocity solutions have only fluctuations of velocity, not of pressure or temperature. The velocity fluctuations in the x, z plane are in the direction of $\vec{k}$ for the first solution, and are normal to $\vec{k}$ for the second solution which is periodic only in time. The viscous temperature solution has no velocity fluctuations in the x, z plane, or pressure fluctuations. We may regard these solutions as the responses to sources of $\tilde{u}$, $\tilde{w}$ and $\hat{\theta}$, and to emphasize this fact the respective solutions have been normalized to make these quantities unity. The second viscous velocity solution still has the interpretation of a normal vorticity wave, as in the incompressible flow, but this wave cannot exist as a pure mode in the boundary layer (Squire mode) because of the a_{68} dissipation term that couples the latter two of Eqs. 8.11 to the first six equations.

Chapter 9

Compressible Inviscid Theory

9.1 Inviscid equations

In compressible flow, even flat-plate boundary layers have inviscid instability, and this instability increases with increasing Mach number. Therefore, the inviscid theory is much more useful in arriving at an understanding of the instability of compressible boundary layers than it is at low speeds. Indeed the initial detailed numerical working out of the viscous theory (Mack, 1969) was greatly facilitated by the insight offered by the inviscid theory. In the limit of infinite Reynolds number, Eqs. 8.9 reduce to

$$\rho\left[i\left(\alpha U+\beta W-\omega\right)\tilde{\alpha}\tilde{u}+\left(\alpha DU+\beta DW\right)\hat{v}\right]=-i\left(\alpha^2+\beta^2\right)\left(\frac{\hat{p}}{\gamma M_1^2}\right), \tag{9.1a}$$

$$i\rho\left(\alpha U+\beta W-\omega\right)\hat{v}=-D\hat{p}\frac{1}{\gamma M_1^2}, \tag{9.1b}$$

$$i\left(\alpha U+\beta W-\omega\right)\tilde{\alpha}\tilde{w}+\left(\alpha DW-\beta DU\right)\hat{v}=0, \tag{9.1c}$$

$$i\left(\alpha U+\beta W-\omega\right)\hat{\varrho}+\rho\left(D\hat{v}+i\tilde{\alpha}\widetilde{U}\right)+D\rho\hat{v}=0, \tag{9.1d}$$

$$\rho\left[i\left(\alpha U+\beta W-\omega\right)\hat{\theta}+DT\hat{v}\right]=-(\gamma-1)\left(D\hat{v}+i\tilde{\alpha}\widetilde{U}\right), \tag{9.1e}$$

$$\hat{p}=\frac{\hat{\varrho}}{\rho}+\frac{\hat{\theta}}{T}. \tag{9.1f}$$

We note that the $\tilde{w}$ momentum equation, Eq. 9.1c, and the energy equation, Eq. 9.1e, are decoupled from the other equations. Therefore, we can eliminate $\tilde{\alpha}\tilde{u}$ and $\hat{\varrho}$ from the latter to arrive at the following two first-order equations for $\hat{v}$ and $\hat{p}$:

$$\left(\alpha U+\beta W-\omega\right)D\hat{v}=\left(\alpha DU+\beta DW\right)\hat{v}+i\left(\alpha^2+\beta^2\right)\left(T-M_1^2\frac{\alpha U+\beta W-\omega}{\alpha^2+\beta^2}\right)\left(\frac{\hat{p}}{\gamma M_1^2}\right), \tag{9.2a}$$

$$D\left(\frac{\hat{p}}{\gamma M_1^2}\right)=-i\rho\left(\alpha U+\beta W-\omega\right)\hat{v}. \tag{9.2b}$$

These equations are the 3D compressible counterparts of Eqs. 3.12. The boundary conditions are

$$\hat{v}(0)=0, \qquad \hat{v}(y) \text{ is bounded as } y\to\infty. \tag{9.3}$$

The inviscid equations can be written in a simplified form if we introduce the Mach number

$$\overline{M}=\frac{\left(\alpha U+\beta W-\omega\right)M_1}{\left(\alpha^2+\beta^2\right)^{1/2}T^{1/2}}. \tag{9.4}$$

For a temporal neutral wave, $\overline{M}$ is real and is the local Mach number of the mean flow in the direction of the wavenumber vector $\vec{k}$ relative to the phase velocity ω_r/k. In all other cases, $\overline{M}$ is complex, but even so

we shall refer to it as the relative Mach number. In terms of $\overline{M}$, Eqs. 9.2 simplify to

$$D\left(\frac{\hat{v}}{\alpha U+\beta W-\omega}\right)=i\left(1-\overline{M}^2\right)\left(\frac{\hat{p}}{\gamma\overline{M}^2}\right), \tag{9.5a}$$

$$D\hat{p}=-i\gamma\overline{M}^2\frac{\left(\alpha^2+\beta^2\right)\hat{v}}{\alpha U+\beta W-\omega}. \tag{9.5b}$$

We observe that these equations are identical to two-dimensional equations ($\beta=0$) when written in the tilde variables of Eq. 2.37. Therefore, inviscid instability is governed by the mean flow in the direction of $\vec{k}$, just as for incompressible flow. Either Eqs. 9.5 or 9.2 can be used for numerical integration, but the latter have the advantage that $\hat{v}$ is a better behaved function near the critical point than is $\hat{v}/(\alpha U+\beta W-\omega)$.

Equation 9.5a is the familiar linearized pressure-area relation of one-dimensional flow. The quantity $\hat{v}/(\alpha U+\beta W-\omega)$ is the amplitude function of the streamtube area change. The other flow variables can be written in a similar manner as

$$\widetilde{U}=i\left[D\widetilde{U}\frac{\hat{v}}{\tilde{\alpha}\widetilde{U}-\omega}+\frac{1}{\tilde{\alpha}}(\tilde{\alpha}\widetilde{U}-\omega)\frac{1}{1-\overline{M}^2}D\left(\frac{\hat{v}}{\tilde{\alpha}\widetilde{U}-\omega}\right)\right], \tag{9.6a}$$

$$\hat{\omega}=i\left[DT\frac{\hat{v}}{\tilde{\alpha}\widetilde{U}-\omega}-(\gamma-1)T\frac{1}{1-\overline{M}^2}D\left(\frac{\hat{v}}{\tilde{\alpha}\widetilde{U}-\omega}\right)\right], \tag{9.6b}$$

$$\hat{\varrho}=i\left[D\rho\frac{\hat{v}}{\tilde{\alpha}\widetilde{U}-\omega}-\rho\frac{\overline{M}^2}{1-\overline{M}^2}D\left(\frac{\hat{v}}{\tilde{\alpha}\widetilde{U}-\omega}\right)\right], \tag{9.6c}$$

$$\tilde{w}=iD\tilde{W}\frac{\hat{v}}{\tilde{\alpha}\widetilde{U}-\omega}. \tag{9.6d}$$

where we have used the tilde variables for simplicity. When the second terms of these equations are written with $\hat{p}$ in place of $\hat{v}/(\tilde{\alpha}\widetilde{U})$, they can be readily recognized as the linearized momentum equation, the isentropic temperature-pressure relation, and the isentropic density-pressure relation, respectively. The first terms are in the nature of source terms, and arise from the combination of a vertical fluctuation velocity and a mean shear. Because Eq. 9.6d is an equation for the vertical vorticity component $\tilde{\alpha}\tilde{w}$, only the source term is present.

A manipulation of Eqs. 9.1 leads to a single second-order equation for $\hat{v}$:

$$D\left[\frac{(\tilde{\alpha}\widetilde{U}-\omega)D\hat{v}-\tilde{\alpha}DU\hat{v}}{1-\overline{M}^2}\right]-(\alpha^2+\beta^2)(\tilde{\alpha}\widetilde{U}-\omega)\hat{v}=0. \tag{9.7}$$

This equation, which in 2D form was used by Lees and Lin (1946), is the 3D compressible counterpart of the Rayleigh equation. A second-order equation for $\hat{v}/(\tilde{\alpha}\widetilde{U}-\omega)$ follows directly from Eq. 9.5:

$$D^2\left(\frac{\hat{v}}{\tilde{\alpha}\widetilde{U}-\omega}\right)+D\left[\ln\left(\frac{\overline{M}^2}{1-\overline{M}^2}\right)\right]D\left(\frac{\hat{v}}{\tilde{\alpha}\widetilde{U}-\omega}\right)-\tilde{\alpha}^2(1-\overline{M}^2)\frac{\hat{v}}{\tilde{\alpha}\widetilde{U}-\omega}=0. \tag{9.8}$$

The corresponding equation for $\hat{p}$ is

$$D^2\hat{p}-D\left[\ln\left(\overline{M}^2\right)\right]D\hat{p}-\left(\alpha^2+\beta^2\right)\left(1-\overline{M}^2\right)\hat{p}=0. \tag{9.9}$$

9.2 Uniform mean flow

In the freestream, Eq. 9.9 reduces to

$$D^2\hat{p}-\left(\alpha^2+\beta^2\right)\left(1-\overline{M}_1^2\right)\hat{p}=0. \tag{9.10}$$

The solution which satisfies the boundary condition at infinity is

$$\frac{\hat{p}}{\gamma M_1^2}=i\left[\frac{\alpha U+\beta W-\omega}{\left(\alpha^2+\beta^2\right)^{1/2}}\right]\exp\left[-\left(\alpha^2+\beta^2\right)^{1/2}\left(1-\overline{M}_1^2\right)^{1/2}y\right], \tag{9.11}$$

which agrees with Eq. 8.14c. Equations 9.11 and 8.14b provide the initial values for the numerical integration.

The freestream solutions may be classified into three groups: subsonic waves with $\overline{M}_1^2 < 1$; sonic waves with $\overline{M}_1^2 = 1$; and supersonic waves with $\overline{M}_1^2 > 1$. Neutral supersonic waves are Mach waves of the relative flow, and can exist as either outgoing on incoming waves. True instability waves, which must satisfy the boundary condition at $y = 0$ as well as infinity are almost all subsonic, but eigenmodes which are supersonic waves of the outgoing family in the freestream have been found for highly cooled boundary layers (Mack, 1969). A combination of incoming and outgoing waves permits the boundary condition at $y = 0$ to be satisfied for any combination of α, β, and ω, as pointed out by Lees and Lin (1946). It is when only one family of waves is present that we have an eigenvalue problem. The combination of both families is the basis of the forcing theory presented in Chapter 11.

9.3 Some mathematical results

The detailed study of the two-dimensional inviscid theory carried out by Lees and Lin (1946) established a number of important results for temporal waves. Lees and Lin classified all instability waves as subsonic, sonic, or supersonic, depending on whether the relative freestream Mach number $\overline{M}_1$ is less than, equal to, or greater than one. Their chief results are:

(i) The necessary and sufficient condition for the existence of a neutral subsonic wave is that there is some point $y_s > y_o$ in the boundary layer where

$$D\left(\rho DU\right) = 0, \tag{9.12}$$

and y_o is the point at which $U = 1 - 1/M_1$. The phase velocity of the neutral wave is c_s, the mean velocity at y_s. This necessary condition is the generalization of Rayleigh's condition for incompressible flow that there must be a point of inflection in the velocity profile for a neutral wave to exist. The point y_s, which plays the same role in the compressible theory as the inflection point in the incompressible theory, is called the generalized inflection point. The proof of sufficiency given by Lees and Lin requires $\overline{M}$ to be everywhere subsonic.

(ii) A sufficient condition for the existence of an unstable wave is the presence of a generalized inflection point at some $y > y_o$, where y_o is the point at which $U = 1 - 1/M_1$. The proof of this condition also requires $\overline{M}$ to be subsonic.

(iii) There is a neutral sonic wave with the eigenvalues $\alpha = 0$, $c = c_o = 1 - 1/M_1$.

(iv) If $\overline{M}^2 < 1$ everywhere in the boundary layer, there is a unique wavenumber α_s corresponding to c_s for the neutral subsonic wave.

Lees and Lin obtained these results by a direct extension of the methods of proof used for incompressible flow. The necessary condition for a neutral subsonic wave was derived from the discontinuity of the Reynolds stress $\tau = -\langle uv \rangle$ at the critical point y_c. As in incompressible flow, τ is constant for a neutral inviscid wave except possibly at the critical point. For $\omega_i = 0$,

$$\tau\left(y_c + 0\right) - \tau\left(y_c - 0\right) = \frac{\pi}{\alpha}\left[\frac{D\left(\rho DU\right)}{DU}\right]_c \langle v_c^2 \rangle. \tag{9.13}$$

Equation 9.13 is the same as Eq. 3.9 in the incompressible theory except that $D(\rho DU)$ appears in place of D^2U. Since τ is zero at the wall and in the freestream by the boundary conditions for a subsonic wave, it follows that $D(\rho DU)$ must be zero at y_c. We may also note that for a neutral supersonic wave, where $c < c_0$ and $\tau(y_c + 0) = (\alpha^2/2)(\overline{M}^2 - 1)^{1/2}$ from the freestream solutions, the discontinuity at the critical point must equal this value of τ and the phase velocity must be other than U_s.

At this point we can examine the numerical consequences of the finding that neutral and unstable waves depend on the existence of a generalized inflection point. For the Blasius boundary layer, D^2U is negative everywhere except at $y = 0$. However, for a compressible boundary layer on an insulated flat plate, $D(\rho DU)$ is always zero somewhere in the boundary layer. Consequently, all such boundary layers are unstable to inviscid waves. Figure 9.1 shows that c_s, the mean velocity at the generalized inflection point and thus the phase velocity of the neutral subsonic wave, increases with increasing freestream Mach number M_1 in accordance with the outward movement of the generalized inflection point. If we recall from Section 6 that inviscid instability increases for the adverse pressure-gradient Falkner-Skan profiles as the inflection point

moves away from the wall, we can expect in this instance that inviscid instability will increase with increasing Mach number. Figure 9.1 also includes both c_0, the phase velocity of a neutral sonic wave, and the phase velocity for which $\overline{M} = -1$ at the wall. In the exact numerical solutions of the boundary-layer equations which were used for Fig. 9.1, the wall is insulated and the freestream temperature T_1^* is characteristic of wind-tunnel conditions. The stagnation temperature is held constant at 311 K until, with increasing M_1, T_1^* drops to 50 K. For higher Mach numbers, T_1^* is held constant at 50 K.

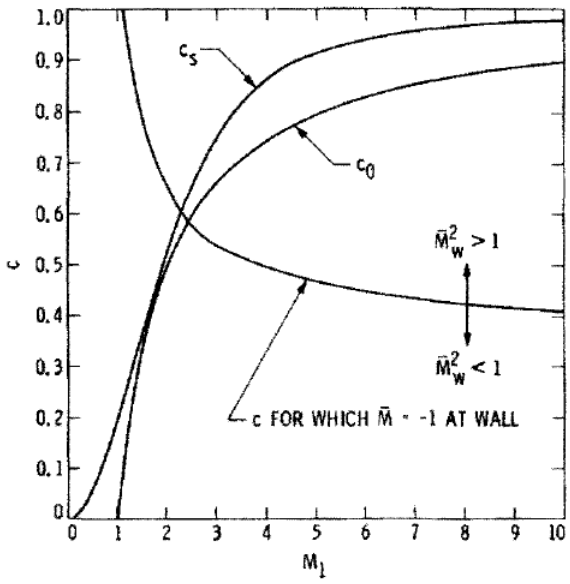

Figure 9.1: Phase velocities of 2D neutral inflectional and sonic waves, and of waves for which relative supersonic region first appears. Insulated wall, wind-tunnel temperatures.

For a wave to be subsonic relative to the freestream, and hence have vanishing amplitude at $y \to \infty$ even when neutral, c must be greater than c_0. It is often said that only subsonic waves are considered in stability theory, but this statement is not entirely correct. It is true that the neutral subsonic wave with eigenvalues α_s, c_s can only exist when $c_s > 1 - 1/M_1$. However, this does not rule out amplified and damped waves with $c < 1 - 1/M_1$, or even neutral supersonic waves with a c different from c_s. Examples of such waves have been found, all of which satisfy the boundary conditions at infinity and so are solutions of the eigenvalue problem. For $\omega_i \neq 0$, the amplitudes of outgoing amplified and incoming damped waves vanish at infinity regardless of the value of c; for neutral waves, the amplitude will only be bounded at infinity when $c < c_0$. What does turn out to be true is that the most unstable waves are always subsonic. Furthermore, for one class of waves, the amplified first-mode waves, the phase velocity is always between c_0 and c_s. This result has important consequences.

9.4 Methods of solution

The methods for obtaining solutions of the inviscid equations for boundary-layer profiles have been patterned after corresponding methods in incompressible flow. Lees and Lin (1946) developed power-series solutions in α^2, and also used the generalizations of Tollmein's incompressible solutions

$$\hat{v}_1(y) = (y - y_c) P_1(y - y_c), \tag{9.14a}$$

$$\hat{v}_2(y) = P_2(y - y_c) + \left(\frac{T^2}{DU^3}\right)_c [D(\rho DU)]_c \hat{v}_1(y) \ln(y - yc), y > y_c. \tag{9.14b}$$

For $y < y_c$, $\ln(y - y_c) = \ln|y - y_c| - i\pi$ as for incompressible flow. The leading terms of P_1 and P_2 are DU_c and T_c/DU_c, respectively, so that $\hat{v}_1$ and $\hat{v}_2$ are normalized here in a different manner than in Section 3.1. These

solutions have been worked out in more detail by Reshotko (1960). Both $\hat{v}$ and $\hat{u}$ have the same analytical behavior as in compressible flow. What is new here is the temperature fluctuation, which, according to Reshotko, has the behavior

$$\hat{\theta} \approx \frac{1}{y - y_c} + \left(\frac{T}{DU}\right)_c [D(\rho DU)]_c \ln(y - y_c) + \cdots . \tag{9.15}$$

Hence, even for a neutral subsonic wave, where $[D(\rho DU)]_c = 0$ and $\hat{v}$ and $\hat{u}$ are both regular, $\hat{\theta}$ has a singularity at y_c.

Two methods have been devised for the numerical integration of the inviscid stability equations. The first method (Lees and Reshotko, 1962) transforms the second-order linear equation into a first-order nonlinear equation of the Riccati type. This equation is solved by numerical integration except for the region around the critical point, where the power series in $y - y_c$ are used. The second method (Mack, 1965a) is a generalization to compressible flow of Zaat's (1958) method. This method has already been described in Section 3.2. For neutral and damped solutions, the contour of integration is indented under the singularity, just as for compressible flow.

9.5 Higher modes

9.5.1 Inflectional neutral waves

Although the Lees-Lin proof for neutral subsonic waves that α_s is a unique function of c_s was dependent on $\overline{M}^2 < 1$, and although Lees and Reshotko (1962) mentioned the possibility that α_s may not be unique for $\overline{M}^2 > 1$, no serious consideration was given to the possibility of multiple solutions until the extensive numerical work of Mack (1963, 1964, 1965b) brought them to light. Similar multiple solutions were found independently at about the same time by Gill (1965b, paper presented in 1964) in his study of "top-hat" jets and wakes. With the benefit of hindsight, it is actually rather easy to demonstrate their existence. The inviscid equations for $\hat{v}/(\tilde{\alpha}\widetilde{U} - \omega)$ and $\hat{p}$, Eqs. 9.8 and 9.9, quite evidently have a different analytical character depending on whether $\overline{M}^2$ is less than or greater than unity. It is instructive, as suggested by Lees [private communication (1964)], to consider α^2 large enough so that the first-derivative term can be neglected. Then Eq. 9.8 reduces to

$$D^2\left[\frac{\hat{v}}{\tilde{\alpha}\widetilde{U} - \omega}\right] - \tilde{\alpha}^2\left(1 - \overline{M}^2\right)\left[\frac{\hat{v}}{\tilde{\alpha}\widetilde{U} - \omega}\right] = 0. \tag{9.16}$$

When $\overline{M}^2 < 1$, the solutions of Eq. 9.16 are elliptic, and it is under this circumstance that Lees and Lin proved the uniqueness of α_s. However, when $\overline{M}^2 > 1$, Eq. 9.16 becomes a wave equation, and as in all problems governed by a wave equation, we can expect there to be an infinite sequence of wavenumbers that will satisfy the boundary conditions. We may note that for a subsonic wave (this terminology still refers to the freestream) and the usual sort of boundary-layer profiles, the relative supersonic region occurs below the critical point where $\overline{M} < 0$.

If y_a is the y where $\overline{M}^2 = 1$, the approximate solutions of Eq. 9.16 of the WKB type are

$$\frac{\hat{v}}{\tilde{\alpha}\widetilde{U} - \omega} = \pm \sin\left[\tilde{\alpha}_{sn} \int_0^y \left(\overline{M}^2 - 1\right)^{1/2} dy\right], y < y_a, \tag{9.17a}$$

$$\frac{\hat{v}}{\tilde{\alpha}\widetilde{U} - \omega} = -i \exp\left[-\tilde{\alpha}_{sn} \int_{y_a}^y \left(1 - \overline{M}^2\right)^{1/2} dy\right], y > y_a, \tag{9.17b}$$

where Eq. 9.17b follows from the boundary condition $\hat{v}(0) = 0$. We have written $\tilde{\alpha}_s$ as $\tilde{\alpha}_{sn}$. The subscript s denotes a neutral subsonic solution as before; the subscript n refers to the multiple solutions. The constant in Eq. 9.17b is chosen as $-i$ to make $\hat{p}$ real and positive for $y > y_a$. Either sign is possible for $y > y_a$. Since $\hat{p}$ is continuous and finite at $y = y_a$, $D[\hat{v}/(\tilde{\alpha}\widetilde{U} - \omega)]$, from Eq. 9.5a, must go to zero as $y \to y_a$ as does $\overline{M}^2 - 1$. The derivative of $\hat{v}/(\tilde{\alpha}\widetilde{U} - \omega)$ gives a factor $(\overline{M}^2 - 1)^{1/2}$, and the required factor of $(\overline{M}^2 - 1)^{1/2}$ can only come from the cosine having a zero at y_a. Consequently,

$$\cos\left[\tilde{\alpha}_{sn}\int_0^{y_a}\left(\overline{M}^2-1\right)^{1/2}dy\right]=0, \tag{9.18a}$$

and

$$\tilde{\alpha}_{sn}\int_0^{y_a}\left(\overline{M}^2-1\right)^{1/2}dy=\left(n-\frac{1}{2}\right), n=1,2,3,\ldots. \tag{9.18b}$$

Equation 9.18b is the final result, and demonstrates that there is an infinite sequence of discrete neutral wavenumbers with the phase velocity c_s. The difference between adjacent values of $\tilde{\alpha}_{sn}$ is

$$\tilde{\alpha}_{s(n+1)}-\tilde{\alpha}_{sn}=\pi\left(\int_0^{y_a}\left(\overline{M}^2-1\right)^{1/2}dy\right)^{-1}. \tag{9.19}$$

We may also observe that according to Eq. 9.18b, the sequence of values of $2\tilde{\alpha}_{sn}$ is $1,3,5,7,\ldots$. This result was first noted and given a physical explanation by Morkovin [private communication (1982)]. Because Eq. 9.16 is only approximate, the magnitude of $\tilde{\alpha}_{sn}$, the difference formula, and the ratio sequence are not expected to be numerically correct. However, as we shall see below, with an important exception they are either correct, or approximately correct.

When the numerical integration of Eqs. 9.2 is carried out for 2D waves with $c=c_s$ and $\omega_i=0$ for the insulated-wall flat-plate boundary layers described in Section 9.3, the α_{sn} which are found by the eigenvalues search procedure are shown in Fig. 9.2. The solution for each n will be referred to as a mode: $n=1$ is the first mode, $n=2$ the second mode, etc. The wavenumbers of the first mode were first computed by Lees and Reshotko (1962). With $c=c_s$, a y_a where $\overline{M}^2=1$ occurs first at $M_1=2.2$ ($y_a=0$). With increasing M_1, the relative sonic point y_a moves out into the boundary layer, and α_{sn} varies in inverse proportion to y_a as required by Eq. 9.18b. No higher modes with $c=c_s$ could be found numerically for $M_1<2.2$, in agreement with the theory given above.

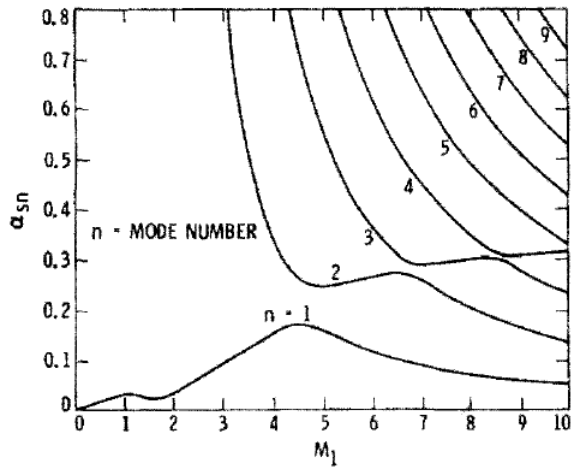

Figure 9.2: Multiple wavenumbers of 2D inflectional neutral waves ($c=c_s$). Insulated wall, wind-tunnel temperatures.

A prominent feature of Fig. 9.2 is that the upward sloping portion of the first-mode curve between $M_1=2$ and 4.5 is in a sense continuous through the other modes, i.e., there is a Mach number range for each mode where the α_{sn} vs. M_1 curve has a positive slope. The end point of this region for one mode is close to the starting point of a similar region for the next higher mode. The approach becomes closer as M_1 increases. The significance of these intervals of positive slope is that they provide the exceptions to the correctness, or approximate correctness, of the results given by, or deduced from, Eqs. 9.18b. Indeed we could well identify these modes as the "exceptional" modes.

With the wavenumbers of the multiple neutral waves established, the next step is to examine the eigenfunctions. For this purpose, the eigenfunction $\hat{p}/(\gamma M_1^2)$ is shown in Fig. 9.3 for the first six modes at

$M_1 = 10$. The first thing to note is that the number of zeroes in $\hat{p}$ is one less than the mode number n. For example, the second mode has one zero, and $\hat{p}(0)$ is 180° out of phase with $\hat{p}(\delta)$; the third mode has two zeroes and $\hat{p}(0)$ is in phase with $\hat{p}(\delta)$. The number of zeroes in $\hat{p}(y)$ is the surest identification of the mode under consideration. By keeping track of the phase difference between $\hat{p}(0)$ and $\hat{p}(\delta)$, it is possible to determine when there is a change from one mode to another.

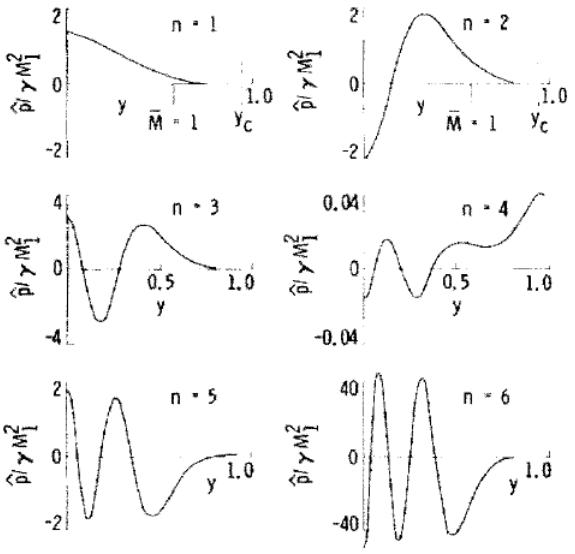

Figure 9.3: Pressure-fluctuation eigenfunctions of first six modes of 2D inflectional neutral waves ($c = c_s$) at $M_1 = 10$. Insulated wall, $T_1^* = 50$ K.

The appearance of the eigenfunctions in Fig. 9.3 confirms the simple theory given above: there is an infinite sequence of periodic solutions in the supersonic relative flow region which can satisfy the boundary conditions. The magnitude of $\hat{p}(0)$ is a minimum for the fourth mode [$\hat{p}(\delta)$ is the same for all modes]. Since the fourth mode at $M_1 = 10$ is on the upward sloping portion of the eigenvalue curve in Fig. 9.2, this is another indication of the special nature of such neutral solutions. For other modes, $\hat{p}(0)/\hat{p}(\delta)$ tends to become large away from $n = 4$, and tends to infinity as $n \to \infty$.

There is one important difference between the simple theory and Fig. 9.3. According to the theory, $\hat{p}(\delta)$ is positive for all modes; there are no zeroes in the interval $y > y_a$, and the number of zeroes in $y < y_a$ increases by one for each successive mode. We see from Fig. 9.3 that $\hat{p}(\delta)$ is negative for $n > 4$, and the number of zeroes in $y < y_a$ is the same for $n = 5$ as for $n = 4$. The total number of zeroes increases by one from $n = 4$ to $n = 5$ only because of the zero in $y > y_a$. However, we note that the "exceptional" mode is extraneous to the simple theory, and preserves something of a first-mode character which probably betrays a different physical origin from the other modes. Indeed, the other higher modes are nothing more than sound waves which reflect back and forth between the wall and the sonic line of the relative flow at $y = y_a$ as first suggested by Lees and Gold (1964). Morkovin's theory is based on this idea, and its duplication of the wavenumber ratio sequence 1,3,5,... attests to its correctness. The "exceptional" modes are not part of this theory; they are perhaps vorticity waves associated with the generalized inflection point as are incompressible and low Mach number first-mode waves. In this view, the modes which have been identified in Figs. 9.2 and 9.3 as first-mode waves for $M_1 > 5$ are not first-mode waves at all; this distinction is reserved for the modes whose wavenumbers increase monotonically with increasing M_1. However, we shall continue to refer to $n = 1$ as the first mode.

9.5.2 Noninflectional neutral waves

A further consequence of a region of supersonic relative flow in the boundary layer is the existence of a class of neutral waves which is completely different from anything encountered in the incompressible theory.

These waves are characterized by having phase velocities in the range $1 \leq c \leq 1 + 1/M_1$. For each phase velocity there is an infinite sequence of wavenumbers, just as for the inflectional neutral waves. A wave with $c = 1$ is at rest with respect to the freestream; a wave with $c = c_{02} = 1 + 1/M_1$ propagates downstream relative to U_1^* with the freestream speed of sound. The Lees-Lin neutral sonic wave propagation upstream relative to U_1^* with the freestream speed of sound.

All of the $1 \leq c \leq 1 + 1/M_1$ waves are subsonic waves, and, because $D(\rho DU) = 0$ in the freestream, there is no discontinuity in the Reynolds stress and the necessary condition for the existence of a subsonic neutral wave is satisfied. Unlike the inflectional neutral waves, $D(\rho DU)$ does not have to be zero in the boundary layer, and the $1 \leq c \leq 1+1/M_1$ waves exist for any boundary layer subject only to the requirement that $\overline{M}^2 > 1$ somewhere. The importance of the $c = 1$ neutral waves is that in the absence of an interior generalized inflection point they are accompanied by a neighboring family of unstable waves with $c < 1$. Consequently, a compressible boundary layer is unstable to inviscid waves whenever $\overline{M}^2 > 1$, regardless of any other feature of the velocity and temperature profiles.

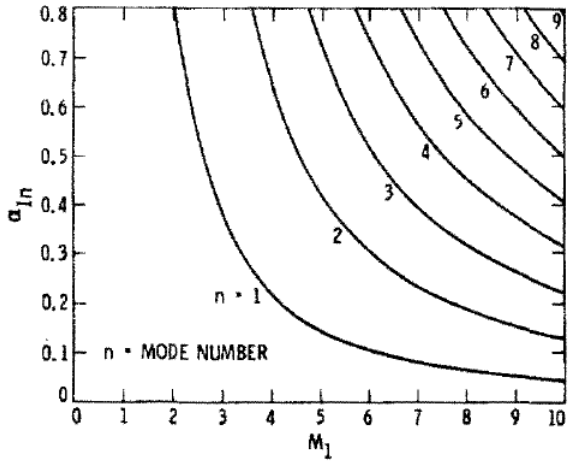

Figure 9.4: Multiple wavenumbers of 2D noninflectional neutral waves ($c = 1$). Insulated wall, wind-tunnel temperatures.

If we examine the inviscid equations 9.2, we see that when $c > 1$ they are no longer singular; i.e., there is no critical layer. Even when $c = 1$, and the critical layer is in a sense the entire freestream, Eq. 9.2a is still not singular because $DU/(U - 1)$ and $\hat{p}(y)/(U - 1)$ both have finite limits as $y \to y_\delta$. We call this class of solutions the noninflectional neutral waves. These waves persist to low subsonic Mach numbers, because, except at $M_1 = 0$, it is always possible to find a c large enough so that $\overline{M} = -1$ somewhere in the boundary layer.

The approximate theory of the preceding section applies to the noninflectional neutral waves just as well as to the inflectional neutral waves provided the initialization is changed for $c = 1$ to make $\hat{v}/(\alpha U - \omega)$ finite in the freestream. This change is needed because with $c = 1$ the wave motion is confined to the boundary layer and $\hat{v}$ must be zero for $y > y_\delta$. An infinite sequence of wavenumbers is obtained with the spacing given by Eq. 9.19, but since c is different from c_s the numerical values are not the same as for the inflectional waves. The wavenumbers obtained from the numerical integration with $c = 1$ are shown in Fig. 9.4 as functions of Mach number. These wavenumbers are denoted by α_{1n}, where the first subscript refers to $c = 1$, and the second is the mode number. There is now no portion of any wavenumber curve with a positive slope, and the spacing agrees reasonably well with the approximate formula. The discrepancy is about 10% for the first two modes, and decreases to about 1% for the fifth and sixth modes.

The eigenfunctions $\hat{p}(y)$ of the first six modes of the noninflectional neutral waves with $c = 1$ at $M_1 = 10$ are shown in Fig. 9.5. Here the ratio $\hat{p}(y)/\hat{p}(0)$ is plotted, rather than $\hat{p}(y)$ with $\hat{p}(\delta)$ fixed as in Fig. 9.3. The appearance of these eigenfunctions is in complete accord with the simple theory, unlike the inflectional neutral waves where the modes on the upward sloping portions of the wavenumber curves interrupt the orderly sequence, and where an outer zero appears in the eigenfunctions for $n > 4$.

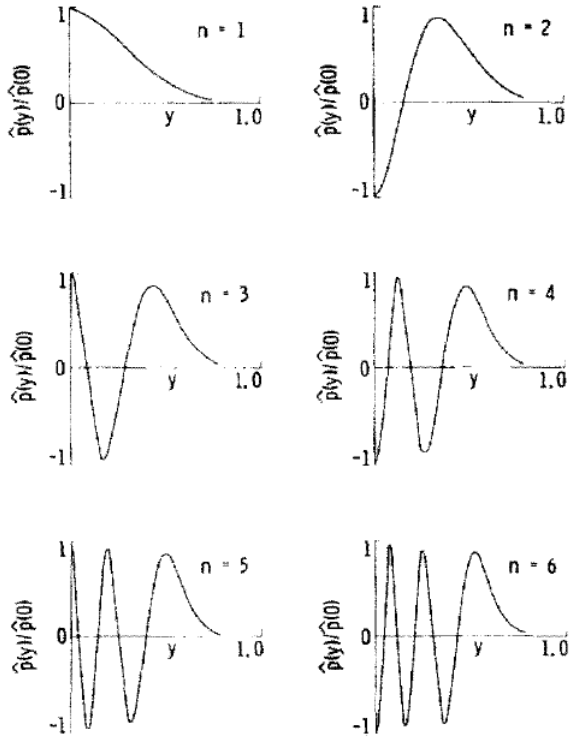

Figure 9.5: Pressure-fluctuation eigenfunctions of first six modes of 2D noninflectional neutral waves ($c = 1$) at $M_1 = 10$. Insulated wall, $T_1^* = 50$ K.

The numerical results for $1 < c < 1 + 1/M_1$ are similar to those presented for $c = 1$. Since these waves have no neighboring unstable or damped waves, they are of less importance in the inviscid theory than the other neutral waves. Consequently, these waves will not be considered further, and the term noninflectional neutral wave will refer only to a $c = 1$ wave. However, we might mention that the viscous counterparts of the $c > 1$ waves, which are damped rather than neutral, do have a role to play in certain cases.

9.6 Unstable 2D waves

A detailed discussion of the eigenvalues of amplified and damped waves as a function of Mach number for the first few modes has been given by Mack (1969). What we are mainly interested in here is the maximum amplification rate of the various modes, and this is shown in Fig. 9.6, where the maximum temporal amplification rate is given as a function of Mach number up to $M_1 = 10$. The corresponding frequencies are shown in Fig. 9.7. We see from Fig. 9.6 that below about $M_1 = 2.2$ the family of boundary layers we are considering is virtually stable to inviscid 2D waves, and that above $M_1 = 2.2$ the second mode is the most unstable mode. The latter result holds for 2D waves in all boundary layers that have been studied, and is one of the features that makes supersonic stability theory so different from the incompressible theory. Not only is there more than one mode of instability, but it is one of the additional modes that is the most unstable. Above $M_1 = 6.5$, the first mode is not even the second most unstable mode. The second-mode amplification rates can be appreciable. At $M_1 = 5$, the amplitude growth over a boundary-layer thickness is about double what is possible in a Blasius boundary layer at the Reynolds number of the maximum amplification rate, and about 25% of the maximum growth in a Falkner-Skan separation boundary layer.

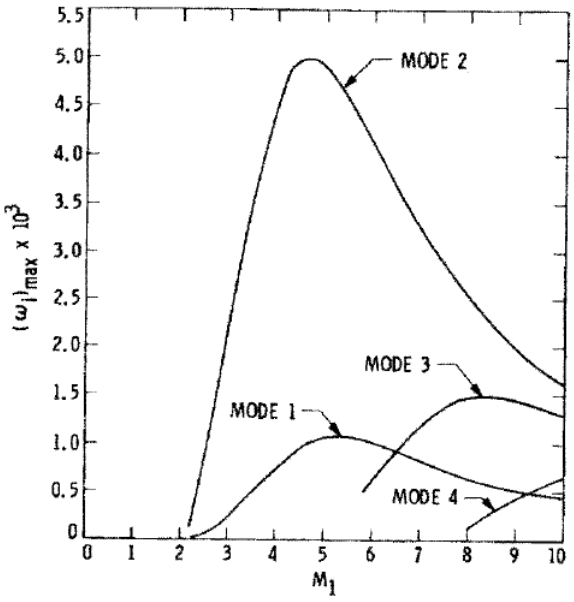

Figure 9.6: Effect of Mach number on maximum temporal amplification rate of 2D waves for first four modes. Insulated wall, wind-tunnel temperatures.

9.7 Three-dimensional waves

In the detailed study of the eigenvalues of unstable 2D first-mode waves (Mack, 1969), it was noted that the phase velocity is always between c_0 and c_s. These two velocities are almost identical near $M_1 = 1.6$, which suggests why boundary layers near that Mach number are almost stable even though the generalized

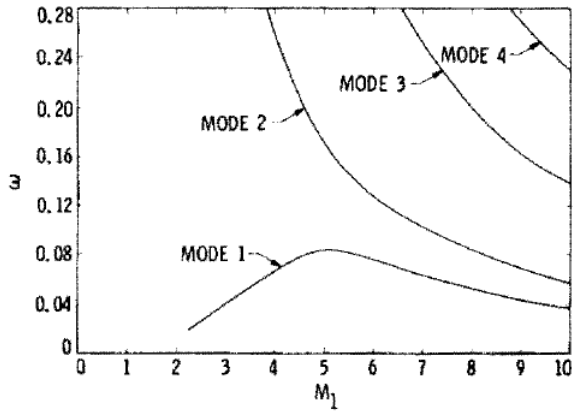

Figure 9.7: Effect of Mach number on frequency of most unstable 2D waves for first four modes. Insulated wall, wind-tunnel temperatures.

inflection point has moved out to $U_s = 0.38$. The inflection point is a fixed feature of the boundary-layer profile, and so is independent of the wave orientation. The phase velocity c_s of a 3D wave is $U_s \cos\psi$, and the phase velocity c_0 is $(1 - 1/\widetilde{M}_1)\cos\psi$, where $\widetilde{M}_1 = M_1 \cos\psi$. Thus as the wave angle ψ increases from zero, c_0 decreases more than by $\cos\psi$, and the difference $c_s - c_0$ increases. Consequently, we can expect the first mode to become more unstable. At the same time the thickness of the supersonic relative flow region, where one exists, will decrease along with $\widetilde{M}_1$ and we shall not be surprised to find that the higher modes become more stable.

Figure 9.8 shows the temporal amplification rate ω_i of the first and second modes at $M_1 = 4.5$ as a function of the frequency ω_r for several wave angles. Three-dimensional first-mode waves are indeed more unstable than 2D waves, and second-mode 3D waves are more stable than the corresponding 2D waves. The latter result also holds for all of the higher modes. The most unstable first-mode wave is at an angle of close to 60°, with an amplification rate about twice the maximum 2D rate and with a frequency a little over one-half of the frequency of the most unstable 2D wave.

At $M_1 = 4.5$, the unstable regions of the first two modes are separated by a damped region for all wave angles. However, at $M_1 = 8.0$, Fig. 9.9 shows that for 2D waves the first three modes are merged into a single unstable region. If we look at Fig. 9.2 we see that at this Mach number the exceptional mode is the third mode. Thus we can note another feature of the neutral wavenumbers α_{sn} of these modes: They serve as the "end points" of the merged unstable regions of the modes lying below them. As the wave angle increases from zero and $\widetilde{M}_1$ decreases, the merging is still in general accord with Fig. 9.2 for $\widetilde{M}_1$, as is confirmed by the calculation of $\widetilde{\alpha}_{sn}$. The same pattern of upward sloping exceptional wave numbers is found for oblique waves as for 2D waves (Mack, 1969). For $\psi = 60°$, the second-mode is stable; for $\psi = 56°$, there are still second-mode unstable waves, as can be verified by examining the phase change across the boundary layer of the pressure fluctuations, even though no peak is visible on the curve of Fig. 9.9.

In Fig. 9.10, the maximum temporal amplification rate with respect to frequency is plotted against the four Mach numbers 4.5, 5.8, 8.0 and 10.0. At all of these Mach numbers the most unstable first-mode wave is at an angle of between 50° and 60°, and has a maximum amplification rate that is roughly double the most unstable 2D wave. The effect of Mach number on the maximum first-mode amplification rate with respect to both frequency and wave angle is shown in Fig. 9.11. The wave angle of the most unstable wave is noted on the figure to within 5°, and the maximum 2D amplification rates are shown for comparison. An interesting change in the relationship between the 2D and 3D amplification rates takes place for $M_1 < 4$. The 3D maximum amplification rate is no longer only double the 2D rate as at higher Mach numbers; instead, at $M_1 = 3.0$ the ratio of the 3D rate to the 2D rate is 5.8, at $M_1 = 2.2$ it is 33, and at $M_1 = 1.8$ it is 130. We recall from Fig. 9.1 that it is near $M_1 = 1.6$ that the difference $c_s - c_0$ is the smallest. Therefore, the sonic limit acts as a severe constraint on the amplification of 2D waves at low Mach numbers. When this constraint

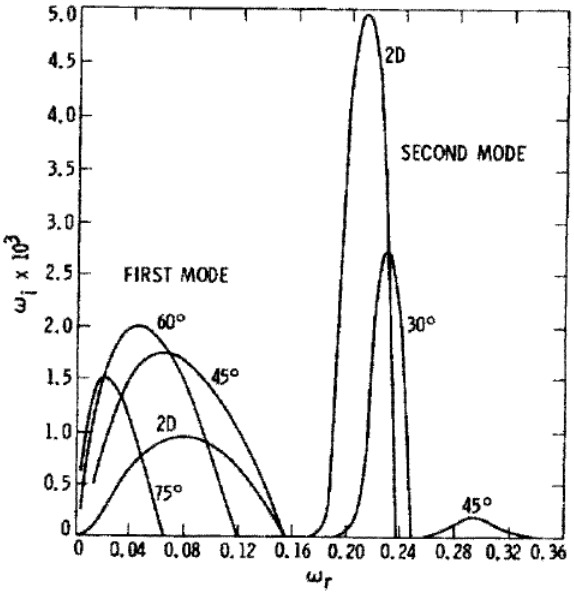

Figure 9.8: Temporal amplification rate of first and second modes vs. frequency for several wave angles at $M_1 = 4.5$. Insulated wall, $T_1^* = 311$ K.

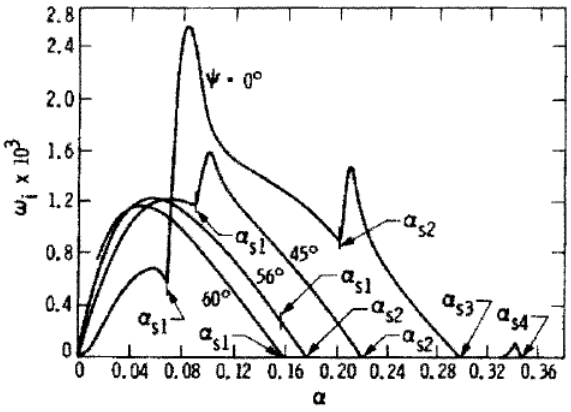

Figure 9.9: Temporal amplification rate as a function of wavenumber for 3D waves at $M_1 = 8.0$. Insulated wall, $T_1^* = 50$ K.

is removed, as it is for 3D waves, the amplification rates increase sharply. We may consider the 3D maximum amplification rate as the one that properly reflects the inherent instability of a given boundary-layer profile.

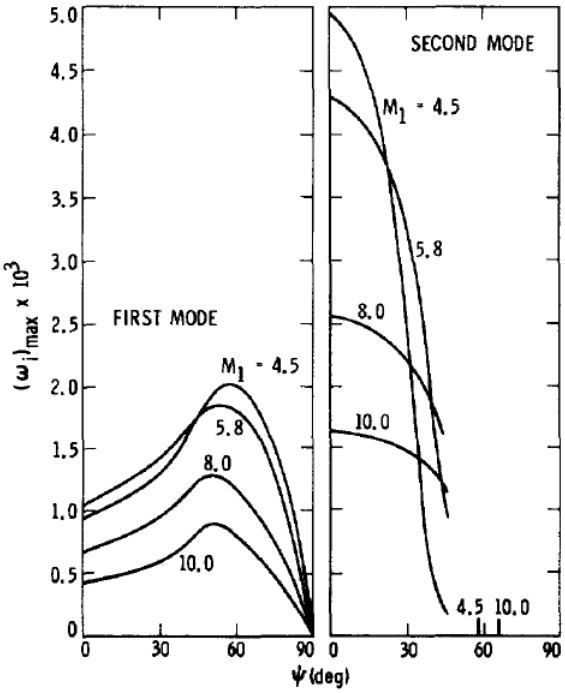

Figure 9.10: Effect of wave angle on maximum temporal amplification rate of first and second-modes at $M_1 = 4.5$, 5.8, 8.0 and 10.0. Insulated wall, wind-tunnel temperatures.

9.8 Effect of wall cooling

Perhaps the most celebrated result of the early stability theory for compressible boundary layers was the prediction by Lees (1947) that cooling the wall stabilizes the boundary layer. This prediction was made on the basis of the asymptotic theory, and a criterion was provided for the ratio of wall temperature to recovery temperature at which the critical Reynolds number becomes infinite. Although Lees's original calculations contained numerical errors, the temperature ratio for complete stabilization was later computed correctly by a number of authors. The most accurate calculations gave the result that complete stability can be achieved for $1 < M_1 < 9$ by sufficient cooling. These calculations can be criticized in three important respects: First, no indication is given as to how the amplification rate varies with wall temperature; second, the calculations are for 2D waves only; and third, no account is taken of the existence of the higher modes. In this Section we shall see that the current inviscid theory can remedy all of these deficiencies.

As the boundary layer is cooled a second generalized inflection point appears for $U < 1 - 1/M_1$. As the cooling progresses, this second inflection point moves towards the first one and then both disappear for highly cooled walls. The complete account, as given by Mack (1969), of how these two inflection points affect the instability of 2D and 3D waves is a lengthy one and also brings in unstable supersonic waves. The conclusion is that when the generalized inflection points disappear, so do the first mode waves, but the higher modes, being dependent only on a relative supersonic region, remain. Some results are shown in Fig. 9.12, where the ratio of the maximum temporal amplification rate to its uncooled value is plotted against the ratio of wall temperature, T_w, to recovery temperature, T_r, at $M_1 = 3.0$, 4.5, and 5.8 for 3D first-mode waves, and at $M_1 = 5.8$ for 2D second-mode waves. In each instance, the wave angle given in the figure is the most unstable. The first-mode waves, even when oblique, can be completely stabilized at the Mach numbers

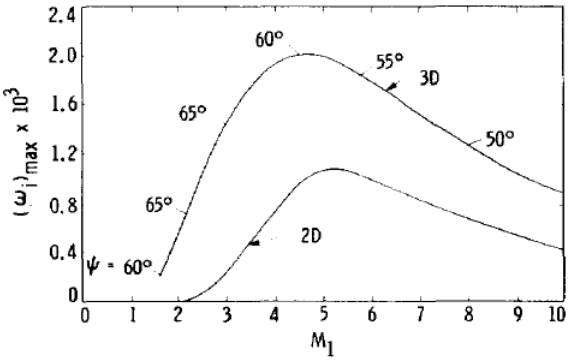

Figure 9.11: Effect of Mach number on maximum temporal amplification rates of 2D and 3D first-mode waves. Insulated wall, wind-tunnel temperatures.

shown, just as originally predicted by Lees (1947). However, the second mode is not only not stabilized, it is actually destabilized, although if the amplification rate is based on the boundary-layer thickness, the increase in ω_i is just about compensated for by the reduction in y_δ and $\omega_i y_\delta$ is virtually unchanged by cooling.

As a final result on the effect of cooling, we give Fig. 9.13 which shows the temporal amplification rate at $M_1 = 10$ as a function of wavenumber for an insulated wall and a highly-cooled wall ($T_w/T_r = 0.05$). For the former, the first four modes are merged to form a single unstable region, and the limiting upper wavenumber is the exceptional wavenumber of Fig. 9.2. For the latter, the unstable regions of the four modes are separate, as is true at lower Mach numbers for an insulated wall, and the maximum amplification rate of each mode is about double the uncooled value.

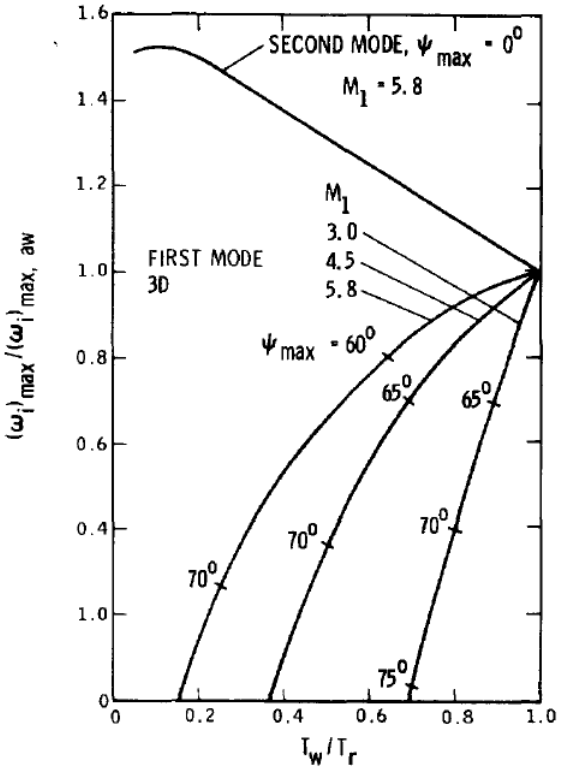

Figure 9.12: Effect of wall cooling on ratio of maximum temporal amplification rate with respect to both frequency and wave angle of first and second modes at $M_1 = 3.0$, 4.5, and 5.8 to insulated-wall maximum amplification rate. Wind-tunnel temperatures.

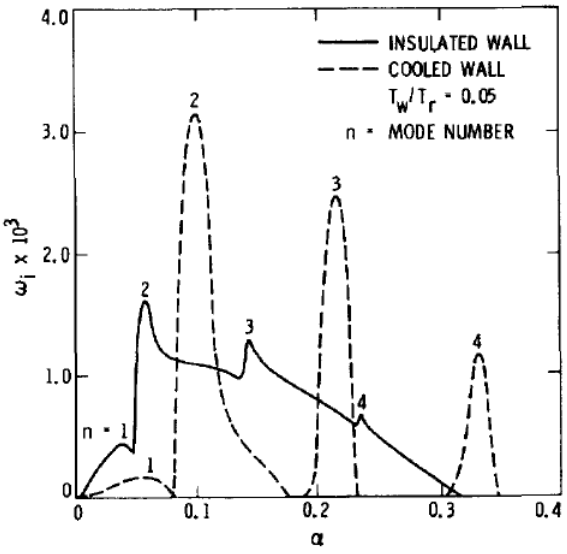

Figure 9.13: Effect of extreme wall cooling on temporal amplification rates of 2D wave for first four modes at $M_1 = 10$, $T_1^* = 50$ K: Solid line, insulated wall; Dashed line, cooled wall, $T_w/T_r = 0.05$.

Chapter 10

Compressible Viscous Theory

The early theoretical work on the viscous stability theory of compressible boundary layers was based on the asymptotic methods that had proven to be successful for incompressible flow. However, these theories, which were developed by Lees and Lin (1946), Dunn and Lin (1955), and Lees and Reshotko (1962), turned out to be valid only up to low supersonic Mach numbers. Some results for insulated-wall flat-plate boundary layers obtained with the asymptotic method are given in Fig. 10.1, and compared with direct numerical solutions of the eigenvalue problem. All numerical results in this Section are for the same family of flat-plate boundary layers used in Section 9. In Fig. 10.1 neutral-stability curves of frequency at $M_1 = 1.6$ and 2.2 as computed from the Dunn-Lin 1955 theory by Mack (1960) are compared with results obtained by numerical integration using both the sixth-order simplified equations of Dunn and Lin, and the sixth-order constant Prandtl number version of the complete stability equations of Appendix A. At $M_1 = 1.6$, the three calculations are in good agreement for $R > 700$, but at $M_1 = 2.2$, the agreement between the Dunn-Lin theory and the numerical solution with the complete equations is poor at all Reynolds numbers. The asymptotic theory is supposed to solve the simplified equations with an error no larger than the error involved in dropping the missing viscous terms. It is evident from the numerical solutions of the Dunn-Lin equations in Fig. 10.1, that the equations are better than the method used to solve them, but even so at $M_1 = 2.2$ the differences compared to the complete equations are too large to permit their use. However, there is little reason in any case to use these equations in numerical work, because they are of the same order as the complete 2D equations, and for 3D waves the sixth-order approximation given in this Section is more accurate.

10.1 Effect of Mach number on viscous instability

The viscous theory must of course be used for all numerical calculations at finite Reynolds numbers. An important theoretical question that we are able to answer with the viscous theory is the influence of Mach number on viscous instability. The definition of viscous instability that we use here for classification purposes is that the maximum amplification rate increases as the Reynolds number decreases. The maximum is with respect to frequency, and also wave angle for 3D waves, at constant Reynolds number, and the amplification rate is referenced to L^* [Eq. 2.57]. A neutral-stability curve with an upper-branch wavenumber which increases with decreasing Reynolds number, as for the Blasius boundary layer, is an indicator of viscous instability. We start by examining the curves of neutral stability for 2D waves presented in Fig. 10.2, where at five Mach numbers the wavenumber is plotted against $1/R$ to emphasize the higher Reynolds number region. The neutral curve at $M_1 = 1.6$ is of the same general type as for a low-speed boundary layer with only viscous instability. The low values of the neutral wavenumbers reflect a drastic weakening of viscous instability compared to the Blasius boundary layer. We already know from Fig. 9.6 that the maximum inviscid amplification rate increases sharply for $M_1 > 2.2$. What we see in Fig. 10.2 is that as the Mach number increases above 1.6, viscous instability continues to weaken and the effect of the increasing inviscid instability extends to lower and lower Reynolds numbers. Finally, at $M_1 = 3.8$ the influence of inviscid instability is dominant at all Reynolds numbers, and no trace of viscous instability can be seen. Viscosity acts only to damp out the inviscid instability, just as for the low-speed Falkner-Skan boundary layers with a strong adverse pressure gradient. As a result, the instability characteristics of flat-plate boundary layers

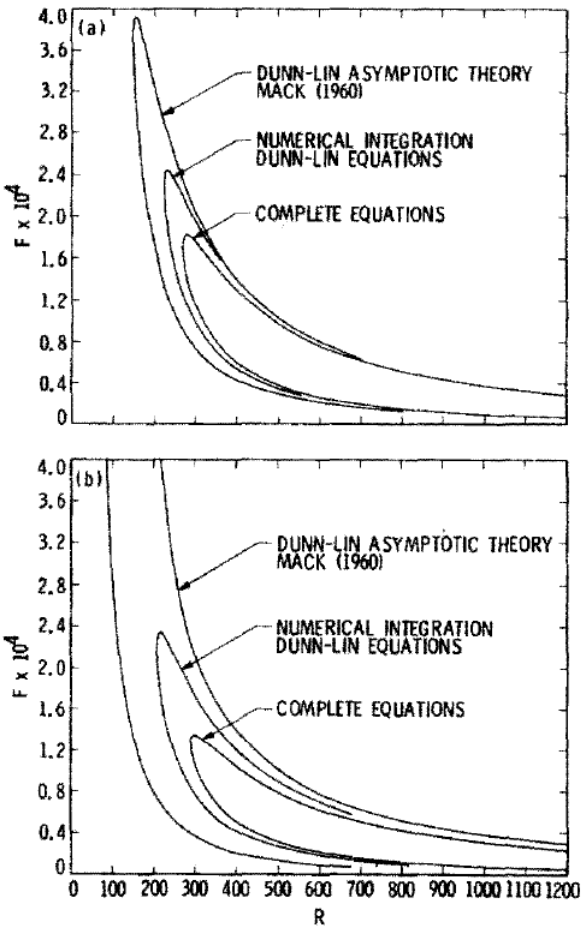

Figure 10.1: Comparison of neutral-stability curves of frequency at (a) $M_1 = 1.6$ and (b) $M_1 = 2.2$. Insulated wall, wind-tunnel temperatures.

above $M_1 = 3$ are more like those of a free shear layer than of a low-speed zero pressure-gradient boundary layer.

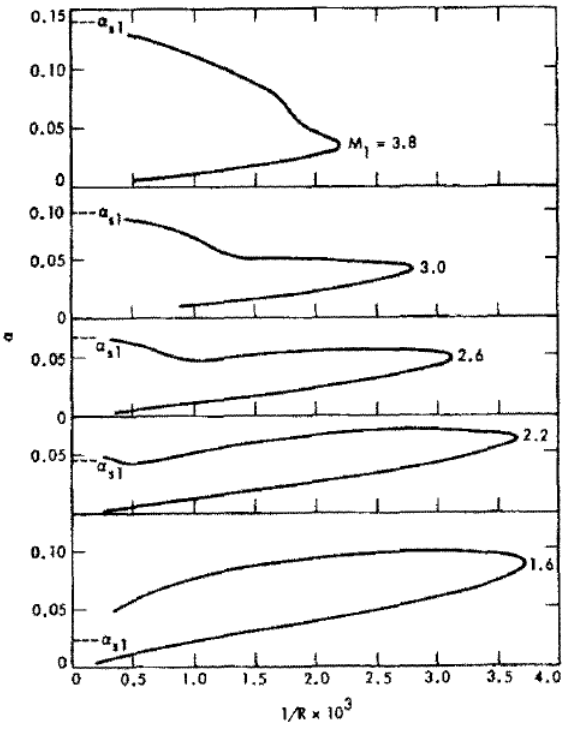

Figure 10.2: Effect of Mach number on 2D neutral-stability curves of wavenumber. Insulated wall, wind-tunnel temperatures.

We have learned in Section 9 that 2D amplification rates above $M_1 = 1$ are strongly influenced by the constraint of the sonic limit on the phase velocity, and do not represent the true instability of a boundary-layer profile. Therefore, to get a complete view of the influence of Mach number on viscous instability we must turn to 3D waves. The instability of 2D and 3D waves up to $M_1 = 3.0$ is summarized in Fig. 10.3, where the maximum temporal amplification rate is given at $M_1 = 1.3$, 1.6, 2.2, and 3.0 as a function of Reynolds number up to $R = 2000$. The most unstable wave angles (to within 5°) of the 3D waves are shown in the figure. It is apparent that these angles differ little from the inviscid values except near the critical Reynolds number at $M_1 = 1.3$. We see that viscous instability, which at $M_1 = 1.3$ is totally responsible for both 2D and 3D instability at the Reynolds numbers of the figure, decreases with increasing M_1 for 3D as well as for 2D waves. However, there is little change in the maximum 3D amplification rate with increasing Mach number, in contrast to the large decrease in the maximum 2D amplification rate. At $M_1 = 3.0$, viscosity acts only to maintain the maximum amplification rate at about the same level down to low Reynolds numbers, rather than as the main source of instability as at lower Mach numbers.

There are unfortunately no calculations available between $M_1 = 3.0$ and 4.5, but the distribution with Reynolds number of the maximum temporal amplification rate is given in Fig. 10.4 at $M_1 = 4.5$, 5.8, and 7.0 for wave angles that are approximately the most unstable. All of these waves are first-mode waves. At $M_1 = 10$ it is difficult to assign a maximum in the first-mode region as the single peak in the ω_i vs α curves for $\psi > 50°$ occurs near the transition from the first to the second mode, and 55° has been rather arbitrarily selected as the most unstable angle. In any case, it is clear from Fig. 10.4 that in this Mach number range there is no viscous instability and the influence of viscosity is only stabilizing.

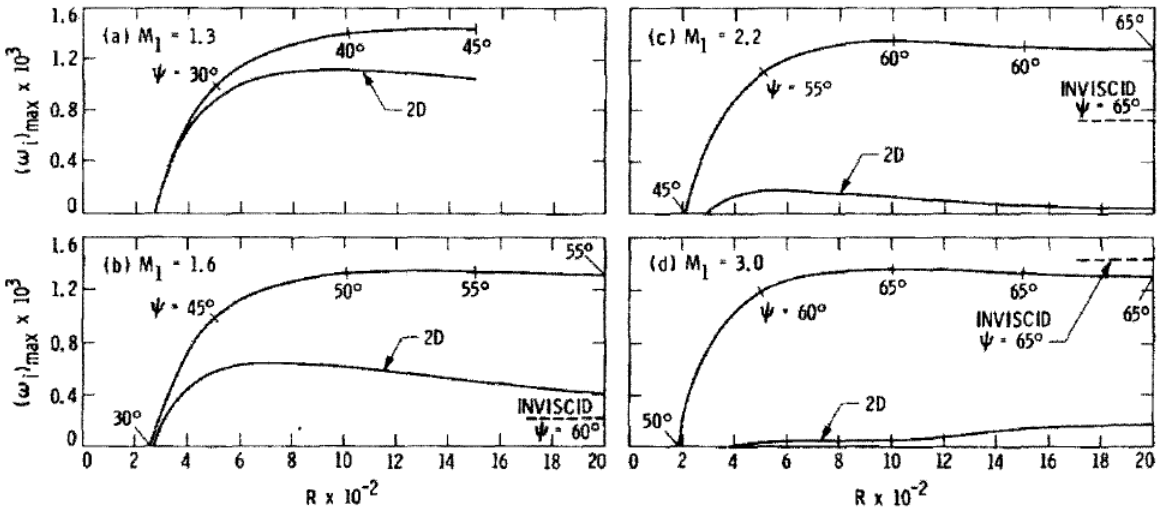

Figure 10.3: Distribution of maximum temporal amplification rate with Reynolds number at (a) $M_1 = 1.3$, (b) $M_1 = 1.6$, (c) $M_1 = 2.2$ and (d) $M_1 = 3.0$ for 2D and 3D waves. Insulated wall, wind-tunnel temperatures.

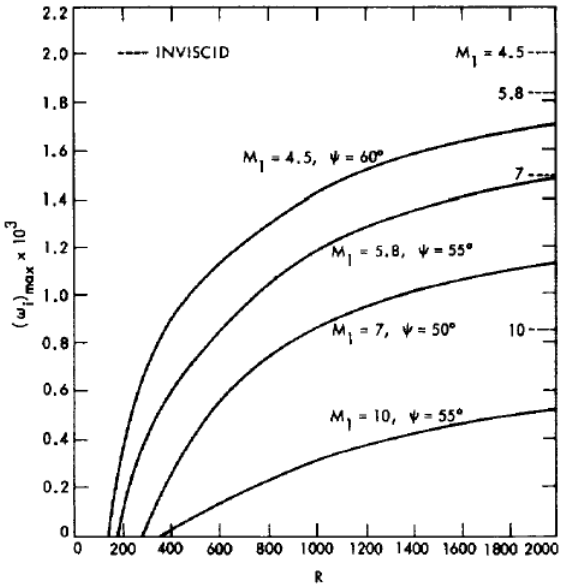

Figure 10.4: Distribution of maximum first-mode temporal amplification rates with Reynolds number at $M_1 = 4.5$, 5.8, 7.0 and 10.0. Insulated wall, wind-tunnel temperatures.

10.2 Second mode

The lowest Mach number at which the unstable second mode region has been located at finite Reynolds numbers is $M_1 = 3.0$, where the minimum critical Reynolds number R_{cr} is 13,900 (Mack, 1984b). As the Mach number increases, the inviscid second-mode maximum amplification rate increases, as shown in Fig. 9.6, and the unstable second-mode region moves rapidly to lower Reynolds numbers. At $M_1 = 3.8$, R_{cr} is 827; at $M_1 = 4.2$ it is 355; and at $M_1 = 4.5$ it is 235. Furthermore, the first and higher-mode unstable regions go through the same process of successive mergers as they do in the inviscid theory. The first merger, between the first and second-mode unstable regions, takes place at about $M_1 = 4.6$. Examples of neutral-stability curves of wavenumber just before merger ($M_1 = 4.5$), and just after merger ($M_1 = 4.8$), are shown in Fig. 10.5. The shapes of the neutral-stability curves, both before and after merger, are such as to suggest that viscosity is only stabilizing for all higher modes, and this is confirmed for the 2D second mode by Fig. 10.6, where the distribution of $(\omega_i)_{\max}$ with Reynolds number is shown for $M_1 = 4.5$, 5.8, 7.0, and 10.0.

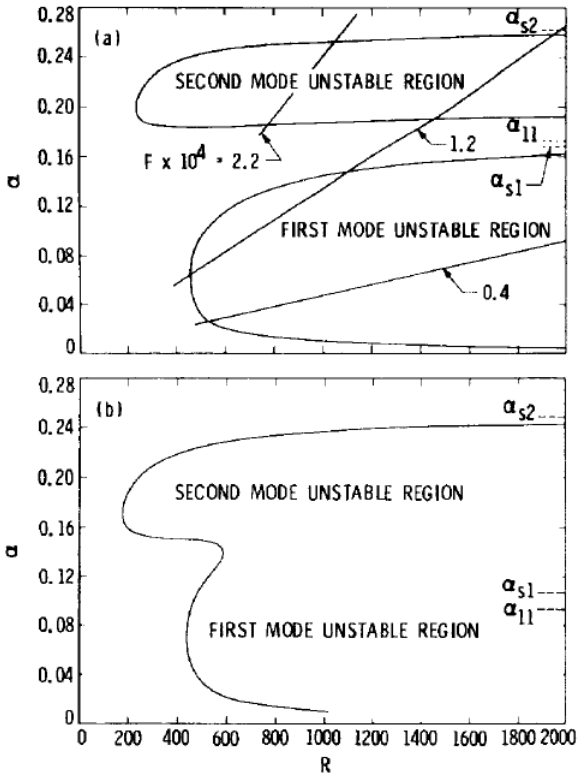

Figure 10.5: Neutral-stability curves of wavenumber for 2D first and second-mode waves at (a) $M_1 = 4.5$ and (b) $M_1 = 4.8$. Insulated wall, wind-tunnel temperatures.

The effect of wave angle on second-mode amplification rates is shown in Fig. 10.7, where $(\omega_i)_{\max}$ is plotted against wave angle for the same Mach numbers as in Fig. 10.6. This figure is to be compared with the comparable inviscid results in Fig. 9.10. In both instances, increasing Mach number brings a reduction in the rapidity with which the maximum amplification falls off with increasing wave angle.

10.3 Effect of wall cooling and heating

Few results have been computed from the viscous theory for boundary layers with cooled and heated walls. One result, shown in Fig. 10.8, gives the effect of heating and cooling on the stability of a low-speed boundary

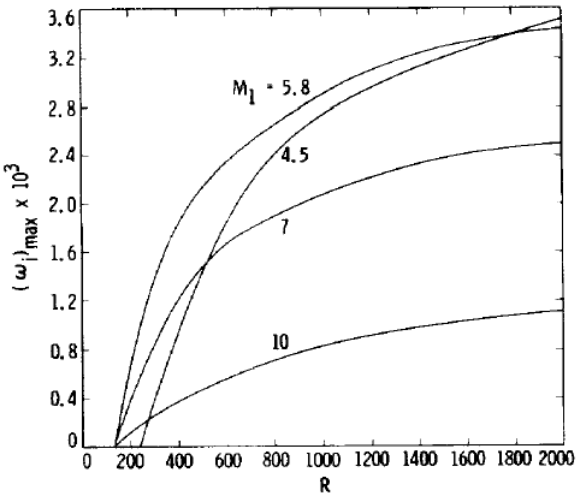

Figure 10.6: Effect of Reynolds number on maximum second-mode temporal amplification rate at $M_1 = 4.5$, 5.8, 7.0 and 10.0. Insulated wall, wind-tunnel temperatures.

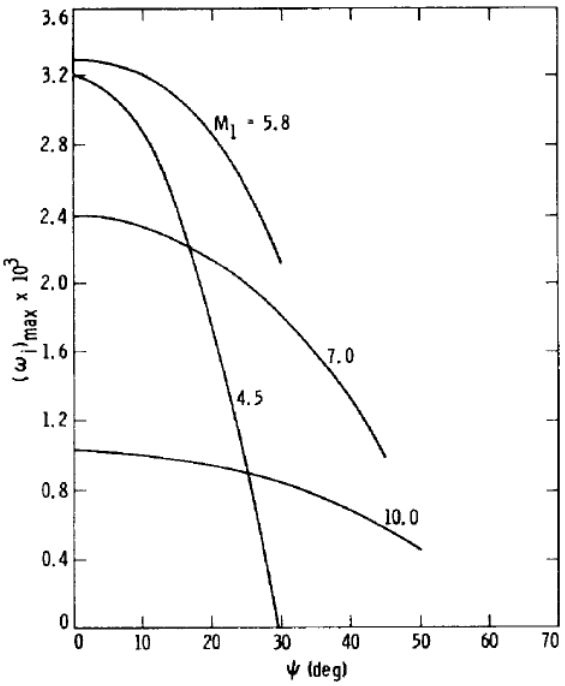

Figure 10.7: Effect of wave angle on second-mode temporal amplification rates at $R = 1500$ and $M_1 = 4.5$, 5.8, 7.0 and 10.0. Insulated wall, wind-tunnel temperatures.

layer ($M_1 = 0.05$). The x-Reynolds numbers of 2D normal modes for three constant values of the N factor, $\ln(A/A_0)_{\max}$, are plotted against the wall temperature ratio T_w/T_r. We see that cooling has a strong stabilizing effect, and that heating has a strong destabilizing effect. The frequencies that correspond to the N factors are also strongly affected by the wall temperatures. For example, at $T_w/T_r = 0.90$, the frequency for $N = 9$ is $F = 0.157 \times 10^{-4}$; at $T_w/T_r = 1.15$, it is $F = 0.445 \times 10^{-4}$.

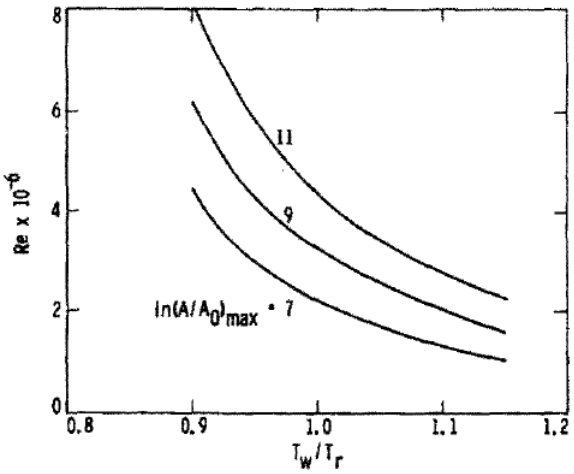

Figure 10.8: Effect of wall cooling and heating on Reynolds number for constant $\ln(A/A_0)_{\max}$ at $M_1 = 0.05$.

As an example of the effect of wall cooling at hypersonic speeds, Fig. 10.9 shows 2D neutral curves at $M_1 = 5.8$ for $T_w/T_r = 1.0$, 0.65, 0.25, and 0.05. The freestream temperature is 50 K except for the lowest wall temperature where it is 125 K. When the wall is cooled to $T_w/T_r = 0.65$, a noticeable stabilization takes place for the first-mode, but only a narrowing of the unstable wavenumber band can be detected in the second-mode region. At the other two temperature ratios, there is no unstable first-mode region. The lowest temperature ratio is of interest because there is no generalized inflection point in the boundary layer, and thus no α_{s2} to serve as the limit of the upper branch of the neutral curve. We may observe that the wavenumbers at the critical Reynolds numbers of the three cooled cases are in the inverse proportion 1.0:0.71:0.48, and the corresponding boundary-layer thicknesses are in the proportion 1.0:0.69:0.53. Consequently, the length scale is the controlling factor in the location of the second-mode unstable region in terms of wavenumber.

10.4 Use of sixth-order system for 3D waves

We have already noted in Section 8.5 that only a single dissipation term couples the energy equation 8.9e to the other equations for a 3D wave in either a 2D or 3D boundary layer, and mentioned the economy measure proposed by Mack (1969) of using the sixth-order system that results from neglecting this term for 3D waves. These equations are essentially the 2D equations in the direction of k. In Table 10.1 the temporal amplification rates computed from the sixth- and eighth-order systems are compared for various wave angles and Reynolds numbers at five Mach numbers. In all cases the waves are close to the most unstable first-mode waves at the particular Mach and Reynolds numbers listed. We see that the sixth-order system is surprisingly good, and can be used at $R = 1500$ for all Mach numbers with a maximum error of less than 5%. The error of the sixth-order system, which depends not only on the Mach and Reynolds number, but also on the wave angle, is usually minimal up to about $\psi = 30°$ and can become large for $\psi > 70°$.

There are three other dissipation terms in the energy equation besides the coupling term, and their effect on the amplification rate has also been examined by Mack (1969) at $R = 1500$ and $M_1 = 2.2$, 5.8, and 10.0. The wavenumbers were the same as in Table 10.1. At $M_1 = 2.2$, the coupling term has the largest influence on the amplification rate. However, at the two higher Mach numbers the other terms increase in importance. Since some terms are stabilizing and others destabilizing, the error with all dissipation terms zero is smaller

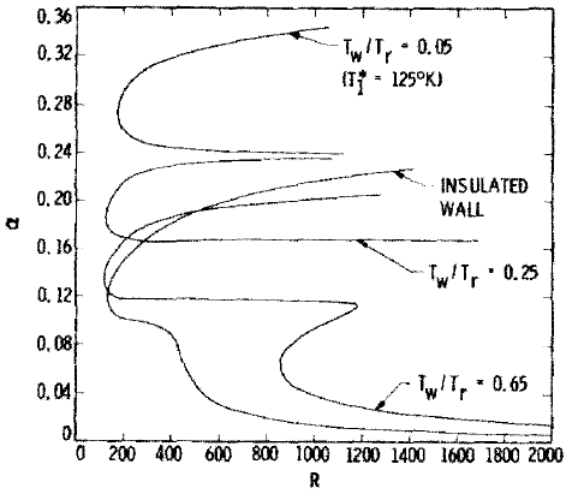

Figure 10.9: Effect of wall cooling on 2D neutral-stability curves at $M_1 = 5.8$, $T_1^* = 50$ K.

Table 10.1: Comparison of temporal amplification rates for 3D waves as computed from sixth-order and eighth-order systems of equations at several Mach numbers

M_1	R	α	ψ	$\omega_i \times 10^3$ 6th order	$\omega_i \times 10^3$ 8th order	% difference
1.3	500	0.075	45°	0.883	0.824	7.2
1.3	1500	0.060	45°	1.467	1.445	1.5
1.6	500	0.070	55°	0.974	0.874	11.4
1.6	1500	0.050	55°	1.384	1.346	2.8
2.2	500	0.055	60°	1.198	1.066	12.4
2.2	800	0.045	60°	1.391	1.300	7.0
2.2	1500	0.035	60°	1.325	1.273	4.1
4.5	500	0.045	60°	1.117	1.039	7.5
4.5	1500	0.050	60°	1.641	1.613	1.7
5.8	500	0.050	55°	0.790	0.736	7.3
5.8	1500	0.060	55°	1.403	1.384	1.4
10.0	1500	0.040	55°	0.444	0.434	2.3

at these two Mach numbers than with only the coupling term zero. It is not known how general this result is, but experience with the Dunn-Lin equations indicates that it is limited to waves with ψ well away from zero.

The small effect of the dissipation terms on the amplification rates of the 3D waves in the above-mentioned calculations is in distinct contrast to what happens when the Dunn-Lin equations are used for 2D waves. The sixth-order system with only the coupling term zero is exact for $\psi = 0$, unlike the Dunn-Lin equations where all of the dissipation terms are neglected along with a number of other terms that are supposed to be of the same order. The differences between the neutral-stability curves in Fig. 10.1 computed directly from the Dunn-Lin equations and those computed from the complete equations testify to the importance of the neglected terms. A calculation at $M_1 = 2.2$ and $R = 600$ for $\alpha = 0.045$ gave the result that the maximum 2D amplification rate from the Dunn-Lin equations is 63% larger than when computed from the complete equations. A more favorable result is obtained at this Mach number for a 60° wave with $\alpha = 0.045$ at $R = 1000$, where the Dunn-Lin equations give an amplification rate that is 15% too high. This is an improvement over the 2D results, but still not as good as the result obtained when only the coupling term is neglected. At $M_1 = 4.5$ and $R = 1500$, the amplification rate of the most unstable first-mode wave computed from the Dunn-Lin equations is in error by 23%; the error for the most unstable (2D) second-mode wave is 14%. The conclusion to be drawn is that the Dunn-Lin approximation is too severe, and the equations are unsuitable for numerical work above about $M_1 = 1.6$. On the contrary, the sixth-order system with only the coupling term neglected can be used for numerical computations where high accuracy is not important, and they offer a substantial saving in computer time and expense.

10.5 Spatial theory

Both the theoretical and numerical aspects of the stability of compressible boundary layers were worked out almost completely on the basis of the temporal theory. In contrast, almost all stability calculations are now routinely done with the spatial theory. Two exceptions are the SALLY (Srokowski and Orszag, 1977) and COSAL (Malik and Orszag, 1981) codes for 3D boundary-layer stability, which calculate eigenvalues from the temporal theory and use the 3D Gaster transformation to convert to spatial eigenvalues. This approach, which introduces a small error into the calculation has the advantage of allowing the use of powerful matrix methods. The COSAL code exploits this possibility by providing a global eigenvalue search which relieves the user from the necessity of making an initial eigenvalue guess.

Some of the extensive temporal calculations of Mack (1969) have been recalculated by El-Hady and Nayfeh (1979) using the spatial theory. All findings were in accord with the temporal calculations. A recent series of spatial calculations by Wazzan et al. (1984) found important differences with the calculations of Mack, but there is good reason to believe that the new calculations are not correct (Mack, 1984b).

As an example of the same calculation performed with the temporal and spatial theories, Figs. 10.10 and 10.11 give the respective maximum amplification rates of the most unstable first and second-mode waves at $R = 1500$ as a function of freestream Mach number. The differences between the temporal and spatial first-mode curves are due to the increase in the group velocity from about 0.4 at $M_1 = 0$ to near 1.0 at high Mach number. However, both curves reflect the fact that at first increasing Mach number brings a reduction in the maximum amplification rate because of the weakening of viscous instability, then the increasing inviscid instability becomes dominant, and finally the increasing boundary-layer thickness causes a proportionate reduction in the amplification rate. Furthermore, it is important to keep in mind that both the spatial theory and the temporal theory plus the Gaster transformation give almost identical values of the amplitude ratio, and so either can be used in transition-prediction calculations.

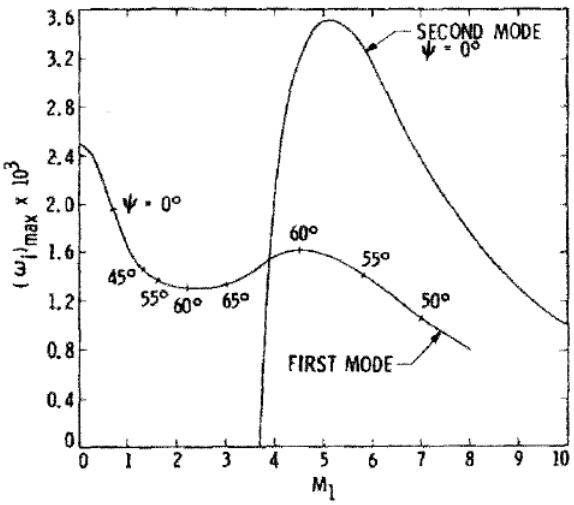

Figure 10.10: Effect of Mach number on the maximum temporal amplification rate of first and second-mode waves at $R = 1500$. Insulated wall, wind-tunnel temperatures.

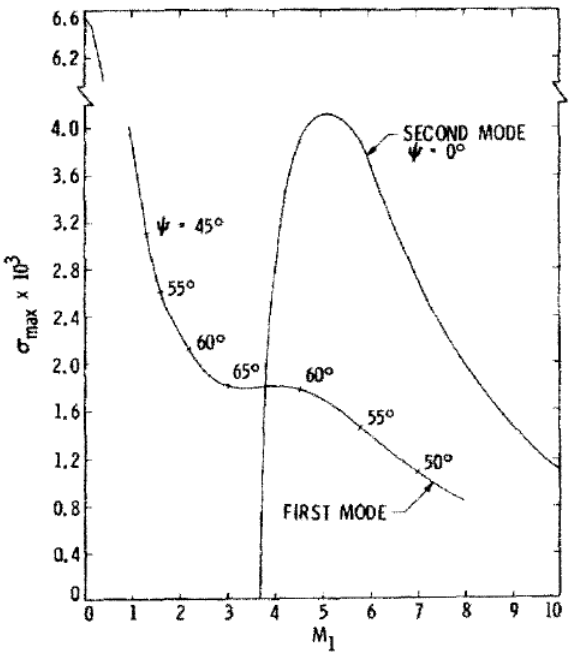

Figure 10.11: Effect of Mach number on the maximum spatial amplification rate of first and second-mode waves at $R = 1500$. Insulated wall, wind-tunnel temperatures.

Chapter 11

Forcing Theory

11.1 Formulation and numerical results

The structure of linear stability theory allows the forced response of the boundary layer on a flat plate to a particular type of external disturbance field to be readily obtained (Mack, 1971, 1975). One of the independent solutions of the stability equations in the freestream is, for $\alpha_i = 0$ and in the limit of large Reynolds number, the inviscid flow over an oblique wavy wall of wavelength $2\pi/\alpha$ moving with the velocity c. The time-independent part of the pressure fluctuation given by this solution is [Eq. 9.11]

$$p = i\gamma M_1 \left(\alpha - \omega\right) e^{\left(i\alpha\left[x \mp \left(\overline{M}_1^2 - 1\right)^{1/2} y\right]\right)} \tag{11.1}$$

For a wave which is oblique to the freestream, α and $\overline{M}_1$ are taken in the direction normal to the constant phase lines in the x,z plane. It is seen from Eq. 11.1 that when $\overline{M}_1 > 1$, the constant phase lines in the x,y plane are Mach waves. With the negative sign in Eq. 11.1, the Mach waves are outgoing, i.e., energy is transported in the direction of increasing y; with the positive sign, the Mach waves are incoming. When $\overline{M}_1 < 1$, the solution with the upper sign decays exponentially upward, and the other solution increases exponentially upward. In stability theory, only solutions which are at least bounded as $y \to \infty$ are permitted, but no such restriction is present in the forcing theory where the incoming wave has been produced elsewhere in the flow. The full viscous counterpart of Eq. 11.1 for an incoming wave has a slow exponential increase upward, which is perfectly acceptable.

The incoming-wave solution bears some resemblance to a Fourier component of the sound field radiated from turbulent boundary layers at high supersonic speeds according to the theory of Phillips (1960). In this theory, each acoustic Fourier component α, β is produced by the same Fourier component of the frozen turbulent field moving at a supersonic source velocity c relative to the freestream. Thus the turbulent boundary layer is decomposed into oblique wavy walls moving supersonically, and the associated outgoing Mach waves are the incoming Mach waves of the receiving laminar boundary layer at $y = 0$. However, in Phillips' theory, the field is random, and each "wavy wall" exists for only a finite time related to the lifetime of an individual turbulent eddy. In the present theory, the incoming wave field is steady to an observer moving with c.

A solution for the boundary-layer response at each Reynolds number can be found for each α, β and c by using both inviscid solutions of the eighth-order system, Eqs. 8.11, together with the usual three viscous solutions which go to zero as $y \to \infty$, to satisfy the boundary conditions as $y = 0$. The combined solution, in addition to giving the boundary-layer response which results from the incoming acoustic wave, also provides the amplitude and phase of the outgoing, or reflected, wave relative to the incoming wave. The combined, or response, wave is neutral in the sense of stability theory, but its amplitude in the boundary layer is a function of Reynolds number. If the local mass-flow fluctuation amplitude $m(y)$ is chosen to represent the amplitude (a hot-wire anemometer measures primarily m), the ratio of m_p, the peak value of $m(y)$, to m_i, the massflow fluctuation of the incoming wave, can be called A/A_1, and used in a manner similar to the amplitude ratio A/A_0 of an instability wave. An increase in m_p/m_i with increasing R represents an "amplification"; a decrease, a "damping".

The most important result of the forcing theory is shown in Fig. 11.1, where m_p/m_i from the viscous theory is plotted against Reynolds number for waves of six dimensionless frequencies in an insulated-wall, flat-plate boundary layer at $M_1 = 4.5$. The waves are 2D, and the phase velocity has been assumed to be $c = 0.65$. We see that the amplitude of each wave starts to grow at the leading edge, reaches a peak at a Reynolds number that varies inversely with frequency, and then declines. The lower the frequency, the higher the maximum value of m_p/m_i. This is the principal result of the forcing theory, and has been found to be true for all boundary layers and all waves regardless of the wave angle and the phase velocity (provided only that $\overline{M}_1 > 1$). As a consequence of this behavior, the forcing mechanism provides boundary-layer waves with amplitudes from 6-14 times as large as freestream sound waves without any instability amplification.

In the inviscid theory, once c and ψ have been specified the only remaining parameter is α. When the mass-flow fluctuation amplitude ratio is plotted against α for a 2D wave with $c = 0.65$ and the same boundary layer as in Fig. 11.1, the inviscid theory gives a result that is significantly different from the viscous theory. Since $F = \alpha c/R$, a wave of given dimensionless frequency F travelling downstream at a constant c will have its dimensionless wavenumber increase linearly with R. Consequently, the α axis is equivalent to the R axis in Fig. 11.1. What we find from the inviscid theory is that inviscid waves decrease in amplitude for $\alpha > 0.0075$. All of the amplitude peaks in Fig. 11.1 occur at an α larger than this except for the lowest frequency. Consequently, the initial growth of Fig. 11.1, which is just what is found in experiments in supersonic and hypersonic wind tunnels with turbulent boundary layers on the tunnel walls, is purely a viscous phenomenon. However, when the viscous response curves from Fig. 11.1 are also plotted against α, they show that the decrease in amplitude which follows the region of growth in Fig. 11.1 is described closely by the inviscid theory. This result is in contrast to stability theory, where the inviscid amplification and damping rates are only approached by the viscous theory in the limit $R \to \infty$. The higher the frequency, the lower the Reynolds number at which the viscous curve joins the inviscid curve.

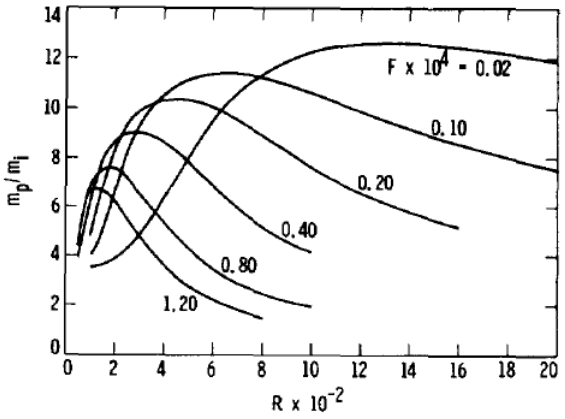

Figure 11.1: Peak mass-flow fluctuation as a function of Reynolds number for six frequencies. Viscous forcing theory; $M_1 = 4.5$, $\psi = 0°$, $c = 0.65$, insulated wall.

11.2 Receptivity in high-speed wind tunnels

The quantity m_p/m_i, interpreted as A/A_1, is the most important result in supersonic and hypersonic wind tunnels. It provides an essential piece of information which has been missing up to now: the relation of the amplitude of a boundary-layer wave to the amplitude of the freestream wave which causes it. In other words, we now have a solution to one particular receptivity problem. Strictly speaking, m_p is equivalent to the A of stability theory only when the m distribution is self-similar, but such is not always the case. However, this situation is no different from the usual comparisons of the quasi-parallel stability theory with experiment, as in 7.5, where the peak m is followed downstream and identified with A even though the amplitude distributions are nonsimilar.

The major difficulty in using the forcing theory as a solution of the receptivity problem is that forced waves are distinct from free waves, and the process by which the former become the latter is unknown. An experiment by Kendall (1971) showed that, as measured by the phase velocity, a forced wave near the leading edge evolves into a free instability wave farther downstream. In the paper from which a portion of the text of this Section has been adapted (Mack, 1975), we assumed that the forcing theory applies up to the neutral-stability point of the particular frequency under consideration, and that stability theory applies downstream of that point. The conversion from one wave to the other would seem most likely to occur if the amplitude distribution through the boundary layer at the neutral-stability point matched the eigenfunction of the instability wave of the same frequency and wavelength. A limited number of calculations at $M_1 = 4.5$ show that the two distributions are indeed close together for the same F, α, and R. With the only mismatch between the two waves a phase-velocity difference of 20%, conversion of forced into free waves can be expected to take place quickly.

Consequently, with the approach just outlined the forcing theory can be used to calculate A_0/A_1, the ratio of the instability wave amplitude at the neutral point to the amplitude of the sound waves radiated by the turbulent boundary layer on the wind-tunnel wall. The subsequent ratio of the instability-wave amplitude to A_1 is found by multiplying A_0/A_1 by the usual amplitude ratio A/A_0 calculated from stability theory. Thus, with the forcing theory we can replace the previously unknown constant A_0 with a known frequency-dependent A_0.

11.3 Reflection of sound waves from a laminar boundary layer

A more straightforward use of the forcing theory is to calculate the reflection of a monochromatic sound wave from a boundary layer. Figure 11.2 gives the ratio A_r, the amplitude of the reflected wave, to A_i, the amplitude of the incoming wave, as a function of α for $c = 0.65$ and the same $M_1 = 4.5$ boundary layer used previously. Figure 11.3 gives the ratio of $\beta(0)$, the pressure fluctuation at the wall, to $\beta_i(0)$, the pressure fluctuation of the incoming wave at the position of the wall with no boundary layer present. In each figure the upper curve is the inviscid result, and the other curves are the viscous results for a series of frequencies.

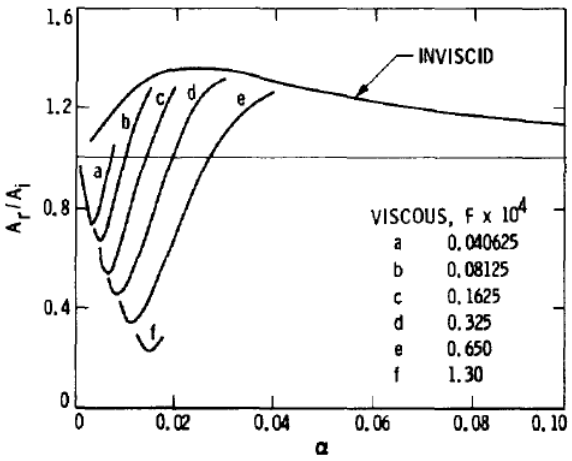

Figure 11.2: Ratio of amplitude of reflected wave to amplitude of incoming wave as function of wavenumber from viscous and inviscid theories; $M_1 = 4.5$, $\psi = 0°$, $c = 0.65$, insulated wall. $T_1^* = 311K$.

According to inviscid theory, when $\alpha = 0$, $A_r/A_i = 1.0$ and $\beta(0)/\beta_i(0) = 2.0$; when $\alpha \to \infty$, $A_r/A_i = 1.0$ and $\beta(0)/\beta_i(0) = 0$. Thus for $\alpha = 0$, the boundary layer effectively has zero thickness and the sound wave reflects as from a solid surface in the absence of a boundary layer. The reflected wave has the same amplitude and phase at $y = 0$ as the incoming wave so that the wall pressure fluctuation is twice $\beta_i(0)$. A the other limit, $\alpha \to \infty$, the boundary layer is infinitely thick compared to the wavelength, and the reflection is the same as from a constant-pressure surface. The amplitude of the reflected wave is again equal to that of the

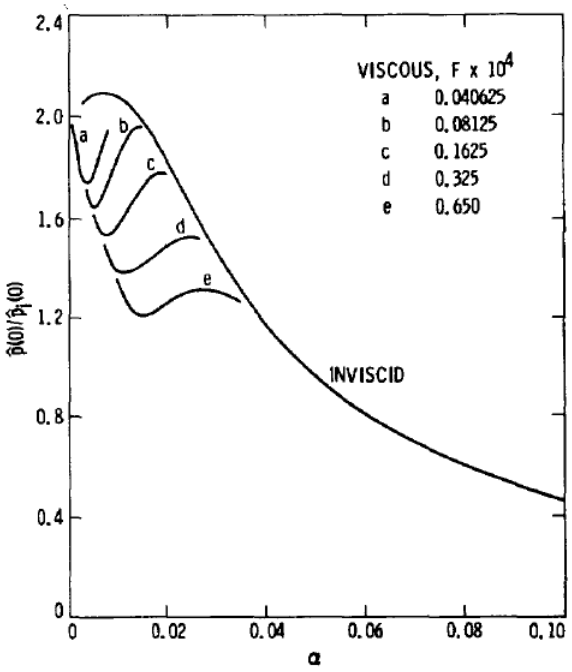

Figure 11.3: Ratio of wall pressure fluctuation to pressure fluctuation of incoming wave; $M_1 = 4.5$, $\psi = 0°$, $c = 0.65$, insulated wall. $T_1^* = 311K$.

incoming wave, but its phase at $y = 0$ differs by 180° from the incoming wave. Thus the pressure fluctuation at the wall is zero. Between these two limits, the amplitude of the reflected wave is always greater than the amplitude of the incoming wave.

The viscous results are quite different. For small α, A_r is always less than A_i. Furthermore, a minimum exists in A_r for each frequency. A similar minimum exists in $\beta(0)$, but it is located at a larger α than is the A_r minimum. If the A_r minimum were to reach zero, that particular α would constitute an instability eigenvalue for the family of incoming waves. However, in stability theory, this type of wave has not been encountered, either as a supersonic wave with $c < 1 - 1/M_1$ as in the present example, or as a subsonic wave with $c > 1 - 1/M_1$ where the amplitude increases exponentially with increasing y. Figure 11.2 indicates that if such an eigenvalue exists it would be at such a low Reynolds number to make the use of the quasi-parallel theory invalid.

When the incoming Mach waves of the external travelling sound field reflect from a solid surface in the absence of a boundary layer, there is no phase shift at the wall. Compression waves reflect as compression waves, and the reflected waves originate at the points where the corresponding incoming waves intersect the surface. However, when a boundary layer is present, there is a phase shift at the wall. Consequently, a reflected Mach wave of the same phase appears to originate at a distance Δ away from the point of intersection. This offset distance, expressed as a ratio to the boundary-layer thickness, is given by

$$\Delta^*/\delta = \frac{c}{FRy_\delta} \left[\theta_i(0) - \theta_r(0)\right], \tag{11.2}$$

where $\theta_i(0)$ is the phase (in radians) of the pressure fluctuation of the incoming wave at the wall, and $\theta_r(0)$ is the same quantity for the reflected wave. When the phase of the reflected wave lags the phase of the incoming wave, the reflected wave originates at a point downstream of the intersection with the incoming wave. When the phase difference is an integer multiple of π, the incoming wave reflects as a wave of the opposite sign at the point of intersection.

In Fig. 11.4, the ratio Δ^*/δ is given at $R = 600$ as a function of frequency for the same conditions as in Figs. 11.2 and 11.3. At only one frequency, $F = 0.975 \times 10^{-4}$, is the offset distance zero. For all smaller

frequencies, the phase of the reflected wave lags behind the phase of the incoming wave, and Δ^* is positive with a maximum of 4.5δ at $F = 0.08 \times 10^{-4}$. Because of the long wavelength at this frequency, this offset is only $0.077\lambda^*$, or 28° in phase. Offsets have been observed experimentally in unpublished measurements of Kendall. The measurements were made with a broad-band hot-wire signal, so no direct comparison with the single-frequency calculations is possible.

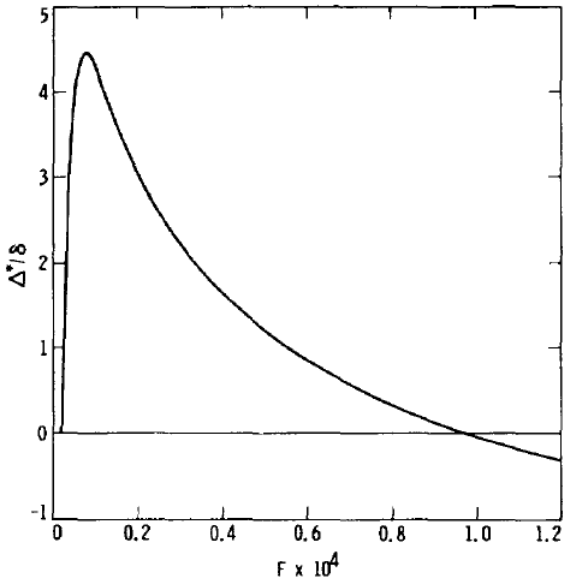

Figure 11.4: Offset distance of reflected wave as function of frequency at $R = 600$; $M_1 = 4.5$, $\psi = 0°$, $c = 0.65$, insulated wall. $T_1^* = 311K$.

11.4 Table of boundary-layer thicknesses

As a final item in Part B, we append Table 11.1 which gives the three common dimensionless boundary-layer thicknesses as functions of the freestream Mach number for the family of insulated-wall, flat-plate boundary layers for which numerical results have been given in Sections 9, 10, and 11. These quantities may be used to convert the α, σ, and R (all based on L^*) into, say, α_δ, σ_δ, and R_δ, based on δ. The conversion is achieved by multiplying α, σ, and R by y_δ.

Table 11.1: Dimensionless boundary-layer thickness ($U = 0.999$), displacement thickness and momentum thickness of insulated-wall, flat-plate boundary layers. (Wind-tunnel temperature conditions.)

M_1	y_δ	y^*_δ	y_θ
0	6.0	1.72	0.664
0.7	6.2	1.92	0.660
1.0	6.4	2.13	0.656
1.6	7.0	2.77	0.648
2.0	7.6	3.37	0.644
2.2	8.0	3.72	0.643
3.0	9.8	5.48	0.642
3.8	12.1	7.83	0.644
4.2	13.5	9.22	0.646
4.5	14.6	10.34	0.646
4.8	15.8	11.55	0.646
5.8	20.0	15.73	0.636
6.2	21.7	17.49	0.629
7.0	25.4	21.19	0.616
7.5	27.8	23.62	0.607
8.0	30.3	26.13	0.598
8.5	32.9	28.72	0.590
9.0	35.5	31.38	0.581
9.5	38.2	34.10	0.573
10.0	41.0	36.88	0.565

Part III

Three-Dimensional Boundary Layers

Chapter 12

Rotating Disk - A Prototype 3D Boundary Layer

Up to this point we have been concerned in the numerical examples exclusively with two-dimensional boundary layers, although the formulations of Chapters 2 and 8 are also valid for three-dimensional boundary layers. In the final three chapters we shall take advantage of this fact to present a number of results for 3D boundary layers. A fundamental difference between the stability of 3D and 2D boundary layers is that a 3D boundary layer is subject to crossflow instability. This type of instability, which cannot occur in a 2D boundary layer, is responsible for early transition on sweptback wings. Its essential features can best be introduced by studying the simple boundary layer on a rotating disk. This self-similar boundary layer of constant thickness was first used for this purpose by Gregory et al. (1955) in their classic paper on three-dimensional boundary-layer instability.

12.1 Mean boundary layer

The exact solution of the Navier-Stokes equations for a rotating disk was given by von Kármán (1921), and later and accurate numerical solution was worked out by Cochran (1934) and is given in Schlichting's (1979) book. We use the coordinate system r^*, θ, z^*, where r^* is the radius, θ is the azimuth angle, and z^* is in the direction of the angular velocity vector $\vec{\Omega}$. The radial, azimuthal and axial velocity components can be written

$$U^*(r^*, z^*) = \Omega^* r^* U(\zeta), \qquad V^*(r^*, z^*) = \Omega^* r^* V(\zeta), \qquad W^*(z^*) = \sqrt{\Omega^* \nu^*} W(\zeta). \tag{12.1}$$

The dimensionless velocity components U, V and W are functions only of the axial similarity variable

$$\zeta = \frac{z^*}{L^*}, \tag{12.2}$$

where

$$L^* = \sqrt{\frac{\nu^*}{\Omega^*}} \tag{12.3}$$

is the length scale. In terms of the length scale and the velocity scale $\Omega^* r^*$, the Reynolds number is

$$R = \frac{\Omega^* r^* L^*}{\nu^*} = \frac{r^*}{L^*}, \tag{12.4}$$

which is simply the dimensionless radial coordinate r. The Reynolds number based on the local azimuthal velocity and radius is

$$Re = \frac{\Omega^* r^{*2}}{\nu^*} = \left(\frac{r^*}{L^*}\right)^2. \tag{12.5}$$

Thus $R = \sqrt{Re}$, just as in the 2D boundary layers we have been studying. The displacement thickness of the rotating-disk boundary layer is $1.271 L^*$.

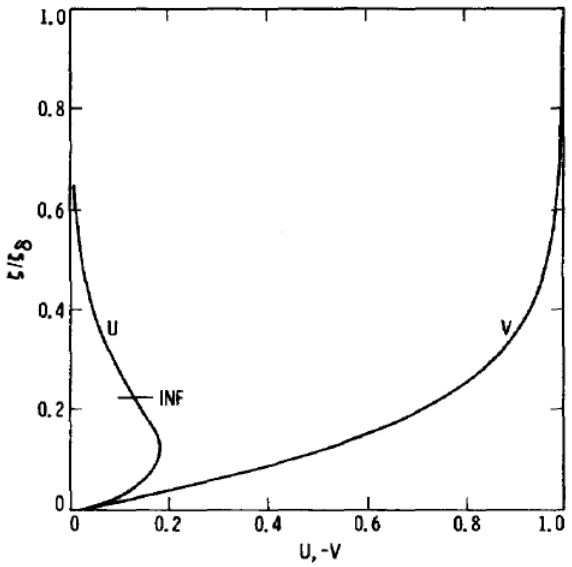

Figure 12.1: Rotating-disk boundary-layer velocity profiles.

The dimensionless azimuthal and radial velocity profiles in the coordinate system rotating with the disk are shown in Fig. 12.1 The azimuthal, or circumferential, profile is of the same type as in a 2D boundary layer with the velocity increasing monotonically from the surface to the outer flow, and it will be referred to as the streamwise profile. With the disk rotating in the direction of positive θ (counterclockwise), the outer flow relative to the disk is in the negative (clockwise) direction. The radial profile is of a type that cannot occur in a 2D boundary layer. The velocity, directed outward from the disk center, is zero both at the wall and in the outer flow, so that there is of necessity and inflection point, which is located at $\zeta = 1.812$, where $U = 0.133$ and $V = -0.760$. The radial velocity, being normal to the streamwise flow, is by definition the crossflow velocity. The maximum radial velocity of $U_{\max} = 0.181$ is located at $\zeta = 0.934$, where $V = -0.496$.u

12.2 Crossflow instability

The phenomenon of crossflow instability was discovered during early work on the flow over swept-back wings. Transition in flight tests was observed by Gray (1952) to occur near the leading edge at abnormally low Reynolds numbers compared to an unswept wing. Flow visualization revealed that the wing surface before transition was covered with closely-spaced parallel streaks in the direction of the local potential flow, as shown in Fig. IX.20 of the review article by Stuart (1963). The streaks were fixed to the wing, and, once formed, did not change with time. They were conjectured to be the result stationary vortices in the boundary layer. This same phenomenon was demonstrated by Gregory et al. (1955) to exist on a rotating disk. The streaks were found by the china-clay technique to take on the form of logarithmic spirals at an angle of about 13° to 14° to the circumferential circumferential direction [see frontispiece of Rosenhead (1963)], with the radius of the spiral decreasing with increasing angle θ. As in the wing experiment, the streak pattern was fixed to the surface, and so could be photographed at the conclusion of the experiment with the disk at rest.

Stuart (Gregory et al., 1955) used an order-of-magnitude argument to reduce the exact linearized Navier-Stokes equations for a rotating disk to the fourth-order Orr-Sommerfeld equation for the determination of eigenvalues. In this case, as we have already discussed in Section 2.4.1, the 3D stability problem reduces to a 2D stability problem for the velocity profile in the direction of the wavenumber vector. Since the velocity profile in a 3D boundary layer, unlike a 2D boundary layer, depends on the direction, there is a different stability problem to solve for each wave direction. The circumferential profile has only viscous instability, and is much too stable to have anything to do with the observed instability phenomena. The radial velocity profile, on the contrary, has inviscid instability because of the inflection point. As the inflection point is

located well away from the disk surface, we can expect there to be a strong instability.

In addition to the inflectional radial profile, there is a whole family of profiles in directions close to the radial which also have inflection points. Stuart noted that for the velocity profile at an angle of $\varepsilon = 13.2°$, where ε is measured from the radius in the positive θ direction, the inflection point is located where the magnitude of the velocity is zero. Consequently, according to the Rayleigh theorem, which was shown to still be valid for this type of profile, a stationary neutral normal mode (phase velocity $c = 0$) can exist with a wave angle equal to ε. Stuart also showed by calculating streamlines in the plane of ζ and the wavenumber vector for the rotating disk with large suction that the stationary inviscid disturbance consists of a system of vortices close to the surface, all rotating in the same direction (clockwise, looking along the spiral towards the disk center) and spaced one wavelength apart, and a second system of vortices farther from the surface. Brown (1960) repeated this calculation for the rotating disk without suction using the viscous equations, and confirmed the vortices near the surface, but not those farther out. The vortices near the surface were in accord with conjectures made earlier. Thus the streaks and the spiral angle were explained as manifestations of inflectional instability associated with the crossflow, and the whole phenomenon was named crossflow instability.

This explanation, while very suggestive, left many questions unanswered. The azimuthal wavelength calculated by Stuart for the inviscid neutral wave gave the result that there should be 113 vortices around the circumference at $R = 443$, whereas in the experiments only about 30 were observed. This discrepancy was attributed to the neglect of viscosity. Another reason for the discrepancy, not mentioned at the time, is that the theory dealt with neutral waves, while the waves that form in the china clay were unstable spatial waves, i.e., they were amplifying in the outward radial direction. Brown (1960) calculated a neutral-stability curve from the Orr-Sommerfeld equation for the velocity profile in the direction 11.5° [said to be measured from the photograph in Gregory et al. (1955)], and also determined the locus in $\alpha - R$ space of unstable stationary temporal waves with this wave angle. According to Brown's calculation, the number of vortices at $R = 433$ is 23.6, and at $R = 540$ is 31.5. These numbers are more in accord with experiment, but no explanation was given as to why these particular waves should be observed.

12.3 Instability characteristics of normal modes

The Orr-Sommerfeld calculations of Brown (1959, 1960, 1961) for various directional velocity profiles gave a critical Reynolds number of about 180. In none of the experiments were waves detected at anything approaching this low a Reynolds number. Malik and Orszag (1981) derived a new system of equations in which all terms of order $1/r$ were retained. These equations are of sixth order for the determination of eigenvalues, rather than fourth order. With the sixth-order equations, the critical Reynolds number was computed to be 287 [later corrected to 275 by Malik (1983, private communication)]. This large difference between the fourth and sixth-order equations casts serious doubt on the use of the former in the rotating disk problem.

The stability analysis is carried out in the polar coordinates r, θ, ζ. The wavenumber vector $\vec{k}$ at an angle ψ to the radial direction has components α in the radial direction and β_θ in the azimuthal direction. The wave angle ψ is measured from the radius and is positive counterclockwise as usual. In Fig 12.2, the spatial amplification rate σ in the radial direction, computed as an eigenvalue with $(\beta_\theta)_i = 0$ from the sixth-order equations of Malik and Orszag (1981), is plotted against the azimuthal wavenumber $\beta_\theta = 2\pi/\lambda_\theta$, where λ_θ is the azimuthal wavelength in radians. This wavenumber expresses the number of wavelengths around a circumference, which, in the present case, is equivalent to the number of vortices. It is related to the wavenumber β based on L^* by $\beta = \beta_\theta/R$. The critical Reynolds number is seen to be about $R = 273$, in reasonable agreement with Malik's most recent value. For R greater than about 400, the maximum spatial amplification rate in Fig. 12.2 is larger than in any 2D Falkner-Skan boundary layer (for the separation profile, $\sigma_{\max} = 48 \times 10^{-3}$). The group-velocity angle ϕ_r of the most unstable normal mode at $R = 500$ is $-83°$ (measured from the radial direction), so that the amplification rate in that direction, $\sigma_g = \sigma \cos\phi_r$, is only 8.9×10^{-3}. The large values in the radial direction can be regarded as a consequence of the long spiral path length rather than a reflection of the inherent instability of the velocity profile.

The wave angle ψ is given in Fig. 12.3 at several Reynolds numbers as a function of β_θ. The interest in this figure is the prominent maximum in ψ that increases with R. To understand this behavior it is

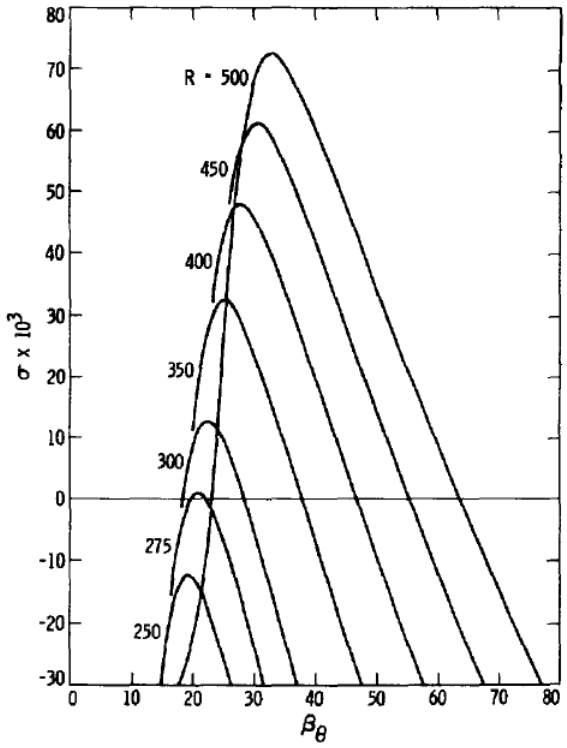

Figure 12.2: Spatial amplification rate vs. azimuthal wavenumber at seven Reynolds numbers for zero-frequency waves; sixth-order system.

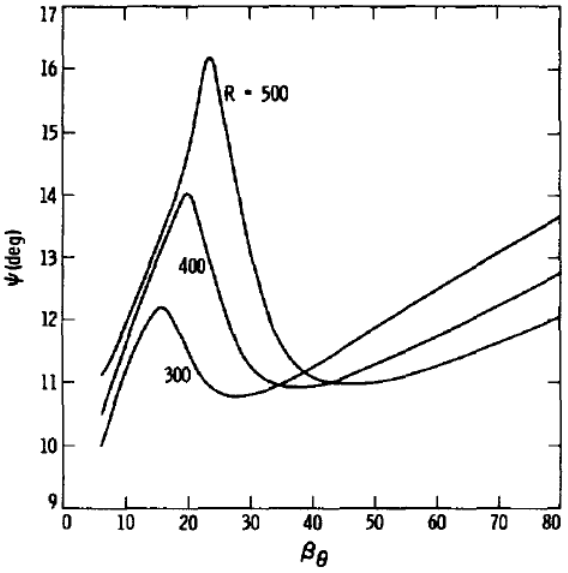

Figure 12.3: Wave angle vs. azimuthal wavenumber at three Reynolds numbers for zero-frequency waves; sixth-order system.

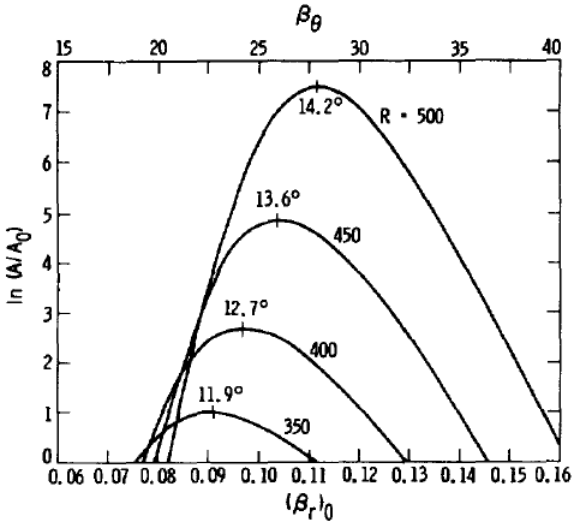

Figure 12.4: $\ln(A/A_0)$ vs. azimuthal wavenumber at four Reynolds numbers for zero-frequency waves and wave angle at peak amplitude ratio; sixth-order system.

necessary to mention that the normal-mode solution represented in Figs. 12.2 and 12.3 is not unique. There is a second solution with larger wave angles that is completely damped for $R \leq 500$. At $R = 500$, the minimum wave angle of this solution is 18.3° at $\beta_\theta = 23.5$, and the minimum damping is 1.8×10^{-3} at $\beta_\theta = 22.2$. At a Reynolds number somewhere above 500, the two solutions exchange identities for certain β_θ, with consequences that have not yet been worked out.

The logarithm of the amplitude ration A/A_0 obtained by integrating σ along the radius is given in Fig. 12.4 at $R = 35$, 400, 450 and 500. The reference amplitude A_0 is at $R = 250$, rather than at the lower-branch neutral point of each Fourier component. The wave angle at the maximum amplitude of each R is noted in the figure. These numerical results differ from those of Malik and Orszag (1981) because here the irrotationality condition, Eq. 2.55c, has been applied to the wavenumber vector of each Fourier component. For the disk, this condition is that the azimuthal wavenumber β_θ, or number of vortices, is constant. That is, in Fig. 12.2 the path of integration is parallel to the ordinate. In Fig. 12.4, $\ln(A/A_0)$ is given as a function of both β_θ and $(\beta_r)_0$, the value of β at the reference Reynolds number of 250. We observe that although the bandwidth of β_θ for which A is greater than A_0 increases with increasing R, the bandwidth for which A/A_0 is within $1/e$ of the maximum amplitude ratio decreases slightly. The values of $\ln(A/A_0)$ in this figure contrast with the much higher values obtained by Cebeci and Stewartson (1980b) from the fourth-order system and the parallel-flow saddle point criterion. Transition is usually observed to start at a Reynolds number in the vicinity of 500, so that the N factors of Fig. 12.4 are of the magnitude customarily associated with transition in 2D boundary layers. Thus we see that crossflow instability in the rotating-disk boundary layer is powerful enough to lead to transition at lower-than-normal Reynolds numbers where the streamwise profile is completely stable.

12.4 Wave pattern from a steady point source

The wave angles and number of vortices at the peak amplitudes of Fig. 12.4 are close enough to what is observed in the experiments to suggest that the normal modes which yield those values are the dominant modes of the stationary wave system that appears in the flow-visualization photographs. However, we are still left without any explanation of how only the most-amplified mode could be present at each radius. The filtering action of the boundary layer is not strong enough to accomplish this, and the constraints of constant F and β_θ do not allow any initial Fourier component to be the most-amplified normal mode at more than one radius. Besides, the experiment of Gregory et al. (1955) showed clearly that a band of circumferential

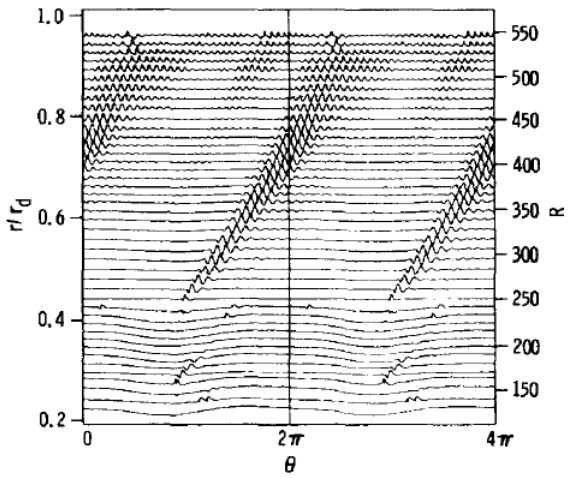

Figure 12.5: Ensemble-averaged normalized velocity fluctuations of zero-frequency waves at $\zeta = 1.87$ on rotating disk of radius $r_d = 22.9$ cm. Roughness element at $R_s = 249$, $\theta_s = 173°$. [After Fig. 18 of Wilkinson and Malik (1983)]

wavelengths is present at each radius, not just the most amplified.

A definite step forward was accomplished by the experiment of Wilkinson and Malik (1983). These investigators used a hot-wire anemometer instead of flow visualization, and so could more accurately resolve the disturbance structure on the disk. Although it had been conjectured by Gregory et al. (1955) that minute roughness might play a role in fixing the vortex pattern with respect to the disk, the Wilkinson-Malik experiment revealed for the first time that the wave pattern responsible for the stationary vortex lines emanates from point sources randomly located on the disk. All of the observed properties of the waves can thus be explained as characteristic features of the interference wave pattern that results from the superposition of the entire azimuthal wavenumber spectrum of equal-phase zero-frequency normal modes produced by the point-source roughness element. The streaks of flow-visualization photographs are the constant-phase lines of the wave pattern. The wave patterns from a number of sources eventually merge and cover the entire circumference of the disk. it is this merged wave pattern that appears in the flow visualization experiments. The much greater sensitivity of the hot wire compared to flow visualization techniques made it possible to detect waves at small radii where the merger was not yet complete.

Wilkinson and Malik (1983) made the phenomenon even clearer by placing an artificial roughness on the disk. The waves from this roughness were of larger amplitude than the waves from the naturally occurring minute roughnesses, and so offered and opportunity to study the essential phenomenon in a purer form. Figure 12.5, taken from Fig. 18 of their paper, shows the steady wave pattern from the single roughness, as well as others from unavoidable natural roughnesses. In this figure, which was obtained by forming an ensemble average of the amplitude measurements at every disk revolution, the amplitudes have been normalized to a constant value of the maximum amplitude at each radius.

The wave pattern of Fig. 12.5 is of the same type that we studied in Chapter 7 for a harmonic point source in a Blasius boundary layer, with due allowance made for the very different instability characteristics of 2D boundary layers and 3D boundary layers with crossflow instability. We therefore modified our calculation procedure for planar boundary layers to fit the different geometry of the rotating disk and the lack of an axis of symmetry, and have calculated the wave pattern produced by a zero-frequency point source located at the Reynolds number of the roughness element in the Wilkinson-Malik experiment (Mack, 1985). The wave forms, normalized to a constant value of the maximum amplitude as in Fig. 12.5, are shown in Fig. 12.6 along with the constant phase lines. The numbering of the constant-phase lines corresponds to the system used by Wilkinson and Malik. it is evident that the calculated wave pattern is in the closest possible agreement with the measured wave pattern as to the location of the constant-phase lines, the number of oscillations at each radius, and the azimuthal wavelength. The latter quantity varies with both the radius and azimuth

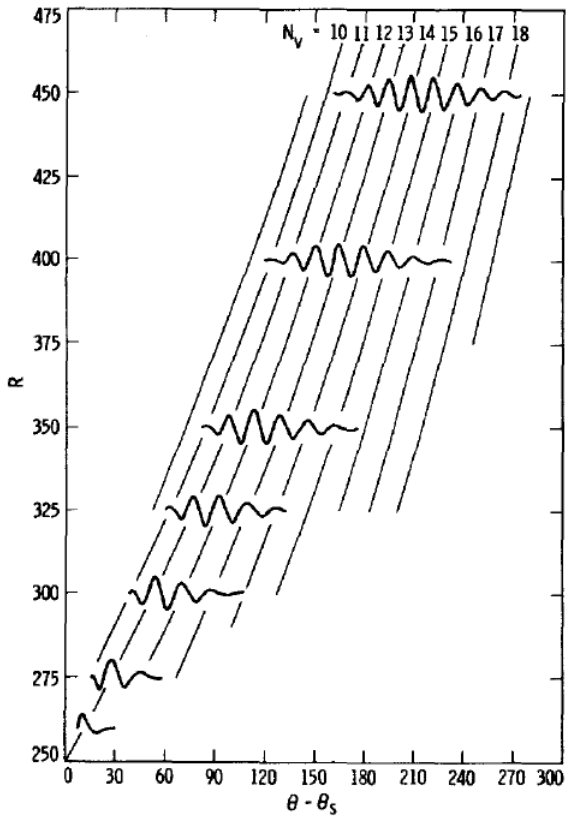

Figure 12.6: Normalized wave forms and constant-phase lines of calculated wave pattern produced by zero-frequency point source at $R_s = 250$ in rotating-disk boundary layer.

angle. The shift of hte wave pattern to the right in Figs. 12.5 and 12.6 with respect to the constant-phase lines is because amplitude propagates essentially along group-velocity trajectories. The agreement between Figs. 12.5 and 12.6 conclusively demonstrates that the observed stationary waves on a rotating disk are the result of the superposition of the entire spectrum of normal modes, both amplified and damped.

The calculated amplitudes along the constant-phase lines are given in Fig. 12.7. Vortex No. 11 is the one that comes from the point source, and it is the only one with an amplitude minimum, which, it should be noted, is well beyond the critical Reynolds number of 273. The reference amplitude of this vortex was selected to fit the minimum amplitude of the experiment, adn then used for all the other vortices. A comparison is given in Fig. 12.8 of the calculated and experimental envelope amplitude distributions at $R = 400$ and 466. In this figure, the experimental amplitudes have been normalized to the arbitrary theoretical maximum amplitude at $R = 400$. At $R = 400$, the agreement is excellent except at the right-hand edge of the wave pattern, where a second wave pattern was present in the experiment. At $R = 466$, the influence of the second wave pattern has spread almost to the center of the principal wave pattern, and is the reason for the disagreement between theory and experiment in Fig. 12.8 to the right of the maximum amplitude.

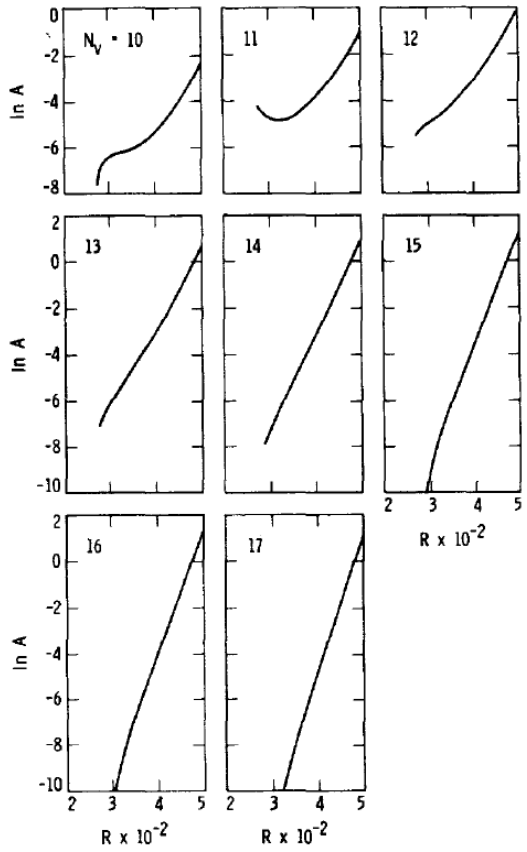

Figure 12.7: Calculated amplitudes along constant-phase lines of wave pattern behind zero-frequency point source at $R_s = 250$ in rotating-disk boundary layer.

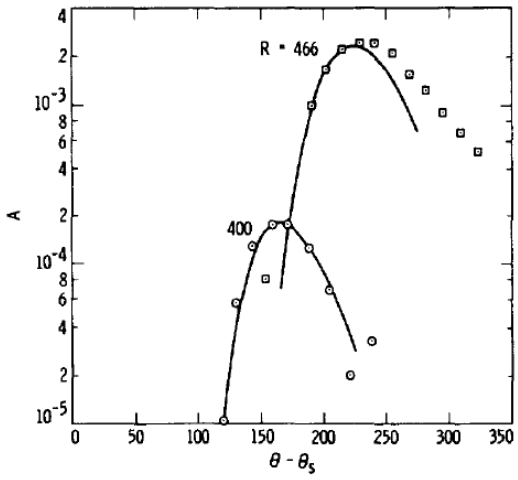

Figure 12.8: Comparison of calculated envelope amplitudes at $R = 400$ and 466 in wave pattern produced by zero-frequency point source at $R_s = 250$ in rotating-disk boundary layer, and comparison with measurements of Wilkinson and Malik (1983)(◯, $R = 397$; □, $R = 466$).

Chapter 13

Falker-Skan-Cooke Boundary Layers

13.1 Mean boundary layer

In order to more fully study the influence of three dimensionality in the mean flow on the boundary-layer stability than is possible with the rotating disk, it is necessary to have a family of boundary layers where the magnitude of the crossflow can be varied in a systemic manner. The two-parameter yawed-wedge flows introduced by Cooke (1950) are suitable for this purpose. One parameter is the usual Falkner-Skan dimensionless pressure-gradient parameter β_h; the other is the ratio of the spanwise and chordwise velocities. A combination of the two parameters makes it possible to simulate simple planar three-dimensional boundary layers.

The inviscid velocity in the plane of the wedge and normal to the leading edge in the direction x_c is

$$U_{c1}^* = c^* \left(x_c^*\right)^m , \tag{13.1}$$

where the wedge angle is $(\pi/2)\beta_h$ and $\beta_h = 2m/(m+1)$ as in Eq. 2.62. We shall refer to this velocity as the chordwise velocity. The velocity parallel to the leading edge, or spanwise velocity, is

$$W_{s1} = \text{const.} \tag{13.2}$$

The subscript 1 refers to the local freestream. For this inviscid flow, the boundary-layer equations in the x_c direction, as shown by Cooke (1950), reduce to

$$f''' + ff'' + \beta_h \left(\frac{m+1}{2} - f'^2\right) = 0. \tag{13.3}$$

This equation is the usual Falkner-Skan equation for a two-dimensional boundary layer, and is independent of the spanwise flow. The dependent variable $f(y)$ is related to the dimensionless chordwise velocity by

$$U_c = \frac{U_c^*}{U_{c1}^*} = \left(\frac{2}{m+1}\right) f'(y), \tag{13.4}$$

and the independent variable is the similarity variable

$$y = y^* \sqrt{\frac{U_{c1}^*}{\nu^* x_c^*}}. \tag{13.5}$$

Once $f(y)$ is known, the flow in the spanwise direction z_s^* is obtained from

$$g'' + fg' = 0, \tag{13.6}$$

where

$$W_s = \frac{W_s^*}{W_{s1}^*} = g(y). \tag{13.7}$$

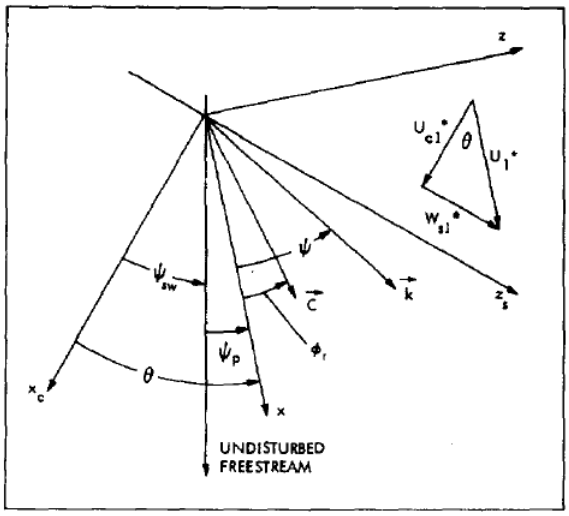

Figure 13.1: Coordinate systems for Falkner-Skan-Cooke boundary layers.

Both $f'(y)$ and $g(y)$ are zero at $y = 0$ and approach unity as $y \to \infty$. Tabulated values of $g(y)$ for a few values of β_h may be found in Rosenhead (1963, p. 470).

The final step is to use $f'(y)$ and $g(y)$ to construct the streamwise and crossflow velocity components needed for the stability equations. A flow geometry appropriate to a swept back wing is shown in Fig. 13.1. There is no undisturbed freestream for a Falkner-Skan flow, but such a direction is assumed and a yaw, or sweep, angle ψ_{sw} is defined with respected to it. the local freestream, or potential flow, is at an angle ψ_p with respect to the undisturbed freestream. It is the potential flow that defines the x, z coordinates of the stability equations. The angle of the potential flow with respect to the chord is

$$\theta = \tan^{-1}\left(\frac{W_{s1}^*}{U_{c1}^*}\right), \tag{13.8}$$

and θ is related to ψ_{sw} and ψ_p by

$$\theta = \psi_{sw} + \psi_p. \tag{13.9}$$

With local potential velocity, $U_1^* = \sqrt{U_{c1}^{*2} + W_{s1}^{*2}}$, as the reference velocity, the dimensionless streamwise and crossflow velocity components are

$$U(y) = f'(y)\cos^2\theta + g(y)\sin^2\theta, \tag{13.10a}$$

$$W(y) = [-f'(y) + g(y)]\cos\theta\sin\theta. \tag{13.10b}$$

These velocity profiles are defined by β_h, which fixes $f'(y)$ and $g(y)$, and the angle θ. We note from Eq. 13.10b that for a given pressure gradient all crossflow profiles have the same shape; only the magnitude of the crossflow velocity changes with the flow direction. In contrast, according to Eq. 13.10a streamwise profiles change shape as θ varies. for $\theta = 0$, $U(y) = f'(y)$; for $\theta = 90°$, $U(y) = g(y)$; for $\theta = 45°$, the two functions make an equal contribution.

When the Eq. 13.10 velocity profiles are used directly in the stability equations, the velocity and length scales of the equations must be the same as in Eq. 13.10. This identifies the velocity scale as U_1^*, the length scale as

$$L^* = \sqrt{\frac{\nu^* x_c^*}{U_{c1}^*}}, \tag{13.11}$$

and the Reynolds number $U_1^* L^*/\nu^*$ as

$$R = \frac{R_c}{\cos\theta}. \tag{13.12}$$

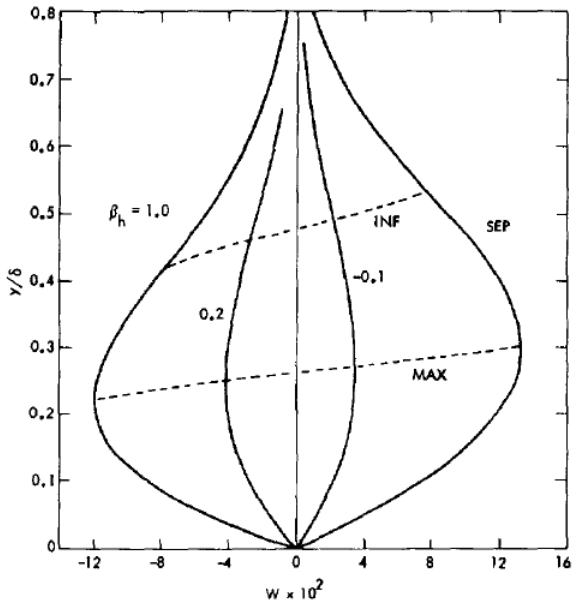

Figure 13.2: Falkner-Skan-Cooke crossflow velocity profiles for $\beta_h = 1.0$, 0.2, -0.1 and SEP (separation, -0.1988377); INF, location of inflection point; MAX, location of maximum crossflow velocity.

where $R_c = (U^*_{c1} x^*_c / \nu^*)^{1/2}$ is the square root of the Reynolds number along the chord. For positive pressure gradients ($m > 0$), $\theta = 90°$ at $x_c = 0$ and $\theta \to 0$ as $x \to \infty$; for adverse pressure gradients ($m < 0$), $\theta = 0°$ at $x_c = 0$ and $\theta \to 90°$ as $x_c \to \infty$. The Reynolds number R_c is zero at $x = 0$ for all pressure gradients, as is R with one important exception. The exception is where $m = 1$ ($\beta_h = 1$). For a 2D planar flow, $\beta_h = 1$ is the stagnation-point solution; here it is the attachment-line solution. In the vicinity of $x_c = 0$, the chordwise velocity is

$$U^*_{c1} = x^*_c \left(\frac{dU^*_{c1}}{dx^*_c} \right)_{x=0} . \tag{13.13}$$

The potential velocity along the attachment line is W^*_{s1}, and the Reynolds number is

$$R_{x=0} = \frac{W^*_{s1}}{\nu^* \left(\dfrac{dU^*_{c1}}{dx^*_c} \right)_{x=0}}, \tag{13.14}$$

a non-zero value.

For our purposes in this chapter, we may regard θ as a free parameter, and use the velocity profiles of Eq. 13.10 at any Reynolds number. However, for the flow over a given wedge, θ can be set arbitrarily at only one Reynolds number. if $\theta_{\rm ref}$ is θ at $R_c = (R_c)_{\rm ref}$, the θ at any other R_c is given by

$$\tan\theta = \tan\theta_{\rm ref} \left[\frac{(R_c)_{\rm ref}}{R_c} \right]^{\frac{m}{m+1}} . \tag{13.15}$$

For $m \ll 1$, the dependence on R_c is so weak that θ is constant almost everywhere. One way of choosing $(R_c)_{\rm ref}$ within the present context is to make it the chord Reynolds number where $\psi_p = 0$; i.e., the local potential flow is in the direction of the undisturbed freestream. Then $\theta_{\rm ref}$ is equal to the yaw angle ψ_{sw}.

Figure 13.2 shows the crossflow velocity profiles for $\theta = 45°$ and four values of β_h. The inflection point and point of maximum crossflow velocity ($W_{\rm max}$) are also noted on the figure. In Fig. 13.3, $W_{\rm max}$ for $\theta = 45°$ is given as a function of β_h from near separation to $\beta_h = 1$. The crossflow velocity for any other flow angle is obtained by multiplying the $W_{\rm max}$ of the figure by $\cos\theta \sin\theta$. The maximum crossflow velocity of 0.133

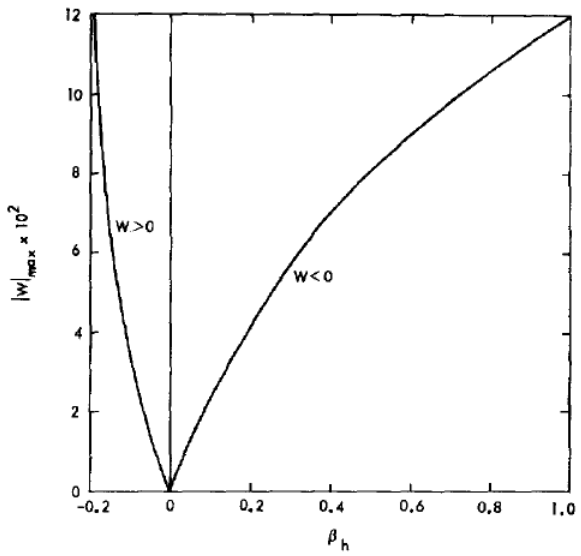

Figure 13.3: Effect of pressure gradient on maximum crossflow velocity; Falkner-Skan-Cooke boundary layers.

is generated by the separation profile rather than by the stagnation profile, where $W_{\max} = 0.120$. However, $W_{\max}$ varies rapidly with β_h in the neighborhood of separation, as do all other boundary-layer parameters, and for $\beta_h = -0.190$, $W_{\max}$ is only 0.102.

The function $g(y)$ is only weakly dependent on β_h, and, unlike $f'(y)$, never has an inflection point even for an adverse pressure gradient. Indeed it remains close to the Blasius profile in shape, as underlined by a shape factor H (ratio of displacement to momentum thickness) that only changes from 2.703 to 2.539 as β_h goes from -0.1988377 (separation) to 1.0 (stagnation). The weak dependence of $g(y)$ on β_h has been made the basis of an approximate method for calculating boundary layers on yawed cylinders. For our purposes, it allows some of the results of the stability calculations to be anticipated. For waves with the wavenumber vector aligned with the local potential flow, we can expect the amplification rate to vary smoothly form its value for a two-dimensional Falkner-Skan flow to a value not too far from Blasius as θ goes from zero to 90°.

The stability results will be presented in terms of the Reynolds number R and the similarity length scale L^*. In order that the results may be converted to the length scales of hte boundary-layer thickness, displacement thickness or momentum thickness, Table 13.1 lists the dimensionless quantities $y_\delta = \delta/L^*$, $y_{\delta^*} = \delta^*/L^*$ and the shape factor H of the streamwise profile for several combinations of β_h and θ. Also listed are $W_{\max}$, the average crossflow velocity $\overline{W} = (\int W\ dy)/y$; $y_{\inf}$, the y of the inflection point of the crossflow velocity profile; and $\varepsilon_{\inf}$, the deflection angle of the streamline at $y = y_{\inf}$. The quantity y_δ is defined as the point where $U = 0.999$.

13.2 Boundary layers with small crossflow

In a two-dimensional boundary layer, the most unstable wave is two dimensional. Therefore, we can expect that in three-dimensional boundary layers with small crossflow, the most unstable wave will have its wavenumber vector nearly aligned with the local potential flow, and we can restrict ourselves to waves with $\psi = 0°$ forthe purpose of determining the maximum amplification rate. This procedure is equivalent to studying the two-dimensional instability of the streamwise profile provided that $\overline{\psi} = 0$ (amplification rate in streamwise direction). In the calculations of this chapter, $\overline{\psi}$ was taken to be either zero or ϕ_g. In the latter case, σ_g is almost identical to σ, which we define as the amplification rate with $\overline{\psi} = 0$, and we shall ignore the difference.

The effect of the flow angle θ on the maximum spatial amplification rate of the waves with $\psi = 0°$ is shown in Fig. 13.4 for $\beta_h = \pm 0.02$ and two Reynolds numbers. The amplification rate $\sigma_{\max}$ is expressed as

Table 13.1: Properties of three-dimensional Falkner-Skan-Cooke boundary layers.

β_h	θ	y_δ	y_{δ^*}	H	$W_{\max}$	$\overline{W}$	$\varepsilon_{\inf}$	$y_{\inf}$
SEP	2.2	8.238	3.495	4.024	0.0102	0.00476	0.487	4.306
	5.0	8.236	3.489	4.010	0.0231	0.01077	1.100	
	10.0	8.229	3.466	3.959	0.0455	0.02123	2.156	
	40.0	8.095	3.075	3.280	0.1310	0.06214	5.709	
	50.0	8.017	2.897	3.064	0.1310	0.06274	5.516	
-0.10	45.0	6.522	1.985	2.698	0.0349	0.01619	1.498	3.213
-0.02	45.0	6.098	1.763	2.609	0.0058	0.00267	0.249	2.940
0.02	45.0	5.931	1.682	2.578	-0.0054	-0.00248	-0.232	2.835
0.04	45.0	5.348	1.646	2.564	-0.0104	-0.00480	-0.449	2.787
0.10	45.0	5.646	1.551	2.529	-0.0239	-0.01094	-1.029	2.659
0.20	45.0	5.348	1.424	2.482	-0.0423	-0.01924	-1.823	2.478
1.0	2.4	3.143	0.6496	2.227	-0.0100	-0.00503	-0.406	1.524
	10.0	3.196	0.6603	2.226	-0.0410	-0.02021	-1.669	
	40.0	3.574	0.8050	2.275	-0.1181	-0.05204	-5.129	
	45.0	3.621	0.8378	2.301	-0.1191	-0.05217	-5.291	
	50.0	3.661	0.8706	2.332	-0.1181	-0.05081	-5.295	
	55.0	3.695	0.9024	2.366	-0.1127	-0.04804	-5.135	
	80.0	3.791	1.0153	2.524	-0.0410	-0.01704	-1.987	
	87.6	3.799	1.0260	2.542	-0.0100	-0.00416	-0.489	

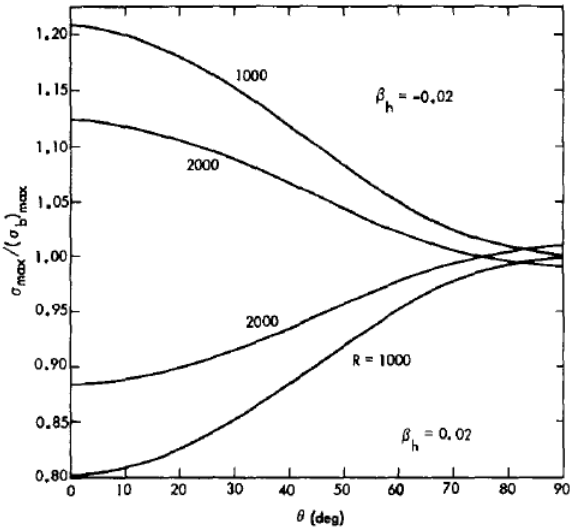

Figure 13.4: Effect of flow angle on maximum amplification rate with respect to frequency of $\psi = 0°$ waves at $R = 1000$ and 2000 in Falkner-Skan-Cooke boundary layers with $\beta_h = \pm 0.02$.

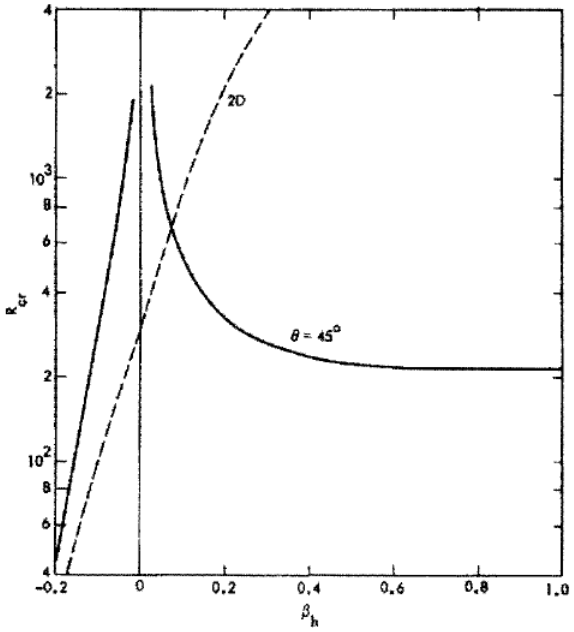

Figure 13.5: Effect of pressure gradient on minimum critical Reynolds number: ——, zero-frequency crossflow instability waves in Falkner-Skan-Cooke boundary layers with $\theta = 45°$; - - -, 2D Falkner-Skan boundary layers [from Wazzan et al. (1968a)].

a ratio to the Balsius value $(\sigma_b)_{\max}$. It will be recalled that with $\beta_h = 0$, $g(y) = f'(y)$, and the velocity profile remains the Blasius function for all flow angles. The effect of a non-zero flow angle with $\beta_h \neq 0$ is destabilizing for a favorable pressure gradient, and stabilizing for an adverse pressure gradient. Consequently, it reduces the pressure-gradient effect of 2D Falkner-Skan boundary layers. The reason for this result is easy to understand by reference to Eq. 13.10. We have already pointed out in Section 13.1 that the spanwise velocity profile $g(y)$ is always close to the Blasius function. Thus as the flow angle increases from zero, the amplification rate must change from the two-dimensional Falkner-Skan value at $\theta = 0°$ to a value not far from Blasius at $\theta = 90°$.

As discussed previously, the only physically meaningful flow with $\theta = 90°$ and a non-zero Reynolds number is the attachment-line flow ($\beta_h = 1$). For all other values of β_h, R at this flow angle must be either zero ($\beta_h > 0$) or infinite ($\beta_h < 0$). With $\beta_h = 1.0$ and $R = 1000$ ($R_\theta = 404.2$, where R_θ is the momentum-thickness Reynolds number), $\sigma_{\max}/(\sigma_b)_{\max} = 0.766$. The minimum critical Reynolds number of this profile is $(R_\theta)_{\rm cr} = 268$ (the parallel-flow Blasius value is 201), yet turbulent bursts have been observed as low as $R_\theta = 250$ for small disturbances by Poll (1977).

We must still show that the waves with $\psi = 0°$ properly represent the maximum instability of three-dimensional profiles with small crossflow. For this purpose a calculation was made of σ as a function of ψ for $\beta_h = -0.02$, $\theta = 45°$, $R = 1000$ and $F = 0.4256 \times 10^{-4}$, the most unstable frequency for $\psi = 0°$ at this Reynolds number. It was found that the crossflow indeed introduces an asymmetry into the distribution of σ with ψ, and the maximum of σ is located at $\psi = -6.2°$ rather than at $0°$. However, this maximum value differs from the $\sigma_{\max}$ of Fig. 13.4 by only 0.7%.

13.3 Boundary layers with crossflow instability only

The main advantage that the Falkner-Skan-Cooke boundary layers offer over the rotating disk boundary layer for studying crossflow instability is that the maximum crossflow velocity is not constant, but is a function of β_h and θ. The crossflow velocity is a maximum at $\theta = 45°$ for a given β_h, and we can expect the crossflow

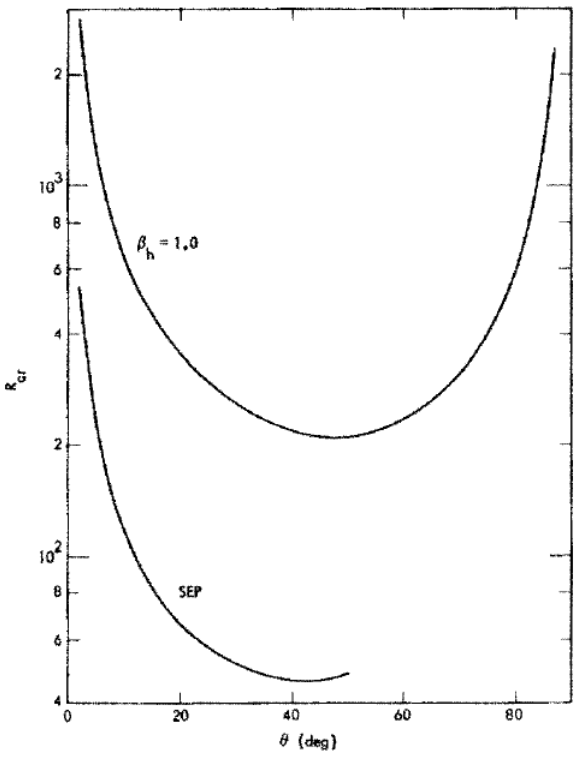

Figure 13.6: Effect of flow angle on minimum critical Reynolds number of zero-frequency crossflow waves for $\beta_h = 1.0$ and -0.1988377 Falkner-Skan-Cooke boundary layers.

instability to also be a maximum near this angle. Figure 13.5 shows the minimum critical Reynolds number $R_{\rm cr}$ at $\theta = 45°$ for the zero-frequency crossflow disturbances as a function of β_h. For comparison, $R_{\rm cr}$ for Tollmien-Schlichting waves in 2-D Falkner-Skan crossflow boundary layers, as computed by Wazzan et al. (1968a), is also given. For adverse pressure gadients, the steady crossflow disturbances become unstable at Reynolds numbers well above the $R_{\rm cr}$ for the 2D profiles. On the contrary, for $\beta_h > 0.07$ the reverse is true, and for most pressure gradients in this range the steady disturbances become unstable at much lower Reynolds numbers than the 2D $R_{\rm cr}$ (for $\beta_h = 1.0$, the 2D $R_{\rm cr}$ is 19,280 compared to $R_{\rm cr} = 212$ for zero-frequency crossflow instability).

The distribution of $R_{\rm cr}$ with θ is shown in Fig. 13.6 for $\beta_h = 1.0$ over the complete range of θ, and for the separation profiles ($\beta_h = -0.1988377$) over the range $0° < \theta < 50°$. Near $\theta = 0°$ and 90°, $R_{\rm cr}$ is very sensitive to θ; near, but not precisely at, $\theta = 45°$ $R_{\rm cr}$ has a minimum. This minimum occurs close to the maximum of the streamline deflection angle at $y = y_{\rm inf}$, $\varepsilon_{\rm inf}$ (see Table 13.1), which, unlike $W_{\rm max}$, is not symmetrical about $\theta = 45°$. Table 13.2 lists the critical wave parameters for a few combinations of β_h and θ. The extensive computations needed to fix these parameters precisely were not carried out in most cases, and so the values in the table are not exact. It can be noted that the relation

$$\psi = \left(\frac{\beta_h}{|\beta_h|}\right)(90 - |\varepsilon|_{\rm inf} \tag{13.16}$$

gives $\psi_{\rm cr}$ to within a degree for the separation profiles, and to within 0.1° for the other profiles of Tables 13.1 and 13.2. This result holds in general for the most unstable wave angle.

As an example of a boundary layer which is unstable at low Reynolds number only as a result of crossflow instability, we select $\beta_h = 1.0$ and $\theta = 45°$, and present results for the complete range of unstable frequencies. Although this pressure gradient can only occur at an attachment line, Fig. 13.5 leads us to expect that all profiles with a strong favorable pressure gradient will have similar results. For this type of profile, the

Table 13.2: Wave parameters at minimum critical Reynolds number of zero-frequency disturbances.

β_h	θ	$R_{\rm cr}$	$k_{\rm cr}$	$\psi_{\rm cr}$
SEP	2.2	535	0.213	-89.41
	5.0	237	0.213	-88.68
	10.0	121	0.215	-87.44
	40.0	46.5	0.230	-83.54
	45.0	46.7	0.230	-83.57
	50.0	48.4	0.231	-83.81
-0.10	45.0	276	0.295	-88.42
-0.02	45.0	1885	0.310	-89.74
0.02	45.0	2133	0.322	89.76
0.04	45.0	1129	0.327	89.53
0.10	45.0	527	0.339	88.93
0.20	45.0	328	0.358	88.12
1.00	2.4	2755	0.553	89.60
	10.0	671	0.547	88.33
	40.0	219	0.545	84.88
	45.0	212	0.540	84.70
	50.0	212	0.540	84.70
	55.0	218	0.538	84.85
	80.0	563	0.532	88.00
	87.6	2325	0.532	89.51

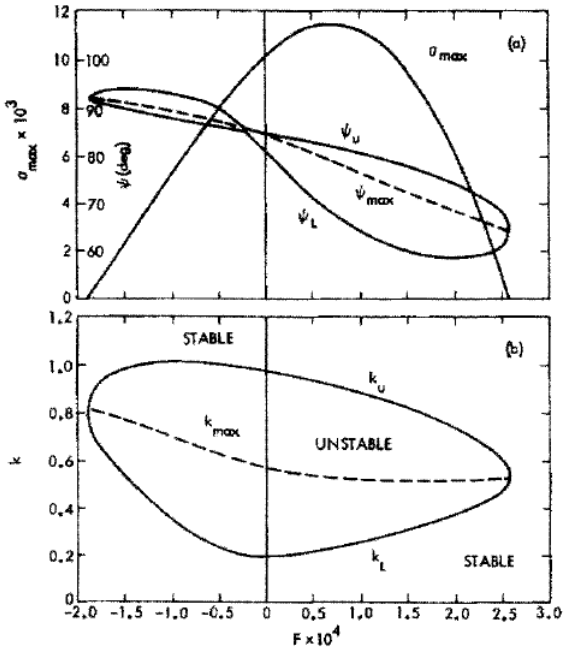

Figure 13.7: Instability characteristics of $\beta_h = 1.0$, $\theta = 45°$ Falkner-Skan-Cooke boundary layers at $R = 400$: (a) maximum amplification rate with respect to wavenumber, and unstable $\psi - F$ region; (b) unstable $k - F$ region.

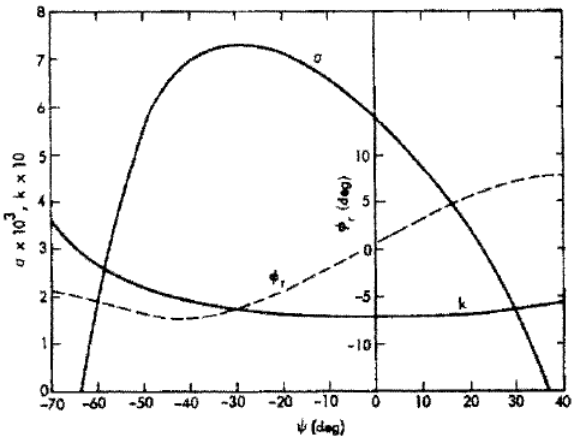

Figure 13.8: Effect of wave angle on amplification rate, wavenumber, and group-velocity angle for $F = 2.2 \times 10^{-4}$ at $R = 276$; $\beta_h = -0.10$, $\theta = 45°$ Falkner-Skan-Cooke boundary layer.

minimum critical Reynolds number of the least stable frequency is very close to the $R_{\rm cr}$ of Fig. 13.5. We therefore choose $R = 400$, which is well above $R_{\rm cr}$ and where the instability is fully developed, and present a summary of the instability characteristics in Fig. 13.7.

Figure 13.7a gives $\sigma_{\max}$ as a function of the dimensionless frequency F, and also shows the portion of the $\psi - F$ plane for which there is instability. The unstable region is enclosed between the curves marked ψ_U and ψ_L. These curves represent either neutral stability points or extrema of ψ. The corresponding wavenumber magnitudes are shown in Fig. 13.7b. The negative frequencies signify that with ψ taken to be continuous through $F = 0$, the phase velocity changes sign. If we choose ψ so that the wavenumber and phase velocity are both positive, then it is ψ that changes sign at $F = 0$. Consequently, there are two groups of positive unstable frequencies with quite different wave angles. The first group, which includes the peak amplification rate, is oriented anywhere from 5° to 31° (clockwise) from the direction opposite to the crossflow direction. The second group is oriented close to the crossflow direction itself.

13.4 Boundary layers with both crossflow and streamwise instability

As an example of a boundary layer which has both crossflow and streamwise instability at low Reynolds numbers, we select $\beta_h = -0.10$ and $\theta = 45°$. In contrast to the previous case, the steady disturbances do not become unstable until a Reynolds number, $R = 276$, where the peak amplification rate is already 7.35×10^{-3}. [For $\beta_h = -0.10$ and $\theta = 0°$, $\sigma_{\max} = 11.0 \times 10^{-3}$ at $F = 2.2 \times 10^{-4}$, according to Wazzan et al. (1968a)]. The distribution of σ with ψ is shown in Fig. 13.8 for $F = 2.2 \times 10^{-4}$, a frequency close to the most unstable frequency of $F = 2.1 \times 10^{-4}$. We see that with a maximum crossflow velocity of 0.0349 (cf. Table 13.1), the distribution of σ about $\psi = 0°$ is markedly asymmetric, and the maximum amplification rate of 7.31×10^{-3} is located at $\psi = -29.4°$ rather than near zero. This asymmetry was barely perceptible for the small crossflow boundary layers of Fig. 13.4, where the crossflow is only one sixth as large. The σ at $\psi = 0°$ of Fig. 13.8 (5.82×10^{-3}) is close to $\sigma_{\max}$ with respect to the frequency of the $\psi = 0°$ waves (5.91×10^{-3}). Since this value is 20% below the peak amplification rate, the $\psi = 0°$ waves are no longer adequate to represent the maximum instability as with small crossflow boundary layers. Fig. 13.8 also gives the distribution with ψ of k and the real group-velocity angle, ϕ_r. The latter quantity remains within ±7.5° of the potential-flow direction throughout the unstable region.

Because $R = 276$ is the minimum critical Reynolds number of the steady disturbances, the unstable region terminates in a neutral stability point at $F = 0$. We are particularly interested here in Reynolds numbers where $F = 0$ is also unstable, and as an example, Fig. 13.9 gives results for all unstable frequencies

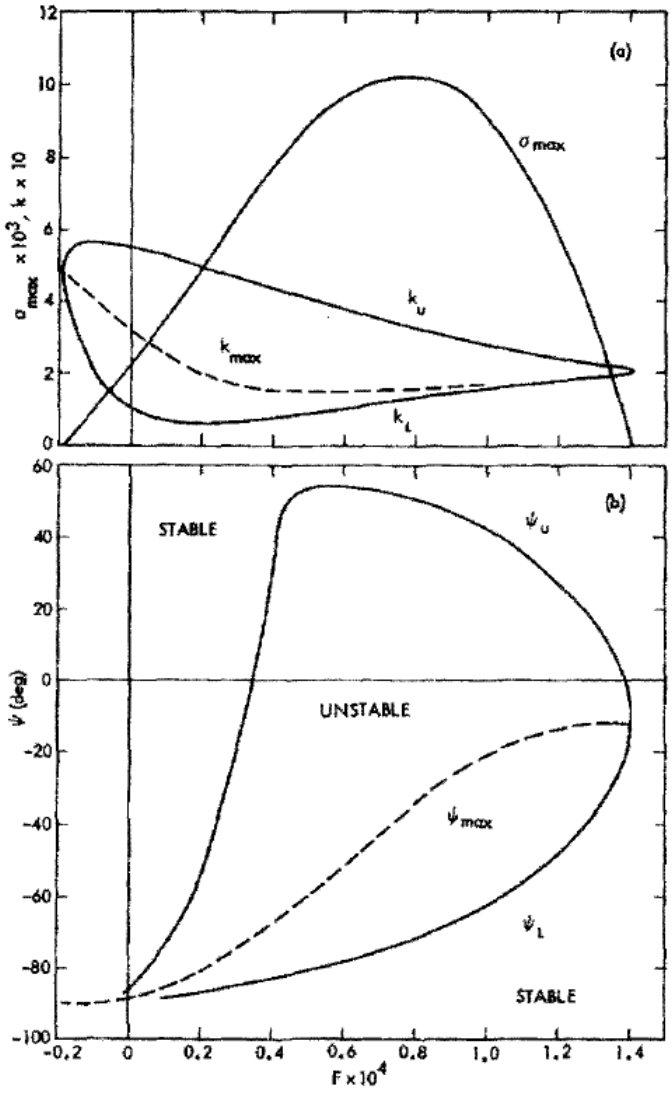

Figure 13.9: Instability characteristics of $\beta_h = -0.10$, $\theta = 45°$ Falkner-Skan-Cooke boundary layer at $R = 555$: (a) maximum amplification rate with respect to wavenumber, and unstable $k - F$ region; (b) unstable $\psi - F$ region.

at $R = 555$. Figure 13.9a shows $\sigma_{\max}$ as a function of F (here, as in Fig. 13.7, $\sigma_{\max}$ is the maximum with respect to k), as well as the unstable region of the $k - F$ plane; the unstable region of the $\psi - F$ plane appears in Fig. 13.9b. These two unstable regions are quite different from those of Fig. 13.7 where there is only crossflow instability. The negative frequencies do resemble those of Fig. 13.7 in that the unstable range of ψ is small, the unstable range of k is large, and with ψ redefined so that $F > 0$, the orientations are close to the crossflow direction. However, for the higher frequencies, which are by far the most unstable, the unstable regions of Fig. 13.9 bear more of a resemblance to those of a 2D boundary layer than to Fig. 13.7. The main differences from the 2D case are the asymmetry about $\psi = 0°$ already noted in Fig. 13.8, the one-sidedness of $\psi_{\max}$, and, for $F < 0.4 \times 10^{-4}$, the replacement of a lower cutoff frequency for instability by a rapid shift with decreasing frequency to waves oriented opposite to the crossflow direction and which are unstable down to zero frequency. The instability shown in Fig. 13.9 represents primarily an evolution of the small crossflow boundary layers of Fig. 13.4 to larger crossflow. Only the lower frequencies, say $F < 0.2 \times 10^{-4}$, have to do with the pure crossflow instability of Fig. 13.7. For frequencies near 0.4×10^{-4}, ψ varies little with k in one part of the unstable region, as with crossflow instability; in the other part, as with streamwise instability, the opposite is true. This behavior becomes more pronounced at high Reynolds numbers.

Chapter 14

Transonic Infinite-Span Swept-Wing Boundary Layer

The 3D boundary layers that have received the most attention in aeronautical practices are those on transonic swept wings. The desirability of maintaining laminar flow on the wings of large transonic aircraft has led to the study of the instability of such boundary layers as a means of estimating the occurrence of transition and the effectiveness of various methods of laminar-flow control. The basic phenomenon of crossflow instability was encountered and its origin explained by the early investigators, as we have learned in Chapter 12, and means of coping with its adverse consequences were developed. However, interest in laminar-flow control was waning by the time computer-aided stability analysis became commonplace in the 1960's, and nothing more was done on the subject of 3D boundary-layer stability following Brown's work (1959; 1960; 1961) until the energy crisis of the mid-1970's. In response to the sudden need for an analysis tool, Srokowski and Orszag (1977) brought out the SALLY code. In spite of using the incompressible stability theory and a non-physical method of computing wave amplitude, this code has been widely used. It has since been superseded by COSAL, a compressible version of SALLY (Malik, 1982). Work that was directed at developing more fundamental methods of stability analysis for swept wing boundary layers was carried out by Cebeci and Stewartson (1980a,b), Lekoudis (1979, 1980), Mack (1979a, 1981), and Nayfeh (1980a,b).

Attention has so far been restricted to infinite-span swept wings. Even with this simplification, the nonsimilarity of the boundary layers has made it necessary to proceed on the basis of specific examples, and to try and glean a general understanding of the instability of this type of boundary layer on the basis of extensive numerical calculations. We shall follow this same practice in this chapter. Detailed numerical results for a single example that were obtained by an application of methods already presented in this document (Mack, 1979a) are given in the hope that a careful study will yield some understanding of the instabilities that arise and the procedures to follow in analyzing them.

14.1 Mean boundary layer

The flow example used in this chapter is the boundary layer on a 35° swept wing of infinite span with a supercritical airfoil section, distributed suction and a chord of $c^* = 2.0$ m (6.55 ft) normal to the leading edge. The undisturbed flow conditions are $M_\infty = 0.89117$, $T^*_\infty = 311$ K, and $p^*_\infty = 0.30663$ atm. The upper surface pressure coefficient C_p is listed in Table 14.1 together with other properties of the potential flow as functions of s^*/c^*, where s^* is the arc length along the airfoil section. The coordinate system is shown in Fig. 14.1. The Reynolds number used in the stability calculations is $R = U_1^* L^*/\nu_1^*$, where U_1^* is the potential velocity. The length scale $L^* = \sqrt{\nu_1^* s^*/U_{c1}^*}$ reduces to the usual boundary-layer length scale when the flow is two-dimensional, and is non-zero at the attachment line. The Reynolds number Re_s is $U_1^* s^*/\nu_1^*$. The velocity derivative which defines m and thus the Hartree β_h was evaluated by the numerical differentiation of U_{c1} as calculated from the pressure coefficient. The very large $-\beta_h$ near the trailing edge have been omitted from the table.

Table 14.2 lists some properties of the boundary-layer solution calculated for the potential flow of Ta-

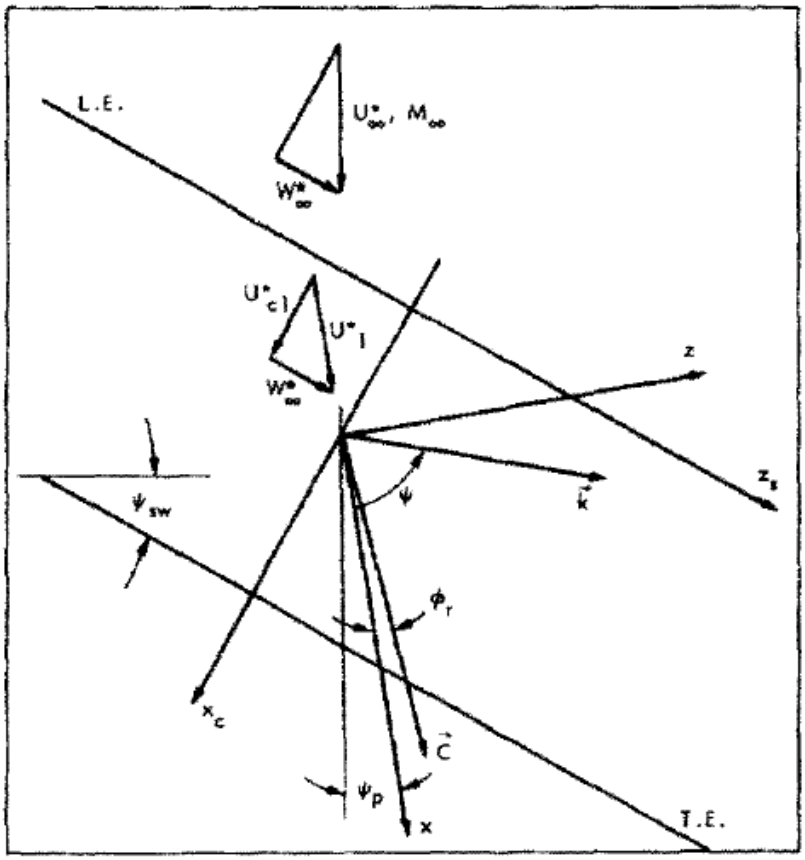

Figure 14.1: Coordinate systems used for infinite-span swept wing.

ble 14.1 and the suction distribution $C_Q(s^*)$ given in the last column. For comparison, the profile parameters of an insulated flat-plate boundary layer with no suction at $M_1 = 1.2$ are $y_\delta = 5.85$, $y_{\delta^*} = 2.31$ and $H = 3.54$. The maximum crossflow is $W_{\max} = -0.115$, and it occurs at station $N = 4$ ($s^*/c^* = 0.0059$). This value is virtually identical to the maximum possible crossflow generated by the Falkner-Skan-Cooke profiles of Chapter 13, where $W_{\max} = -0.119$ for $\beta_h = 1.0$ and $\psi_{sw} + \psi_p = 45°$. Although the pressure gradient first becomes adverse at $N = 14$, $W_{\max}$ does not change sign until $N = 21$. For $N = 15$ to 26 ($S^*/c^* = 0.128$ to 0.625), there are two inflection points in the crossflow velocity profile. Up to $N = 20$ ($s^*/c^* = 0.364$), W has the same sign at both inflection points; for $N > 20$, W has opposite signs. There is a reverse crossflow from $N = 17$ to 27 ($s^*/c^* = 0.211$ to 0.661). The angle ε_i is the angle of the velocity vector at the y of the inflection point of the crossflow velocity profile. When there are two inflection points, the listed ε_i is for the outer point when $W_{\max} < 0$, and for the inner point when $W_{\max} > 0$.

Table 14.1: Properties of potential flow

N	s^*/c^*	M_1	C_p	β_h	ψ (deg)	$Re_s \times 10^{-6}$	R	$L^* \times 10$ (cm)
1	0	0.4859	0.7652	1.0000	55.00	0	221	0.0560
2	0.0011	0.4934	0.7527	0.9770	45.23	0.009	224	0.0560
3	0.0033	0.5424	0.6680	0.9306	29.26	0.028	225	0.0593
4	0.0059	0.6261	0.5151	0.8753	16.96	0.056	301	0.0632
5	0.0087	0.7186	0.3375	0.7798	8.95	0.091	355	0.0682
6	0.0120	0.8033	0.1715	0.6721	3.91	0.132	412	0.0747
7	0.0157	0.8806	0.2051	0.6000	0.42	0.180	470	0.0818
8	0.0199	0.9487	-0.1104	0.5300	-2.06	0.235	529	0.0896
9	0.0246	1.0084	-0.2225	0.4759	-3.90	0.296	588	0.0978
10	0.0299	1.0623	-0.3206	0.4351	-5.34	0.363	647	0.1064
11	0.0358	1.1095	-0.4041	0.3900	-6.46	0.437	705	0.1153
12	0.0492	1.1863	-0.5338	0.2975	-8.06	0.604	823	0.1339
13	0.0651	1.2306	-0.6050	0.1583	-8.87	0.800	944	0.1535
14	0.0938	1.2462	-0.6295	-0.0137	-9.14	1.152	1131	0.1841
15	0.1281	1.2402	-0.6201	-0.0594	-9.03	1.573	1323	0.2152
16	0.1675	1.2316	-0.6066	-0.0558	-8.87	2.056	1513	0.2462
17	0.2113	1.2236	-0.5943	-0.0518	-8.75	2.595	1701	0.2767
18	0.2591	1.2180	-0.5850	-0.0449	-8.64	3.182	1884	0.3065
19	0.3101	1.2126	-0.5765	-0.0515	-8.55	3.809	2063	0.3354
20	0.3636	1.2071	-0.5676	-0.0721	-8.45	4.467	2235	0.3634
21	0.4190	1.1990	-0.5544	-0.1315	-8.30	5.146	2400	0.3903
22	0.4754	1.1864	-0.5339	-0.2205	-8.06	5.836	2559	0.4162
23	0.5132	1.1762	-0.5172	-0.2203	-7.86	6.300	2661	0.4329
24	0.5508	1.1704	-0.5076	-0.1231	-7.75	6.761	2758	0.4488
25	0.5882	1.1663	-0.5008	-0.1882	-7.67	7.218	2850	0.4640
26	0.6250	1.1558	-0.4831	-0.4625	-7.45	7.666	2940	0.4788
27	0.6610	1.1419	-0.4596	-0.6677	-7.17	8.101	3027	0.4933
28	0.6962	1.1257	-0.4320	-0.9785	-6.82	8.521	3109	0.5074
29	0.7302	1.1058	-0.3976	-1.6025	-6.38	8.919	3188	0.5213
30	0.7631	1.0826	-0.3568	-2.8420	-5.84	9.293	3262	0.5351
31	0.7946	1.0553	-0.3080	-	-5.16	9.634	3333	0.5490
32	0.8246	1.0225	-0.2483	-	-4.29	9.933	3399	0.5636
33	0.8532	0.9820	-0.1732	-	-3.12	10.172	3461	0.5799
34	0.8803	0.9366	-0.0874	-	-1.65	10.345	3519	0.5982
35	0.9059	0.8960	-0.0094	-	-0.18	10.479	3573	0.6169

Table 14.2: Properties of mean boundary layer

N	y_δ	y_{δ^*}	H	R	$W_{\max}$	ε_i (deg)	$C_Q \times 10^3$
1	3.847	1.0800	2.693	239	0	0	0
2	3.843	1.0428	2.603	234	-0.0408	-1.977	0
3	3.891	1.0157	2.538	259	-0.0936	-4.362	0
4	3.950	0.9914	2.506	299	-0.1146	-5.142	0
5	3.980	0.9511	2.480	338	-0.1116	-4.857	0.735
6	4.017	0.9372	2.513	386	-0.0984	-4.198	0.700
7	4.115	0.9819	2.614	462	-0.0866	-3.654	0.630
8	4.218	1.0274	2.689	544	-0.0783	-3.283	0.530
9	4.344	1.0921	2.787	642	-0.0717	-3.004	0.430
10	4.475	1.1590	2.870	749	-0.0669	-2.795	0.290
11	4.632	1.2468	2.974	879	-0.0633	-2.632	0.163
12	4.900	1.3860	3.106	1141	-0.0568	-2.341	0.155
13	5.141	1.5201	3.229	1435	-0.0485	-1.963	0.143
14	5.442	1.7004	3.352	1924	-0.0337	-1.317	0.143
15	5.635	1.8110	3.398	2395	-0.0215	-0.840	0.143
16	5.709	1.8341	3.371	2776	-0.0111	-0.520	0.143
17	5.732	1.8292	3.345	3112	-0.0094	-0.349	0.143
18	5.721	1.8030	3.306	3397	-0.0065	-0.242	0.143
19	5.706	1.7815	3.287	3675	-0.0046	-0.170	0.143
20	5.685	1.7603	3.265	3934	-0.0031	-0.117	0.143
21	5.685	1.7608	3.270	4226	0.0059	0.273	0.143
22	5.701	1.7754	3.279	4653	0.0113	0.637	0.143
23	5.708	1.7825	3.280	4743	0.0148	0.851	0.143
24	5.623	1.7076	3.184	4709	0.0155	0.853	0.214
25	5.494	1.6023	3.079	4567	0.0155	0.816	0.288
26	5.369	1.5099	2.997	4440	0.0191	1.011	0.370
27	5.217	1.4001	2.894	4238	0.0251	1.478	0.490
28	5.028	1.2685	2.770	3944	0.0309	1.873	0.610
29	4.827	1.1350	2.650	3618	0.0369	2.241	0.755
30	4.608	0.9964	2.523	3250	0.0432	2.601	0.930
31	4.392	0.8694	2.409	2898	0.0498	2.975	1.090
32	4.205	0.7671	2.317	2608	0.0579	3.441	1.215
33	4.062	0.6933	2.245	2399	0.0690	4.100	1.300
34	3.952	0.6344	2.172	2233	0.0816	4.854	1.380
35	3.853	0.5780	2.097	2065	0.0912	5.330	1.450

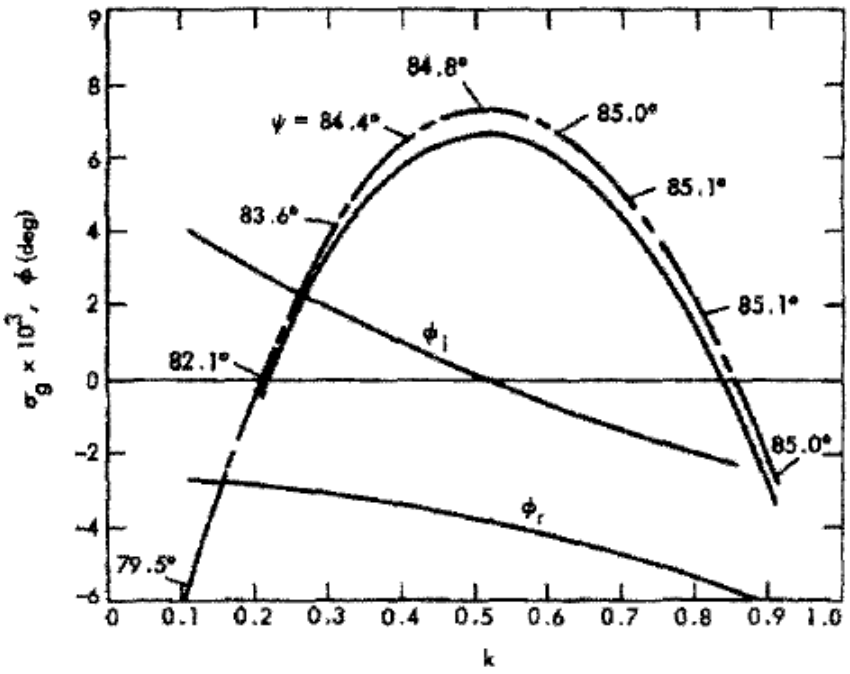

Figure 14.2: Amplification rate, wave angle, and group-velocity angle as functions of wavenumber at $N = 4$ ($R = 301$) for $F = 0$: $- \cdot -$, incompressible theory; —,sixth-order compressible theory; 35° swept wing.

14.2 Crossflow instability

Surprisingly little crossflow is required for crossflow instability to occur. For example, it was found with the similar boundary layers of Chapter 13 that for $\beta_h = \pm 0.02$ and $\psi_{sw} + \psi_p = 45°$ (the angle that generates the maximum crossflow for a given pressure gradient), the critical Reynolds number of crossflow instability for both boundary layers is close to 1100 even though $W_{\max}$ is only about 0.6%.

Figure 14.2 gives gives a comparison of the distribution of the amplification rate σ_g with the magnitude of the wavenumber vector $\vec{k}$ as computed at $N = 4$ from both the incompressible and sixth-order compressible stability theories. It is evident that the incompressible theory gives reasonably good results, with $\sigma_{\max} = 7.30 \times 10^{-3}$ compared to 6.59×10^{-3} from the compressible theory, a difference of 10.8%. The eigth-order compressible equations give $\sigma_{\max} = 6.51 \times 10^{-3}$, a difference of only 1.2% from the sixth-order system. Consequently, there is little reason to use the eighth-order system, and for a general study of crossflow instability near the leading edge the incompressible theory is adequate.

The angle ψ of the wavenumber vector as computed from the incompressible theory is also shown in Fig. 14.2. Almost identical results are given by the compressible theory. The narrow bandwidth of unstable ψ and wide bandwidth of unstable k is characteristic of crossflow instability. The sharpness of the angular "tuning" increases as the crossflow decreases. For example, at $N = 17$ where $W_{\max} = -0.0094$, the bandwidth of unstable k is about the same as in Fig. 14.2, but the bandwidth of unstable ψ is only 0.15°.

It is of interest to note that the angle $\psi = 84.8°$ at the maximum amplification rate is almost identical to the angle $90 - |\varepsilon_i|$ ($= 84.9°$), where ε_i is the angle defined in Section 14.1 and listed in Table 14.2. The near equality of these two angles has been found to be true in general for crossflow instability as $90 - |\varepsilon_i|$ is given the sign of $W_{\max}$. When there are two inflection points and W has the same sign at each ($15 \le N \le 20$), it is the outer point, where DW is a maximum, that is significant for instability. When W has opposite signs at the two inflection points ($21 \le N \le 26$), it is the inner point, where DW is a minimum, that is significant. The above convenient relation between ψ and ε_i makes it easy to compute an initial eigenvalue for crossflow instability.

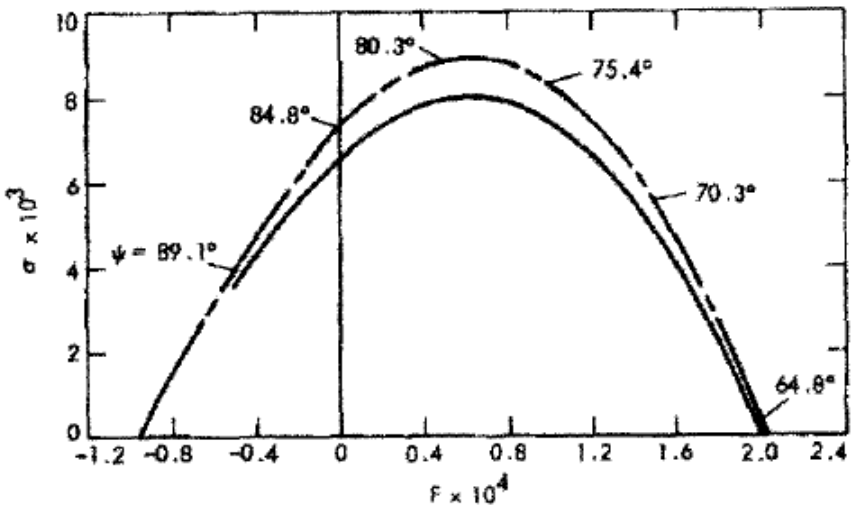

Figure 14.3: Unstable frequency range at $N = 4$ ($R = 301$) for $k = 0.520$: $- \cdot -$, incompressible theory; —, sixth-order compressible theory; 35° swept wing.

The real and imaginary parts of ϕ are also shown in Fig. 14.2. The real part, ϕ_r, has the same sign as $W_{\max}$, and ϕ_r at $k_{\max}$, the wavenumber for maximum amplification rate, is proportional to $W_{\max}$. At $k_{\max}$, $\psi - \phi_r = 88.6°$. Further back on the wing, this difference approaches 90° as the crossflow diminishes. The imaginary part of ϕ, ϕ_i, reverses sign at the point of maximum amplification rate, a behavior that is true at all stations.

Although crossflow instability has been defined as the existence of unstable steady disturbances, a whole band of frequencies becomes unstable at about the same critical Reynolds number. Figure 14.3 gives σ as a function of F at $N = 4$ as calculated from both the incompressible and sixth-order compressible theories for $k = 0.520$, and the $k_{\max}$ of $F = 0$. It is apparent that the effect of compressibility is about the same for all frequencies as for $F = 0$. The values of $\sigma_{\max} \times 10^3$ for $k = 0.520$ are: incompressible, 8.91; sixth-order compressible, 8.00; eighth-order compressible, 7.90.

There are both positive and negative unstable frequencies in Fig. 14.3. The negative frequencies simply mean that with the direction of $\vec{k}$ defined by the values of ψ shown in the figure, the phase velocity is negative. If, instead, the direction of $\vec{k}$ had been defined in the usual manner to be the direction of the phase velocity, there would be two groups of positive unstable frequencies. For the positive frequencies of Fig. 14.3, $\vec{k}$ is within 25° of the direction opposite to the crossflow; for the negative frequencies, $\vec{k}$ is within 5° of the direction of the crossflow. The sign convention of Fig. 14.3 has been adopted so that the maximum instability will always be associated with a positive frequency, and this nonstandard definition of $\vec{k}$ is used here, as in Section 13.3, to make it easier to plot the numerical results.

There is a wide band of unstable frequencies in Fig. 14.3. The dimensional frequency corresponding to $F = 2.0 \times 10^4$ is 57.8 kHz, and the most unstable frequency is about 17 kHz. The unstable bandwidth becomes much narrower further downstream as both the crossflow and maximum amplificatoin rate decrease. It was found in Mack (1979b) that for a boundary layer with crossflow instability only, $k_{\max}$ does not vary much with frequency for $F > 0$. For $F < 0$, $k_{\max}$ does change with frequency. It is estimated from Chap. 13 that the unstable region of negative frequencies at $N = 4$ extends to $F = -1.5 \times 10^{-4}$ with $\psi = 92°$, and that the maximum amplification rate of the wave with $\vec{k}$ in the crossflow direction is about one-half of that for the steady disturbance.

As crpssflow instability is an example of inflectional instability, it is possible to deduce something about the stability characteristics from the location of the inflection point of the relevant velocity profile. It is not necessary for this purpose to consider the generalized inflection point of the compressible theory which is little different from the true inflection point at transonic Mach numbers. The relevant velocity profile is the one in the direction of $\vec{k}$. For the most unstable stationary wave ($\psi = 84.8°$), this profile has reverse flow,

and the inflection point occurs almost at the zero velocity point in accordance with the theory of Stuart (Gregory et al., 1955). Inflectional profiles exist for ψ both greater and less than 84.8°. The sign of the mean velocity at the inflection point determines the sign of the frequency (except very near $F = 0$ because of the finite Reynolds number). The profiles with $\psi > 84.8°$ give the negative frequencies; the profiles with $\psi < 84.8°$ the positive frequencies.

14.3 Streamwise instability

Along with crossflow instability, which is particular to three-dimensional boundary layers, there are also inflectional and viscous instabilities which are more like those of a two-dimensional boundary layer, but with modifications due to the crossflow. This type of instability will be called streamwise instability, and it refers to all instabilities that are not associated with a directional velocity profile of the type of the crossflow and reverse-flow profiles.

As suction is more effective at controlling streamwise than crossflow instability, only the latter instability is present over most of the wing chord in the present flow example. The region of streamwise instability starts at $N = 14$ ($s^*/c^* = 0.094$), according to the compressible theory, and extends to $N = 25$ ($s^*/c^* = 0.588$). Some stability characteristics at $N = 15$ ($s^*/c^* = 0.128$), where the edge Mach number of 1.24 is close to tits maximum value, are shown in Fig. 14.4. Figure 14.4a gives the distributions of $\sigma_{\max}$ and F with wave angle from the incompressible and sixth-order compressible theories. The crossflow instability region ($\psi > 80°$) is not shown. The crossflow ($W_{\max} = -0.0215$) has introduced an asymmetry into the distributions, but otherwise the results resemble what might have been expected from assuming that 2D results could be applied to 3D boundary layers. The two maxima in the amplification rate of the compressible theory contrast with the single maximum of the incompressible theory, and are in complete accord with 2D stability theory at $M_1 = 1.24$.

The reason that Fig. 14.4a resembles the results for a two-dimensional flat-plate boundary layer with no suction is that the shape factor H at $N = 15$ is almost the same as for such a boundary layer at the same Mach number, and the crossflow is not only small, but still in the direction associated with a favorable pressure gradient. The two inflection points of the directional velocity profiles, which exist for $-90° < \psi < -60°$, are unimportant except near $\psi = -90°$, because one is located near the wall and the other at the edge of the boundary layer. Consequently, what Fig. 14.4 shows is viscous instability, just as for a flat-plate boundary layer at the same Mach number.

The maximum amplification rate with respect to wavenumber is shown in Fig. 14.4b as a function of frequency for both crossflow and streamwise instability. It is evident that the incompressible theory gives a totally misleading result as to the importance of streamwise instability at this station. The two maxima of Fig. 14.4a are shown by two separate curves. The crossflow instability has the same general features as at $N = 4$, but with and unstable frequency band only about one-seventh as wide (cf. Fig 14.3). Also the corresponding ψ are much closer to 90° for both positive and negative frequencies: $83.8° < \psi < 89.4°$ for $F > 0$; $89.4° < \psi < 90.4°$ for $F < 0$. It might also be observed that for $\psi = 90°$, the maximum amplification rate is about one-half of its $F = 0$ value, as surmised for $N = 4$.

The term streamwise instability covers such a wide variety of possibilities that it is worthwhile to give an additional example. Figure 14.5 is the counterpart at $N = 23$ ($s^*/c^* = 0.513$) to Fig. 14.4. At this station, the crossflow over the inner two-thirds of the boundary layer has reversed, but is even smaller than at $N = 15$ ($W_{\max} = 0.0113$). The adverse pressure gradient is larger ($\beta_h = -0.22$), but because the suction is also larger there is still no inflection point in the streamwise velocity profile.

It is seen from Fig. 14.5a that the waves with $\psi < 0$ are much more unstable than those with $\psi > 0$ even though the maximum crossflow is positive. The reason is that for $\psi < -40°$ the directional velocity profiles have inflection points well out in the boundary layer (e.g., at $U = 0.30$ for $\psi = -70°$). A significant difference between Fig. 14.5 and Fig. 14.4 is that the smooth $\sigma_{\max}$ curves of the former do not permit a clear distinction to be made between crossflow and streamwise instability. The frequencies near zero (say, $F < 0.04 \times 10^{-4}$) have the characteristics of crossflow instability (wide band of unstable wavenumbers, narrow band of unstable angles); the larger frequencies (say, $F > 0.12 \times 10^{-4}$) have the characteristics of streamwise instability (narrow band of unstable wavenumbers, wide band of unstable angles). The intermediate frequencies, including the most unstable, have the characteristics of streamwise instability for a narrow band of small wavenumbers,

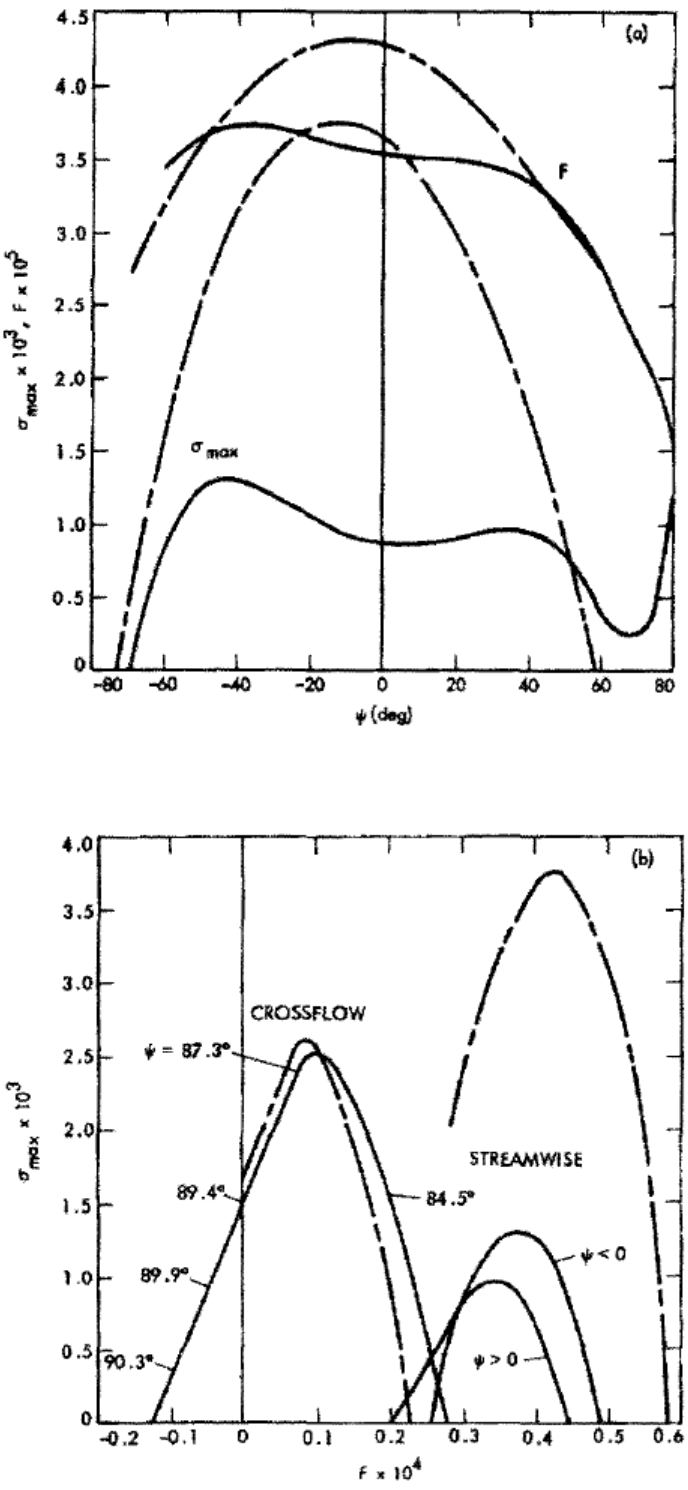

Figure 14.4: Crossflow and streamwise instability at $N = 15$ ($R = 1323$); (a) maximum amplification rate (with respect to frequency) and frequency as functions of wave angle; (b) maximum amplification rate (with respect to wavenumber) as function of frequency: $- \cdot -$, incompressible theory; —, sixth-order compressible theory; 35° swept wing.

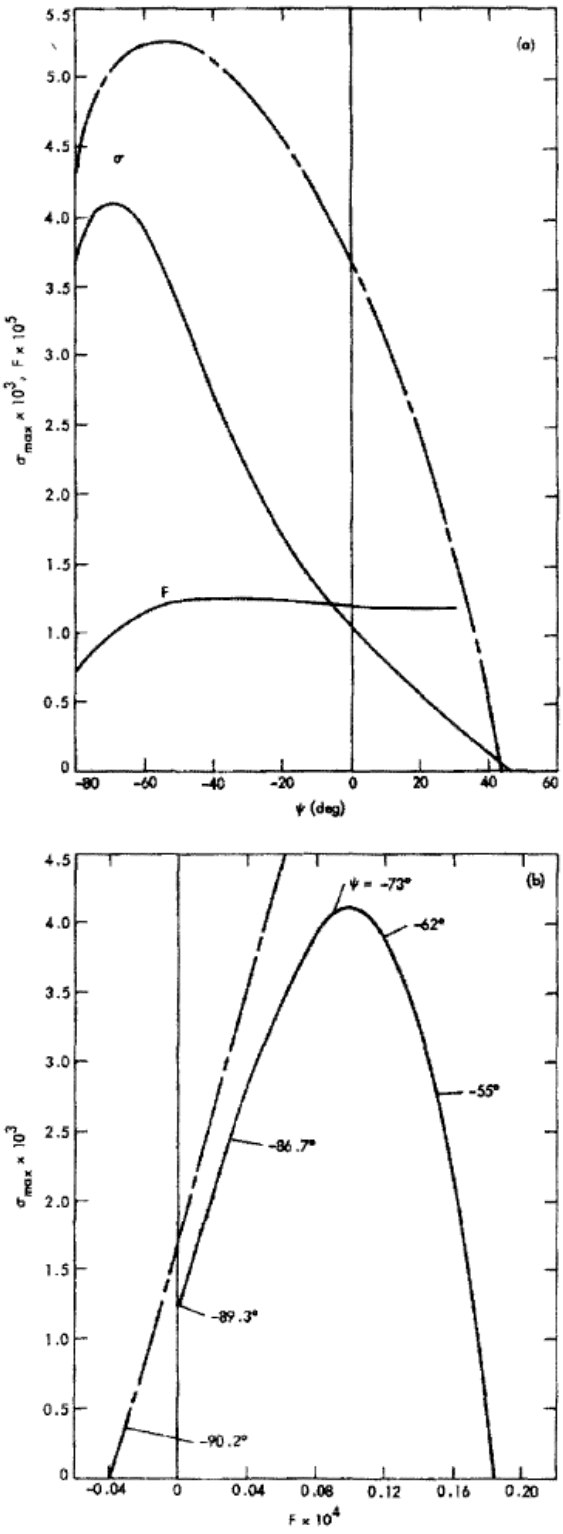

Figure 14.5: Crossflow and streamwise instability at $N = 23$ ($R = 2661$). (a) Maximum amplification rate (with respect to frequency) and frequency as function of wavenumber angle; (b) maximum amplification rate (with respect to wavenumber) as function of frequency: $- \cdot -$, incompressible theory; —, sixth-order compressible theory; 35° swept wing.

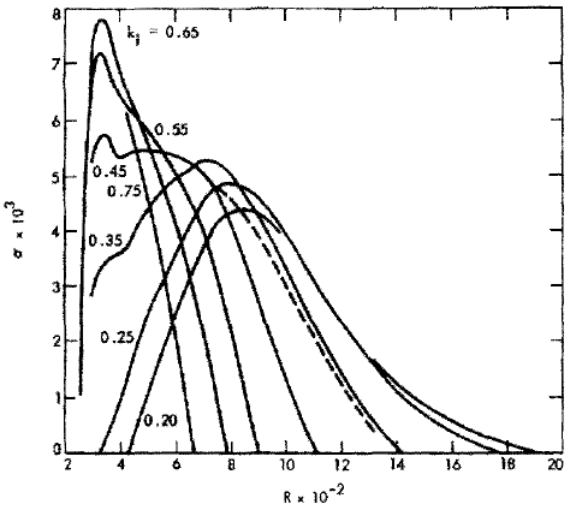

Figure 14.6: Amplification rates of seven zero-frequency wave components in forward instability region of 35° swept wing with irrotationality condition applied to wavenumber vector: —, incompressible theory; - - -, sixth-order compressible theory for $k_1 = 0.35$.

and of crossflow instability for a wide band of larger wavenumbers.

The effect of compressibility is large and similar to that at $N = 15$ (Fig. 14.4) in the streamwise instability region, and is also a good deal larger in the crossflow instability region than at either $N = 4$ (Figs. 14.3 and 14.4) or $N = 15$. Indeed the peak amplification rate of the incompressible theory differs by 27% from the sixth-order compressible value and the corresponding wave angle by 15°, whereas the maximum incompressible amplification rate of the steady disturbances is in error by 40%. The latter difference decreases further back on the wing as the amplification rate increases (to 14% at $N = 35$), but is always larger than in the negative crossflow region on the forward part of the wing.

It is important to note the narrow bandwidth of unstable frequencies in Fig. 14.5b compared to Figs. 14.4b and 14.3. The largest unstable frequency at $N = 23$ is only 5.2 kHz, and the most unstable frequency is 2.9 kHz. Consequently, almost all unstable frequencies that exist upstream of $N = 23$ cannot persist to this station as amplified waves even when they are kinematically possible.

14.4 Wave amplitude

The wave amplitude rather than the local amplification rate is what is of interest in transition studies. In this section, the irrotationality condition on $\vec{k}$ will be applied to the calculation of amplitude ratios of single Fourier components. The SALLY stability code of Srokowski and Orszag (1977) calculates $\ln(A/A_0)$ by what is called the envelope method, i.e., by integrating $(\sigma_g)_{\max}$ along the trajectory defined by the real part of the group velocity. As a result, the amplitude ratio increases monotonically to the end of hte instability region. Here, a band of wavenumbers with the same frequency is followed downstream starting at the first unstable station, $N = 3$ ($s^*/c^* = 0.0033$). The resulting amplification rates for seven initial wavenumbers with zero frequency are shown in Fig. 14.6 as computed from the incompressible theory. The listed initial wavenumbers are those at $N = 3$. For comparison, a portion of the $k_i = 0.35$ curve as computed from the sixth-order compressible theory is also shown.

For $R < 1000$, the different initial wavenumbers in Fig. 14.6 act much like different frequencies in a 2D boundary layer. The lower the initial wavenumber, the further downstream is its unstable region. For $R > 1000$, a rather different pattern is apparent in Fig. 14.6. The initial wavenumber of the wave component which has the maximum amplification rate at a given station becomes a slowly varying function of Reynolds number. In other words, a single Fourier component is nearly the most unstable over a wide range of

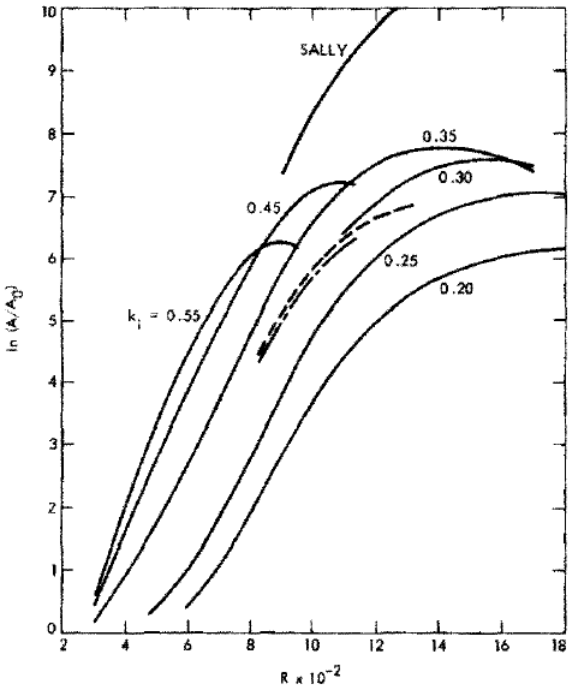

Figure 14.7: $\ln(A/A_0)$ of six zero-frequency wave components in forward instability region of 35° swept wing with irrotationality condition applied to wavenumber vector and comparison with SALLY code; —, incompressible theory; - - -, sixth-order compressible theory for $k_1 = 0.35$; $- \cdot -$, eighth-order compressible theory for $k_1 = 0.35$.

Reynolds numbers. it is this pattern that prevails in the entire rear crossflow instability region. There the wave component with $k_i = 0.35$ at $N = 21$ ($R = 2400$, $s^*/c^* = 0.419$) is the most unstable from $R = 2600$ to at least $R = 3570$ ($s^*/c^* = 0.906$). Consequently, in this region the procedure we are using here gives the same result for the amplitude ratio as does the SALLY code.

The $\ln(A/A_0)$ values that correspond to the amplification rates of Fig. 14.6 are shown in Fig 14.7 for six Fourier components along with the result given by the SALLY code (computed by Dr. A. Srokowski). The present method gives a peak in the envelope curve, $\ln(A/A_0)_{\max}$ vs. R, at about $R = 1400$ ($s^*/c^* = 0.128$). In contrast, the curve from the SALLY code continues to rise to a value of $\ln(A/A_0) = 11.2$ at $R = 1880$ ($s^*/c^* = 0.259$). The peak with the irrotationality condition is a consequence of following Fourier components from a more unstable region to a less unstable region, and can also be encountered in 2D boundary layers with laminar-flow control.

Two additional curves included in Fig. 14.7 give $\ln(A/A_0)$ for $k_i = 0.35$ as computed from the sixth- and eighth-order compressible equations. The peak $\ln(A/A_0)$ of the latter is about 6.9 compared to 7.8 from the incompressible theory and 11.2 from the SALLY program. Consequently, the method of integrating the maximum amplification rate overestimates the peak amplitude ratio by over 70 times.

As both Figs. 14.3 and 14.4b show that a non-zero frequency has the maximum amplification rate for crossflow instability, it is also a non-zero frequency that gives the maximum amplitude ratio. The possible importance of these frequencies is, however, counteracted by the narrowing of the unstable frequency bandwidth in the downstream direction. The results is that at $N = 15$ the frequency with the maximum amplitude ratio is the low frequency $F = 0.05 \times 10^4$ (1.4 kHz), and the peak $\ln(A/A_0)$ of this frequency is only 2% larger than for zero frequency. Of course, larger differences than this exist upstream of $N = 15$ where higher frequencies are still unstable.

at station $N = 35$ in the rear crossflow instability region, the amplitude ratio of the most unstable zero-frequency wave component, $k_i = 0.35$, is 6.54 according to the incompressible theory, a result almost

identical to the SALLY value of $n = 6.46$. However, compressibility cannot be neglected in this region as it was in the forward instability region. The sixth-order compressible theory gives $ln(A/A_0) = 5.25$ at $N = 35$; thus the incompressible theory overestimates $\ln(A/A_0)$ by 25%.

Streamwise instability is limited to the region from $N = 15$ to $N = 25$ ($s^*/c^* = 0.588$) and leads to smaller amplitude ratios than does crossflow instability. As these waves travel downstream, their wave angle ψ remains very close (within about 1°) to its initial value, in contrast to the crossflow disturbances which are required by the dispersion relation to keep their angles within the narrow band set by the profile angle ε_i. According to Fig. 14.7b, $F = 0.375 \times 10^{-4}$ is the most unstable frequency for streamwise instability at $N = 15$. However, this and the neighboring unstable frequencies damp out quickly in the downstream direction. The frequencies which give the largest amplitude ratios are those which are unstable at $N = 23$ ($s^*/c^* = 0.513$), where the largest amplification rates of streamwise instability occur. For example, $F = 0.09 \times 10^{-4}$ becomes unstable at $N = 21$ and has a peak $\ln(A/A_0)$ of 2.3 at $N = 25$ for an initial wave angle of $-70°$; $F = 0.15 \times 10^{-4}$ becomes unstable at $N = 20$ and has a smaller peak at $N = 24$. Consequently, the maximum amplitude growth of streamwise-instability waves is only about 1% of that of the crossflow disturbances. Examples of amplification rates for a wing without suction may be found elsewhere (Mack, 1981).

Appendix A

Coefficient Matrix of Compressible Stability Equations

There are 30 non-zero elements of the coefficient matrix $a_{i,j}(y)$ of Eq. 8.11. The Z_1 equation has only one non-zero coefficient:

$$a_{12} = 1. \tag{A.1}$$

The Z_2 equation has six non-zero coefficients:

$$a_{21} = \frac{iR}{\mu T}\left(\alpha U + \beta W - \omega\right) + \alpha^2 + \beta^2, \tag{A.2a}$$

$$a_{22} = -\frac{1}{\mu}\frac{d\mu}{dT}DT, \tag{A.2b}$$

$$a_{23} = \frac{R}{\mu T}\left(\alpha DU + \beta DW\right) - i\frac{1}{\mu}\left(\alpha^2 + \beta^2\right)\frac{d\mu}{dT}DT - i\frac{1}{3}\left(1 + 2d\right)\left(\alpha^2 + \beta^2\right)\frac{DT}{T}, \tag{A.2c}$$

$$a_{24} = \frac{iR}{\mu}\left(\alpha^2 + \beta^2\right) - \frac{1}{3}\left(1 + 2d\right)\left(\alpha^2 + \beta^2\right)\gamma M_1^2\left(\alpha U + \beta W - \omega\right), \tag{A.2d}$$

$$a_{25} = \frac{1}{3}\frac{1}{T}\left(1 + 2d\right)\left(\alpha^2 + \beta^2\right)\left(\alpha U + \beta W - \omega\right) - \frac{1}{\mu}\frac{d\mu}{dT}\left(\alpha D^2U + \beta D^2W\right) - \frac{1}{\mu}\frac{d^2\mu}{dT^2}DT\left(\alpha DU + \beta DW\right), \tag{A.2e}$$

$$a_{26} = -\frac{1}{\mu}\frac{d\mu}{dT}\left(\alpha DU + \beta DW\right). \tag{A.2f}$$

The Z_3 equation has four non-zero coefficients:

$$a_{31} = -i, \tag{A.3a}$$

$$a_{33} = \frac{DT}{T}, \tag{A.3b}$$

$$a_{34} = -i\gamma M_1^2\left(\alpha U + \beta W - \omega\right), \tag{A.3c}$$

$$a_{35} = \frac{i}{T}\left(\alpha U + \beta W - \omega\right). \tag{A.3d}$$

The Z_4 equation is the only one that requires a lengthy manipulation to derive. With

$$E = \frac{R}{\mu} + i\frac{2}{3}(2+d)\gamma M_1^2(\alpha U + \beta W - \omega), \tag{A.4}$$

the six non-zero coefficients are

$$a_{41} = -\frac{i}{E}\left[\frac{2}{\mu}\frac{d\mu}{dT}DT + \frac{2}{3}(2+d)\frac{DT}{T}\right], \tag{A.5a}$$

$$a_{42} = -\frac{i}{E}, \tag{A.5b}$$

$$a_{43} = \frac{1}{E}\left[-\left(\alpha^2+\beta^2\right) + \frac{2}{3}(2+d)\frac{DT^2}{T}\frac{1}{\mu}\frac{d\mu}{dT} + \frac{2}{3}(2+d)\frac{D^2T}{T} - \frac{iR}{\mu T}(\alpha U + \beta W - \omega)\right], \tag{A.5c}$$

$$a_{44} = -\frac{i}{E}\frac{2}{3}(2+d)\gamma M_1^2\left[(\alpha U + \beta W - \omega)\frac{1}{\mu}\frac{d\mu}{dT}DT + \alpha DU + \beta DW + \frac{DT}{T}(\alpha U + \beta W - \omega)\right], \tag{A.5d}$$

$$a_{45} = \frac{i}{E}\left[\frac{1}{\mu}\frac{d\mu}{dT}(\alpha DU + \beta DW) + \frac{2}{3}(2+d)\left(\frac{1}{\mu}\frac{d\mu}{dT}\frac{DT}{T}(\alpha U + \beta W - \omega) + \frac{(\alpha DU + \beta DW)}{T}\right)\right], \tag{A.5e}$$

$$a_{46} = \frac{i}{E}\frac{2}{3}(2+d)(\alpha U + \beta W - \omega). \tag{A.5f}$$

The Z_5 equation has only one non-zero coefficient:

$$a_{56} = 1. \tag{A.6}$$

The Z_6 equation has six non-zero coefficients:

$$a_{62} = -2\sigma(\gamma-1)M_1^2\frac{(\alpha DU + \beta DW)}{(\alpha^2+\beta^2)}, \tag{A.7a}$$

$$a_{63} = \frac{R\sigma}{\mu}\frac{DT}{T} - i2\sigma(\gamma-1)M_1^2(\alpha DU + \beta DW), \tag{A.7b}$$

$$a_{64} = -i\frac{R\sigma}{\mu}(\gamma-1)M_1^2(\alpha U + \beta W - \omega), \tag{A.7c}$$

$$a_{65} = i\frac{R\sigma}{\mu T}(\alpha U + \beta W - \omega) + \alpha^2 + \beta^2 - \frac{D^2T}{\kappa}\frac{d\kappa}{dT} - \frac{DT^2}{\kappa}\frac{d^2\kappa}{dT^2} - \sigma(\gamma-1)M_1^2\frac{1}{\mu}\frac{d\mu}{dT}\left(DU^2 + DW^2\right), \tag{A.7d}$$

$$a_{66} = -\frac{2}{\kappa}\frac{d\kappa}{dT}DT, \tag{A.7e}$$

$$a_{68} = -2\sigma(\gamma-1)M_1^2\frac{(\alpha DW - \beta DU)}{(\alpha^2+\beta^2)}. \tag{A.7f}$$

The Z_7 equation has only one non-zero coefficient:

$$a_{78} = 1. \tag{A.8}$$

The Z_8 equation has five non-zero coefficients:

$$a_{83} = \frac{R}{\mu T}\left(\alpha DW - \beta DU\right), \tag{A.9a}$$

$$a_{85} = -\frac{1}{\mu}\frac{d\mu}{dT}\left(\alpha D^2 W - \beta D^2 U\right) - \frac{1}{\mu}\frac{d^2\mu}{dT^2} DT\left(\alpha DW - \beta DU\right), \tag{A.9b}$$

$$a_{86} = -\frac{1}{\mu}\frac{d\mu}{dT}\left(\alpha DW - \beta DU\right), \tag{A.9c}$$

$$a_{87} = \frac{iR}{\mu T}\left(\alpha U + \beta W - \omega\right) + \alpha^2 + \beta^2, \tag{A.9d}$$

$$a_{88} = -\frac{1}{\mu}\frac{d\mu}{dT} DT. \tag{A.9e}$$

In these equations, the ratio of the second to the first viscosity coefficient

$$d = \frac{\lambda}{\mu} \tag{A.10}$$

is taken to be a constant and equal to 1.2. (Stokes' assumption corresponds to $\lambda = 0$).

In the numerical computations, we use

$$\begin{aligned} \mu^* \times 10^5 &= 1.458\frac{T^{*3/2}}{T^* + 110.4}, \quad && T^* \geq 110.4\text{K} \\ &= 0.0693873 T^*, && T^* < 110.4\text{K} \end{aligned} \tag{A.11}$$

for the viscosity coefficient in cgs units, and

$$\kappa^* = 0.6325\frac{T^{*1/2}}{1 + \left(245.4/T^*\right) 10^{-12/T^*}} \tag{A.12}$$

for the thermal conductivity coefficient in cgs units. The Prandtl number $\sigma = c_p^* \mu^* / \kappa^*$ is computed as a function of temperature from μ^*, κ^*, and a constant specific heat of $c_p^* = 0.24$.

Appendix B

Freestream Solutions of Compressible Stability Equations

In the freestream $U = U_1$, $W = W_1$, $T = 1$, $\mu = 1$, $\kappa = 1/\sigma_1$, and all y derivatives of mean-flow quantities are zero. The first six of Eqs. 8.11 can be written as three second-order equations:

$$D^2 V_1 = b_{11} V_1 + b_{12} V_2 + b_{13} V_3, \tag{B.1a}$$

$$D^2 V_2 = b_{22} V_2 + b_{23} V_3, \tag{B.1b}$$

$$D^2 V_3 = b_{32} V_2 + b_{33} V_3, \tag{B.1c}$$

where

$$V_1 = Z_z, \qquad V_2 = Z_4, \qquad V_3 = Z_5. \tag{B.2}$$

The three coefficients of Eq. B.1a are

$$b_{11} = \alpha^2 + \beta^2 + iR\left(\alpha U_1 + \beta W_1 - \omega\right), \tag{B.3a}$$

$$b_{12} = i\left(\alpha^2 + \beta^2\right)\left[R + \frac{i}{3}(1+d)\gamma M_1^2\left(\alpha U_1 + \beta W_1 - \omega\right)\right], \tag{B.3b}$$

$$b_{13} = -(1+2d)\left(\alpha^2 + \beta^2\right)\left(\alpha U_1 + \beta W_1 - \omega\right). \tag{B.3c}$$

The two coefficients of Eq. B.1b are

$$b_{22} = \alpha^2 + \beta^2 - \frac{R}{E_1}\left[\gamma M_1^2 - \frac{2}{3}(2+d)\sigma(\gamma-1)M_1^2\left(\alpha U_1 + \beta W_1 - \omega\right)\right], \tag{B.4a}$$

$$b_{23} = \frac{R}{E_1}\left[1 - \frac{2}{3}(2+d)\sigma\right]\left(\alpha U_1 + \beta W_1 - \omega\right). \tag{B.4b}$$

where E_1 is Eq. A.4 evaluated in the freestream. The two coefficients of Eq. B.1c are

$$b_{32} = -i(\gamma-1)M_1^2\sigma\left(\alpha U_1 + \beta W_1 - \omega\right), \tag{B.5a}$$

$$b_{33} = \alpha^2 + \beta^2 + i\sigma R\left(\alpha U_1 + \beta W_1 - \omega\right). \tag{B.5b}$$

The six solutions of Eqs. B.1 have the form

$$V^{(i)}(y) = B^{(i)}\exp(\lambda_i y), \quad (i = 1, 6), \tag{B.6}$$

where the $V^{(i)}$ are the six three-component solution vectors, the λ_i are the six characteristic values, and the $B^{(i)}$ are the six three-component characteristic vectors. Upon substituting Eq. B.6 into Eqs. B.1, the

characteristic values are found to be

$$\lambda_{1,2} = \mp \left\{ \frac{1}{2}\left(b_{22}+b_{33}\right) - \left[\frac{1}{4}\left(b_{22}-b_{33}\right)^2 + b_{23}b_{32}\right]^{1/2} \right\}^{1/2}, \tag{B.7a}$$

$$\lambda_{3,4} = \mp \left(b_{11}\right)^{1/2}, \tag{B.7b}$$

$$\lambda_{5,6} = \mp \left\{ \frac{1}{2}\left(b_{22}+b_{33}\right) + \left[\frac{1}{4}\left(b_{22}-b_{33}\right)^2 + b_{23}b_{32}\right]^{1/2} \right\}^{1/2}, \tag{B.7c}$$

$$\tag{B.7d}$$

where the numbering has been arranged so that the first two of these will correspond to the first two of Eq. 2.49.

The last two of Eqs. 8.11 give a fourth uncoupled second-order equation

$$D^2 Z_7 = \left[\alpha^2 + \beta^2 + iR\left(\alpha U_1 + \beta W_1 - \omega\right)\right] Z_7, \tag{B.8}$$

with characteristic values

$$\lambda_{7,8} = \mp \left[\alpha^2 + \beta^2 + iR\left(\alpha U_1 + \beta W_1 - \omega\right)\right]^{1/2}, \tag{B.9}$$

which are the same as the characteristic values $\lambda_{3,4}$.

The components of the characteristic vector corresponding to λ_3 are

$$B_1^{(3)} = 1, \qquad B_2^{(3)} = 0, \qquad B_3^{(3)} = 0, \tag{B.10}$$

and to λ_1 and λ_5 are,

$$B_1^{(j)} = \frac{b_{12}\left(b_{33}-\lambda_j^2\right) - b_{13}b_{32}}{\lambda_j^2 - b_{11}}, \tag{B.11a}$$

$$B_2^{(j)} = b_{33} - \lambda_j^2, \tag{B.11b}$$

$$B_3^{(j)} = -b_{32}. \tag{B.11c}$$

$$\tag{B.11d}$$

The components of the characteristic vectors of the original solutions are:

$$\begin{aligned} &A_1^{(j)} = B_1^{(j)}, \qquad A_2^{(j)} = \lambda_j B_1^{(j)}, \qquad A_4^{(j)} = B_2^{(j)}, \\ &A_5^{(j)} = B_3^{(j)}, \qquad A_6^{(j)} = \lambda_j B_3^{(j)}, \qquad (j = 1, 6), \end{aligned} \tag{B.12}$$

and the component $A_3^{(j)}$ is found from the continuity equation:

$$\lambda_j A_3^{(j)} = -iB_1^{(j)} - i\left(\alpha U_1 + \beta W_1 - \omega\right)\left(\gamma M_1^2 B_2^{(j)} - B_3^{(j)}\right). \tag{B.13}$$

References

Bellman, R.E. and Kalaba, R.E. 1965 Quasilinearization and Boundary-Value Problems, American Elsevier, N.Y.

Betchov, R. and Criminale, W.O. 1967 Stability of Parallel Flows, Academic Press, N.Y.

Bouthier, M. 1972 Stabilité linéaire des écoulements presque paralléles, *J. de Mécanique*, Vol. 11, pp. 599–621.

Bouthier, M. 1973 Stabilité linéaire des écoulements presque paralléles, Partie II, *J. de Mécanique*, Vol. 12, pp. 76–95.

Brown, W.B. 1959 Numerical Calculation of the Stability of Cross Flow Profiles in Laminar Boundary Layers on a Rotating Disc and on a Swept Wing and an Exact Calculation of the Stability of the Blasius Velocity Profile, Report N. NAI 59-5, Northrop Aircraft Inc., Hawthorne, CA.

Brown, W.B. 1960 Exact Numerical Solution of the Stability Equations of the Laminar Boundary Layer, Paper presented at International Congress of Applied Mechanics, Stresa, Italy.

Brown, W.B. 1961 A Stability Criterion for Three-Dimensional Laminar Boundary Layers, in "Boundary Layer and Flow Control" (G. V. Lachmann, ed.), Vol. 2, pp. 913–923, Pergamon Press, London.

Brown, W.B. 1962 Exact Numerical Solutions of the Complete Linearized Equations for the Stability of Compressible Boundary Layers, Norair Report No. NOR-62-15, Northrop Aircraft Inc., Hawthorne, CA.

Brown, W.B. and Sayre, P.H. 1954 An Exact SOlution of the Orr-Sommerfeld Stability Equation for Low Reynolds Numbers, Report No. BLC-43, Northrop Aircraft Inc., Hawthorne, CA.

Cebeci, T. and Stewartson, K. 1980a Stability and Transition in Three-Dimensional Flows, *AIAA J.*, Vol. 18, pp. 398–405

Cebeci, T. and Stewartson, K. 1980b On the Prediction of Transition in Three-Dimensional Flows, in "Laminar-Turbulent Transition" (R. Eppler and H Fasel, eds.), Springer Verlag, Berlin.

Cochran, W.G. 1934 The Flow due to a Rotating Disk, *Proc. Cambridge Phil. Soc.*, Vol. 30, pp. 165–375.

Conte, S.D. and Miles, J.W. 1959 On the Numerical Integration of the Orr-Sommerfeld Equation, SIAM J. Vol. 7, pp. 361–366.

Conte, S.D. 1966 The numerical solution of linear boundary value problems, SIAM Review. Vol. 8, pp. 309–321.

Cooke, J.C. 1950 The Boundary layer of a Class of Infinite Yawed Cylinders, *Proc. Cambridge Phil. Soc.*, Vol. 46, pp. 645–648.

Corner, D., Houston, D.T.R. and Ross, M.A.S. 1976 Higher Eigenstates in Boundary-Layer Stability Theory, *J. Fluid Mech.*, Vol. 77, pp. 81–103.

Criminale, W.O. and Kovasnay, L.S.G. 1962 The Growth of Localized Disturbances in a Laminar Boundary Layer, *J. Fluid Mech.*, Vol. 14, pp. 59–80.

Davey, A. 1973 A Simple Numerical Method for Solving Orr-Sommerfeld Problems, Quart. J. Mech. Appl. Math., Vol. 26, pp. 401–411.

Davey, A. 1977 On the Numerical Solution of Difficult Eigenvalue Problems, *J. Comp. Phys.*, Vol. 24, pp. 331–338.

Davey, A. 1979 On the Removal of the Singularities from the Riccati Method, *J. Comp. Phys.*, Vol. 30, pp. 137–144.

Davey, A. 1981 A Difficult Numerical Calculation Concerning the Stability of the Blasius Boundary Layer, in Proceedings of Numbrecht Conf.

Demetriades, A. 1977 Laminar Boundary Layer Stability Measurements at Mach 7 Including Wall Temperature Effects, AFOSR TR-77-1311.

Dougherty, N.S. and Fisher, D.F. 1980 Boundary Layer Transition on a 10° Cone: Wind Tunnel/Flight Data Correlations, *AIAA Paper No. 80-0154*; also see NASA TP 1971 1982.

Dryden, H. 1959 Transition from Laminar to Turbulent Flow, in "Turbulent Flows and Heat Transfer" (C. C. Lin, ed.), pp. 1–74, Princeton Univ. Press, Princeton

Drazin, P.G. and Howard, L.N. 1966 Hydrodynamic Stability of Parallel Flow of Inviscid Fluid, in "Advances in pplied Mechanics" (G. Kuerti, ed.), Vol. 9, pp. 1–89, Academic Press, N.Y.

Drazin, P.G. and Reid, W.H. 1981 Hydrodynamic Stability, Cambridge Univ. Press, Cambridge.

Dunn, D.W. and Lin, C.C. 1955 On the Stability of the Laminar Boundary Layer in a Compressible Fluid, *J. Aero. Sci.*, Vol. 22, pp 455–577.

El-Hady, N.M. and Nayfeh, A.H. 1979 Nonparallel Stability of Compressible Boundary-layer Flows, Report VPI-E-79-13, Virginia Polytechnic Institute and State Univ., Blacksburg, VA.

Fjortoft, R. 1950 Application of Integral Theorems in Deriving Criteria of Stability for Laminar Flows and for the Baroclinic Circular Vortex, Geofys. Publ., Vol. 17.

Foote, J.R. and Lin, C.C. 1950 Some Recent Investigations in the Theory of Hydrodynamic Stability, *J. Fluid Mech.*, Vol. 8, pp. 165–280.

Gallagher, A.P. and Mercier, A.M. 1962 On the Behavior of Small Disturbances in Plane Couette Flow, Part I, *J. Fluid Mech.*, Vol. 13, pp. 91–100.

Gaster, M. 1962 A Note on a Relation between Temporally Increasing and Spatially Increasing Disturbances in Hydrodynamic Stability, *J. Fluid Mech.*, Vol. 14, pp. 222–224.

Gaster, M. 1963 On the Stability of Parallel Flows and the Behavior of Separation Bubbles, Ph.D. Thesis, Univ. of London.

Gaster, M. 1965a On the Generation of Spatially Growing Waves in a Boundary Layer, *J. Fluid Mech.*, Vol. 22, pp. 433–441.

Gaster, M. 1965b The Role of Spatially Growing Waves in the Theory of Hydrodynamic Stability, in "Progress in Aeronautical Sciences" (D. Küchemann and L. H. G. Sterne, eds.), Vol. 6, Pergamon Press, Oxford

Gaster, M. 1968 The Development of Three-Dimensional Wave Packets in a Boundary Layer, *J. Fluid Mech.*, Vol. 32, pp. 173–184.

Gaster, M. 1974 On the Effect of Boundary Layer Growth in Flow Stability, *J. Fluid Mech.*, Vol. 66, pp. 465–480.

Gaster, M. 1975 A Theoretical Model of a Wave Packet in the Boundary Layer on a Flat Plate, *Proc. Roy. Soc. A*, Vol. 347, pp. 271–289.

Gaster, M. 1978 On the Application of Ray Mathematics to Non-Conservative Systems, Proceedings of NSF Regional Conference on Geophysical Fluid Dynamical Wave Mathematics, pp. 61–66, Univ. of Washington, Seattle, Wash.

Gaster, M. 1981a On Transition to Turbulence in Boundary Layers, in "Transition to Turbulence" (R. E. Meyer, ed.), Proceedings of Symposium, Univ. of Wisconsin 1980, Academic Press, N.Y.

Gaster, M. 1981b Propagation of Linear Wave Packets in Laminar Boundary Layers, *AIAA J.*, Vol. 19, pp. 419–423.

Gaster, M. 1982a Estimates of Errors Incurred in Various Asymptotic Representations of Wave Packets, *J. Fluid Mech.*, Vol. 121, pp. 365–377.

Gaster, M. 1982b The Development of a Two-Dimensional Wave Packet in a Growing Boundary Layer, *Proc. Roy. Soc. A*, Vol. 384, pp. 317–332.

Gaster, M. and Davey, A. 1968 The Development of Three-Dimensional Wave Packets in Inviscid Parallel Flows, *J. Fluid Mech.*, Vol. 32, pp. 801–808.

Gaster, M. and Grant, I. 1975 An Experimental Investigation of the Formation and Development of a Wave Packet in a Laminar Boundary Layer, *Proc. Roy. Soc. A*, Vol. 347, pp. 253–269.

Gilev, V.M., Kachanov, Y.S. and Kozlov, V.V. 1981 Development of Spatial Wave Packets in a Boundary Layer, Preprint No. 34-81, Inst. of Theoretical and Appl. Math., USSR Acad. Sci., Novosibirsk.

Gill, A.E. 1965a A Mechanism for Instability of Plane Couette Flow and of Poiseuille Flow in a Pipe, *J. Fluid Mech.*, Vol. 21, pp. 505–511.

Gill, A.E. 1965b Instabilities of "Top-Hat" Jets and Wakes in Compressible Fluids, *Phys. Fluids*, Vol. 8, pp. 1428–1430.

Godunov, S.K. 1961 On the Numerical Solution of boundary value Problems for Systems of Ordinary Differential Equations, *Uspekhi Mat. Nauk*, Vol. 16, pp. 171–174.

Gray, W.E. 1952 The effect of wing sweep on laminar flow, *Royal Aircraft Establishment.*

Gregory, N., Stuart, J.T. and Walker, W.S. 1955 On the Stability of Three-Dimensional Boundary Layers with Application to the Flow Due to a Rotating Disk, *Phil. Trans. Roy. Soc. A*, Vol. 248, pp. 155–199.

Grosch, C.E. and Salwen, H. 1968 The Stability of Steady and Time-Dependent Plane Poiseuille Flow, *J. Fluid Mech.*, Vol. 34, pp. 177–205.

Grosch, C.E. and Salwen, H. 1978 Continuous Spectrum of the Orr-Sommerfelf Equation. Part I. The Spectrum and the Eigenfunctions, *J. Fluid Mech.*, Vol. 87, pp. 333–354.

Hama, F.R., Williams, D.R. and Fasel, H. 1980 Flow Field and Energy Balance According to the Spatial Linear Stability Theory of the Blasius Boundary Layer, in "Laminar-Turbulent Transition" (R. Eppler and H. Fasel, eds.), pp. 73–85, Springer, Berlin.

Hefner, J.N., and Bushnell, D.M. 1979 Application of Stability Theory to Laminar Flow Control, *AIAA Paper No. 79-1493.*

Heisenberg, W. 1924 Über Stabilität und Turbulenz von Flüssigkeitsströmen, Ann. Phys.-Lpz. (4), Vol. 79, pp. 577–627 (also NACA TM No. 1291).

Herbert, T. 1983a On perturbation methods in nonlinear stability theory, *J. Fluid Mech.*, Vol. 126, pp. 167–186.

Herbert, T. 1983b Secondary instability of plane channel flow to subharmonic three-dimensional disturbances, *Phys. Fluids*, Vol. 26, pp. 871–874.

Howard, L.N. 1961 Note on a paper of John W. Miles, *J. Fluid Mech.*, Vol. 10, pp. 509–512.

Jaffe, N.A., Okamura, T.T. and Smith, A.M.O. 1970 Determination of Spatial Amplification Factors and Their Application to Prediction Transition, *AIAA J.*, Vol. 8, pp. 301–308.

Jordinson, R. 1970 The Flat Plate Boundary Layer. Part I. Numerical Integration of the Orr-Sommerfeld Equation, *J. Fluid Mech.*, Vol. 43, pp. 801–811.

Jordinson, R. 1971 Spectrum of Eigenvalues of the Orr-Sommerfeld Equation for Blasius Flow, *Phys. Fluids*, Vol. 14, pp. 2535–2537.

Joseph, D.D. 1976 Stability of Fluid Motions, Springer Tracts on Natural Philosophy, Vol. 27 and 28, Springer, Berlin.

Kaplan, B. and Moore, A.H. 1964 Implicit Finite Difference Techniques for Solving Transient Heat Conduction Problems, Air Force Inst. Tech., Wright-Patterson AFB, OH.

Kármán, Th. von 1921 Über laminare und turbulente Reibung, ZAMM, Vol. 1, pp. 233–252. (also NACA TM No. 1092, 1946)

Kelvin, Lord 1880 On a Disturbing Infinity in Lord Rayleigh's Solution for Waves in a Plane Vortex Stratum, Math. and Phys. Papers, Vol. 8, pp. 186–187, Cambridge Univ. Press, Cambridge.

Kendall, J.M. 1967 Supersonic Boundary-Layer Stability Experiments, in Proceedings of Boundary Layer Transition Study Group Meeting (W. D. McMauley, ed.), Aerospace Corp. Report No. BSD-TR-67-213, Vol. II.

Kendall, J.M. 1971 JPL Experimental Investigations, in Proceedings of the Boundary-Layer Transition Workshop, Vol. IV, Aerospace Corp., San Bernardino, CA.

Kendall, J.M. 1975 Wind Tunnel Experiments Relating to Supersonic and Hypersonic Boundary-Layer Transition, *AIAA J.*, Vol. 13, pp. 240–299.

Küchemann, D. 1938 Störungsbewegungen in einger Gasströmung mit Grenzschicht, ZAMM, Vol. 18, pp. 207–222.

Kümmerer, H. 1973 Numerische Untersuchungen zur Stabilität ebener laminarer Grenzschichtströmungen, Dissertation, Universität Stuttgart.

Kurtz, E.F., Jr. 1961 Study of the Stability of Parallel Flows, Ph.D. Thesis, Massachusetts Institute of Technology, Cambridge, MA.

Kurtz, E.F., Jr. and Crandall, S.H. 1962 Computer-aided Analysis of Hydrodynamic Stability, J. Math. Phys., Vol. 41, pp. 264–279.

Lakin, W., Ng, B. and Reid, W.H. 1978 Approximation to the Eigenvalue Relation for the Orr-Sommerfeld Equation, *Phil. Trans. Roy. Soc. A*, Vol. 289, pp. 147–371.

Landahl, M.T. and Kaplan, R.E. 1965 Effect of Compliant Walls on Boundary Layer Stability and Transition, AGARDograph 97, Part 1, pp. 363–394, NATO, Paris.

Laufer, J. and Vrebalovich, T. 1960 Stability and Transition on a Supersonic Laminar Boundary Layer on an Insulated Flat Plate, *J. Fluid Mech.*, Vol. 9, pp. 257–299.

Lees, L. 1947 The Stability of the Laminar Boundary Layer in a Compressible Fluid, NACA Tech. Report No. 876

Lees, L. 1952 Instability of Laminar Flows and Transition to Turbulence, Consolidated Aircraft Corp., San Diego, CA, Report No. ZA-7-006.

Lees, L. and Gold, H. 1964 Stability of Laminar Boundary Layers and Wakes at Hypersonic Speeds: Part I. Stability of Laminar Wakes, Inter. Symp. on Fundamental Phenom. in Hypersonic Flow, GALCIT Memo., California Institute of Technology, Pasadena, CA.

Lees, L. and Lin, C.C. 1946 Investigation of the Stability of the Laminar Boundary Layer in a Compressible Fluid, NACA Tech. Note No. 1115.

Lees, L. and Reshotko, E. 1962 Stability of the Compressible Laminar Boundary Layer, *J. Fluid Mech.*, Vol. 12, pp. 555–590.

Lekoudis, S. 1979 Stability of Three-Dimensional Boundary Layers over Wings with Suction, *AIAA Paper No. 79-0265.*

Lekoudis, S. 1980 Stability of the Boundary Layer on a Swept Wing with Wall Cooling. *AIAA J.*, Vol. 18, pp. 1029–1035.

Lighthill, M.J. 1963 Introduction. Boundary Layer Theory, in "Laminar Boundary Layers" (L. Rosenhead. ed.), pp. 46–113.

Lin, C.C. 1945 On the Stability of Two-Dimensional Parallel Flows, Parts I, II, III, *J. Fluid Mech.*, Vol. 3, pp. 117–142, 218–234, 277–301.

Lin, C.C. 1954 Some Physical Aspects of the Stability of Parallel Flows, Proc. Nat. Acad. Sci., Vol. 40, pp. 741–747.

Lin, C.C. 1955 The Theory of Hydrodynamic Stability, Cambridge Univ. Press, Cambridge.

Lin, C.C. 1961 Some Mathematical Problems in the Theory of the Stability of Parallel Flows, *J. Fluid Mech.*, Vol. 10, pp. 430–438.

Mack, L.M. 1960 Numerical Calculation of the Stability of the Compressible Laminar Boundary Layer, Jet Propulsion Laboratory, Report No. 20-122, Pasadena, CA.

Mack, L.M. 1963 The Inviscid Stability of the Compressible Laminar Boundary Layer, in "Space Programs Summary," No. 37-23, p. 297, Jet Propulsion Laboratory, Pasadena, CA.

Mack, L.M. 1964 The Inviscid Stability of the Compressible Laminar Boundary Layer: Part II, in "Space Programs Summary," No. 37-26, Vol. IV, p. 165, Jet Propulsion Laboratory, Pasadena, CA.

Mack, L.M. 1965a Computation of the Stability of the Laminar Boundary Layer, in "Methods in Computational Physics" (B. Alder, S. Fernbach and M. Rotenberg, eds.), Vol. 4, pp. 247–299, Academic Press, N.Y.

Mack, L.M. 1965b Stability of the Compressible Laminar Boundary Layer According to a Direct Numerical Solution, in AGARDograph 97, Part I, pp. 329–362.

Mack, L.M. 1969 Boundary-Layer Stability Theory, Jet Propulsion Laboratory, Pasadena, CA, Document No. 900-277, Rev. A.

Mack, L.M. 1971 Progress in Compressible Boundary Layer Stability Computations, in Proceedings of the Boundary Layer Transition Workshop, Vol. 1, pp. 1-1 to 1-19, Aerospace Corp., San Bernardino, CA.

Mack, L.M. 1975 Linear Stability and the Problem of Supersonic Boundary-Layer Transition, *AIAA J.*, Vol. 13, pp. 278–289.

Mack, L.M. 1976 A Numerical Study of the Temporal Eigenvalue Spectrum of the Blasius Boundary Layer, *J. Fluid Mech.*, Vol. 79, pp. 497–520.

Mack, L.M. 1977 Transition Prediction and Linear Stability Theory, in AGARD Conference Proceedings No. 224, pp. 1-1 to 1-22, NATO, Paris.

Mack, L.M. 1979a On the Stability of the Boundary Layer on a Transonic Swept Wing, *AIAA Paper No. 79-0264*.

Mack, L.M. 1979b Three-Dimensional Effects in Boundary-Layer Stability, in Proceedings of Twelfth Symposium on Naval Hydrodynamics, pp. 63–70, National Academy of Sciences, Washington, D.C.

Mack, L.M. 1981 Compressible Boundary-Layer Stability Calculations for Sweptback Wings with Suction, *AIAA J.*, Vol. 20, pp. 363–369.

Mack, L.M. 1984a Line Sources of Instability Waves in a Blasius Boundary Layer, *AIAA Paper No. 84-0168*.

Mack, L.M. 1984b Remarks on Disputed Results in Compressible Boundary-Layer Stability Theory, *Phys. Fluids*, Vol. 27, pp. 342–347.

Mack, L.M. 1985 The Wave Pattern Produced by a Point Source on a Rotating Disk, *AIAA Paper No. 85-0490*.

Mack, L.M. and Kendall, J.M. 1983 Wave Pattern Produced by a Localized Harmonic Source in a Blasius Boundary Layer, *AIAA Paper No. 83-0046*.

Mack, L.M. and Morkovin, M.V. 1971 High-Speed Boundary-Layer Stability and Transition, Recorded Lecture Series, AIAA, N.Y.

Malik, M.R. 1982 COSAL - A Black-Box Compressible Stability Analysis Code for Transition Prediction in Three-Dimensional BOundary Layers, NASA CR-165925

Malik, M.R. and Orszag, S.A. 1981 Efficient Computation of the Stability of Three-Dimensional Boundary Layers, *AIAA Paper No. 81-1277*.

Malik, M.R., Wilkinson, S.P. and Orszag, S.A. 1981 Instability and Transition in Rotating Disk Flow, *AIAA J.* Vol. 19, pp. 1131–1138.

Schlichting, H. 1971a Statistical Fluid Mechanics, Volume I: Mechanics of Turbulence, M.I.T. Press, Cambridge, MA.

Schlichting, H. 1971b Statistical Fluid Mechanics, Volume II: Mechanics of Turbulence, M.I.T. Press, Cambridge, MA.

Morkovin, M.V. 1968 Critical Evaluation of Transition from Laminar to Turbulent Shear Layers with Emphasis on Hypersonically Travelling Bodies, Report AFFDL-TR-68-149, Wright-Patterson Air Force Base, Ohio.

Morkovin, M.V. 1978 Instability, Transition to Turbulence, and Predictability, AGARDograph No. 236, NATO, Paris.

Morkovin, M.V. 1983 Understanding Transition to Turbulence in Shear Layers, Report AFOSR FR-83, Illinois Institute of Technology, Chicago, IL.

Morkovin, M.V. 1985 Guide to Experiments in Instability and the Laminar Turbulent Transition in Shear Layers, in Notes from AIAA Professional Study Seminar: Instabilities and Transition to Turbulence, Cincinnati, Ohio.

Murdock, J.W. and Stewartson, K. 1977 Spectra of the Orr-Sommerfeld Equation, *Phys. Fluids*, Vol. 20, pp. 1404–1416.

Nachtsheim, P. 1963 Stability of Free-Convection Boundary Layer Flows, NASA Tech. Note No. D-2089.

Nachtsheim, P. 1964 An Initial Value Method for the Numerical Treatment of the Orr-Sommerfeld Equation for the Case of Plane Poiseuille Flow, NASA Tech. Note No. D-2414.

Nayfeh, A.H. 1980a Stability of Three-Dimensional Boundary Layers, *AIAA J.*, Vol. 18, pp. 406–416.

Nayfeh, A.H. 1980b Three-Dimensional Stability of Growing Boundary Layers, in "Laminar-Turbulent Transition" (R. Eppler and H. Fasel, eds.), pp. 201–217, Springer, Berlin.

Nayfeh, A.H. and Padhye, A. 1979 The Relation between Temporal and Spatial Stability in Three-Dimensional Flows, *AIAA J.*, Vol. 17, pp. 1084–1090.

Ng, B. and Reid, W.H. 1979 An Initial Value Method for Eigenvalue Problems Using Compound Matrices, *J. Comp. Phys.*, Vol. 30, pp. 135–136.

Ng, B. and Reid, W.H. 1980 On the Numerical Solution of the Orr-Sommerfeld Equation: Asymptotic Initial Conditions for Shooting Method, *J. Comp. Phys.*, Vol. 38, pp. 275–293.

Noether, F. 1921 Das Turbulenzproblem, ZAMM, Vol. 1, pp. 125–138.

Obremski, H.T., Morkovin, M.V. and Landahl, M.T. 1969 A Portfolio of Stability Characteristics of Incompressible Boundary Layers, AGARDograph No. 134, NATO, Paris.

Orszag, S.A. 1971 Accurate Solution of the Orr-Sommerfeld Stability Equation, *J. Fluid Mech.*, Vol. 50, pp. 689–703.

Osborne, M.R. 1967 Numerical Methods for Hydrodynamic Stability Problems, SIAM J. Appl. Math., pp. 539–557.

Pfenninger, W. 1977 Laminar Flow Control-Laminarization, in "Special Course on Concepts for Drag Reduction," AGARD Report No. 654, pp. 3-1 to 3-75, NATO, Paris.

Phillips, O. 1960 On the Generation of Sound by Supersonic Shear Layers, *J. Fluid Mech.*, Vol. 9, pp. 1–28.

Poll, D.I.A. 1977 Leading Edge Transition on Swept Wings, in "Laminar-Turbulent Transition," AGARD Conference Proceedings No. 224, pp. 21-1 to 21-11, NATO, Paris.

Prandtl, L. 1921 Bemerkungen über die Enstehung der Turbulenz, ZAMM, Vol. 1, pp. 431–436.

Pretsch, J. 1942 Anfachung instabler Störungen in einer laminaren Reigungsschicht, Jb. deutsch. Luftfahrtfor., pp. 154–171.

Radbill, J.R. and Van Driest, E.R. 1966 A New Method for Prediction of Stability of Laminar Boundary Layers, AFOSR Report No. 66-0702.

Rayleigh, Lord 1880 On the Stability or Instability of Certain Fluid Motions, in "Scientific Papers," Vol. 1, pp. 474–487, Cambridge Univ. Press, Cambridge

Rayleigh, Lord 1887 On the Stability or Instability of Certain Fluid Motions. II, in "Scientific Papers," Vol. 3, pp. 17–23, Cambridge Univ. Press, Cambridge

Rayleigh, Lord 1892 On the Question of the Stability of the Flow of Fluids, in "Scientific Papers," Vol. 3, pp. 575–584, Cambridge Univ. Press, Cambridge

Rayleigh, Lord 1895 On the Stability or Instability of Certain Fluid Motions. III, in "Scientific Papers," Vol. 4, pp. 203–219, Cambridge Univ. Press, Cambridge

Rayleigh, Lord 1913 On the Stability of the Laminar Motion of an Inviscid Fluid, in "Scientific Papers," Vol. 6, pp. 197–204, Cambridge Univ. Press, Cambridge

Reid, W.H. 1965 The Stability of Parallel Flows, in "Basic Developments in Fluid Dynamics" (M. Hold, ed.), Vol. 1, pp. 249–307, Academic Press, N.Y.

Reshotko, E. 1960 Stability of the Compressible Laminar Boundary Layer, GALCIT Memo. No. 52, California Institute of Technology, Pasadena, CA.

Reshotko, E. 1962 Stability of Three-Dimensional Compressible Boundary Layers, NASA Tech. Note D-1220.

Reshotko, E. 1976 Boundary Layer Stability and Transition, *Annu. Rev. Fluid Mech.*, Vol. 8, pp. 311–349.

Reynolds, O. 1895 On the Dynamical Theory of Incompressible Viscous Fluids and the Determination of the Criterion, *Phil. Trans. Roy. Soc. A*, Vol. 186, pp. 123–164.

Rosenhead, L. 1963 Laminar Boundary Layers, Oxford Univ. Press, Oxford.

Saric, W.S. and Nayfeh, A.H. 1975 Non-parallel Stability of Boundary Layer Flows, *Phys. Fluids*, Vol. 18, pp. 945–950.

Saric, W.S. and Nayfeh, A.H. 1977 Nonparallel Stability of Boundary Layers with Pressure Gradients and Suction, in AGARD Conference Proceedings No. 224, NATO, Paris.

Schlichting, H. 1933a Zur Entstehung der Turbulenz bei der Plattenströmung, Nachr. Ges. Wiss. Göttingen, Math.-phys. Kasse, pp. 181–208.

Schlichting, H. 1933b Berechnung der Anfachung kleiner Störungen bei der Plattenströmung, ZAMM, Vol. 13, pp. 171–174.

Schlichting, H. 1935 Amplitudenverteilung und Energiebilanz der kleinen Störungen bei der Plattengrenzschicht, Nachr. Ges. Wiss. Göttingen, Math.-phys. Kasse, Vol. 1, pp. 47–78.

Schlichting, H. 1940 Über die theoretische Berechnung der kritischen Reynoldschen Zahl einer Reibungaschicht in beschleunigter ind verzögerter Stromung, J. deutsch. Luftfahrtfor. I, p. 97.

Schlichting, H. 1959 Entstehung der Turbulenz, in "Handbuch der Physik" (S. Flugge, ed.), Vol. VIII/I, pp. 351–450, Springer, Berlin.

Schlichting, H. 1979 Boundary Layer Theory (7th Ed.), McGraw-Hill, N.Y.

Schubauer, G.B. and Skramstad, H.K. 1947 Laminar Boundary Layer Oscillations and Transitions on a Flat Plate, *J. Aero. Sci.*, Vol. 14, pp. 69–76; also NACA Report 909, 1948.

Scott, M.R. and Watts, H.A. 1977 Computational Solution of Linear Two-Point Boundary Value Problems and Orthonormalization, SIAM J. Numer. Anal., Vol. 14, pp. 40–70.

Shen, S.F. 1964 Stability of Laminar Flows, in "Theory of Laminar Flows" (F.K. Moore, ed.), pp. 719–853, Princeton Univ. Press, Princeton.

Smith, A.M.O. and Gamberoni, N. 1956 Transition, Pressure Gradient and Stability Theory, Report No. 26388, Douglas Aircraft Co., Inc., El Segundo, CA.

Squire, H.B. 1933 On the Stability of Three-Dimensional Disturbances of Viscous Flow between Parallel Walls, *Proc. Roy. Soc. A*, Vol. 142, pp. 621–628.

Srokowski, A. and Orszag, S.A. 1977 Mass Flow Requirements for LFC Wing Design, *AIAA Paper No. 77-1222.*

Stetson, K.F., Thompson, E.R., Donaldson, J.C. and Siler, L.G. 1983 Laminar Boundary Layer Stability Experiments on a Cone at Mach 8. Part 1: Sharp Cone, *AIAA Paper No. 83-1761.*

Stetson, E.R., Donaldson, J.C. and Thompson, E.R. 1984 Laminar Boundary Layer Stability Experiments on a Cone at Mach 8. Part 2: Blunt Cone, *AIAA Paper No. 84-0006.*

Stuart, J.T. 1963 Hydrodynamic Stability, in "Laminar Boundary Layers" (L. Rosenhead, ed.), pp. 629–670, Oxford Univ. Press, Oxford.

Tani, I. 1969 Boundary-Layer Transition, *Annu. Rev. Fluid Mech.*, Vol. 1, pp. 169–196.

Tani, I. 1981 Three-Dimensional Aspects of Boundary-Layer Transition, Proc. Indian Acad. Sci. (Engg. Br.), Vol. 4, Pt. 2, pp. 219–238.

Tatsumi, T. and Gotch, K. 1971 in Instability of Continuous Systems (H. Leipholz, ed.), p. 368.

Taylor, G.I. 1915 Eddy Motion in the Atmosphere, *Phil. Trans. Roy. Soc. A*, Vol. 215, pp. 1–26.

Taylor, G.I. 1938 Some Recent Developments in the Study of Turbulence, Proceedings of 5th Inter. Congr. Appl. Mech., Cambridge, MA, pp. 294–310.

Thomas, L.H. 1953 The Stability of Plane Poiseuille Flow, *Phys. Rev.*, Vol. 91, pp. 780–783.

Tollmien, W. 1929 Über die Entstehung der Turbulenz, Nachr. Ges. Wiss. Göttingen, Math.-phys. Klasse, pp. 21–44.

Tollmien, W. 1935 Ein allgemeines Kriterium der Instabilität laminarer Geschwindigkeitsverteilungen, Nachr. Ges. Wiss. Göttingen, Math.-phys. Klasse, Vol. 50, pp. 79–114.

Van Ingen, J.L. 1956 A Suggested Semi-Empirical Method for the Calculation of the Boundary Layer Transition Region, Univ. of Tech., Dept. Aero. Eng., Report VTH-74, Delft, Holland.

Van Stijn, T.L. and Van De Vooren, A.I. 1982 An Accurate Method for Solving the Orr-Sommerfeld Equation, *J. Eng. Math.*, Vol. 14, pp. 17–26.

Van Stijn, T.L. and Van De Vooren, A.I. 1983 On the Stability of Almost Parallel Boundary-Layer Flows, *Computers and Fluids*, Vol. 10, pp. 223–241.

Wasow, W. 1948 The Complex Asymptotic Theory of a Fourth Order Differential Equation of Hydrodynamics, *Ann. Math. (2)*, Vol. 49, pp. 852–871.

Wazzan, A.R., Okamura, T.T. and Smith, A.M.O. 1968a Spatial and Temporal Stability Charts for the Falkner-Skan Boundary-layer Profiles, Report No. DAC-67086, McDonnell-Douglas Aircraft Co., Long Beach, CA.

Wazzan, A.R., Okamura, T.T. and Smith, A.M.O. 1968b The Stability of Water Flow over Heated and Cooled Flat Plates, *J. Heat Transfer*, Vol. 90, pp. 109–114.

Wazzan, A.R., Taghavi, H. and Keltner, G. 1984 The Effect of Mach Number on the Spatial Stability of Adiabatic Flat Plate Flow to Oblique Disturbances, *Phys. Fluids*, Vol. 27, pp. 331–341.

White, F.M. 1974 Viscous Fluid Flow, McGraw-Hill, N.Y.

Wilkinson, S.P. and Malik, M.R. 1983 Stability Experiments in Rotating-Disk Flow, *AIAA Paper No. 83-1760.*

Zaat, J.A. 1958 Numerische Beiträge zur Stabilitätstheorie der Grenzschichten, Grenzschichtforschung Symp., IUTAM, pp. 127–138, Springer, Berlin.

Acknowledgement

This paper represents the results of research carried out at the Jet Propulsion Laboratory, California Institute of Technology under NASA Contract No. NAS7-918.

Support from the Fluid and Thermal Physics Branch of the Aerospace Research Division, Office of Aeronautics and Space Technology, NASA, for the preparation of this document is gratefully acknowledged.